



UNIVERSITA' DEGLI STUDI DI TORINO

DOCTORAL SCHOOL OF SCIENCES AND INNOVATIVE
TECHNOLOGIES

INDIRIZZO IN FISICA ED ASTROFISICA

Measurement of D^+ meson production in p–Pb collisions with the ALICE detector

Autor:
Riccardo Russo

Supervisor: Stefania Beole'
Co-Supervisor: Francesco Prino
Examiner: Jaroslav Bielčik

Vorrei iniziare ringraziando i miei genitori, Pino e Cristina, per avermi sostenuto in 21 lunghi anni di formazione. Loro e le mie sorelle sono la famiglia che augurerei a chiunque di avere.

Questo lavoro non si sarebbe mai concluso senza la preziosa e costante guida di Stefania e Francesco, che mi hanno introdotto in un ambiente di lavoro stimolante ed altamente formativo, accompagnandomi in tutte le prove che si sono presentate.

Ringrazio Elena Bruna, collega ed amica, che e' stata una guida nella mia analisi di fisica in particolare durante il primo anno. Lavorare con lei mi ha reso piu' indipendente e mi ha permesso di proseguire piu' autonomamente l'analisi dei dati protone piombo. Inoltre ringrazio la sua disponibilita' nei giorni prima della discussione.

Vorrei anche ringraziare Davide Caffarri e Zaida Conesa del Valle (che se leggera', capira' benissimo anche in italiano). Loro sono stati i coordinatori del gruppo di lavoro da noi chiamato "D2H" durante il periodo in cui ho svolto l'analisi di dottorato, e sono riusciti a coordinare ottimamente il mio lavoro e quello di altri per ottenere i risultati di fisica esposti in questa tesi.

Esprimo un pensiero a parte per il collega ed amico Gian Michele, che ha vissuto il periodo di scrittura della tesi un anno fa, nella scrivania accanto alla mia. E' stato di grande aiuto sia direttamente, mettendo a mia disposizione la sua maggiore esperienza, sia indirettamente mostrandomi come portare a termine un dottorato nel migliore dei modi.

Inoltre ringrazio:

- *Stefania Bufalino per il grande supporto durante l'anno al CERN. Sono molto felice che si ritrasferisca da noi a Torino*
- *le amiche di Torino: Sarah, Sara, Cristina ed Anastasia, la nostra new entry*
- *gli amici di Torino: Maximiliano, Stefano, Niccolo', Bruno Alessandro ed il Prof. Massimo Masera*
- *Yasser, che come me si dottora il 31/03/2015 e insieme a me ha negli ultimi due anni ha subito il furto di: quattro PC, documenti, passaporto, permesso di soggiorno, due cellulari, valigie con tutti gli indumenti e di certo sto dimenticando qualcosa.*
- *gli amici di Ginevra: Andrea, Martino, Stefano, Chiara, Federica, Emilia, Raffaella, Cristina. Avete reso il mio anno a Ginevra un anno migliore*
- *Grazia per il grande impegno nel prendersi cura in prima persona del Paper R_{pPb}*
- *Chiara Oppedisano per le consulenze in particolare sui Capitoli 3 e 7*

UNIVERSITA' DEGLI STUDI DI TORINO

Abstract

Measurement of D^+ meson production in p-Pb collisions with the ALICE detector

by Riccardo RUSSO

This thesis describes the measurement of D^+ -meson production in p-Pb collisions at $\sqrt{s_{NN}} = 5.02$ TeV at the Large Hadron Collider with the ALICE detector.

The main goal of the experimental programs on ultra-relativistic heavy ion collisions at the LHC is the production and characterization of the Quark Gluon Plasma (QGP), a phase of nuclear matter in which strongly interacting constituents (quarks and gluons) are deconfined. Heavy quarks are considered effective probes of the properties of the QGP as they are created on a short time scale, with respect to that of the QGP, and subsequently interact with it.

Moreover, for a proper assessment of the characteristics of the matter produced in heavy-ion collisions, it is important to disentangle the final state effects due to the formation of a QGP from the initial state effects due to the fact that nuclei are present in the colliding system. Both initial and final state effects may lead to qualitatively similar phenomena in the observables of interest.

The measurement of charmed meson production in proton-nucleus collisions allows to assess initial state effects present in nuclear collisions, under the assumption that an extended deconfined medium is not created in this kind of interactions. The nuclear modification factor of D mesons in p-Pb collisions (R_{pPb}) is essential for a complete understanding of the modification of D mesons momentum distributions observed in Pb-Pb collisions at $\sqrt{s_{NN}} = 2.76$ TeV, which is interpreted as due to the c -quark energy loss in the medium. In addition, some of the results obtained from high-multiplicity p-Pb collisions at LHC, such as the ridge structure in the two-particle correlation function, turned out to be unexpected, and have been interpreted in terms of final state effects such as hydrodynamic flow. These aspects make a study of charmed meson production in p-Pb collisions as a function of the event multiplicity of great interest.

In the first Chapter of this thesis, an introduction to the physics of heavy-ion collisions will be given. The second Chapter will be dedicated to a description of heavy flavour production in proton-proton, proton-nucleus and nucleus-nucleus collisions, focusing in particular on the initial and final state effects present in nuclear interactions. In Chapter three, the main features of the ALICE apparatus will be discussed, with a specific focus on the detectors that are directly involved in the D^+ -meson analyses. In Chapter four, the procedure used to extract the D^+ -meson yield from the p-Pb data sample collected in 2013 by the ALICE Collaboration is described. Chapter five is focused on the measurement of the prompt D^+ -meson nuclear modification factor in p-Pb collisions at $\sqrt{s_{NN}} = 5.02$ TeV which was published in [1]. Chapter six describes a data-driven method for separating the contribution of prompt D^+ mesons from that of D^+ mesons coming from B-hadron decays alternative to the one based on theoretical calculations used in [1]. In the last Chapter the measurement of D^+ -meson production as a function of event multiplicity will be discussed.

The measurements presented in this thesis were approved by the ALICE Collaboration and presented in various conferences. The few measurements that are not yet approved will report the label "This Thesis".

*Abstract***Measurement of D^+ meson production in p–Pb collisions with the ALICE detector**

by Riccardo RUSSO

Questa tesi espone la misura della produzione di mesoni D^+ in collisioni protone piombo a $\sqrt{s_{NN}} = 5.02$ TeV con l'esperimento ALICE a LHC.

Il principale obiettivo degli esperimenti sulle collisioni di ioni pesanti ultrarelativistiche e' la produzione e la caratterizzazione del plasma di quark e gluoni (QGP), una fase della materia nucleare in cui i costituenti elementari del nucleo (quark e gluoni) sono deconfinati. I quark pesanti sono considerati utili sonde per lo studio del QGP perche' vengono creati in tempi brevi rispetto alla durata della fase di QGP con il quale interagiscono. Inoltre, per una completa caratterizzazione della materia prodotta in collisioni nucleari, e' importante distinguere gli effetti di stato finale dovuti alla formazione del QGP da quelli di stato iniziale dovuti al fatto che le particelle che collidono sono nuclei. Entrambe le categorie di effetti possono risultare in fenomeni qualitativamente simili nelle osservabili di interesse.

La misura della sezione d'urto di produzione di mesoni charmati in collisioni protone nucleo permette di evidenziare gli effetti di stato iniziale presenti nelle collisioni nucleari, se si assume che in queste collisioni non si crei un mezzo deconfinato esteso. Il fattore di modificazione nucleare dei mesoni D in collisioni protone piombo (R_{pPb}) e' una quantita' fondamentale per comprendere la modifica delle distribuzioni in momento dei mesoni D osservata in collisioni piombo piombo ad una energia nel centro di massa $\sqrt{s_{NN}} = 2.76$ TeV, interpretata come un effetto della perdita di energia dei quark c nel mezzo. Inoltre, alcune delle misure ottenute in collisioni protone piombo ad alta molteplicita' a LHC hanno dato risultati inaspettati, che sono stati interpretati come effetti di stato finale e di flusso idrodinamico. Lo studio della produzione di mesoni charmati in funzione della molteplicita' in collisioni protone piombo ha quindi un suo interesse.

Nel primo capitolo di questa tesi verra' introdotta la fisica delle collisioni nucleari. Il secondo capitolo e' dedicato alla produzione di quark pesanti in collisioni protone protone, protone nucleo e nucleo nucleo, con un'attenzione particolare sugli effetti di stato iniziale e finale. Il terzo capitolo descrive sommariamente l'apparato dell'esperimento ALICE, approfondendone le componenti maggiormente usate nello studio dei mesoni D . Il quarto capitolo descrive la strategia di ricostruzione dei mesoni D in collisioni protone piombo. Il quinto capitolo e' dedicato alla misura del fattore di modificazione nucleare dei mesoni D^+ in collisioni protone piombo ad un'energia nel centro di massa di $\sqrt{s_{NN}} = 5.02$ TeV, risultato pubblicato in [1]. Il sesto capitolo descrive un metodo di sottrazione dei mesoni D da decadimento di quark beauty basato sui dati, alternativo a quello basato su predizioni teoriche utilizzato in [1]. L'ultimo capitolo discute la misura della produzione di mesoni D^+ in funzione della molteplicita' dell'evento protone piombo.

I risultati presentati in questa tesi sono stati approvati dalla Collaborazione ALICE, e presentati a diverse conferenze internazionali. Alcuni risultati non ancora approvati sono mostrati con l'etichetta "This thesis".

Contents

Abstract	ii
Abstract	ii
Contents	iv
1 Introduction: Quarks, Gluons and Quark-Gluon Plasma	1
1.1 Quantum Chromodynamics and Confinement	1
1.1.1 Confinement	4
1.1.2 Deconfinement	5
1.2 Lattice QCD	8
1.2.1 Lattice QCD predictions	9
1.3 Heavy Ion Collisions	11
1.3.1 Geometry and evolution	11
1.3.2 Glauber Model	13
1.4 Heavy-ion physics observables	16
1.4.1 Thermal photons	16
1.4.2 Hadronic abundances	17
1.4.3 Transverse momentum spectra of hadrons	19
1.4.4 Hadronization	20
1.4.5 Elliptic flow	21
1.4.6 Higher order armonics	23
1.4.7 Observables related to chiral symmetry restoration	25
1.4.8 Quarkonia	26
2 Heavy flavours as probes of the QGP	28
2.1 Charm quark production in pp collisions [2]	29
2.1.1 Parton Distribution Functions: $\mathbf{PDF}(\mathbf{x}_a, Q^2)$	30
2.1.2 Partonic cross-section: $\sigma_{ab \rightarrow q\bar{q}}$	31
2.1.3 Fragmentation Functions: $D_{q \rightarrow H}(z_q, Q^2)$	33
2.1.4 Some results in pp(\bar{p})	35
2.2 Charm quark production in ultrarelativistic heavy-ion collisions	38
2.2.1 Initial State Effects	40
2.2.2 Hot Nuclear Matter Effects	43
2.2.2.1 Collisional Energy Loss	44
2.2.2.2 Radiative Energy Loss	44

2.2.3	Charm quark thermalization	46
2.2.4	Some results from pA collisions	48
2.2.5	Some results from AA collisions	50
3	p–Pb collisions with the ALICE detector	57
3.1	ALICE Detector	59
3.1.1	Inner Tracking System (ITS)	60
3.1.2	Time Projection Chamber (TPC)	62
3.1.3	Time of Flight Detector (TOF)	63
3.1.4	V0 detector	63
3.1.5	Zero Degree Calorimeter (ZDC)	64
3.2	ALICE Performance	65
3.2.1	Trigger	65
3.2.2	Background rejection	65
3.2.3	Track and vertex reconstruction	67
3.2.4	Particle Identification	69
3.3	Centrality determination with ALICE	71
3.3.1	Centrality determination in Pb–Pb collisions	72
3.3.2	Centrality determination in p–Pb collisions	74
3.3.3	Biases on centrality in p–Pb collisions	76
3.3.3.1	Multiplicity bias	76
3.3.3.2	Jet-veto bias	79
3.3.3.3	Geometrical bias	79
4	Reconstruction of prompt D^+ mesons in p–Pb collisions	84
4.1	D^+ meson signal in p–Pb collisions	85
4.1.1	Event Selection	87
4.1.2	Track Selection	88
4.1.3	Kinematical and topological selection	89
4.1.4	Particle Identification	96
4.2	Monte Carlo simulations of $D^{+/-}$ mesons in ALICE	98
4.2.1	Monte Carlo data sample	99
4.2.2	Acceptance and efficiency computation	100
5	Prompt D^+-meson production in p–Pb collisions	102
5.1	Signal Extraction	104
5.2	Cross section calculation	109
5.3	Acceptance and efficiency corrections	110
5.4	Beauty Feed-down subtraction	113
5.5	The pp reference at 5.02 TeV	114
5.5.1	pp reference at $\sqrt{s} = 2.76$ TeV	116
5.5.2	pp reference at $\sqrt{s} = 5.02$ TeV	117
5.6	Systematic uncertainties	118
5.6.1	Systematic uncertainty due to the yield extraction	119
5.6.2	Systematic uncertainty due to topological cut efficiency	120
5.6.3	Systematic uncertainty due to PID	121
5.6.4	Systematic due to the p_T shape of generated D^+ mesons	122

5.6.5	Systematic uncertainty due to track reconstruction efficiency . . .	123
5.6.6	Systematic uncertainty due to beauty feed-down subtraction . . .	123
5.6.7	Systematic uncertainty on pp reference (only for measurement) . .	125
5.6.8	Luminosity and branching ratio	125
5.7	Results	126
5.7.1	D ⁺ -meson cross section	126
5.7.2	D ⁺ -meson nuclear modification factor	127
5.7.3	Comparison to model calculations	128
5.7.4	Comparison to results with heavy-flavour decay electrons and muons	130
5.7.5	Comparison to some results in the beauty sector	131
5.7.6	Conclusions	131
6	Data-driven beauty feed-down subtraction	134
6.1	Impact parameter distributions	136
6.1.1	Prompt D ⁺ mesons in MC simulations	136
6.1.2	Feed-down D ⁺ -meson in MC simulations	136
6.1.3	Impact Parameter distributions in data	143
6.2	Fit method	145
6.3	Systematic uncertainties	148
6.3.1	Systematic uncertainty on fit method	148
6.3.2	Systematic uncertainty on sideband subtraction	150
6.3.3	Systematic uncertainty on the p _T shape of generated D ⁺ mesons in MC	151
6.4	Results	152
7	D⁺-meson production as a function of multiplicity	154
7.1	D ⁺ -meson Q _{pPb}	156
7.1.1	Signal Extraction	157
7.1.2	Acceptance and efficiency corrections	160
7.1.3	Systematic Uncertainties	161
7.1.4	Results	163
7.2	D ⁺ -meson production as a function of charged particle multiplicity	167
7.2.1	Charged particle multiplicity determination and correction	167
7.2.2	Signal Extraction	171
7.2.3	Selection efficiency correction and beauty feed-down subtraction . .	173
7.2.4	Systematic Uncertainties	174
7.2.4.1	Systematic uncertainty on the yield extraction	174
7.2.4.2	Systematic uncertainty on the topological cut efficiency . .	175
7.2.4.3	Systematic uncertainty on PID	176
7.2.4.4	Systematic uncertainty on beauty feed-down subtraction . .	177
7.2.4.5	Systematic uncertainty on the determination of N _{ch} . . .	178
7.2.5	Results	178
8	Conclusions	182
A	R_{pPb} equations	184
B	ALICE Coordinate System	185

Chapter 1

Introduction: Quarks, Gluons and Quark-Gluon Plasma

1.1 Quantum Chromodynamics and Confinement

During the 60's the strong force was by far the most poorly understood among the four fundamental interactions. Many new particles were discovered in those years beside proton, neutron and electron in high energy experiments. Gell-Mann (Nobel prize, 1969) suggested that these new particles could be grouped in multiplets (singlets, octets, decuplets) each one composed of particles having roughly the same mass, hypothesizing the existence of an underlying new physics obeying an unknown internal symmetry between pointlike constituents. The observation of strange particles suggested that the symmetry group could be SU(3), and that hadrons consist of elementary constituents named quarks, that belong to the fundamental representation of SU(3): the up and down quarks are the constituents of ordinary matter (protons and neutrons), while the strange quark is present in strange particles [3]. All hadrons known at that time were grouped in non-fundamental representations of the SU(3) group, octets and decuplets (the same way nucleons and pions were identified as representations of the isospin SU(2) symmetry). Figure 1.1 shows the Δ decuplet, which however exhibits an evident violation of the Pauli principle: Δ^{++} , Δ^- and Ω have 3 quarks of the same flavour in the same spin state and this forbids their wave function

$$\psi = \psi(x) * \psi_{flavour} * \psi_{spin} \tag{1.1}$$

to be completely antisymmetric.

This puzzle led to the introduction of a new degree of freedom for quarks named color,

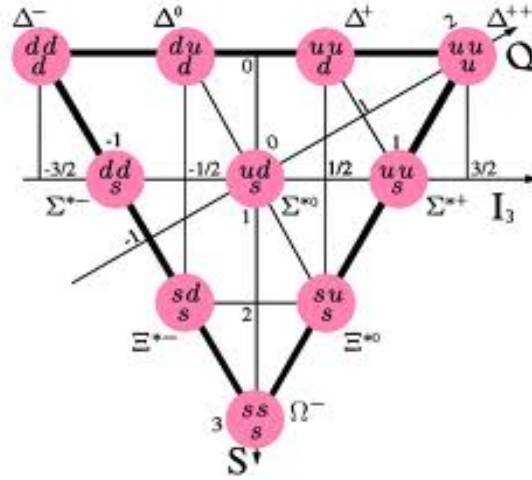


FIGURE 1.1: The Δ decuplet: three axis are shown, relative to the quantum numbers that identify each particle: isospin, electric charge and strangeness

with the following properties:

- there are 3 colors for quarks and 3 anticolors for antiquarks
- all hadrons in nature show up in a colorless combination of quarks, that is 3 different colored quarks (baryons) or a quark with one color and an antiquark with the respective anticolor (mesons); this property is necessary to explain why this new degree of freedom never shows up in hadronic interactions

In the late 60's, experiments carried out to explore the electromagnetic structure of protons by mean of electromagnetic probes (electrons and muons), showed clearly that, above a few GeV/c of momentum transfer, scattering occurs between the accelerated electrons (or muons) and pointlike constituents. These deep inelastic scattering (DIS) experiments lead Feynman (Nobel prize, 1965) to the formulation of the parton theory, in which protons are made of elementary constituents; partons and quarks are the same thing, and DIS experiments were actually the first observation of quarks [4].

In those years the importance of gauge theories was becoming evident, based on the success of Quantum ElectroDynamics (QED), a theory based on the $U(1)$ symmetry group with one conserved charge. It was argued that analogously the strong interaction could be described by a gauge theory invariant under $SU(3)$ group transformations (local rotations in color space) with three conserved colour charges.

In QED the gauge transformations correspond to changes in the phase of the wave function

$$\psi \rightarrow e^{i\alpha}\psi \quad (1.2)$$

and if the transformation is local ($\alpha = \alpha(x)$) the derivative of the wavefunction varies by a non-trivial term

$$\partial_\mu\psi \rightarrow \partial_\mu e^{i\alpha}\psi = e^{i\alpha}(\partial_\mu\psi) + e^{i\alpha}(i\partial_\mu\alpha)\psi \quad (1.3)$$

The unwanted second term is cancelled by the gauge change of the electromagnetic potential A_μ ,

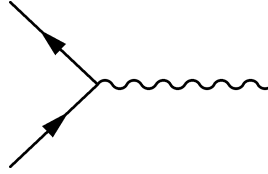
$$A_\mu \rightarrow A_\mu + \frac{1}{e}\partial_\mu\alpha \quad (1.4)$$

if the potential is added to the derivative operator in minimal coupling $(\partial_\mu\psi + ieA_\mu)$. The QED lagrangian is thus obtained as

$$L_{QED} = i\bar{\psi}\gamma^\mu(\partial_\mu\psi + ieA_\mu)\psi - m\psi\bar{\psi} - \frac{1}{4}F_{\mu\nu}F^{\mu\nu} \quad (1.5)$$

where the electromagnetic field tensor $F_{\mu\nu} = \partial_\mu A_\nu - \partial_\nu A_\mu$ is also invariant under the Gauge transformation of Equation 1.4.

From this Lagrangian the following interaction vertex between two fermions and the QED vector boson, i.e. the photon, is obtained



In QCD there are three colors, so the wave function has three components in color space, $\psi = (\psi_r, \psi_b, \psi_g)$; then a color gauge transformation is described by a 3×3 unitary matrix U with $\det(U)=1$, and $\psi \rightarrow U\psi$. U can be written as e^{iL} with L hermitian, and being $\det(U)=1$, L must also be traceless. All traceless 3×3 hermitian matrices can be written as a linear combination of the eight Gell-Mann matrices λ_a

$$L = \sum_{i=1}^8 \theta_i \lambda_i \quad (1.6)$$

If the transformation operated by U is local,

$$U(x) = e^{i\sum_{i=1}^8 \theta_i(x)\lambda_i} \quad (1.7)$$

the derivative acquires an unwanted additional term:

$$\partial_\mu(U(x)\psi) = U\partial_\mu\psi + (\partial_\mu U)\psi = U[\partial_\mu\psi + U^*(\partial_\mu U)\psi] \quad (1.8)$$

There is now an additional term $U^*(\partial_\mu U)$, where U^* is the hermitian conjugate of U . This contribution is cancelled with the introduction of a color potential A_μ which is a 3×3 matrix and can be represented as a linear combination of the Gell-Mann matrices

$$A_\mu(x) = \frac{1}{2} \sum_{a=1}^8 A_\mu^a(x)\lambda_a \quad (1.9)$$

where A_μ^a are eight real potentials: one has to introduce eight color potentials instead of one like in the electromagnetic case (Equation 1.4). If the potential changes under local rotations as

$$A_\mu \rightarrow U^* A_\mu U - i\frac{1}{g}U^*(\partial_\mu U) \quad (1.10)$$

where we have introduced the coupling strength g , the minimally coupled derivative remains invariant under the gauge transformation

$$(\partial_\mu - igA_\mu)U\psi = U(\partial_\mu - igA_\mu)\psi \quad (1.11)$$

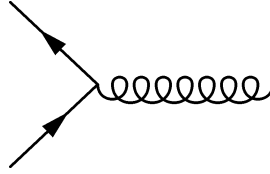
By defining

$$F_{\mu\nu}^a = \partial_\mu A_\nu^a - \partial_\nu A_\mu^a + gf_{abc}A_\mu^b A_\nu^c \quad (1.12)$$

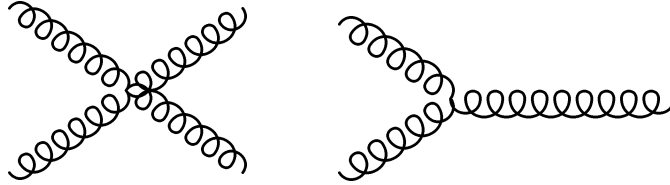
where f_{abc} are the structure constants of SU(3), we obtain a gauge invariant lagrangian for QCD¹ [5]

$$L_{QCD} = -\frac{1}{4}F_{\mu\nu}^{(a)}(x)F_{(a)}^{\mu\nu}(x) + \bar{\psi}(x)(i\gamma_\mu\partial^\mu + g\gamma_\mu A_{(a)}^\mu(x))\psi(x) - m\bar{\psi}(x)\psi(x) \quad (1.13)$$

In order to get local invariance, 8 gauge fields have been introduced: gluons are thus the vector bosons of the theory explaining the strong interaction. They are massless vector bosons, interacting with quarks via the following vertex present in the lagrangian



very similar to the QED vertex, but also among themselves [6].



The last vertices are characteristic of non-abelian theories such as QCD². They derive from the fact that in QCD (contrary to QED) the force mediators carry a non-zero value of the color charge.

1.1.1 Confinement

The concept of confinement was introduced by Gross, Politzer and Wilczek in 1964 [7] (Nobel prize in 2004).

The renormalization corrections in QCD include those similar to the QED ones (Figure 1.2) but also those characteristic of a non-abelian theory (Figure 1.3) This leads to the following scaling rule for the strong coupling constant

$$\alpha_s(|q^2|) = \frac{\alpha_s(\mu^2)}{1 + (\alpha_s(\mu^2)/12\pi)(33 - 2n_{flavour}) \ln(\frac{|q^2|}{\mu^2})} \quad (1.14)$$

where μ is the momentum scale considered and $n_{flavour}$ is the number of flavours considered in the theory. Considering three flavours, the coupling constant increases with

¹the term $m\bar{\psi}\psi$ explicitly breaks the SU(3) gauge symmetry, but when QCD is coupled to electroweak theory to complete the Standard Model the Higgs mechanism is introduced to restore the symmetry

²QCD is non-abelian because the generators of the transformation group, the λ matrices, do not commute among themselves

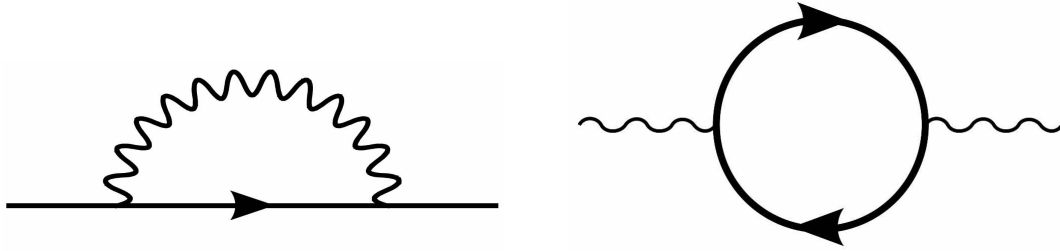


FIGURE 1.2: Left: self energy of a fermion. Right: vacuum polarization diagram.

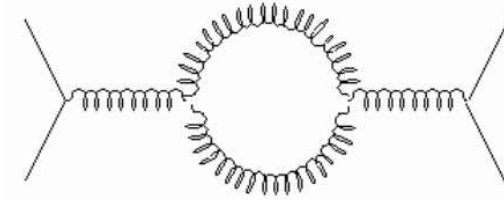


FIGURE 1.3: Correction to the gluon propagator characteristics of QCD: this diagram is possible because of the self-interaction of gluons

decreasing momentum scale μ , and the perturbative approach is therefore no longer valid. The same formula may be expressed in the following way

$$\alpha_s(|q^2|) = \frac{12\pi}{(33 - 2n_{flavour}) \ln(\frac{|q^2|}{\Lambda_{\text{QCD}}})} \quad (1.15)$$

where Λ_{QCD} is the momentum scale at which alpha diverges. This means that as one tries to pull apart two colored quark constituting a colorless meson, their strong interaction gets more and more intense: the potential between them has the form

$$V(r) = -\frac{\alpha}{r} + Kr \quad (1.16)$$

and increases linearly with distance for $r > 1$ fm, so that for a certain distance it becomes energetically convenient to create a $q\bar{q}$ pair with the right colors to create 2 new colorless mesons [8]. This simple example explains color confinement. All hadronic states we observe in nature, such as nucleons in heavy nuclei, are colorless states and they interact with a force which is the residual of the color interaction among their constituents.

1.1.2 Deconfinement

The first hint of existence for a phase transition in ordinary nuclear matter at high temperatures was given by Rolf Hagedorn's statistical model for hadronic systems [9]. The model predicted the density of a given hadron species of mass m in the system

$$\frac{d\rho}{dm} \approx m^a e^{m/m_0} \quad (1.17)$$

where a and m_0 are model parameters. In 1965 Hagedorn showed that this exponential behaviour results in a limiting temperature T_c for the energy density of the system not to diverge. The interpretation given at that time was that an increase of energy at T_c results

in the creation of heavier hadrons, without increasing the average system momenta. Later Cabibbo and Parisi [10] suggested that Hagedorn's exponential spectrum of hadronic states is not necessarily connected with a limiting temperature, but is present in any system which undergoes a second order phase transition, e.g. from ordinary nuclear matter to a different phase in which quarks and gluons are not confined.

Ten years later, shortly after the formulation of QCD, a very simple phenomenological model for hadron structure was introduced, the MIT Bag Model [11]. In the simplest version of this model hadrons are containers of massless quarks, free to move on a limited volume. Inside this volume quarks are allowed to move as quasi-free particles. Their wave function can be obtained from the Dirac equation and the short-distance scale characteristic of the bag allows the use of a perturbative approach to QCD. The vacuum surrounding the bag exerts an inward pressure B , which represents long-distance, non perturbative phenomena of QCD (confinement).

In this simplified massless model the Dirac equation

$$(i\gamma^\mu p_\mu - m) = 0 \quad (1.18)$$

becomes

$$(\gamma^0 p_0 - \vec{\gamma} \cdot \vec{p}) = 0 \quad (1.19)$$

In the Dirac representation of the Gamma matrices the equation can be written as

$$\begin{pmatrix} p^0 & \vec{\sigma} \cdot \vec{p} \\ \vec{\sigma} \cdot \vec{p} & -p^0 \end{pmatrix} \begin{pmatrix} \varphi_+ \\ \varphi_- \end{pmatrix} = 0 \quad (1.20)$$

where σ are the 2x2 Pauli matrices. This equation can be solved analytically and its lowest energy solutions are

$$\varphi_+ = N e^{-ip^0 t} j_0(p^0 R) \chi_+ \quad \varphi_- = N e^{-ip^0 t} \vec{\sigma} \cdot \hat{r} j_1(p^0 R) \chi_- \quad (1.21)$$

where j_0 and j_1 are the Bessel functions, χ_+ and χ_- the Weil spinors and both wave functions are normalized to the number of quarks inside the bag N .

Confinement can be imposed requiring the current flux

$$J_\mu = \bar{\varphi} \gamma_\mu \varphi \quad (1.22)$$

through the bag surface of radius R to be zero

$$n^\mu J_\mu = 0 \quad (1.23)$$

being \vec{n} the vector normal to the bag surface. This requirements translate into

$$\bar{\varphi} \varphi|_{r=R} = [j_0(p^0 R)]^2 - (\vec{\sigma} \cdot \hat{r})^2 [j_1(p^0 R)]^2 = 0 \quad (1.24)$$

This condition is fulfilled if $p^0 R = 2.04$, which means that the energy of the quarks inside the bag is $E = 2.04N/R$. Including the potential energy of the external pressure B , the total energy becomes $E = 2.04N/R + 4\pi/3R^3 B$. The bag is in equilibrium if $\partial E/\partial R = 0$, i.e.

$$4\pi R^2 B - \frac{2.04N}{R^2} = 0 \quad (1.25)$$

For a proton ($N=3$, $R = 0.8$ fm) we obtain $B^{1/4} = 206$ MeV. We can get some quantitative estimations of the critical parameters by applying statistical thermodynamics with some simple hypotheses. In the high temperature limit we consider a system of non interacting,

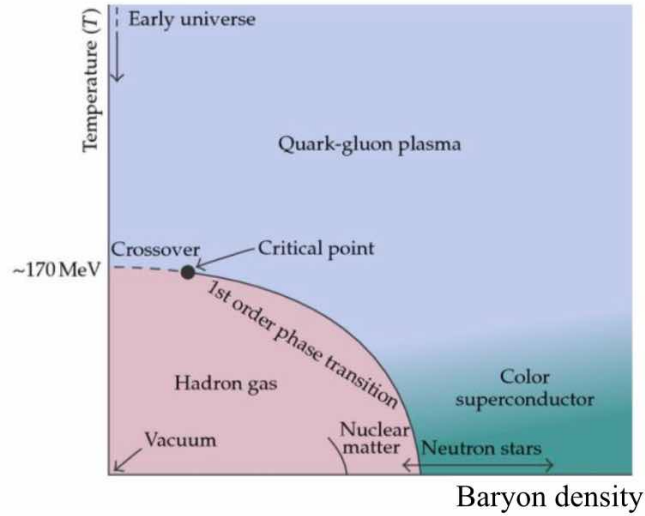


FIGURE 1.4: Phase diagram of QCD

massless quarks, antiquarks and gluons, with the further hypothesis that the net baryon number is zero. Quarks and gluons are confined inside the bag and exert a pressure on its boundaries. The partial pressures of the different constituents inside the bag can be obtained by adapting the Maxwell-Boltzmann equation for blackbody radiation [12]; the expression for their sum is

$$P = [g_g + \frac{7}{8} \times (g_q + g_{\bar{q}})] \frac{\pi^2}{90} T^4 \quad (1.26)$$

where g_q and g_g are the quarks and gluons number of degrees of freedom, respectively. For gluons we have two polarization states, so $g_g = 16$; for quarks we have

$$g_q = g_{\bar{q}} = N_{Colour} N_{Flavour} N_{Spin} \quad (1.27)$$

and in the simple case of 2 flavours $g_{total} = 37$. Hence we find that the critical temperature at which the internal pressure overcomes the critical bag pressure B is $T = 144$ MeV. Note that this result only holds if the quark gluon system has no boundary.

If now we imagine to put a very large number of baryons into a cylinder and compress it adiabatically with a piston, keeping $T = 0$, the quark wave functions will start to overlap and according to Pauli's exclusion principle the kinetic energy will rise [13]. The pressure of the system will thus increase until deconfinement occurs. For a bag pressure $B^{1/4} = 206$ MeV, the critical value of the baryon number density in the 2 flavour hypothesis will be

$$n_B^{QGP} = 0.72/\text{fm}^3 \quad (1.28)$$

which is about 5 times the normal nuclear matter density [14].

We discussed two limiting cases in which deconfinement occurs via heating or compression only. In other cases, pressure can be increased by applying compression and heating at the same time and the transition will then occur at intermediate temperatures and baryon densities. Thus we can draw a simple phase diagram where a phase transition leads to quark and gluon deconfinement. Ordinary nuclear matter lies on the $T \sim 0$ axis, with quarks and gluons having approximately a momentum of 200 MeV/c, that is the Fermi momentum. In the bottom left-hand corner the behaviour of QCD can be described in terms of a hadron gas, meaning that the dominant degrees of freedom are the

hadronic ones; after deconfinement new degrees of freedom appear (i.e. the color ones) and the physics of the system evolves to a state called Quark-Gluon Plasma (**QGP**). This happens moving vertically towards higher temperatures.

Another interesting region is at low temperature and large baryon density. This is the phase for compressed nuclear matter that might exist in the interior of neutron stars. In this region theories have been developed that predict a behaviour of quarks and gluons in nearby hadrons similar to the behaviour of electrons in superconductor, i.e. formation of Cooper pairs of quarks driven by the attractive component of the QCD interaction. This behaviour is known as Color Superconductivity [15].

All previous results have been derived from the bag model; this model however also predicts the existence of many exotic states that have never been observed. To have better qualitative results, one must deal with QCD, even if a perturbative approach to the theory is not always possible.

1.2 Lattice QCD

The numerical calculations used to extract quantitative results employ the lattice approach, introduced in 1974 by Kenneth Wilson (Nobel Prize 1982). The fundamental idea of lattice QCD is to discretize space and "time"³ points, creating a "lattice" of points located at a certain distance from each other. The QCD quantities of interest are computed on the lattice, obtaining results that depend on the distance of separation and are finally extrapolated to the continuum limit to obtain physical results. By introducing a minimum distance scale a momentum cut-off is defined, making possible numerical evaluation of integrals in a non-perturbative QCD regime.

The approach to this method begins considering the analogy of the Feynman path integral to the partition function in quantum mechanics: the mechanical amplitude for a system to be initially located at (x_a, t_a) and to end up at (x_b, t_b) is given by

$$\text{Amplitude} |(x_a, t_a) \rightarrow (x_b, t_b)| = \langle x_b | e^{-iH(t_b-t_a)} | x_a \rangle = \sum_{\text{all paths}} e^{iS_M} \quad (1.29)$$

where S_M is the action related to one path calculated using the Minkowsky metric tensor $g_{\mu\nu}$ with diagonal elements (1,-1,-1,-1). In statistical quantum mechanics the partition function Z is the sum of the expectation values of the operator $e^{-\beta_B H}$ ($\beta_B = 1/kT$), with the sum to be carried out over all possible states of the system

$$Z = \sum_{x_a} \langle x_a | e^{-\beta_B H} | x_a \rangle \quad (1.30)$$

To reconduct ourselves to the path integral formulation of the partition function

- we introduce the imaginary time coordinate τ with $t = -i\tau$ and allow τ to range from $\tau_a = 0$ to $\tau_b = \beta_B$ (so the exact meaning of time in this formulation is temperature)
- we impose the periodic boundary condition that the configuration at τ_b is the same as that at τ_a

³we will see later the exact meaning of time variables in this context

- we perform an additional summation over the states of the system

The computation of the partition function is thus reduced to a path integral. A detailed explanation of these passages can be found in [14].

The partition function can be evaluated by generating quark and gluon field configurations on the discrete lattice. Each configuration will give one addendum in Equation 1.29. From the partition function many observables of the system can be evaluated, e.g. pressure

$$\frac{p}{T^4} = \frac{1}{VT^3} \ln Z \quad (1.31)$$

However results depend on the lattice spacing used in the computation. Physics results are those extrapolated to the continuum limit.

The computing power needed sets a limit on the lattice spacing which can be used, typically larger than 0.1 fm and with 32^3 lattice sites in three dimensional space and 16 points on the "time" axis [8].

1.2.1 Lattice QCD predictions

LQCD calculations have been performed in different conditions. In the pure gauge approximation, only the gluonic degrees of freedom are considered, while fermions and antifermions are treated as static and infinitely massive, meaning that the values of their field configurations are not considered in the simulation process. In this framework, the potential between two static, infinitely massive quarks can be calculated [16]. The results of MC calculations clearly show that the potential has a linear confining part at long distances and a Coulomb attractive part at short distances (Equation 1.16), and has no significant dependence on the lattice spacing used in the simulation [13].

The inclusion of fermionic fields in lattice calculations makes the situation more complicated. The reasons for this are:

- fermion fields must be defined on the lattice sites, and their derivatives, appearing in the QCD lagrangian (Equation 1.13), must be approximated by differences
- the Pauli principle requires fermion fields to anticommute: the functional integral thus becomes a determinant running over all of the lattice sites, requiring a huge computing power [5]

Many different frameworks have been developed to treat fermion fields in the proper way, usually with 2 or 3 different flavours (u,d,s) and different mass values. Different estimates of the transition temperature T_{crit} have been obtained using different discretization schemes in the fermion sector [17] and are reported in Table 1.1.

The behaviour of pressure is presented in Figure 1.5 (left). No sharp change is seen in correspondence to the phase transition to a QGP phase, and the arrows indicate the limiting values according to the Stephan-Boltzmann Law in the different cases (Equation 1.26). This values are not reached even at the highest temperature, indicating that no ideal gas behaviour occurs [12], and that strong interactions between q, \bar{q} and gluons are still present.

Lattice QCD also predicts the order of the phase transition: while a first order transition would lead to a discontinuity in the energy density between the plasma phase and the

	T_{crit}
Pure Gauge	271 ± 2 MeV
2 light flavours	173 ± 4 MeV
3 light flavours	154 ± 8 MeV

TABLE 1.1: Critical temperature values obtained with different mass and flavour hypotheses

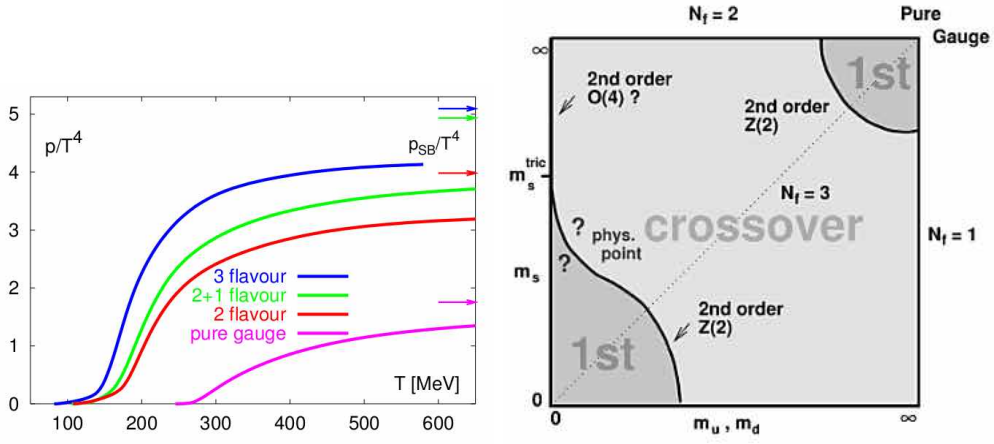


FIGURE 1.5: Left: pressure vs temperature from IQCD predictions. Predictions are shown in the pure-gauge scenario, in a 2 and 3 light quarks scenario and in the (2+1) scenario, considering two lighter and one heavier quark. The arrows on the right indicate the Stephan-Boltzmann value for each scenario. Right: order of the phase transition as a function of quark masses

hadron gas, a second order transition would lead to a rapid change in the thermodynamical variables as the critical temperature is approached. In Figure 1.5 (right) we see that in the pure gauge theory the transition is of the first order. Also in the case of 2 (u,d) or 3 (u,d,s) massless (or light) quarks the transition is first order, while for intermediate values of the quark masses IQCD predicts the existence of a crossover between the 2 phases. If we look at the QCD phase diagram (Figure 1.4) the prediction is that the crossover takes place above a critical temperature, below which the transition is of first order [8].

The effective quark mass⁴ [18] is measured by the expectation value of the corresponding term in the Lagrangian, the chiral condensate $\langle \bar{\psi}\psi \rangle(T)$. The predictions for two flavour QCD (with $M_q \sim 0.3$ GeV/ c^2) in Figure 1.6 (left) show that the effective quark mass has a rapid drop around T_{crit} , and its susceptibility defined as $\chi_m = \partial \langle \bar{\psi}\psi \rangle(T) / \partial m_q$ has a peak in the same region. The meaning of this drop in the effective quark mass towards current quark mass values around T_{crit} is that the QCD Lagrangian (Equation 1.13), which is not invariant under chiral transformation⁵, recovers chiral symmetry at high

⁴In the low energy limit of QCD, a description of quark dynamics by means of perturbation theory is not possible. At low energy the interactions between valence quarks and sea quarks have great significance and this is evident looking at the mass of the proton, which is about $O(100)$ higher than the sum of its constituents quarks "current" masses, i.e. the m_q values in the QCD lagrangian. The non-perturbative behaviour of QCD confers to quark a dynamically-generated mass, which is the "effective" mass.

⁵A chiral transformation acts on a Dirac fermion as $\psi \rightarrow e^{\alpha\gamma^5} \psi$. The QCD Lagrangian kinetic and gauge coupling terms are in fact invariant under this transformation. The mass term breaks this symmetry.

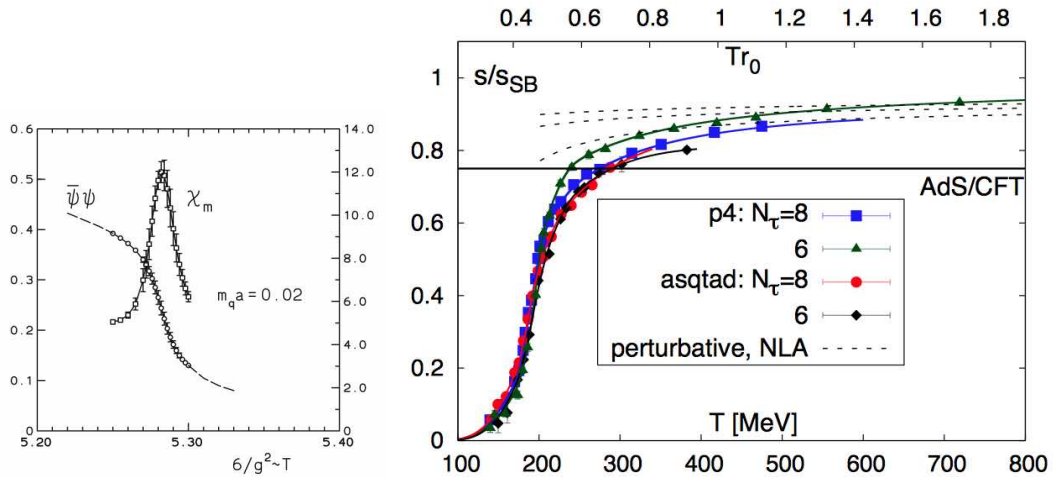


FIGURE 1.6: Left: chiral condensate value vs T from lQCD predictions. Right: pressure (relative to Stephan-Boltzmann value) vs temperature diagram for different lattice QCD calculations (N_τ is the number of lattice sites in the τ direction). The AdS/CFT value is also included

temperature. In fact the QCD lagrangian chiral symmetry is broken by the mass term $m\bar{\psi}\psi$, and this is reflected in the mass values of hadrons. If chiral symmetry was valid at low energies, all states with the same quantum numbers and opposite parity should have the same mass. This is not the case in nature, for example the ρ ($J^P = 1^-$) and a_1 ($J^P = 1^+$) mesons have masses $770 \text{ MeV}/c^2$ and $1260 \text{ MeV}/c^2$, respectively.

For completeness it should be also mentioned that lattice calculations are not the only tool to access non-perturbative phenomena in QCD. An approach based on a string theoretical construction, the Anti-de Sitter/Conformal Field Theory correspondence (AdS/CFT), has shown to be a useful tool to study non-perturbative phenomena of non-Abelian gauge theories, like those involved in QGP phenomenology [19]. This method can be used to compute several observable relative to the deconfined phase, e.g. the pressure as a function temperature, shown in Figure 1.6 (right).

1.3 Heavy Ion Collisions

The QCD phase diagram (Figure 1.4) clearly shows that, to observe the deconfined state of nuclear matter described above, extreme conditions of density or temperature have to be achieved. While indirect observation of the high density region can be provided by the study of compact astrophysical objects, the high temperature regions at low (≈ 0) baryochemical potential correspond to what the universe looked like about 10^{-6} s after the Big Bang. Current technologies allow access these regions by colliding heavy nuclei at high energies.

1.3.1 Geometry and evolution

Figure 1.7 schematizes the geometry of a heavy-ion collision: in the left panel, the incoming nuclei (A_1 and A_2) approach each other at ultrarelativistic speeds and are

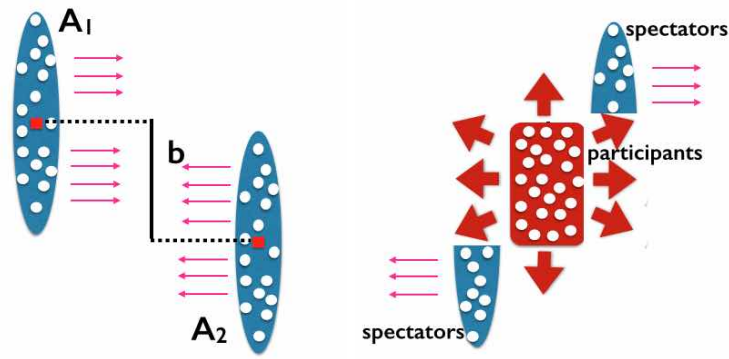


FIGURE 1.7: Schematic representation of a collision between two nuclei, before (left) and after (right) the interaction

thus Lorentz contracted along the direction of their motion. The vector that connects their two centres in the plane orthogonal to the direction of their motion is the impact parameter, b . In the right panel, the situation right after the collision is shown. The overlapping region of the colliding nuclei is the volume in which multiple scattering among the nucleons occurs, while the non-overlapping regions of the nuclei move away from the interaction point. We can divide nucleons in two groups: spectators nucleons do not experience any interaction during the nuclear collision, while participant nucleons experience at least one interaction.

Now let's concentrate on the system created in the collision, that undergoes the evolution depicted in Figure 1.8:

- during the first stages of the collision partons of the incoming nucleons undergo a large number of binary scatterings. The total energy is converted into the creation of new partons, so a high multiplicity system forms. The system is originally not in thermal equilibrium, which is expected to be reached within ~ 1 fm/c;
- the system reaches thermal equilibrium and its initial temperature depends on the centre-of-mass energy and on the atomic mass number of the nuclei. As shown in Section 1.4.1, exact measurement of the initial temperature depends on models

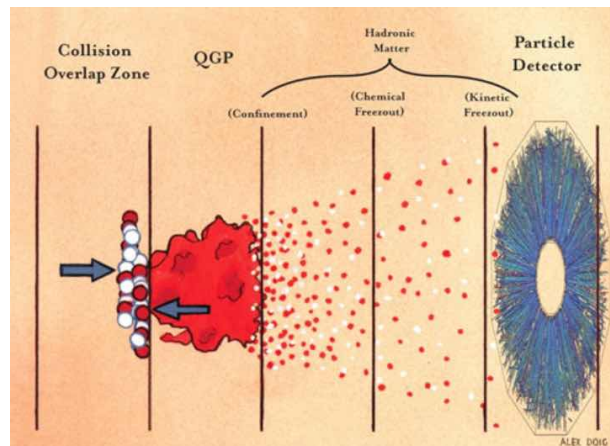


FIGURE 1.8: Evolution of a heavy-ion collision

which still have large uncertainties; anyway once equilibrium is achieved ($\tau_{\text{eq}} \sim 1$ fm/c) temperatures reached in heavy ion collisions both at RHIC ($\sqrt{s_{\text{NN}}} = 200$ GeV) and LHC ($\sqrt{s_{\text{NN}}} = 2.76$ TeV) are estimated⁶ to be well above the T_{crit} predicted by lQCD (Table 1.1), and deconfinement is expected to occur. The lifetime of the QGP phase depends on both centre-of-mass energy and system size, and is estimated as $1 \div 4$ fm/c at RHIC energies and ~ 10 fm/c at LHC energies

- this "fireball" expands cooling down until T_{crit} (Table 1.1) is reached. Below this point QGP phase can no longer exist and the system hadronizes. At this point, the hadronic gas continues its expansion and cooling
- hadrons reinteract inelastically, so the relative hadronic abundances in the system are not fixed. Below a certain temperature, T_{chem} (~ 160 MeV/c, Section 1.4.2), inelastic interaction cease: this is the **chemical freeze-out**. The relative hadronic abundances are fixed, however elastic interactions are still possible
- hadrons reinteract elastically, so the kinematic spectrum is not fixed. Below a certain temperature, T_{kin} (~ 100 MeV/c, Section 1.4.3), elastic interactions cease. The momentum spectrum of each hadron species is fixed: this is the **kinetic freeze-out**. Hadrons continue their path with no further interactions

The goal of experiments with heavy-ion collisions at high-energies is to detect these particles or their decay products to investigate the overall history of the interaction.

1.3.2 Glauber Model

We can describe the collision represented in Figure 1.7 at femtoscopic scales using three fundamental quantities: the impact parameter \mathbf{b} , the number of participant nucleons N_{part} and the total number of binary nucleon-nucleon collisions N_{coll} . The Glauber model is a theoretical semi-classical tool developed to describe the geometry of the colliding nuclei and allow us to calculate N_{part} and N_{coll} as a function of the impact parameter [20].

The model needs in principle two input quantities:

- the nucleon density distribution $\rho(r)$
- the inelastic nucleon-nucleon cross section $\sigma_{\text{inel}}^{NN}$. The elastic and diffractive components of the total nucleon-nucleon cross-section are ignored

The model views the collision of two nuclei in terms of the individual interactions of the constituents nucleons. One approach to get quantitative results with the Glauber model is within the Optical Limit, which depends on the following assumptions

- typical size of nucleon much lower than the typical size of nucleus
- neutrons and protons are treated in the same way
- each binary nucleon-nucleon interaction is independent from the presence of other nucleons in the colliding system

⁶see Section 1.4.1

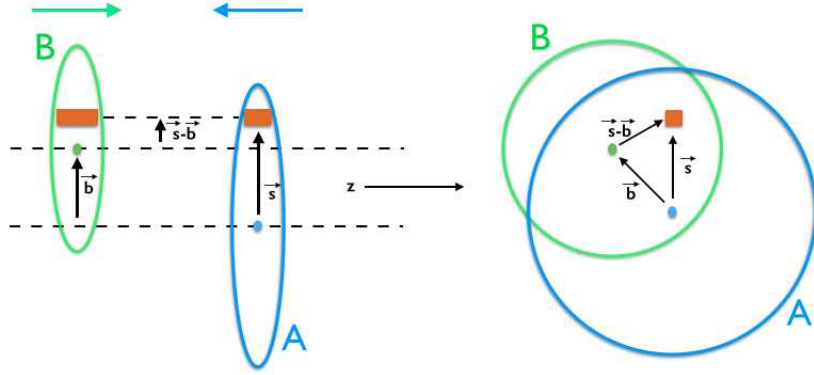


FIGURE 1.9: Schematic representation of the two nuclei before the collision

- the colliding nuclei, as well as their nucleons, are undeflected by the collision
- each nucleon always interacts with same inelastic cross section in subsequent collisions

Let's consider Figure 1.9: two heavy ions, A and B, collide with impact parameter \mathbf{b} . Focusing on the area located at a coordinate \mathbf{s} from the center of the nucleus A in the transverse plane, we define $\mathbf{s} - \mathbf{b}$ the position of this area with respect to the centre of the nucleus B. The probability per unit transverse area of a given nucleon of A to be located in the considered area is

$$\hat{T}_A(\mathbf{s}) = \int \hat{\rho}(\mathbf{s}, z_A) dz_A \quad (1.32)$$

where $\hat{\rho}(\mathbf{s}, z_A)$ is the normalized probability per unit volume for finding the nucleon at location (\mathbf{s}, z_A) . A similar expression follows for a nucleon in nucleus B. The product

$$\hat{T}_A(\mathbf{s})\hat{T}_B(\mathbf{b}-\mathbf{s})d^2s \quad (1.33)$$

gives the probability per unit area of nucleons being located in the respective overlapping target and projectile elementary areas d^2s . Integrating this quantity over the whole overlapping region we get the thickness function

$$\hat{T}_{AB}(\mathbf{b}) = \int \hat{T}_A(\mathbf{s})\hat{T}_B(\mathbf{b}-\mathbf{s})d^2s \quad (1.34)$$

which has the units of an inverse area. The probability for the two nucleons considered to interact is $\hat{T}(\mathbf{b})\sigma_{\text{inel}}^{\text{NN}}$. The probability of having n such interactions is given by the binomial distribution

$$P(n, \mathbf{b}) = \binom{AB}{n} [\hat{T}(\mathbf{b}) \sigma_{\text{inel}}^{\text{NN}}]^n [1 - \hat{T}(\mathbf{b}) \sigma_{\text{inel}}^{\text{NN}}]^{AB-n} \quad (1.35)$$

where the number of combinations for finding n collisions out of AB possible nucleon-nucleon interactions appears. We can get the total interaction probability between the

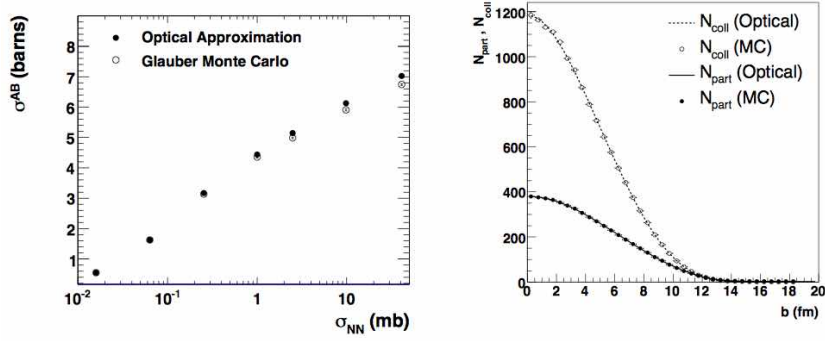


FIGURE 1.10: Left: total nuclear cross section vs $\sigma_{\text{inel}}^{\text{NN}}$ for Au-Au collisions. Right: N_{part} and N_{coll} for Au-Au collisions.

nuclei A and B (for a given impact parameter \mathbf{b}) summing on all possible "trials"

$$\frac{d^2\sigma_{\text{inel}}^{\text{AB}}}{db^2} = \sum_{n=1}^{\text{AB}} P(n, \mathbf{b}) = 1 - [1 - \hat{T}_{\text{AB}}(\mathbf{b})\sigma_{\text{inel}}^{\text{NN}}]^{\text{AB}} \quad (1.36)$$

The total number of nucleon-nucleon collisions is the mean value of the binomial distribution

$$N_{\text{coll}}(b) = \sum_{n=1}^{\text{AB}} nP(n, b) = \text{AB}\hat{T}_{\text{AB}}(b)\sigma_{\text{inel}}^{\text{NN}} \quad (1.37)$$

Another implementation of the Glauber model is based on Monte Carlo simulations. In this approach, the two nuclei A and B are composed of nucleons whose 3D coordinates are randomly generated according to their nuclear density distributions. As the two nuclei collide, a single nucleon-nucleon collision takes place if their distance d in the plane orthogonal to the beam axis satisfies

$$d < \sqrt{\sigma_{\text{inel}}^{\text{NN}}/\pi} \quad (1.38)$$

If a large number of collisions with impact parameter \mathbf{b} distributed according to $d\sigma/db \propto 2\pi b$ is simulated, the distribution for N_{part} and N_{coll} are obtained (Figure 1.10 - right panel). These distributions show good agreement with the calculation in Optical Approximation. In the left panel of Figure 1.10 the total nuclear cross section vs nucleon-nucleon inelastic cross-section is shown, computed in both the Optical Approximation and in the Glauber MC framework. Small discrepancies appear for the higher nucleon-nucleon cross-section values. This is mainly due to the fact that in the Optical Approximation the incoming nucleon sees the incoming nucleus as a smooth density object and does not account for event-by-event density fluctuations.

Of course the impact parameter \mathbf{b} is not an accessible quantity, but it can be related to experimental observables. This will be discussed in the Chapter 3. However to fully understand some of the results shown in next section it is necessary to mention that collisions with a small value of the impact parameter are called central collisions, those with large values of impact parameter are called peripheral collisions. Considering a sample of AA collisions, events are usually divided in percentiles of certain observables correlated to the impact parameter, and these percentiles are called centrality classes. For instance, the 0-10% centrality class defined based on charged-particles multiplicity corresponds to the 10% events with the highest charged-particles multiplicity.

1.4 Heavy-ion physics observables

The particle multiplicities produced in ultra-relativistic heavy-ion collisions are much larger than the ones obtained in proton-proton, proton-electron and electron-electron collisions. Systems created in high-energy nuclear interactions show a higher degree of complexity, due to the structured evolution described in Section 1.2.1.

The study of relativistic heavy-ion collisions started in the 70s at the Lawrence Berkeley National Laboratory, where a linear accelerator designed for heavy-ions was built. Accelerated nuclei were sent to the LBNL synchrotron (Bevatron) that could accelerate them at about $1 A$ GeV/c.

The effort continued in both Europe and US at CERN and Brookhaven, respectively. The Alternating Gradient Synchrotron (AGS) at Brookhaven National Laboratory accelerated Si ions up to $15 A$ GeV. The CERN heavy-ion program at the Super Proton Synchrotron started in 1986 accelerating nuclei with equal numbers of protons and neutrons, due to the capabilities of the ion injector. Subsequently an injector was constructed to accommodate arbitrarily heavy nuclei and the use of Pb beams at $160 A$ GeV started in 1995.

Until 2010 the highest energies in heavy ion collisions were reached at the Relativistic Heavy Ion Collider (RHIC) in Brookhaven. The experimental activities are still ongoing, with two experiments still taking data: PHENIX and STAR. The colliding systems explored at RHIC up to now are p-p, d-Au, Cu-Cu, Cu-Au, Au-Au and U-U, with a maximum center-of-mass energy for Au-Au collisions $\sqrt{s_{NN}} = 200$ GeV.

Recently the Large Ion Collider at the LHC started its heavy-ion programme and the first Pb-Pb collisions at $\sqrt{s_{NN}} = 2.76$ TeV were recorded in 2010. Three experiments have a heavy-ion program: ALICE, ATLAS and CMS.

In the next sections we will discuss a list of observables carrying information on the system produced in ultra-relativistic heavy-ion collisions. Note that partonic energy-loss in the hot medium will not be mentioned here as it will be one of the main topics of Chapter 2.

1.4.1 Thermal photons

Photons produced in heavy-ion collisions can be divided in three groups [21]:

- **decay photons** coming from decays of other particles (mainly $\pi^0 \rightarrow \gamma + \gamma$). These are also present in small system collisions (p-p, e-e, etc.)
- **prompt photons** coming from initial partonic processes with large Q^2 (e.g. $g + q \rightarrow q + \gamma$); these are also present in small system collisions (p-p, e-e, etc.) and have large momenta (≥ 3 GeV/c)
- **thermal photons** coming from thermal radiation of the QGP: these are peculiar of nuclear collisions, where the strong interacting medium is expected to form, and have lower momenta (≤ 2 GeV/c)

While photons belonging to the first group come from secondary vertices, prompt and thermal photons originate at the interaction point and are thus called "direct" photons. For what concerns thermal photons, theory can predict their transverse momentum distributions, taking into account the full evolution of the system. The final spectrum will

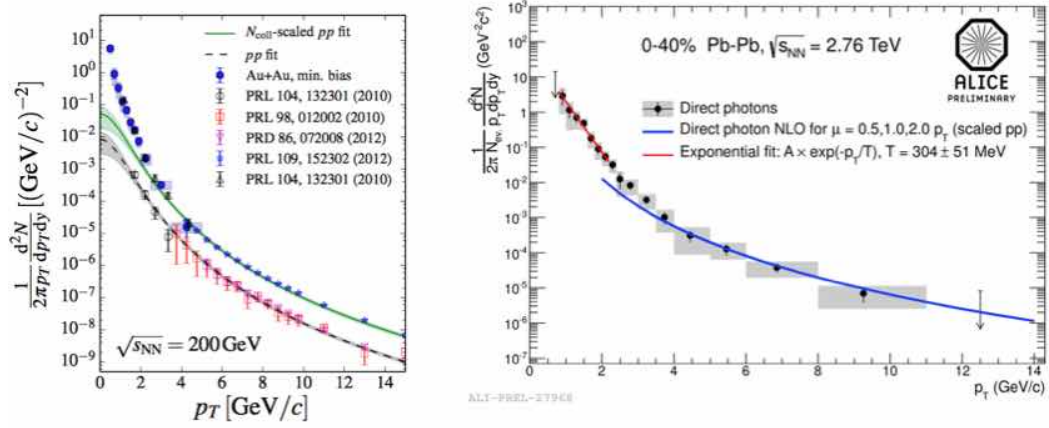


FIGURE 1.11: Left: the filled blue points correspond to the p_T differential cross section of direct photons in minimum bias in Au–Au collisions at $\sqrt{s_{NN}} = 200 \text{ GeV}$ [22]. Right: direct photons p_T spectrum in Pb–Pb collisions at $\sqrt{s_{NN}} = 2.76 \text{ TeV}$ [23].

be the convolution of all photons emitted during the temperature history of the fireball $T(t)$. Fitting the direct photon spectra could yield the initial temperature T_0 of the fireball, but still theory predictions depend on a large number of parameter. These are currently not completely understood, in particular the time it takes to the system to reach thermal equilibrium τ_{eq} and the dynamical parameters of the expansion.

What one can do is to consider the fireball as a static thermal source at constant temperature that emits photons accordingly to a Maxwell-Boltzmann exponential rate $\sim e^{-p_T/T}$. Fitting the momentum spectrum of direct photons at low p_T with this exponential will provide an "effective temperature", a sort of temporal mean from the very initial stages to hadronization, which is expected to take place at $T_c \sim 170 \text{ MeV}$.

Figure 1.11 shows direct photon measurements performed by the PHENIX (left, [22]) and ALICE (right, [23]) experiments. The exponential fit is superimposed to the low p_T points for the ALICE measurements (red curve), yielding an effective temperature $T = 304 \pm 51 \text{ MeV}$. For the PHENIX measurement, fits have been performed dividing the minimum bias sample in four different centrality classes yielding results that are compatible within uncertainties. For the most central events at RHIC energies one gets $T = 239 \pm 25^{sys} \pm 7^{sys} \text{ MeV}$. Both values of effective temperature are well above the critical temperature for deconfinement expected from lattice QCD calculations.

1.4.2 Hadronic abundances

For central ultra-relativistic nuclear collisions light hadrons yields can be described very well within the statistical hadronization model [24]. The chemical freeze-out temperature T_{chem} , the baryo-chemical potential μ_b ⁷ and the fireball volume V are the parameters of

⁷In particle physics reactions a qqq baryon is always created or destroyed pairwise with a $\bar{q}\bar{q}\bar{q}$ anti-baryon. There is no process within QCD which can change the number of baryons N_B minus the number of anti-baryons $N_{\bar{B}}$; in other words we can identify a conserved quantum number $B = N_B - N_{\bar{B}}$ called baryon number. Quarks and anti-quarks carry $B = \pm 1/3$ respectively. Now, for systems in which baryon number is allowed to vary (such as the Grand Canonical Ensemble), the most convenient thermodynamic potential to consider is the grand canonical potential $\Omega(T, V, \mu_b) = E - TS - \mu_b B$. Thermodynamic equilibrium is reached when Ω is minimised, and for a system in equilibrium we recognise μ_b as the increase in E whenever B increases by one.

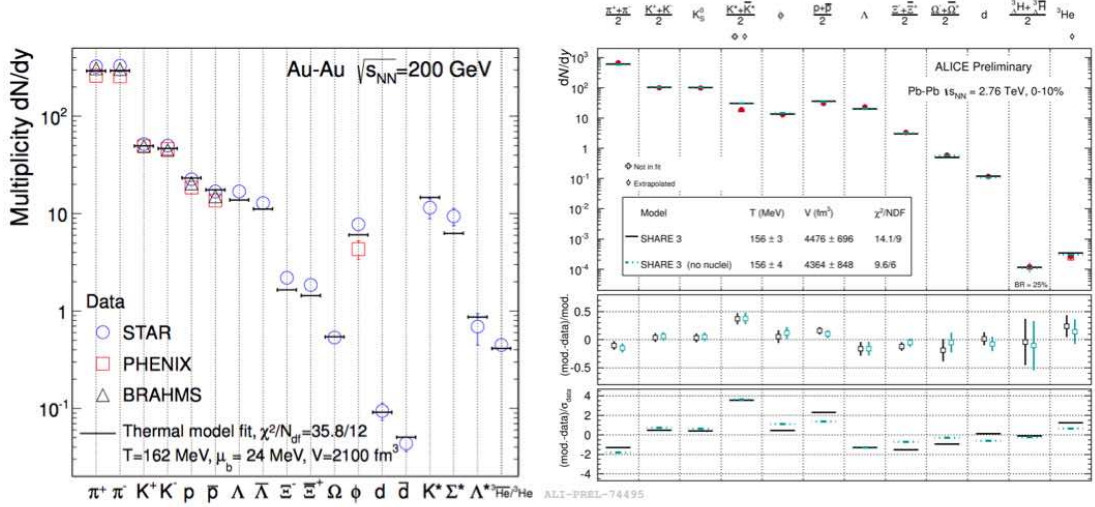


FIGURE 1.12: Left: p_T integrated hadronic abundances in Au-Au at $\sqrt{s_{NN}} = 200$ GeV [25]. Right: p_T integrated hadronic abundances in central Pb-Pb at $\sqrt{s_{NN}} = 2.76$ TeV [26].

the model, which assumes that the system is in chemical and thermal equilibrium. The basic quantity used to compute the hadronic composition of thermal yields measured in heavy ion collisions is the partition function $Z(T, V)$. Considering a system in equilibrium that exchanges energy and particles with the outside (Grand Canonical Ensemble), the partition function for a certain hadronic species i is

$$\ln Z_i = \frac{V g_i}{2\pi^2} \int_0^\infty \pm p^2 dp \ln[1 \pm \exp(-(E_i - \mu_i)/T)] \quad (1.39)$$

where g_i (μ_i) is the spin degeneracy factor (chemical potential) for the hadron species i and the $+$ ($-$) is for fermions (bosons). The total number of hadrons of specie i at equilibrium is given by

$$N_i = -T \frac{\partial \ln Z_i}{\partial \mu_i} \quad (1.40)$$

This model can be used to fit experimental data of particles multiplicities and extract T and μ_b . One can get rid of the fit parameter V fitting particles ratios. At LHC energies the baryon/antibaryon ratio is sufficiently close to 1, so that μ_b can be fixed at 0.

The temperatures values extracted at low energies first increase sharply with increasing beam energy and level off near $T_{\text{chem}} \approx 162$ MeV for energies $\sqrt{s_{NN}} > 20$ GeV [25]. Figure 1.12 shows the results for RHIC experiments [25] (left) and ALICE [26] (right). RHIC results indicate $T_{\text{chem}} = 162$ MeV and a small, but non vanishing, chemical potential $\mu_b = 24$ MeV. The overall trend of the data is very well reproduced by the calculations. However, the yield of protons and anti-protons from PHENIX and BRAHMS is overpredicted, while the yield of multi-strange baryons is generally underpredicted, leading to a rather poor χ^2 value of the fit. ALICE results for central Pb-Pb collisions are fitted with and without considering light nuclei yields and the two methods give compatible results for $T_{\text{chem}} = 154$ MeV and for the volume at chemical freeze-out $V = 4476$ fm³. The rather low temperature obtained from ALICE results is due to the unexpectedly low yields of protons and anti-protons. The exclusion of protons and anti-protons from the fit leads to a very good description of all remaining data, with excellent χ^2 of the fit and $T_{\text{chem}} = 164$ MeV, completely in line with expectations as pointed out in [25].

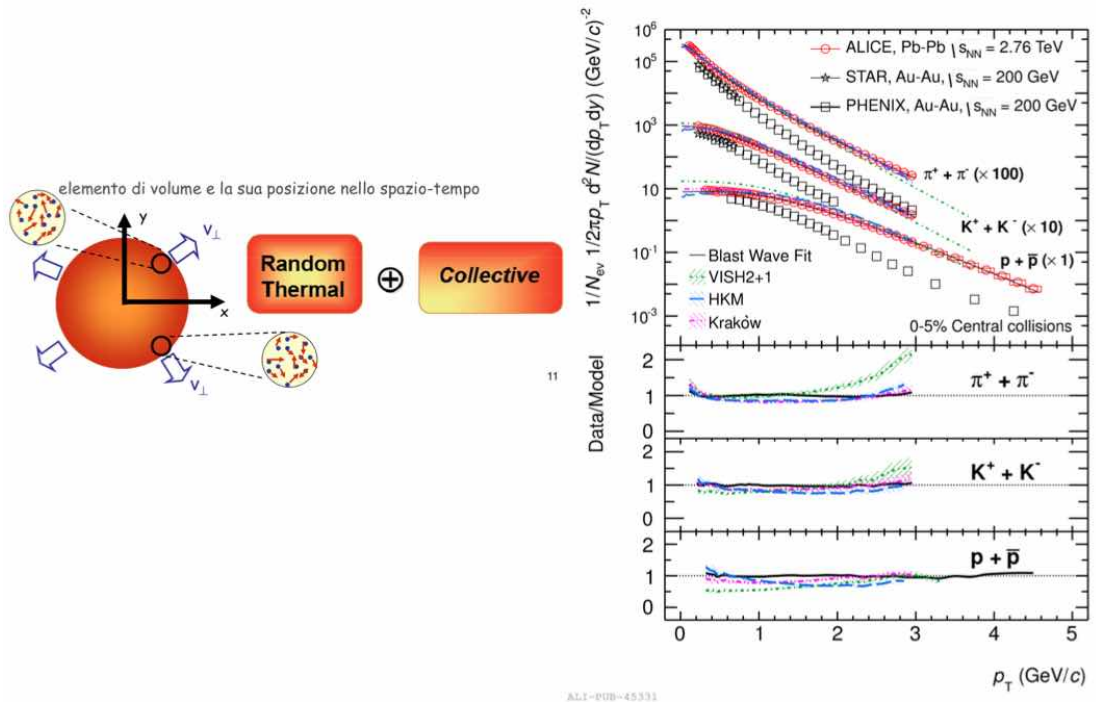


FIGURE 1.13: Left: schematic representation of radial flow. Right: pion, proton and kaons p_T spectra in central AA collisions from ALICE, STAR and PHENIX [27].

1.4.3 Transverse momentum spectra of hadrons

The yields of most of the produced particles get fixed at chemical freeze-out. The abundances can still vary due to decays.

After some time, when the inter-particle distance becomes so large that the elastic interactions stop, the system undergoes kinetic freeze-out. At this stage, the transverse momentum spectra of the produced particles are fixed. At the kinetic freeze-out the expanding system can be considered as a static thermal source in equilibrium at a temperature T_{kin} , so that the emission rate of hadrons can reasonably be a Maxwell-Boltzmann exponential slope $\sim e^{-p_T/T_{slope}}$. However, fitting the momentum spectra of different hadrons (e.g. pions and protons) one gets different T_{slope} values. This is understood considering that the dynamic of particles at this stage is not only determined by their elastic interactions, but also by the collective expansion of the system, i.e. by the “radial flow” depicted in left panel of Figure 1.13. The temperature value extracted from a fit to a given hadronic species is thus the sum of two contributions, a random thermal motion characterized by the temperature T_{kin} and a collective expansion:

$$T_{slope} = T_{kin} + \frac{1}{2}mv_{\perp}^2 \quad (1.41)$$

where v_{\perp} is the mean radial velocity of particles expanding with the fireball.

A fit to the spectra with the so-called blast-wave function ⁸ [28] allows one to extract T_{kin} , the temperature at which elastic interactions among particles cease, and $\beta_{\perp} = v_{\perp}/c$.

The right panel of Figure 1.13 shows the p_T distributions of pions, kaons and protons

⁸A model that takes into account radial flow and hadron yield from resonances decay, and assumes a thermal source at equilibrium

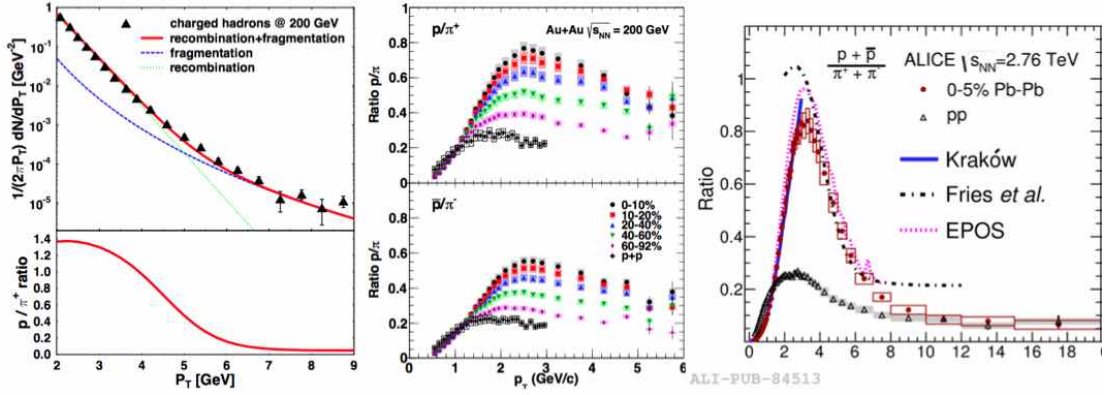


FIGURE 1.14: Left panel: Fries model fit to PHENIX charged hadron p_T spectrum in minimum bias Au–Au collisions at $\sqrt{s_{NN}} = 200$ GeV [29]. Central: PHENIX p/π and \bar{p}/π^- ratios in five centrality classes (also ratios from pp collisions are shown) Au–Au collisions at $\sqrt{s_{NN}} = 200$ GeV [30]. Right panel: p/π ratios measured with ALICE for central Pb–Pb and pp collisions at $\sqrt{s_{NN}} = 2.76$ TeV and comparison to models [31].

(summed to those of their respective antiparticles) from Pb–Pb collisions at $\sqrt{s_{NN}} = 2.76$ TeV in the 0–5% centrality class, measured by the ALICE Collaboration [27]. The same measurements from PHENIX and STAR Collaborations in Au–Au collisions at $\sqrt{s_{NN}} = 200$ GeV are also shown. The spectra shapes show a significant change from RHIC to LHC energies, having a distinctly harder distribution. This indicates a stronger radial flow at higher energies, and fitting ALICE spectra with the blast wave function one gets $\langle\beta_T\rangle = 0.65 \pm 0.02$ and $T_{kin} = 95 \pm 10$ MeV for central (0–5%) Pb–Pb collisions at $\sqrt{s_{NN}} = 2.76$ TeV. Both values are about 10% higher than what is extracted from RHIC data at similar centralities.

Calculation based on hydrodynamics also reproduce the spectra measured by the three collaborations, in agreement with the hypothesis of a collective expansion.

1.4.4 Hadronization

In high-energy elementary particle collisions the transition from quarks to hadrons is a non-perturbative QCD phenomenon. The hadronisation process can be described by the fragmentation function $D_h^i(z)$, which represents the probability of parton i to fragment to hadron h carrying a fraction z of its energy. Fragmentation functions can be obtained from global analysis in e^+e^- , e^+p and $p-p$ collisions. In event generators such as PYTHIA the fragmentation process is usually implemented via a parton shower and subsequent color string hadronization.

In ultrarelativistic heavy-ion collisions, however, the creation of a hot medium can affect the production of hadrons as well as their momentum distributions. Beside the influence of the radial flow already discussed, the hadronization mechanism itself can be modified [29], since now a hadron can be formed not only by a fragmenting quark, but also by two or three quarks that are close to each other both in space and in momentum and recombine. This can affect the final momentum distributions of hadrons, since while in the fragmentation processes the hadron momentum is a fraction of the parent parton one, the momentum of hadrons originating from recombination is the sum of up to three different contributions.

Recombination is expected to dominate for low p_T partons in the medium, and models

have been developed to predict hadron spectra in scenarios taking into account recombination at low p_T and fragmentation at high- p_T , such as the Fries model in Figure 1.14 (left) [29]. The model is used to fit PHENIX data for the charged hadron transverse momentum spectrum and the top panel shows the recombination and fragmentation contributions to the fit function.

An observable predicted by this model is the proton to pion ratio in A–A collisions, shown in the bottom-left panel of Figure 1.14. An enhancement of the p/π ratio is predicted for $2 < p_T < 4$ GeV/c, followed by a decrease. Also other models based on recombination draw the same qualitative conclusions [32].

The central panel of Figure 1.14 shows the p/π ratio measured as a function of p_T by PHENIX for Au–Au collisions at $\sqrt{s_{NN}} = 200$ GeV [30] for different centralities. A peak is visible for all centralities around $p_T = 2.5$ GeV/c, however the behaviour of the p/π and \bar{p}/π^- ratio is substantially different from the model predictions in the low- p_T region. This is due to the fact that the model does not take into account the radial flow that differently affects the transverse momentum distribution of pions and protons, in particular shifting heavier hadrons (in this case protons) to higher p_T values.

The right panel of Figure 1.14 shows the ALICE results for central Pb–Pb collisions at $\sqrt{s_{NN}} = 2.76$ TeV [31]. The peak position is around $p_T = 3$ GeV/c and its value is about 20% above the one measured by PHENIX. The Fries model predictions superimposed in Figure 1.14 qualitatively describe the shape of the ratio down to ~ 2 GeV/c. The Krakow model [33], which agrees well with the data below ~ 2 GeV/c, is based on a hydrodynamical evolution of the partonic stage followed by statistical hadronization.

1.4.5 Elliptic flow

In non-central collisions, the spatial anisotropy of the overlap region of the colliding nuclei is converted into a momentum anisotropy of the final state particles due to interactions among the medium constituents. The anisotropy is quantified by the coefficients of the Fourier expansion of the distribution of the final state particle azimuthal angles relative to the reaction plane, which is defined by the impact parameter of the collision and the

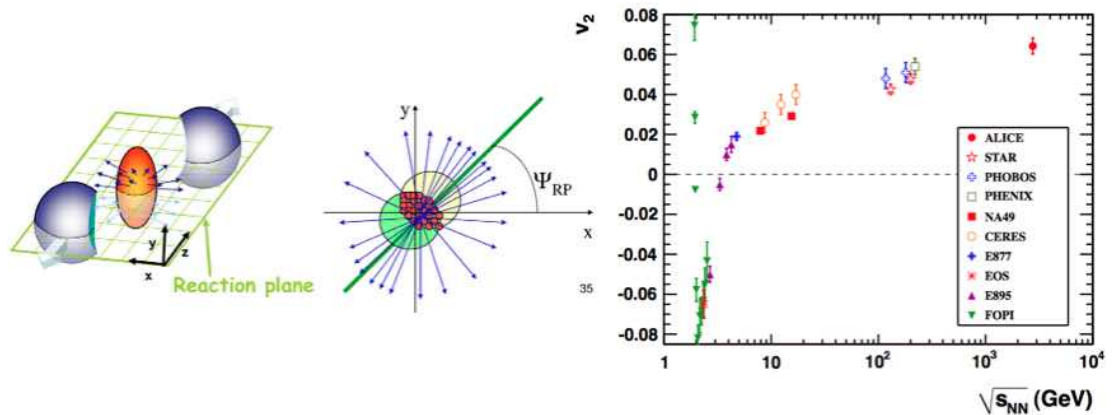


FIGURE 1.15: Left: a non central heavy-ion collision showing how the reaction plane is defined. Right: p_T integrated elliptic flow values for semicentral events collisions as a function of $\sqrt{s_{NN}}$ [34].

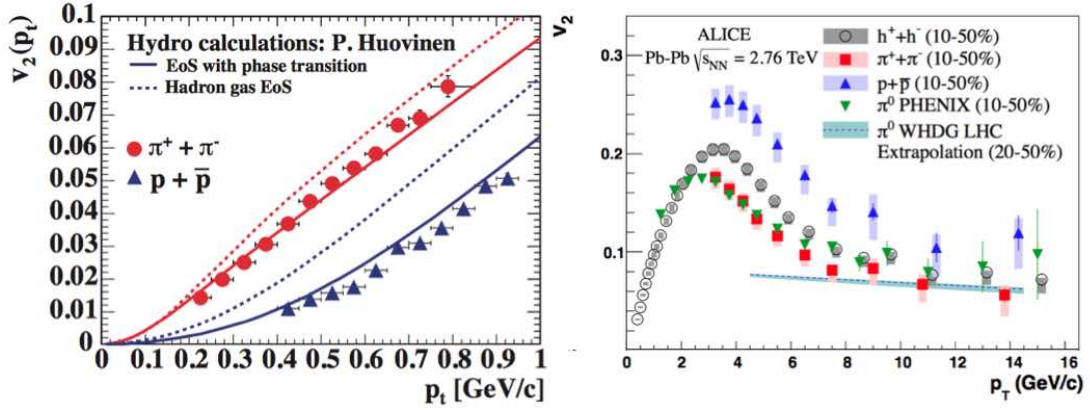


FIGURE 1.16: Left: PHENIX low p_T measurements of v_2 compared to hydrodynamical calculations [35]. Right: ALICE results for proton and pion v_2 from semicentral Pb–Pb events at $\sqrt{s_{NN}} = 2.76$ TeV [36]

beam direction

$$\frac{dN}{d(\phi - \Psi_{RP})} = \frac{N_0}{2\pi} (1 + 2v_1 \cos(\phi - \Psi_{RP}) + 2v_2 \cos(2(\phi - \Psi_{RP})) + \dots) \quad (1.42)$$

where Ψ_{RP} is depicted as in Figure 1.15 (center). The second coefficient v_2 is the elliptic flow coefficient and represents an elliptic distribution of particles in the transverse plane.

This effect is negligible in central collisions ($\mathbf{b} \sim 0$) and increases when going towards higher values of \mathbf{b} (semiperipheral collisions) due to increasing eccentricity of the overlap region of the colliding nuclei. In the most peripheral collisions, however, this effect decreases again since the particle densities achieved do not build up sufficiently strong pressure gradients that can translate the initial spatial anisotropy into an observable momentum anisotropy.

The right panel of Figure 1.15 shows the p_T integrated elliptic flow results from different experiments as a function of $\sqrt{s_{NN}}$ ranging from few GeV up to RHIC and LHC energies [34]. The ALICE results is for the 20–30 % centrality range, other results correspond to similar centrality intervals. Going from RHIC to LHC energies, a 30% increase of the p_T -integrated v_2 values is observed.

Most of the observed v_2 is expected to form at early times of the collision, when the spatial anisotropy is at its maximum. However, interactions among the constituents do occur also in the hadronic phase of the fireball’s evolution, and it is reasonable to argue that part of the elliptic flow may build up after hadronization. Figure 1.16 (left panel) shows RHIC results for p_T differential v_2 of identified pions and protons at very low p_T . Hydrodynamics predictions are superimposed for both species, one (continuous line) taking into account a deconfined state that undergoes a phase transition to hadron gas, the other for a hadron gas system. The predictions including a deconfined state better agree with both data sets [35]. The right panel of Figure 1.16 shows the p_T differential v_2 of identified pions and protons measured by ALICE [36]. In this higher p_T region the situation is reversed, i.e. v_2 of protons is higher than that of pions, and could be interpreted as the effect of recombination: hadrons inherit the flow component of the recombined parent quarks, resulting in an increased elliptic flow of baryons compared to mesons [37]. However also the different radial flow push on π and protons can produce the same qualitative effect.

Another important factor that needs to be taken into account when looking at elliptic

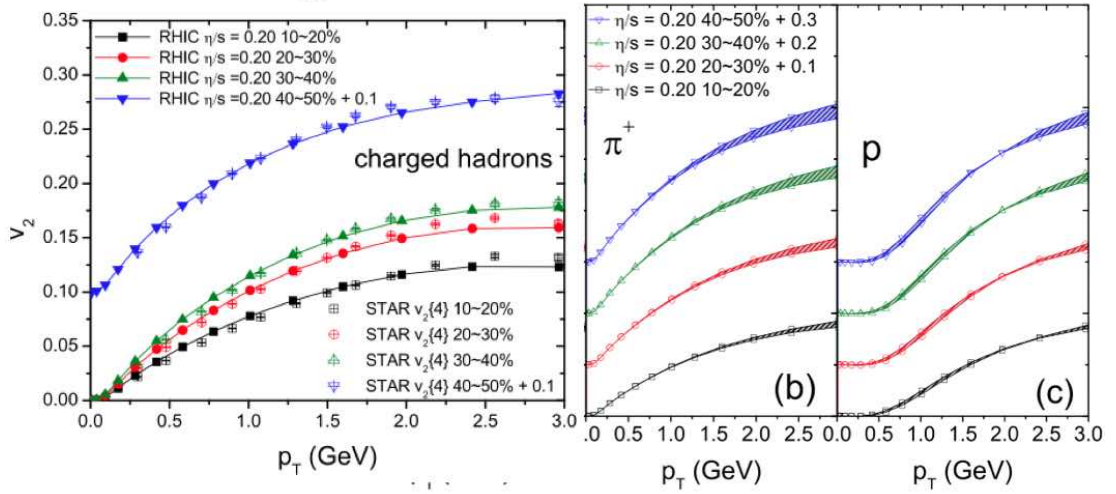


FIGURE 1.17: Left: p_T differential elliptic flow for charged hadrons from Au+Au collisions at $\sqrt{s_{NN}} = 200$ GeV of different centralities. Open symbols are experimental data from the STAR experiment for v_2 , lines with filled symbols of the same shape are the corresponding hydrodynamic fits from [40]. Right: ALICE results for proton and pion p_T differential v_2 from Pb–Pb events at $\sqrt{s_{NN}} = 2.76$ TeV at different centralities. Shaded regions correspond to hydrodynamic extrapolations at higher energies of the same calculations showed in the left panel [40].

flow measurements is how momentum and energy are transported inside the medium. A good way to study this theoretical aspect is to look at shear viscosity to entropy ratio η/s . Theoretical arguments, based on the AdS/CFT conjecture, suggest a universal lower bound of $1/4\pi$ for the ratio of shear viscosity to entropy density [38] in the QGP phase. Viscous hydrodynamic predictions from Luzum and Romatschke reasonably reproduced RHIC elliptic flow data with shear viscosity values $\eta/s=0.08\div 0.16$ [39]. Figure 1.17 shows viscous hydrodynamic predictions for elliptic flow measurements at both RHIC and LHC energies with $\eta/s=0.2$ [40]. The left panel shows the hydrodynamically calculated differential elliptic flow for unidentified charged hadrons compared to STAR v_2 data, for four centrality classes ranging from semi-central to mid-peripheral collisions. With $\eta/s = 0.20$, viscous hydrodynamics gives an excellent description of the STAR v_2 data. Extrapolating the same calculation at LHC energies keeping the same $\eta/s=0.2$ value a good agreement with centrality dependent v_2 measurements for pions and protons performed by the ALICE Collaboration [36] is achieved.

Preliminary studies of possible temperature dependent variations of η/s are ongoing, as well as developments of dynamical models for the pre-thermal evolution of the collision fireball to better quantify the transport properties of the QGP and its behaviour as a non-perfect fluid with very low (but not zero) shear viscosity.

1.4.6 Higher order armonics

In a non-central heavy ion collision the beam axis and the impact parameter define the reaction plane Ψ_{RP} as reported in previous section. Assuming a smooth matter distribution in the colliding nuclei, all odd coefficients of Equation 1.42 are zero by symmetry. However, fluctuations in the matter distribution, including contributions from fluctuations in the positions of the nucleons participating in the collision, give rise to

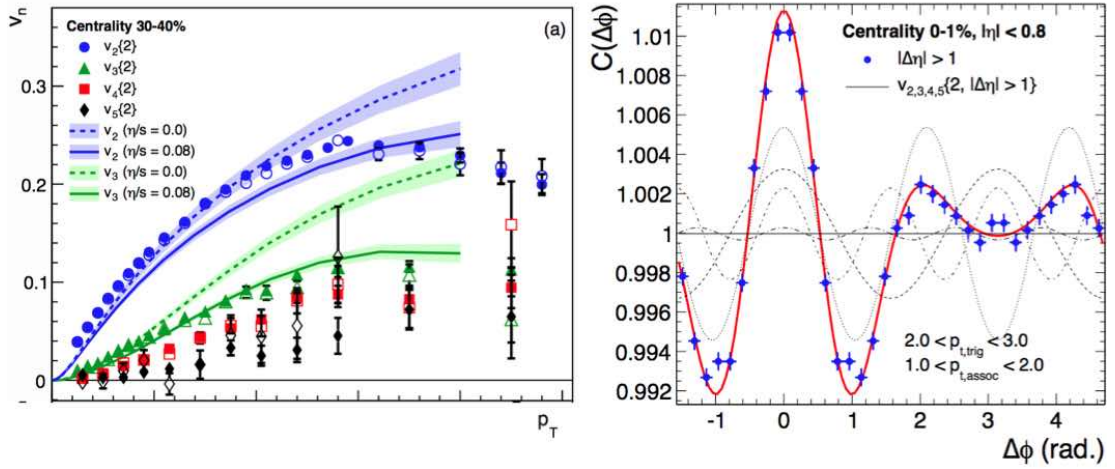


FIGURE 1.18: Left: ALICE p_T differential results for v_2 , v_3 , v_4 and v_5 obtained with a two particle correlation analysis of data from semicentral Pb–Pb collisions at $\sqrt{s_{NN}} = 2.76$ TeV [42]. Right: two-particle azimuthal correlations observed in 0-1% Pb–Pb collisions and expected azimuthal correlation shape obtained combining the Fourier harmonics weighted by the v_n coefficients [42].

odd harmonics like v_3 and v_5 . The measurement of these odd harmonics together with the fourth harmonic v_4 is interesting not only to study event-by-event fluctuations of the initial geometric configuration. In fact, as shown in [41], deviations from the ideal fluid behaviour governed by the η/s shear viscosity have larger effects on higher order harmonics than on v_2 .

Figure 1.18 shows the p_T differential v_2 , v_3 , v_4 and v_5 measured by the ALICE Collaboration with a two particle correlation analysis of data from semicentral Pb–Pb collisions at $\sqrt{s_{NN}} = 2.76$ TeV [42]. The results for v_2 and v_3 are compared to hydrodynamic predictions using Glauber initial conditions and different values of η/s from [43]. At low p_T , the p_T dependence of v_2 and v_3 is described well by these predictions, however the p_T dependence of v_2 is better described by $\eta/s=0$ while the p_T dependence of v_3 is better described by $\eta/s=0.08$.

The right panel of Figure 1.18 shows the two-particle azimuthal correlations measured in very central Pb–Pb collisions for trigger particles in the range $2 < p_{T, \text{trig}} < 3.0$ GeV/c and associated particles in $1 < p_{T, \text{assoc}} < 2.0$ GeV/c for pairs in $|\Delta\eta| > 1$, measured by calculating

$$C(\Delta\varphi) = \frac{N_{\text{mixed}}}{N_{\text{same}}} \frac{dN_{\text{same}}/d\Delta\varphi}{dN_{\text{mixed}}/d\Delta\varphi} \quad (1.43)$$

where $\Delta\varphi = \varphi_{\text{trig}} - \varphi_{\text{assoc}}$, $dN_{\text{same}}/d\Delta\varphi$ ($dN_{\text{mixed}}/d\Delta\varphi$) is the number of associated particles as function of $\Delta\varphi$ within the same (different) event, and N_{same} (N_{mixed}) the total number of associated particles in $dN_{\text{same}}/d\Delta\varphi$ ($dN_{\text{mixed}}/d\Delta\varphi$). A clear doubly-peaked correlation structure centered at $\Delta\varphi = \pi$ with respect to the trigger particle is visible. The red line corresponds to the azimuthal correlation shape obtained combining the Fourier harmonics associated to v_2 , v_3 , v_4 and v_5 coefficients weighted by their values measured at the corresponding p_T . The combination of these harmonics gives a natural description of the observed doubly-peaked correlation structure centered at $\Delta\varphi = \pi$, opposite to the trigger particle. This implies that the measured anisotropic flow Fourier coefficients, including the odd ones arising from initial state fluctuations in the matter distribution, give a natural description of this structure.

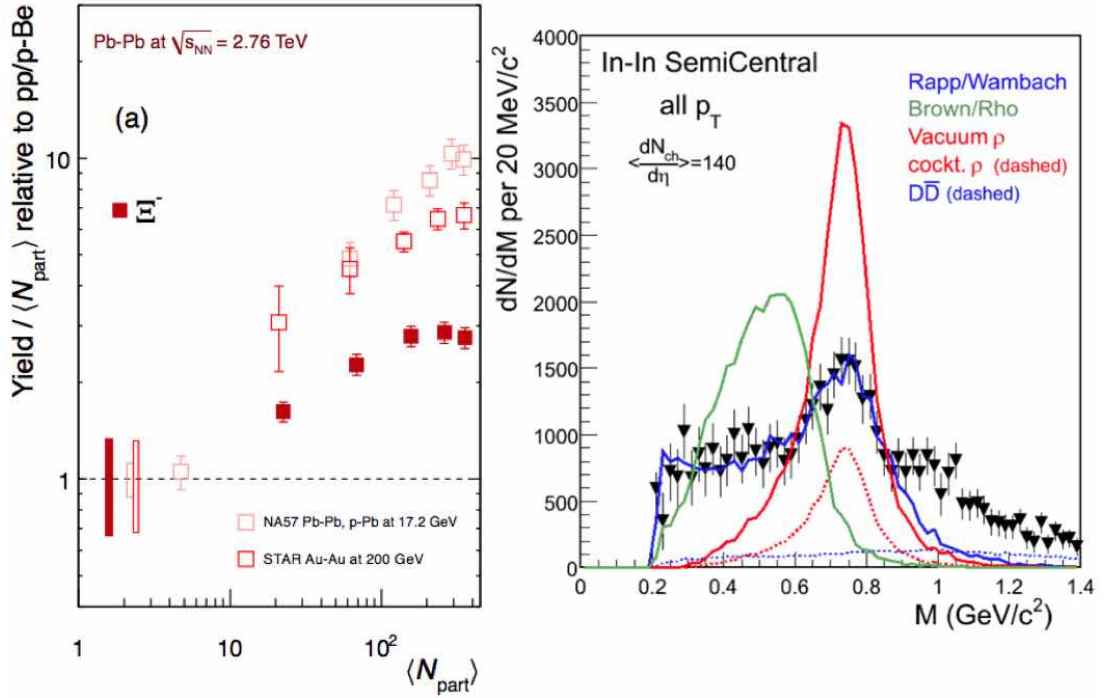


FIGURE 1.19: Left: ALICE measurement of Ξ meson strangeness enhancement factor as a function of $\langle N_{\text{part}} \rangle$. Results from NA57 and STAR are also shown [45]. Right: invariant mass spectrum of dimuons from ρ meson decays from the NA60 Collaboration [46].

1.4.7 Observables related to chiral symmetry restoration

The evolution of the effective quark mass parameter $\langle \bar{\psi}\psi \rangle$ with temperature (Figure 1.6) shifts the strange quark mass from its "dressed" value of about 500 MeV/c² to the current mass value ~ 150 MeV/c². This would make strange quarks creation (via $gg \rightarrow s\bar{s}$) more frequent in a deconfined QGP medium. However, it was shown that, at the same entropy-to-baryon ratio, the plasma in equilibrium does not contain more strangeness than an equilibrated hadron gas at the same temperature. What could signal the presence of a deconfined phase followed by hadronization via recombination are multi-strange baryons. If hadronization only occurs via fragmentation (e.g. in pp collisions), multi-strange baryons formation from single $s(\bar{s})$ quarks only takes place if all the other valence quarks are created separately [44]. In a QGP system multi-strange baryon formation is favoured by recombination of the more abundant $s(\bar{s})$ quarks.

ALICE measured Ξ baryon p_T differential cross-section in Pb–Pb collisions at $\sqrt{s_{\text{NN}}} = 2.76$ TeV. Figure 1.19 shows the strangeness enhancement factor for Ξ baryons, defined as the ratios of the Ξ baryon yield measured in Pb–Pb collisions, normalized to the mean number of participant nucleons $\langle N_{\text{part}} \rangle$, to the corresponding quantity in pp (or p–Be) interactions at the same energy [45]. Comparing the ALICE measurements with those from the experiments NA57 at the SPS (Pb–Pb collisions at $\sqrt{s_{\text{NN}}} = 17.2$ GeV) and STAR at RHIC (Au–Au collisions at $\sqrt{s_{\text{NN}}} = 200$ GeV), the enhancements are found to decrease with increasing centre-of-mass energy. Ξ baryon enhancement factor is larger than unity for all considered intervals, and increases with $\langle N_{\text{part}} \rangle$.

The spontaneous breaking of chiral symmetry manifests itself also in the violation of the mass degeneracies within chiral multiplets (ρ and a_1 , as seen in Section 1.1.3). Its

restoration should thus modify the mass and decay width of hadrons that form in the hot QCD medium, for instance theoretical models for the ρ meson in-medium production predict a mass shift and a broadening of its Breit-Wigner amplitude [47]. The ρ meson has a life-time comparable to the QGP phase duration ($\sim 10^{-23}$ s) and can thus decay in the medium. Its leptonic (e^+e^- or $\mu^+\mu^-$) decay mode provides a cleaner signal with respect to its (more probable) hadronic decays. Figure 1.19 (right) shows NA60 precision measurements of low-mass di-muon pair invariant mass distributions in 158 A GeV⁹ semicentral In-In collisions at the CERN SPS [46]. The vacuum ρ scenario is clearly ruled out. The in-medium broadening scenario (Rapp/Wambach [47]) appears more realistic. However, the nearly symmetrical broadening around the ρ pole seen in the data is not reproduced by this model and no shift in mass is visible. More detailed work including precise p_T dependences is under way to consolidate these findings.

1.4.8 Quarkonia

At high temperatures, quark-gluon plasma is expected to reduce the range of the attractive force between heavy quarks and antiquarks, and above a given critical temperature it prevents the formation of bound states.

The $q\bar{q}$ potential present in heavy quark bound states is the one reported in Equation 1.16 containing a Coloumbian term analogue to the QED one and a confinement term, which takes into account non-perturbative effects of QCD.

QGP formation however modifies this potential; the confinement term disappears after QGP formation while the color attractive term between q and \bar{q} gets screened by the presence of deconfined quarks and gluons. Assuming the following form

$$V(r) = -\frac{\alpha}{r} e^{-\frac{r}{\lambda_D}} \quad (1.44)$$

which is the expression of the Yukawa potential, where λ_D is the Debye screening length, related to the maximum distance two quarks can have in order to form a bound state. The length λ_D decreases as the temperature of the plasma increases.

Quarkonia states formed by heavy $q\bar{q}$ pairs can be used to prove this effect. Among charmonia states ($c\bar{c}$ pairs) the J/Ψ meson is the most stable, with a binding energy $\Delta E=0.64$ GeV, while Ψ' mesons are weakly bound ($\Delta E= \sim 0.05$ GeV). It follows that the Ψ' is expected to start dissociating at temperatures lower than the J/Ψ . The same holds in the bottomonium ($b\bar{b}$) family, where the most bound state is $\Upsilon(1S)$ ($\Delta E= \sim 1$ GeV), followed by $\Upsilon(2S)$ ($\Delta E= \sim 0.54$ GeV) and $\Upsilon(3S)$ ($\Delta E= \sim 0.20$ GeV). Figure 1.20 (left panel) shows a compilation of medium temperatures relative to the critical temperature (T_{crit}) at which quarkonium states are expected to be dissociated in the quark-gluon plasma. Each horizontal bar corresponds to one estimation and its temperature extension represents the range where the quarkonia state undergoes a modification until it completely melts [48]. The techniques used in the calculations are lattice QCD, QCD sum rules, AdS/CFT, effective field theories and potential models.

Experimentally, J/Ψ production was studied in heavy-ion collisions at the Super Proton Synchrotron (SPS) and at the Relativistic Heavy Ion Collider (RHIC), covering a large energy range from about 20 to 200 GeV center-of-mass energy per nucleon pair. At the SPS the measured J/Ψ suppression is compatible with the melting of the excited states (at SPS energies about 40% of the yield comes from Ψ' and χ_c decays) whereas the RHIC data suggest a small amount of suppression for the direct J/Ψ [48]. Recent results from

⁹fixed-target experiment

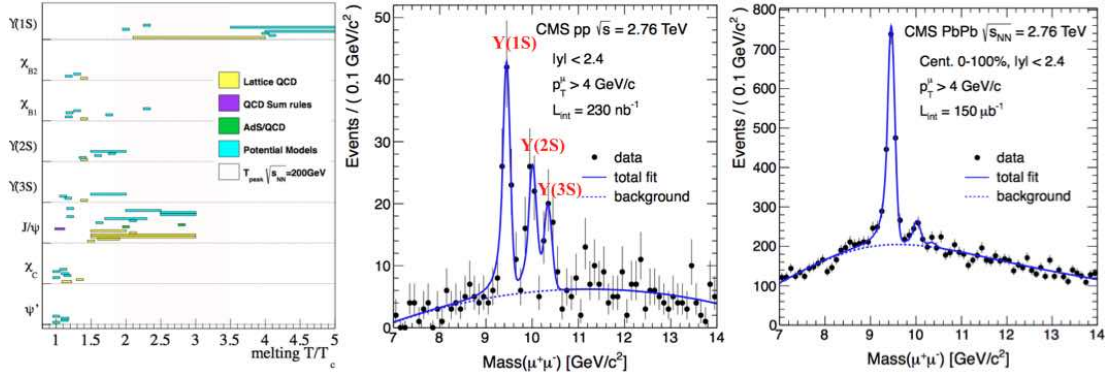


FIGURE 1.20: Left panel: Compilation of dissociation temperatures for different quarkonia states obtained with different theoretical models [48]. Central: CMS invariant mass distributions for di-muon in pp collisions at $\sqrt{s} = 2.76$ TeV, showing the three bottomonium peaks. Right panel: CMS invariant mass distributions for di-muon in Pb-Pb collisions at $\sqrt{s_{NN}} = 2.76$ TeV [49].

ALICE suggest that at LHC energies dissociation competes with J/Ψ production via (re)combination of charm quarks in the hot medium [50]. In fact at LHC energies the cross section for $c\bar{c}$ pair production is much higher than at SPS, making recombination effects more relevant.

The central and right panels of Figure 1.20 show the di-muon invariant mass spectrum for $\Upsilon(1S)$, $\Upsilon(2S)$ and $\Upsilon(3S)$ in pp and Pb-Pb collisions measured by the CMS Collaboration [49]. Their comparison clearly shows a suppression of the $\Upsilon(2S)$ and $\Upsilon(3S)$ peaks with respect to the $\Upsilon(1S)$ one in Pb-Pb collisions, in accordance with predictions of sequential melting showed in the left panel of Figure 1.20.

In conclusion the study of quarkonia production can provide a direct way to connect experimental high-energy nuclear physics to lattice QCD predictions, such as sequential quarkonia states suppression.

Chapter 2

Heavy flavours as probes of the QGP

The production of charm quarks in hadronic collisions is of great interest for many reasons. First, their mass value is well above the QCD confinement energy scale, and perturbative expansion of QCD diagrams for the calculation of the cross sections should in principle be valid. Data on particles containing c -quarks can thus be a benchmark for perturbative QCD calculations and provide constraints on the parameters used in the theory. Furthermore the comparison of c -quark related observables in pp and AA collisions is sensitive to any dynamical influence of the QGP medium on the evolution of heavy quarks that are predominantly produced in the very early stages of the nuclear interaction and traverse the entire evolution of the strongly-interacting medium.

Observables related to charm quark production can be divided in two categories, open and hidden charm:

- hidden charm states are all $c\bar{c}$ bound states (J/Ψ , Ψ' , etc.) and are easily reconstructed through their decay into lepton pairs (e^+e^- or $\mu^+\mu^-$)
- open charm states are hadrons in which $c(\bar{c})$ quarks bind to other lighter quarks. They include mesons (D^0 , D^+ , D^{*+} ..) and baryons (Λ_c , Ξ_c) and are experimentally detected by reconstructing their decay products:
 - hadronic decay modes: these allow a full reconstruction of the charm hadron kinematics, i.e. the value of the open heavy-flavour hadron transverse momentum, azimuthal angle, etc. are measured
 - semileptonic decay modes: a high- p_T lepton coming from the open heavy-flavour hadron decay is detected. To separate leptons from charm and beauty hadron decays different analysis strategy are available (impact parameter studies, $e-h$ correlations). This allows an inclusive measurement of open heavy-flavour hadrons properties and theoretical models can be compared to the measured leptonic transverse momentum distributions

In this chapter we will briefly introduce those aspects of pQCD relevant for charm quark production in hadronic collisions, and compare them to some measurements performed in $pp(\bar{p})$ collisions. The influence of cold and hot nuclear matter effects on c -quark production and evolution in pA and AA collisions constitutes the second part of the chapter, concluded by a brief review of experimental results.

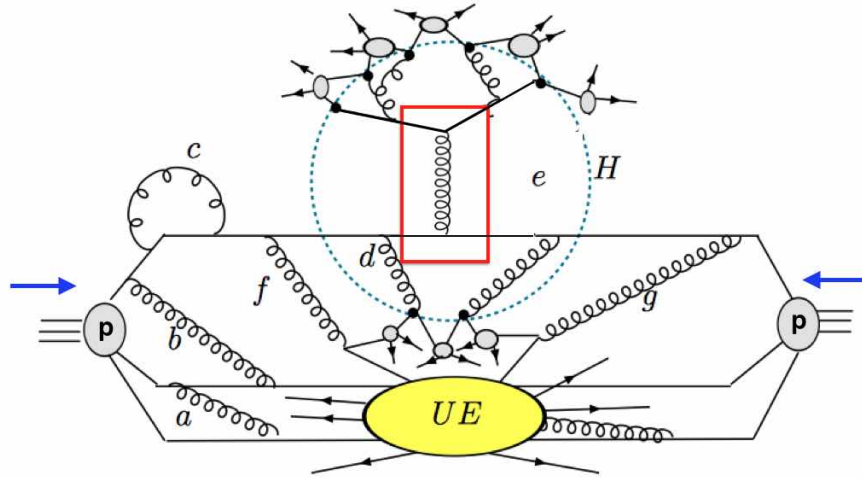


FIGURE 2.1: Schematic view of a pp interaction in which a hard scattering between two valence quarks (red box) takes place

2.1 Charm quark production in pp collisions [2]

Let's consider the hadronic interaction depicted in Figure 2.1, where two protons collide inelastically at high centre-of mass energy (several hundreds GeV). The two particles interact because of the hard (large momentum transfer Q^2) inelastic process among two constituent partons. In this example two valence quark interact, but in this energy regime also sea quarks and gluons can contribute.

Before the interaction occurs the valence quarks of the protons are constantly held together by the exchange of virtual gluons. These gluons are mostly soft, like a and b , since they are the expression of the QCD confinement. Gluons with high virtuality¹ like c prefer to be reabsorbed by the emitting parton since their exchange is not compatible with the stability of the proton. The Heisenberg principle predicts the time scale of these gluon exchanges, which is (in natural units) the inverse of the gluon virtuality $\tau=1/Q^2$ so that the hard gluon (c) lifetime is much shorter than the one of a and b which is $\sim 1/m_p$.

The inelastic scattering in the red box is characterized by large momentum transfers (we are considering a pp collision with \sqrt{s} at the scale of hundreds GeV) and it also happens on a very short time scale, which means that the soft-gluon mediated interactions (a, b, d, f, g) of the involved parton with the rest of the proton can be neglected, since they happen on a longer time scale. The struck quark simply does not have enough time to communicate that it is being kicked away from the proton.

The proton fragments excluded from the hard scattering will continue their evolution interacting on a low momentum scale and hadronizing into colorless states, constituting the Underlying Event (UE - yellow box).

The hard scattering in our example generates a $q\bar{q}$ pair at high virtuality, which could be a $c\bar{c}$ pair. These two quarks will emit gluons, that can in turn generate quark pairs and so on (parton shower). Once the virtuality scale of the produced particles is reduced to hadronic mass values hadronization occurs.

¹Virtual particles do not obey the formula $m^2c^4 = E^2 - p^2c^2$ and are said to be off-shell. A virtual gluon will behave kinematically as a massive particle and is short-lived. A virtual quark will have a kinematic mass value higher than its current mass.

The evolution depicted above can be expressed by the factorization theorem:

$$\sigma_{pp \rightarrow Hx} = \sum_{a,b} PDF(x_a, Q^2) PDF(x_b, Q^2) \sigma_{ab \rightarrow q\bar{q}} D_{q \rightarrow H}(z_q, Q^2) \quad (2.1)$$

where $\sigma_{ab \rightarrow Hx}$ is the inclusive cross-section for the production of a given hadron H in pp collisions and:

- the sum runs over all the possible combinations of parton pairs participating to the hard scattering, including sea quarks and gluons
- $\sigma_{ab \rightarrow q\bar{q}}$ is the partonic cross section for the production of the quark pair $q\bar{q}$. Given the large momentum transfer of the hard interaction, this cross section is calculable with perturbative QCD
- $PDF(x_a, Q^2)$ and $PDF(x_b, Q^2)$ are the Parton Distribution Functions of the two partons involved in the interaction inside the protons. They are the probability distributions of the fraction of proton momentum carried by the interacting parton
- $D_{q \rightarrow H}(z_q, Q^2)$ is the quark fragmentation function and represents the probability that the quark q produces a hadron H carrying a fraction z of its momentum

For light quarks and gluons, which have low (or zero) mass, also production via soft processes is possible. This means that to give a theoretical description of light flavour hadron production one has to deal with non-perturbative aspects of QCD.

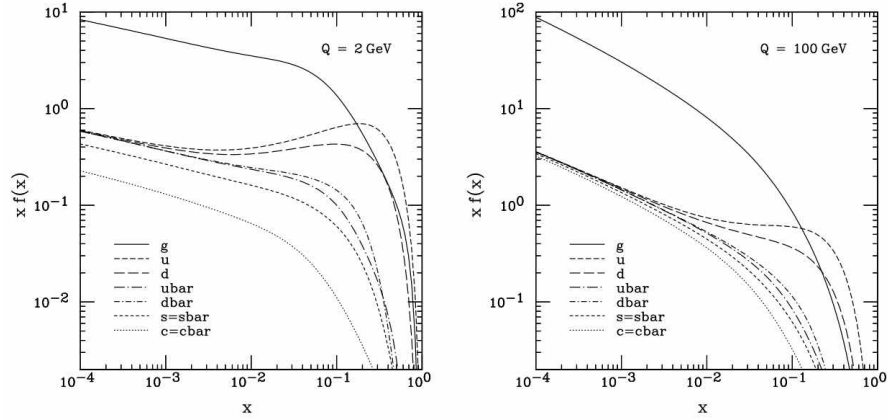
If the $q\bar{q}$ produced in the hard scattering are $c\bar{c}$ (or $b\bar{b}$) pairs, their mass $m_c \gg \Lambda_{QCD}$ will set a scale for the momentum transfer of the binary partonic interaction, assuring that its cross section will be calculable by perturbative QCD. This means that the study of charmed hadrons allows to better separate the non-perturbative and perturbative factors of Equation 2.1 when observing a hadronic cross-section.

The members of Equation 2.1 will be now discussed.

2.1.1 Parton Distribution Functions: PDF(x_a, Q^2)

In an electron-proton scattering the proton structure is investigated by an electromagnetic probe, i.e. an off-shell photon. The virtuality of the photon (Q^2) sets the time scale of the interaction and at sufficiently high Q^2 it will hit a single and substantially free quark carrying a fraction x of the total proton momentum. The probability $f(x)$ of finding a parton with a fraction x of the total momentum depends in general on the parton type, e.g. considering valence quarks the u and d quarks have different $f(x)$. However also the Q^2 of the interaction plays a role, since a gluon emitted with momentum $q < Q$ by the probed parton will not have enough time to be reabsorbed before the interaction with the photon takes place, and the parton momentum fraction x will appear lower. The distribution $f(x, Q^2)$ depends on the energy at which the parton is probed, and corresponds to the PDFs introduced in Equation 2.1. The evolution with Q^2 of a given PDF is given by the Altarelli-Parisi differential equation

$$\frac{df(x, \mu)}{d \log \mu^2} = \frac{\alpha_s}{\pi} \int_x^1 \frac{dy}{y} f(y, \mu) P_{q\bar{q}}(x/y) \quad (2.2)$$

FIGURE 2.2: CTEQ6M parton distribution functions at $Q = 2$ and 100 GeV [53].

where $P_{q\bar{q}}(x/y)$ describes the probability that a quark with a momentum fraction x emits a gluon keeping a fraction y of its momentum and μ is the factorization scale at which the PDFs are evaluated. Qualitatively, the factorization scale corresponds to the resolution with which the hadron is being probed.

In Deep Inelastic Scattering (DIS) the virtual photon can also interact with the sea $q\bar{q}$ pairs generated by gluon splitting. If the virtuality of the photon is high enough, the time scale of the hard interaction is so short that gluon fluctuations in virtual $c\bar{c}$ pairs become visible. For instance, in ep collisions at $x \sim 0.01$ and $Q^2 \sim 100$ GeV², charm contributes approximately to 25% of the total Neutral Current² (NC) DIS cross-section [51].

PDFs are extracted from experimental data of NC and Charged Current (CC) scatterings in high-energy ep collisions. The most recent PDFs sets are based on data coming from the Hadron Elektron Ring Anlage (HERA) collider, where electrons(positrons) and protons were collided at \sqrt{s} up to ~ 300 GeV. The ZEUS and H1 experiments have taken data on NC and CC in DIS, measuring in particular D mesons cross-section as a function of x and Q^2 that brings information on c -quark PDFs. The PDFs are extracted from a theoretical fit to the experimental data. The PDF uncertainties depend on the treatment of non-perturbative effects, the impact of missing higher-order perturbative terms and the choice of the QCD parameters (μ_F , μ_R ³, quark masses) for what concerns the theoretical inputs, and of course on the statistical and systematic uncertainties of the fitted data. As an example, in Figure 2.2 the CTEQ6M⁴ PDF at $Q = 2$ and 100 GeV are shown. Details on the CTEQ6M fit can be found in [53].

2.1.2 Partonic cross-section: $\sigma_{ab \rightarrow q\bar{q}}$

Let us limit ourselves to the production of heavy-quark pairs ($Q\bar{Q}$). In pQCD the leading order processes to be considered are:

- quark-antiquark annihilation $q\bar{q} \rightarrow Q\bar{Q}$

²When the Q^2 of the interaction overcomes the electroweak vector bosons mass threshold, the mediator of the DIS event can also be a W^\pm or a Z boson

³The renormalization scale μ_R is the energy scale used in the evaluation of α_s . The factorization scale μ_F is the scale used in the evolution of the parton densities (eq. 2.2 [52])

⁴Coordinated Theoretical-Experimental Project on QCD

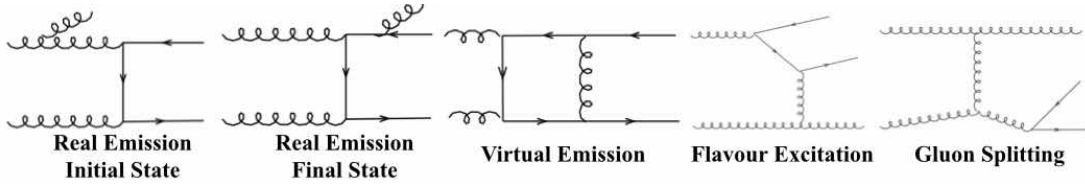


FIGURE 2.3: NLO diagrams for heavy-quark pairs production

- gluon-gluon fusion $gg \rightarrow Q\bar{Q}$

The amplitudes of both processes are finite, due the mass of the heavy quark that sets the scale both in the s and t production channels. At high energies these amplitudes can be expressed as [52]:

$$\lim_{\hat{s} \rightarrow \infty} \hat{\sigma}_{q\bar{q} \rightarrow Q\bar{Q}} \propto \frac{1}{\hat{s}} \quad \lim_{\hat{s} \rightarrow \infty} \hat{\sigma}_{gg \rightarrow Q\bar{Q}} \propto \frac{1}{\hat{s}} L(\beta) \quad L(\beta) = \frac{1}{\beta} \log\left(\frac{1+\beta}{1-\beta}\right) - 2 \quad (2.3)$$

with $\beta = \sqrt{1 - \frac{4m^2}{\hat{s}}}$ and \hat{s} the partonic centre-of-mass energy. From these formulas we can draw some conclusions

- At large \hat{s} the $q\bar{q} \rightarrow Q\bar{Q}$ vanishes more quickly
- For two heavy quarks of mass m_1 and m_2

$$\lim_{\hat{s} \rightarrow \infty} \frac{\hat{\sigma}_{gg \rightarrow Q_1\bar{Q}_1}}{\hat{\sigma}_{gg \rightarrow Q_2\bar{Q}_2}} = 1 - \frac{\log(m_1^2/m_2^2)}{\log(\hat{s}/m_2^2)} \quad \lim_{\hat{s} \rightarrow \infty} \frac{\hat{\sigma}_{q\hat{q} \rightarrow Q_1\bar{Q}_1}}{\hat{\sigma}_{q\hat{q} \rightarrow Q_2\bar{Q}_2}} = 1 - O(m_1^4/\hat{s}^2) \quad (2.4)$$

which at $\sqrt{\hat{s}} = 100$ GeV means

$$\frac{\sigma(gg \rightarrow b\bar{b})}{\sigma(gg \rightarrow c\bar{c})} \sim 0.7 \quad \frac{\sigma(q\hat{q} \rightarrow b\bar{b})}{\sigma(q\hat{q} \rightarrow c\bar{c})} \sim 0.99 \quad (2.5)$$

The inclusion of Next to Leading Order (NLO) diagrams in the calculation should make the pQCD picture of heavy-flavour production more realistic. In particular uncertainties related to the factorization μ_F and renormalization μ_R scales should be reduced.

NLO diagrams are shown in Figure 2.3. Ultraviolet divergences in the virtual diagrams are removed by the renormalization process. Real emission by initial state parton is re-absorbed in the PDFs as explained before. Real emission by final state heavy-quarks is collinear safe since the quarks mass value prevents gluon emission at small angles. However, when the momenta of the produced quarks become large with respect to the heavy-quark mass, large logarithms of the ratio $\frac{p_T}{m}$ arise to all orders in the perturbative expansion of the cross-section, and spoil its convergence. Two examples are the Flavour Excitation and Gluon Splitting diagrams in Figure 2.3, and their inclusion in the calculation originates similar large logarithms at higher orders of perturbative expansion.

Different theoretical framework have been developed to deal with these large influence of higher-order corrections in perturbative calculations:

- **Fixed Order Next-to-Leading Log (FONLL)** [54]: the p_T spectrum of heavy-flavour production is obtained at NLO accuracy in α_s , while leading logarithmic (LL) terms of the form $\alpha_s^2 (\alpha_s \log \frac{p_T}{m})^k$ and next-to-leading logarithmic (NLL) terms

of the form $\alpha_s^3(\alpha_s \log \frac{p_T}{m})^k$ are resummed in the pQCD expansion. Uncertainties depend on the heavy-quark mass value, and the renormalization and factorization scales μ_R and μ_F

- **General-Mass Variable-Flavour-Number Scheme (GM-VFNS)** [55]: this framework adopts the minimal subtraction scheme⁵ considering a massive charm quark. The number of active quarks in the calculations depends on the factorization scale μ_F : for low values of μ_F only g, u, d and s are considered. Charm is included if $\mu_F > m_c$

Both frameworks however are collinearly-factorized, which means that the transverse momenta of the incoming partons are zero. As seen previously at LHC energies charm production is dominated by gluon fusion processes, which means that in a collinearly-factorized framework transverse momenta of produced charm quark and antiquark are equal. Thus collinear factorization cannot be used for studies of correlation observables for charmed meson pairs. In the k_T -**factorization** approach, off-shell leading order matrix elements for $gg \rightarrow c\bar{c}$ together with unintegrated gluon densities (UGDF) that depend on the transverse momentum of the gluon, k_T , as well as the usual dependence on x and on the factorization scale are used [56]. Predictions for D-meson production in pp collisions have recently been published and their comparison to ALICE measurements will be shown in Section 2.1.4.

2.1.3 Fragmentation Functions: $D_{q \rightarrow H}(z_q, Q^2)$

The process of heavy-quarks fragmenting into hadrons is non-perturbative, but the fragmentation functions can be extracted from data.

In e^+e^- collisions the energy of the primary heavy quark pair before the perturbative (hard gluon emission) and non perturbative (soft gluon emission, hadronization) processes is known. The measurement of hadronic cross sections in e^+e^- annihilation via a virtual photon (γ) or Z boson, $e^+e^- \rightarrow \gamma(Z) \rightarrow H$ (H is a generic hadron) can be fitted with electroweak theoretical calculations that take into account pQCD (gluon radiation) and electroweak (photon radiation) effects.

Figure 2.4 (left) shows Belle results for D^+ meson production in e^+e^- collisions at $\sqrt{s} = 10.6$ GeV [57]. The D^+ meson cross section is shown as a function of $x_p = \vec{p}^{D^+} / \vec{p}_{max}^{D^+}$

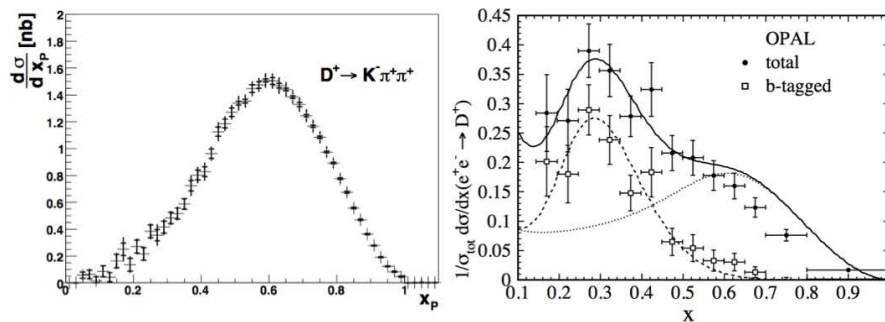


FIGURE 2.4: Belle (left [57]) and OPAL (right [58]) results for D^+ meson cross-section as a function of x_p

⁵renormalization scheme used to absorb the infinities that arise in perturbative calculations beyond leading order, introduced by 't Hooft (Nobel Prize 1999)

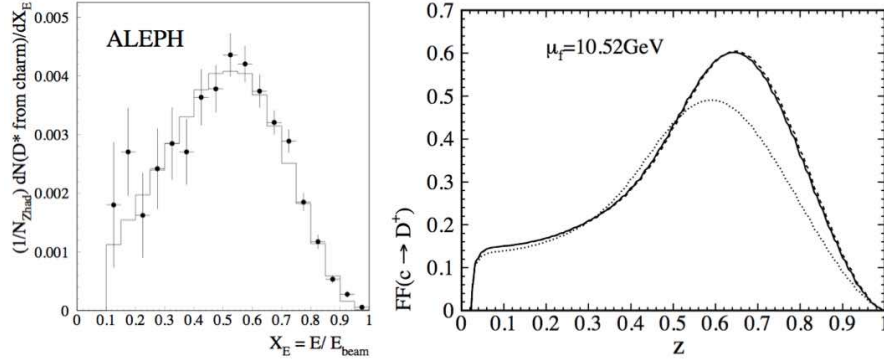


FIGURE 2.5: Left: ALEPH distribution of $X_E=E/E^{\text{beam}}$ for the D^{*+} meson cross-section from the $c\bar{c}$ source [59]. Right: fragmentation function of c -quarks into D^+ mesons at the reference scale $\mu_F=10.52$ GeV from Belle and CLEO data [57].

with $\vec{p}_{max}^{D^+} = \sqrt{s/4 - m_{D^+}^2}$. This measurement excludes the fraction of D^+ mesons coming from B hadron decays, giving access to the c quark fragmentation functions.

The right panel of Figure 2.4 shows the same results from e^+e^- collisions at $\sqrt{s} = 91.2$ GeV [58] measured by the OPAL collaboration at LEP. Here the total D^+ meson normalized cross section is shown, and the cross section of b -quark-initiated D^+ is superimposed. A theoretical fit is superimposed to extract the c -quark-initiated, b -quark-initiated, and total contributions, respectively.

The charm fragmentation function used to extract the FONLL predictions that will be reported in the next paragraph are obtained from fits to D^{*+} fragmentation data in $e^+e^- \rightarrow Z \rightarrow c\bar{c}$ events published by the ALEPH collaboration [59]. The ALEPH distribution of $X_E=E/E^{\text{beam}}$ for the D^{*+} meson cross-section from the $c\bar{c}$ source (Figure 2.5 - right) is fitted with a convolution of a perturbative contribution D_N^{pQCD} (which describes the production of a c quark in the hard interaction) and a non-perturbative fragmentation function $D_{BCFY,N}^V(r, z)$ describing its hadronization into the D^{*+} [60]:

$$\sigma_N(c \rightarrow D^{*+})(r, z) = D_N^{pQCD} * D_{BCFY,N}^V(r, z) \quad (2.6)$$

The term $D_{BCFY,N}^V(r, z)$ depends on the non-perturbative parameter $r = \frac{M_H - M_Q}{M_H}$ (M_H and M_Q are the masses of the charmed hadron and of charm, respectively) and on z , the longitudinal momentum fraction of the hadron relative to the fragmenting heavy quark. The functional form of $D_{BCFY,N}^V(r, z)$ (which describes the fragmentation of c -quarks into a vector meson state like D^{*+}) can be found in [61] together with that of $D_{BCFY,N}^P(r, z)$, describing the transition of a c -quark into a pseudoscalar meson state like D^+ . The fit to ALEPH data allows to fix the r parameter to 0.1, and the fragmentation functions of the different D meson states are obtained as linear combination $D_{BCFY,N}^V(r, z)$ and $D_{BCFY,N}^P(r, z)$, with the corresponding branching ratios as coefficients. As an example, for D^{*+} and D^+ we get

$$D^{c \rightarrow D^{*+}}(z) = \text{BR}(c \rightarrow D^{*+}) D_{BCFY,N}^V(z) = 0.233 D_{BCFY,N}^V(z) \quad (2.7)$$

$$\begin{aligned} D^{c \rightarrow D^+}(z) &= \text{BR}(c \rightarrow D^+) D_{BCFY,N}^P(z) + \text{BR}(c \rightarrow D^{*+}) \text{BR}(D^{*+} \rightarrow D^+) D_{BCFY,N}^V(z) = \\ &= 0.162 D_{BCFY,N}^P(z) + 0.072 D_{BCFY,N}^V(z) \end{aligned} \quad (2.8)$$

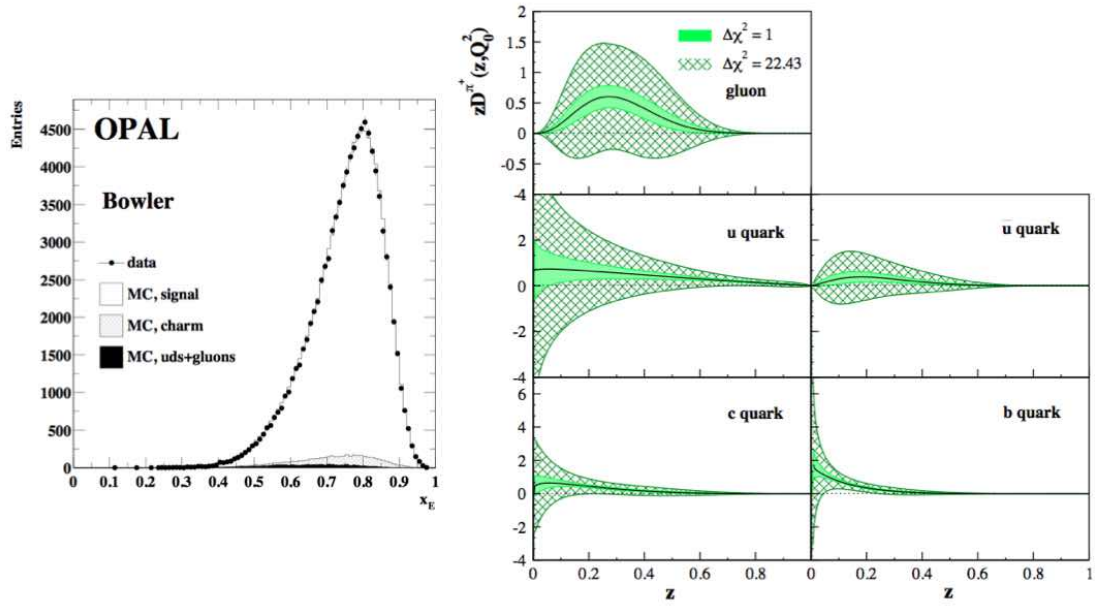


FIGURE 2.6: Left: inclusive fragmentation function of b quarks into B hadrons measured by the OPAL Collaboration in e^+e^- collisions at $\sqrt{s} = 91.2$ GeV [63]. Right: π^+ fragmentation functions from global fit to single-inclusive electron-positron annihilation data and semi-inclusive deep inelastic scattering asymmetry data from HERMES and COMPASS, as detailed in [64].

The GM-VFNS predictions use fragmentation functions for D^0 , D^+ and D^{*+} determined via a fit to e^+e^- data at $\sqrt{s} = 10.52$ GeV from Belle and CLEO Collaborations [57], as exposed in [62]. The fitted fragmentation function of c -quarks into D^+ mesons is shown in Figure 2.5 (right) at the reference scale $\mu_F=10.52$ GeV, and the Altarelli Parisi equation (Equation 2.2) predicts their evolution at other energy scales.

The $c \rightarrow D^+$ fragmentation function in Figure 2.5 (right) shows a peak structure at high (~ 0.7) values of the fractional momentum z . This feature is also visible in the inclusive fragmentation function of b quarks into B hadrons measured by the OPAL Collaboration in e^+e^- collisions at $\sqrt{s} = 91.2$ GeV [63], shown in Figure 2.6 (left) together with a MC fit based on Bowler fragmentation model [65] highlighting the low contributions from charm, gluons and light quarks. Heavy flavored mesons retain a large fraction of the momentum of the primordial heavy quark, in contrast to light hadrons fragmentation processes. Figure 2.6 (right) shows π^+ fragmentation functions from global fit to single-inclusive electron-positron annihilation data and semi-inclusive deep inelastic scattering asymmetry data from HERMES and COMPASS, as detailed in [64].

2.1.4 Some results in $p\bar{p}$

I will now discuss four measurement of open-charm production in $p\bar{p}$ or $p\bar{p}$ collisions together with predictions from the pQCD calculations described previously

- Figure 2.7 (left) shows the D^{*+} p_T differential cross section in $p\bar{p}$ collisions at $\sqrt{s} = 1.96$ TeV measured by CDF [66]. The cross-section is measured only for D mesons coming from c -quark fragmentation (prompt D mesons) and excludes the fraction of D meson coming from beauty hadron decays (feed-down D mesons). The

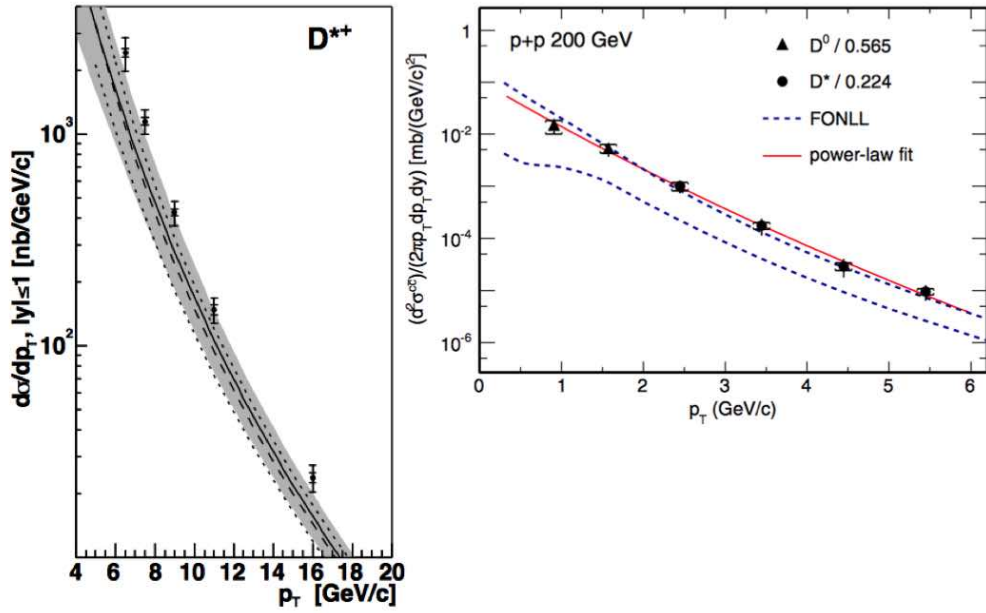


FIGURE 2.7: Left: D^{*+} differential cross section measurement for $|y| < 1$ in $p\bar{p}$ collisions at $\sqrt{s} = 1.96$ TeV [66]. The inner bars represent the statistical uncertainties; the outer bars are the quadratic sums of the statistical and systematic uncertainties. The solid curves are the theoretical predictions for FONLL, with the uncertainties indicated by the shaded bands. The dashed curve is the theoretical prediction from GM-VFNS, the dotted lines indicate the uncertainty. Right: p_T differential cross section of $c\bar{c}$ pairs measured by STAR in pp collisions at $\sqrt{s} = 200$ GeV [67]. The dashed blue lines represent the limits of FONLL predictions.

measurements are compared to both FONLL and GM-VFNS calculations. The uncertainties on the calculated cross sections are evaluated by varying independently the renormalization and factorization scales. The measured differential cross sections are higher than the theoretical predictions by about 100% at low p_T and 50% at high p_T . However, they are compatible within uncertainties.

- Figure 2.7 (right) shows the p_T differential $c\bar{c}$ cross section in pp collisions at $\sqrt{s} = 200$ GeV measured by STAR at mid-rapidity [67]. The $c\bar{c}$ cross-section derives from the D^0 and D^{*+} cross-sections divided by the corresponding c -quark fragmentation fraction values. FONLL calculations are superimposed, the upper and lower limits derive from the variation of the factorization and renormalization scales. These results are consistent with the upper limit of the FONLL pQCD calculations.
- Figure 2.8 shows the prompt D^+ p_T differential cross sections in pp collisions at $\sqrt{s} = 7$ TeV (left) and $\sqrt{s} = 2.76$ TeV (right) measured by the ALICE Collaboration in $|y| < 0.5$ compared to both FONLL and GM-VFNS models [68]. Both calculations use the CTEQ6.6 parametrizations of the PDFs, and their uncertainties correspond to the variation of m_c , μ_R and μ_F parameters used in the calculations. The central values of the FONLL predictions lie systematically below the data, as for the first two measurements (CDF and STAR). The GM-VFNS central points lie systematically above the data. However both models are consistent with data within uncertainties. Figure 2.9 (left) shows the 7 TeV data (same as in the left

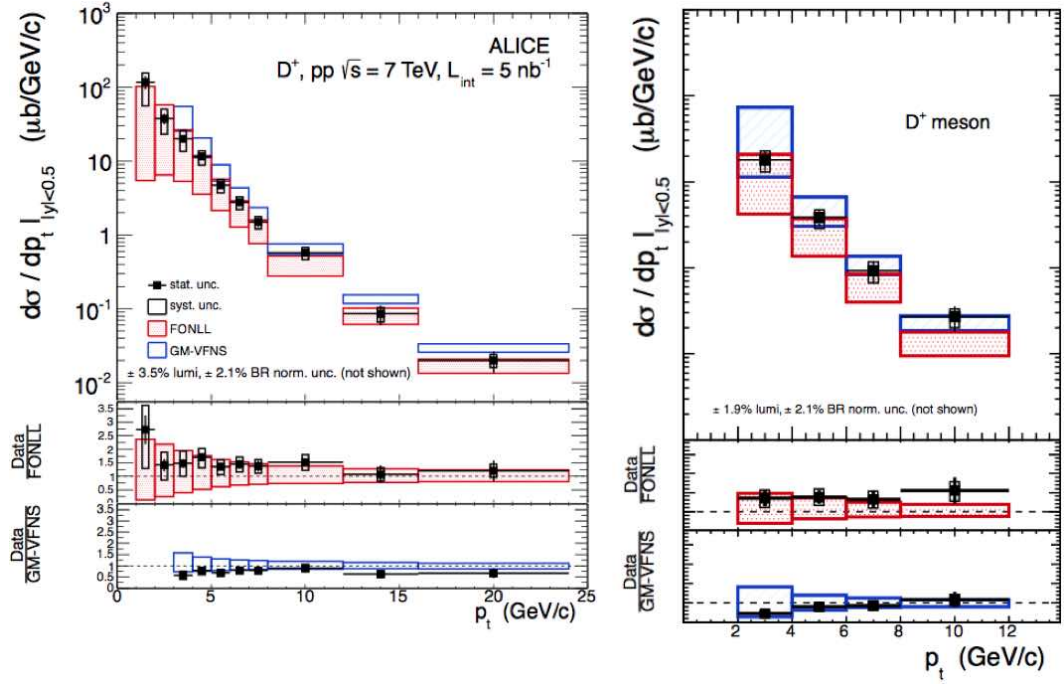


FIGURE 2.8: Prompt D^+ differential cross section measurement ($|y| < 0.5$) in pp collisions at $\sqrt{s} = 7$ TeV (left) and $\sqrt{s} = 2.76$ TeV (right). Both FONLL and GM-VFNS predictions are shown [68].

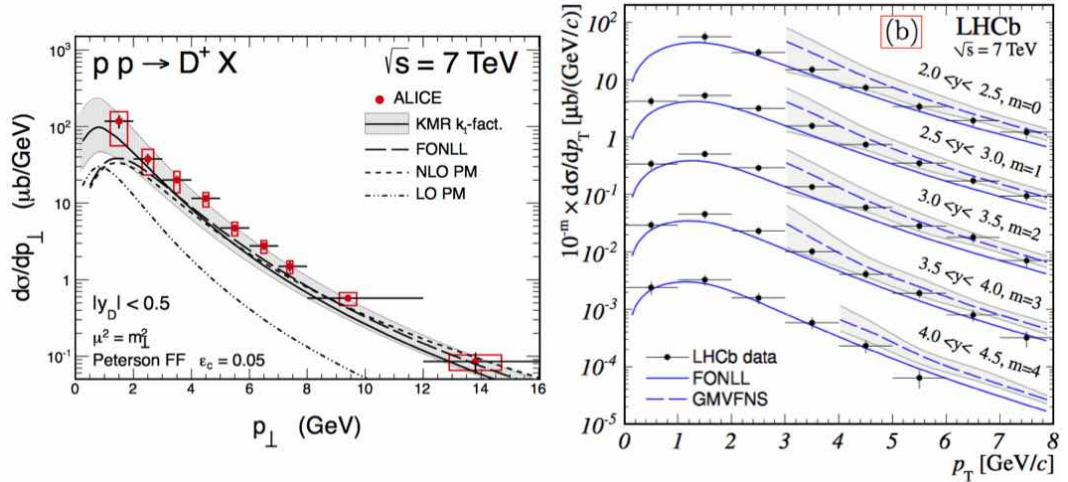


FIGURE 2.9: Left: prompt D^+ differential cross section measurement ($|y| < 0.5$) in pp collisions at $\sqrt{s} = 7$ TeV with FONLL, GM-VFNS and k_T factorization predictions [69]. Right: prompt D^+ p_T differential cross section in pp collisions at $\sqrt{s} = 7$ TeV measured by the LHCb Collaborations in five rapidity intervals. The measurement relative to each rapidity interval is scaled by 10^{-m} where m is indicated close to each set of points [70].

panel of Figure 2.8) together with FONLL, GM-VFNS and k_T factorization predictions [69]. The k_T factorization approach reproduces the data only if the KMR UGDFs are used. All other unintegrated gluon distributions strongly underpredict the experimental results. This may suggest that some mechanism of charm production, like double parton scattering, is still missing.

The total charm production cross section was extrapolated to the full phase space using the sum of the total production cross section for D^0 and D^+ divided by the sum of their fragmentation ratios. The total production cross section for D^{*+} divided by its fragmentation ratio using the inverse of the squared statistical uncertainties as weights. The values obtained are

$$\sigma(c\bar{c}) = 8.5 \pm 0.5(\text{stat})_{-2.4}^{+1.0}(\text{syst}) \pm 0.1(\text{BR}) \pm 0.2(\text{frag}) \pm 0.3(\text{lum})_{-0.4}^{+5.0}(\text{extr}) \text{ mb}^6$$

at $\sqrt{s} = 7 \text{ TeV}$ and

$$\sigma(c\bar{c}) = 4.8 \pm 0.8(\text{stat})_{-1.3}^{+1.0}(\text{syst}) \pm 0.06(\text{BR}) \pm 0.1(\text{frag}) \pm 0.1(\text{lum})_{-0.4}^{+2.6}(\text{extr}) \text{ mb}$$

at $\sqrt{s} = 2.76 \text{ TeV}$.

- Figure 2.9 (right) shows the prompt D^+ p_T differential cross section in pp collisions at $\sqrt{s} = 7 \text{ TeV}$ measured by the LHCb Collaboration compared to both FONLL and GM-VFNS pQCD calculations [70]. The cross-section is measured in five rapidity intervals in the region $2 < y < 4.5$. Both models are consistent with data within uncertainties (FONLL uncertainties are not shown) and the same behaviour (FONLL central value underestimating the data, GM-VFNS overestimating the data) observed in ALICE and CDF measurements is found. These data together with other LHCb measurements relative to D^0 , D^{*+} and D_s^+ mesons allow the extraction of the total charm cross-section inside the acceptance region of the measurements, $0 < p_T < 8 \text{ GeV}/c$ and $2 < y < 4.5$:

$$\sigma(c\bar{c})_{p_T < 8 \text{ GeV}/c, 2 < y < 4.5} = 1419 \pm 12(\text{stat}) \pm 116(\text{syst}) \pm 65(\text{frag}) \mu\text{b}$$

2.2 Charm quark production in ultrarelativistic heavy-ion collisions

Heavy quarks in heavy-ion collisions are produced via the same mechanism described in the previous section for pp collisions, i.e. via hard partonic scattering processes occurring on short time scales. The formation time of a heavy-quark pair ($\tau \sim 1/Q^2$, which for charm formation at the threshold is $\sim 10^{-2} \text{ fm}/c$) is shorter than the time needed for the QGP to reach thermal equilibrium ($\sim 1 \text{ fm}/c$, see Section 1.3.1), so that heavy quark are predominantly produced in the very initial stages of the collision. In fact, even if inelastic scatterings among partons occur in the QGP fireball, the characteristic temperatures in this phase (i.e. the relevant momentum scale) are too low for thermal heavy-flavour production, whose contribution is small even at RHIC and LHC energies⁷ [71]. This means that:

⁶BR = from branching ratios uncertainties, frag = from fragmentation function uncertainties, lum = luminosity uncertainty, extr = full phase space extrapolation uncertainty

⁷Some works have shown the possibility of significant thermal contribution to charm quark production at LHC energies, but assuming high values of initial temperature ($\sim 750 \text{ MeV}$) and bare mass of light constituents (light quarks, gluon) in the QGP [71] [72]

- heavy quarks (like charm) experience the full evolution history of the expanding fireball, and are thus good probes of hot QCD medium
- heavy quarks production in AA collisions is proportional to the total number of binary collisions N_{coll} that took place in the nuclear interaction

But how can we extract information from heavy-flavour probes in heavy-ion collisions? If we look at Equation 2.1 we have to take into account that the PDFs are in general modified in a nuclear environment, as it will be discussed later. We can also expect that the part relative to fragmentation functions won't be valid in heavy-ion collisions, since quark fragmentation is not the only hadronization mechanism as already mentioned in Section 1.4.4. Also the full fragmentation process of hard partons could be affected by the presence of the dense QCD medium. Besides these aspects we also have to consider interactions between heavy quarks and the medium, that can modify the kinematics of heavy quarks prior to their hadronization. We can divide the phenomena influencing heavy-flavour production in heavy-ion collisions in two categories:

- **Cold Nuclear Matter Effects** are not due to QGP formation, but to the fact that the colliding particles are nuclei: for example, as far as heavy flavour production is concerned, PDFs in nuclei differ from those in free nucleons, and influence the heavy quark production kinematic. These effects should be also visible in p–A and e–A collisions.
- **Hot Medium Effects** are due to QGP formation, and are expected to be present only if the energy density and temperature achieved in the collision are high enough to allow the transition to the deconfined state. They include the interaction of the heavy-quark with the medium and the way it hadronizes.

If these effects influence heavy-quark production and dynamics, we cannot consider ultrarelativistic heavy-ion collisions as a superposition of incoherent nucleon-nucleon interactions. The p_T differential cross section for heavy-flavour observables will not be the one measured in pp collisions multiplied by the average Glauber N_{coll} of the event class considered.

When we measure the yield of some observable in AA collisions, we define the **nuclear modification factor** as the ratio of the observables yield in AA collisions and the one in pp collisions scaled by the average number of binary collisions $\langle N_{\text{coll}} \rangle$ obtained from Glauber calculation for the AA centrality class considered

$$R_{AA} = \frac{Yield^{AA}}{\langle N_{\text{coll}} \rangle Yield^{pp}} \quad (2.9)$$

In the case of the modification of the p_T distributions, R_{AA} can be expressed as:

$$R_{AA}(p_T) = \frac{dN^{AA}/dp_T}{\langle N_{\text{coll}} \rangle dN^{pp}/dp_T} = \frac{dN^{AA}/dp_T}{\langle T_{AA} \rangle d\sigma^{pp}/dp_T} \quad (2.10)$$

In case no modification (due to either cold or hot nuclear matter effect) is present, we expect R_{AA} to be equal to 1, and AA collisions can be treated as a superposition of N_{coll} nucleon-nucleon collisions. On the contrary any modification that affects the production rate and the momenta distributions of the considered observables in nuclear collisions

leads to an R_{AA} different than 1.

The same observable can be computed in pA collisions as:

$$R_{pA}(p_T) = \frac{dN^{pA}/dp_T}{\langle N_{\text{coll}} \rangle dN^{pp}/dp_T} = \frac{d\sigma^{pA}/dp_T}{A d\sigma^{pp}/dp_T} \quad (2.11)$$

where A is the mass number of the colliding nucleus.

In the following sections we will examine cold and hot nuclear matter effects, presenting some experimental results that will make more complete the discussion of QGP physics of Chapter 1.

2.2.1 Initial State Effects

The presence of a nucleus in the initial state induces modifications in the heavy quarks production mechanism with respect to what happens in pp interactions. In this section we are going to discuss:

- nuclear modification of the PDFs
- k_T broadening and Cronin enhancement
- energy loss in cold nuclear matter

Parton distribution functions in nuclei differ from those measured in free nucleons. This was first observed by the European Muon Collaboration (EMC) at CERN in 1983 in muon-nuclei DIS experiments. In particular in Figure 2.10 (left) we see the ratio of the DIS cross-section in nuclei (Fe, Cu) to the one in deuterium as a function of Bjorken x measured by EMC and by SLAC E139 experiment. This ratio is proportional to the ratio of the structure functions $F_2^{\text{Fe,Cu}}$ and F_2^d in nuclei and deuterium [73]. We can divide this measurement in four region of Bjorken x :

- the region $0.8 < x < 1$ the ratio is above unity which is explained by the effect of the nucleon motion inside the nucleus (Fermi motion)
- in the interval $0.3 < x < 0.8$ the ratio is lower than unity and this suppression is called the EMC effect
- for $0.1 < x < 0.3$, the ratio is above unity; the effect is small (of the order of a few percent) and does not reveal a dependence on the atomic mass number. This is the nuclear anti-shadowing region.
- for small values of Bjorken x , $x < 0.05 - 0.1$, the ratio is noticeably suppressed. The suppression increases with increasing atomic number A and decreasing x . This is the nuclear shadowing region.

This modifications influence charm quark production, as it can be deduced when looking at Equation 2.1. For what concerns the theoretical explanation of the **EMC** effect, several phenomenological hypotheses have been proposed [74]:

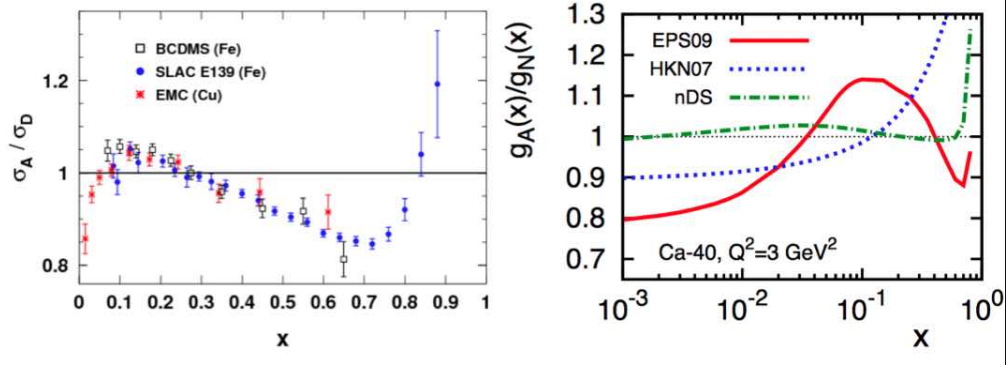


FIGURE 2.10: Left: measurement of nuclear PDFs modification in Fe and Cu from several experiments. Right: The EPS09 fit to the nuclear PDFs data, together with other models

- **x rescaling:** values of x of partons in nuclei are shifted to lower values with respect to the free nucleon case. This may either arise from conventional nuclear binding leading to a reduced effective mass of partons (and thus lower effective x values) or from the presence of π fields in the intense nuclear potential that enhance the number of degrees of freedom among which the total nuclear momentum is shared
- **Q^2 rescaling:** the effective Q^2 value with which parton in nuclei are probed in DIS experiments is larger than the measured one, if we assume that quarks are confined into larger volumes when bound into nuclei with respect to the free nucleon case. We can expect confinement scale to be larger if we consider the overlap of nucleon wave functions or the formation of nucleon clusters

In the **shadowing region**, two main explanations have been proposed:

- a modification of the interaction of the virtual photon with the atomic nucleus due to fluctuations of the virtual photon into quark-antiquark pairs (i.e. vector mesons having the same quantum numbers as the photon). Such a pair then interacts with the nucleus via the strong interaction. Since the strength of the latter is much larger than the electromagnetic one, the interaction does no longer happen incoherently with all the nucleons in the nucleus but preferentially with those at the front surface. These photonic fluctuations are visible when small Bjorken x values are being probed. The nucleons being in the ‘shadow’ of the nucleons at the front surface then do not or much less contribute to the interaction, resulting in a reduction of the cross section
- in the laboratory rest-frame ultrarelativistic heavy-ions are Lorentz-contracted. This enhances the partonic densities and in particular the gluon density is expected to saturate at very low- x , leading to gluon fusion process. The BKFL equations are evolution equations (like DGLAP) that predict the evolution of PDFs going to lower x -values. They don’t take into account gluon fusion processes and lead to an uncontrolled increase of gluon densities at low- x . The Color Glass Condensate (CGC) is a phenomenological model for shadowing that assumes the existence of a saturation scale Q_s^2 below which the BKFL also take into account recombination effects [75].

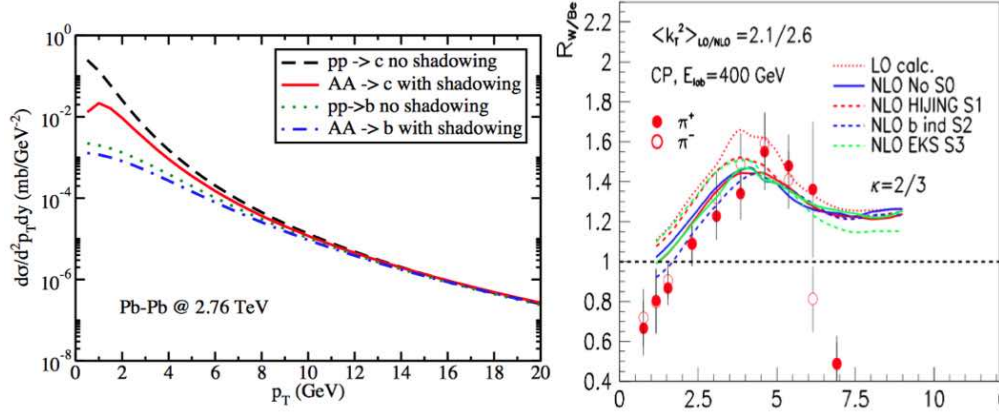


FIGURE 2.11: Left: NLO pQCD predictions for $c\bar{c}$ and $b\bar{b}$ production in Pb–Pb collisions at $\sqrt{s_{\text{NN}}} = 2.76$ TeV with and without the EPS09 parametrization of nuclear PDFs. Right: the ratio of the pion nuclear modification factors obtained colliding 400 GeV/ c protons on W and Be target, respectively

QCD global analyses on experimental data allow to parametrize the nuclear PDFs as well as their dependence on Q^2 values and atomic mass number. The **EPS09**⁸ parametrization of PDFs is extracted from a NLO pQCD analysis with three different experimental inputs, deep inelastic l -A scattering, Drell-Yan dilepton production in p-A collisions, and inclusive pion production in d-Au and p-p collisions at RHIC [76]. The fit to experimental data is shown in Figure 2.10 (right) together with parametrizations from other analyses (HKN07, more details in [77]).

The influence of these modifications of the PDFs on the transverse momentum spectrum of heavy-flavour hadrons can be visualized if we consider the collision of two nucleons at a certain \sqrt{s} . Two partons undergoing a hard scattering process will have (neglecting their intrinsic transverse momenta) the four-momenta $(x_1, 0, 0, x_1)\sqrt{s}$ and $(x_2, 0, 0, -x_2)\sqrt{s}$, respectively. If a heavy-quark pair is created, the square of their invariant mass $M_{Q\bar{Q}}$ is given by

$$M_{Q\bar{Q}}^2 = x_1 x_2 s \quad (2.12)$$

and their rapidity $y_{Q\bar{Q}}$

$$y_{Q\bar{Q}} = \frac{1}{2} \ln \frac{E + p_z}{E - p_z} = \frac{1}{2} \ln x_1/x_2 \quad (2.13)$$

From these two relations we can derive

$$x_1 = \frac{M_{Q\bar{Q}}}{s_{\text{NN}}} e^{+y_{Q\bar{Q}}} \quad x_2 = \frac{M_{Q\bar{Q}}}{s_{\text{NN}}} e^{-y_{Q\bar{Q}}} \quad (2.14)$$

that can be easily [78] generalized in case we collide two nuclei of atomic and mass number (A_1, Z_1) and (A_2, Z_2) with the same accelerating device. In this case the centre-of-mass energy per nucleon pair is $\sqrt{s_{\text{NN}}} = \sqrt{\frac{Z_1 Z_2}{A_1 A_2}} \sqrt{s}$ and the following relation holds

$$x_1 = \frac{Z_1}{A_1} \frac{M_{Q\bar{Q}}}{s_{\text{NN}}} e^{+y_{Q\bar{Q}}} \quad x_2 = \frac{Z_2}{A_2} \frac{M_{Q\bar{Q}}}{s_{\text{NN}}} e^{-y_{Q\bar{Q}}} \quad (2.15)$$

From these relations we deduce that the x values probed at mid-rapidity ($y=0$) are of the same order of magnitude for the two quarks taking part to the hard interaction.

⁸Eskola, Paukkunen, Salgado

The value of x decreases with increasing centre-of-mass energy. At LHC energies, low (compared to the quark mass) transverse momentum charm-quarks probe x values of the order of 10^{-4} , which are in the shadowing region [79].

Figure 2.11 shows the cross section for $c\bar{c}$ and $b\bar{b}$ production at mid-rapidity in pp and Pb–Pb collisions at $\sqrt{s_{NN}}=2.76$ TeV, respectively. The predictions for Pb–Pb are obtained from NLO pQCD (as the pp ones) and the EPS09 parametrization of PDFs. The effect is more evident for $c\bar{c}$, where at low p_T the cross-section (rescaled by the number of binary collisions) is lower than in pp collisions. This can be understood if we look at Equation 2.15: at low p_T we are probing the shadowing region of Bjorken x , where nuclear PDFs are suppressed, leading to a reduction of the $c\bar{c}$ production cross-section according to Equation 2.1.

The so-called **Cronin enhancement** was first observed in p–W fixed-target experiments at Fermilab [80]. This effect consists in an enhancement above unity of the nuclear modification factor of produced particles at intermediate p_T ($2\div 6$ GeV/ c). It can be interpreted in terms of multiple elastic interactions of the projectile parton in the nucleus prior to the hard scattering. These elastic interactions confer to the projectile an extra quantity of transverse momentum before the hard scattering occurs, leading to a broadening of the momentum distributions for the produced particles. The results of the measurement of the π nuclear modification factor in p–W collisions relative to the one in p–Be collisions is shown in Figure 2.11(right). The models describing the effect may be classified according to the physical object which is undergoing rescatterings (the projectile hadron or its partons), and to the hardness of the rescattering processes taken into account [81]. Another effect that could be present is the energy loss of partons traversing cold nuclear matter. In the BDMPS model [82] the energy loss

$$\langle\Delta E\rangle\propto\alpha_s C_R\hat{q}L^2\tag{2.16}$$

is proportional to the square of the traversed distance L^2 , C_R is the colour charge of the parton projectile ($4/3$ for quarks, 3 for gluons) and \hat{q} is a parameter depending on the characteristics of the medium. The BDMPS model, which is also valid in case the traversed medium is the QGP, will be discussed in next Section. Here the previous formula will be used to have some estimates on the energy loss in cold medium: for $\hat{q}=0.01$ GeV²/fm, $C_R=4/3$ and $L=10$ fm, the expected energy loss is $\langle\Delta E\rangle\approx 2$ GeV ($L/10$ fm) [82].

The study of cold nuclear matter effects is not straightforward when one looks at A–A results, since any observed modification of transverse momentum spectra with respect to pp collisions could be also due to the creation of the QGP affecting particle production. However cold nuclear matter effects can be studied in p–A collisions, under the assumption that energy densities and temperature achieved in this kind of collisions are not high enough for an extended QGP phase to form.

2.2.2 Hot Nuclear Matter Effects

As mentioned at the beginning of this section, $c\bar{c}$ pairs are produced in the very early stages of a AA collision and are thus good probes of the high-density medium created. Their interactions with the medium constituents modifies their dynamical properties, and this modifications can be studied by measuring charmed hadron production as introduced at the beginning of this chapter. In particular in this section we will discuss heavy quarks energy loss in the hot medium, to which both collisional and radiative

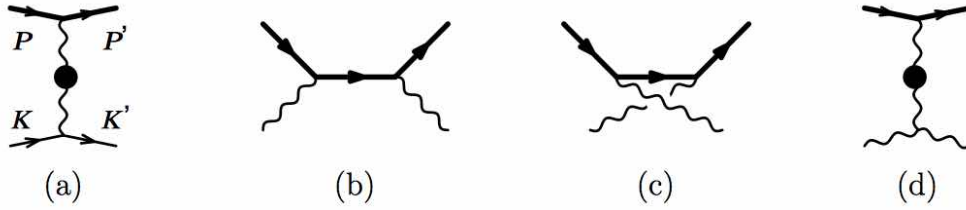


FIGURE 2.12: Amplitudes for heavy quark elastic scattering in a QGP. A curly line denotes a gluon.

processes contribute.

2.2.2.1 Collisional Energy Loss

High energy partons propagating through a QGP suffer energy loss via elastic scattering off particles (quarks and gluons) in the plasma. This mechanism is very similar in structure to ionization energy loss of charged particles in ordinary matter via electromagnetic interactions. The first quantitative calculations of this effect were performed by Bjorken [83] and a similar formalism was carried out by Peigne' in [84] for heavy and light quarks with initial energy $E \gg T, m_q$, where m_q is the mass of the light constituents of the medium. In the case the incoming particle is a heavy-flavour quark Q of mass $M \gg T$ and energy $E \gg M$, we can neglect s -channel diagrams with quarks or antiquarks of the same flavour in the plasma (because their abundance is negligible), and the scattering amplitude is given by the diagrams shown in Figure 2.12, where elastic scattering occurs with gluons and u, d and s quarks. Summing these amplitudes at the leading order gives [84]

$$\frac{dE(Q)}{dx} = \frac{4\pi\alpha_s T^2}{3} \left[(1 + n_f/6) \ln\left(\frac{ET}{m_D}\right) + \frac{2}{9} \ln\left(\frac{ET}{M}\right) + O(1) \right] \quad (2.17)$$

where n_f is the number of flavours considered in the scattering diagrams of Figure 2.12 and m_D is the Debye screening mass of the plasma $m_D = 4\pi\alpha_s T^2 (1 + n_f/6)$. The analogous calculation for a light quark q (in the limit $E \gg T$) also has to take into account s -diagrams for elastic scatterings and gives

$$\frac{dE(q)}{dx} = \frac{4\pi\alpha_s T^2}{3} \left[(1 + n_f/6) \ln\left(\frac{ET}{m_D}\right) + O(1) \right] \quad (2.18)$$

Due to the additional logarithm in Equation 2.12, when $E \gg M/T$ the collisional loss is larger for a heavy than for a light quark. Taking $E \rightarrow \infty$ and $n_f = 3$,

$$\frac{\frac{dE(Q)}{dx}}{\frac{dE(q)}{dx}} = 1.15 \quad (2.19)$$

2.2.2.2 Radiative Energy Loss

Another source of energy loss is gluon radiation. This process is analogous to the QED brehmstrahlung of high-energy electrons traversing ordinary matter, and is often named

"gluonstrahlung". The gluon emission off high energy partons happens via interactions with the medium constituents, and the radiated gluon of energy ω undergoes a number of rescatterings in the medium. This number is given by its formation time $t_{form} = \omega/k_{\perp}^2$ and its mean free path λ_g in the medium. The gluon will thus accumulate a transverse momentum $k_{\perp}^2 \sim \mu^2 t_{form}/\lambda$ and the total number of scattering centres participating coherently to the emission of the gluon is $N_{coh} = t_{form}/\lambda = \sqrt{\omega/\mu^2\lambda}$. As shown in [85] and [86] the differential radiated power is

$$\frac{dW}{dzd\omega} = \frac{\alpha_s C_R}{\pi\omega\lambda} \sqrt{\frac{\mu^2\lambda}{\omega}} = \frac{\alpha_s C_R}{\pi\omega} \sqrt{\hat{q}} \quad (2.20)$$

where C_R is the colour charge of the parton projectile (4/3 for quarks, 3 for gluons). The parameter $\hat{q} = \mu^2/\lambda$ is the transport coefficient and is proportional to the density of the scattering centres in medium. Typical estimated values are $\hat{q} \sim 0.01$ GeV²/fm for cold nuclear matter and $\hat{q} \sim 0.2$ GeV²/fm for hot nuclear matter.

The medium induced radiation vanishes for $\omega < \hat{q}L^2$, where L is the distance traversed in the medium, as the formation time of such gluons starts to exceed the length of the medium.

Integrating over ω and multiplying by L as explained in [87], one obtains the average energy loss⁹

$$\langle \Delta E \rangle \propto \frac{1}{4} \alpha_s C_R \hat{q} L^2 \quad (2.21)$$

For hot QCD matter having temperature $T=250$ MeV the above formula for $L=10$ fm gives $\langle \Delta E \rangle = 20\alpha_s$ GeV. If $\alpha_s = \frac{1}{3} \div \frac{1}{2}$ we get $\langle \Delta E \rangle \sim 10$ GeV/fm.

No dependence on the projectile parton mass is present. However as shown in [85], when we look at gluon emission off heavy quarks the angular emission probability is

$$dP = \frac{\alpha_s C_F}{\pi} \frac{d\omega}{\omega} \frac{k_{\perp}^2 dk_{\perp}^2}{(k_{\perp}^2 + \omega^2\theta_0^2)^2} \quad (2.22)$$

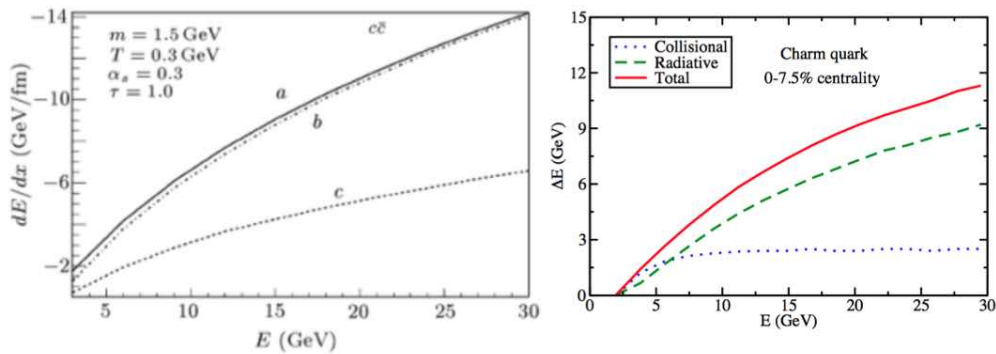


FIGURE 2.13: Left: dE/dx predictions for c quarks as a function of the initial c -quark energy. The solid line is the calculation performed for light quarks, the pin-dotted line is for c quarks without dead-cone effect and the dotted line is for c quarks taking into account dead-cone effect [88]. Right: energy loss of charm quarks as a function of their initial energies [89].

⁹in the approximation where the medium consists of static scattering centers and the the projectile and the outgoing gluon undergo many soft scatterings with the medium (multiple-soft scattering approximation)

and we see that the emission is suppressed for angles $\theta < \theta_0 = M/E$. This effect is known as the dead cone phenomenon. Reference [85] also demonstrates that this effect is relevant up to an energy of the heavy quark $E_{HQ} = M\sqrt{\hat{q}L^3} \sim 100$ GeV at LHC energies. Figure 2.13(left) shows a quantitative estimation of the effect calculated as in [88]. The parameter values used in the calculation are also shown in the figure, m is the c quark mass value, and the three curves represent the energy loss per unit length as a function of the initial partonic energy for light quarks and charm quarks with and without including the dead cone effect. The inclusion of the dead cone effect clearly reduces the energy loss of heavy quarks, and the suppression of gluon emission for $\theta < \theta_0 = M/E$ implies the following relation:

$$\Delta E_g > \Delta E_{u,d,s} > \Delta E_c > \Delta E_b \quad (2.23)$$

and one can expect:

$$R_{AA}(b) > R_{AA}(c) > R_{AA}(g, u, d, s) \quad (2.24)$$

However this relation has to be interpreted keeping in mind that the initial transverse momentum spectrum of quarks produced in the collisions plays a role in the final R_{AA} of hadrons that one observes. In fact for a given value of ΔE , the steeper the transverse momentum distribution of the quark, the lower the resulting nuclear modification factor will be.

The right panel of Figure 2.13 shows an estimate of the average energy loss of charm quarks as a function of their initial energy separating the collisional and radiative contributions. These predictions are obtained describing the heavy quark evolution in the QGP medium with a modified version of the Langevin equation [89] that also takes into account gluon radiation:

$$\frac{d\vec{p}}{dt} = -\nu_D(p)\vec{p} + \vec{\xi} + \vec{f}_g \quad (2.25)$$

where the first two terms on the right-hand side are the drag force and the thermal random force that describe the collisional contribution, and the third term describes the recoil force exerted on heavy quarks due to gluon radiation. In this model, collisional energy loss dominates at low energies, while medium-induced gluon radiation dominates at high energies where the dead cone effect gets suppressed.

Another effect affecting c quark related observables is the hadronization mechanism in the QGP, which was described in Section 1.4.4.

2.2.3 Charm quark thermalization

The elliptic flow, already introduced in the previous section, can be compared to models that take into account the hydrodynamic evolution of a thermalized medium. The thermalization of light components of the QGP is reached via multiple scatterings and is expected within 1 fm/c from the nuclear interaction (Section 1.3.1). Due to their mass values, heavy quarks thermalization requires a longer time interval to be established and it is even possible that it is not reached at all in the heavy-ion collisions studied so far. In the previous sections the energy loss mechanisms of heavy quarks in the medium was introduced, whose effect is the sum of multiple elastic and inelastic interactions. Since on average the momentum transfer of each interaction is small compared to the heavy quark energy, the Langevin approach of Equation 2.23 can be used. This approach was applied for charm quark in an expanding finite-size QGP medium in [90]. The initial conditions of the hydrodynamic calculation are tuned to describe the hadronic data in

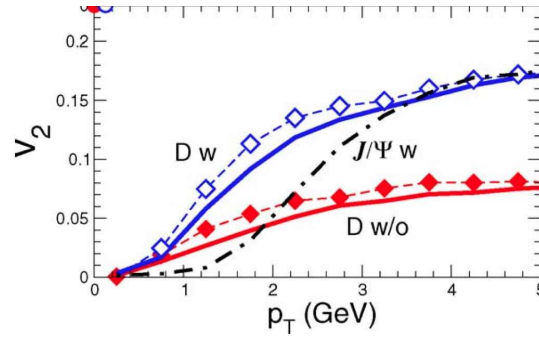


FIGURE 2.14: Predictions for D meson and heavy-flavour decay electron v_2 obtained from a coalescence model with and without considering full thermalization of charm quarks in the medium [91].

the soft sector, such as hadron yields, spectra, rapidity-distributions as well as radial and elliptic flow from RHIC data. The QCD medium experiences a sudden thermalization at an initial time $\tau_0 = 0.6$ fm/c, at which the hydrodynamic evolution begins. The charm quark thermalization criterion is based on a comparison of the charm quark energy distribution to the medium temperature. Once the energy and momentum distributions of the charm quark ensemble yield thermal distributions with a temperature corresponding to the medium temperature, the selected charm quark ensemble has thermalized in the medium at that given temperature and selected time step. The result of this study is that charm quark thermalization does not occur within the lifetime of the QGP phase, and a quasi-equilibrium state is achieved after about 8 fm/c, exceeding the expected lifetime of the QGP phase at RHIC (1–4 fm/c, Section 1.3.1).

In case of complete thermalization, then the pressure gradients acting on heavy quarks are the same acting on light quarks, and due to the higher mass the v_2 of charm quark should be smaller than the one of light quarks. In case no thermalization is reached, charm quark v_2 should in principle be zero at low p_T , but at high p_T energy loss plays a role, since heavy quarks directed out of plane have to traverse a longer path inside the medium, lose more energy and this reflects in a non-zero v_2 .

The elliptic flow of charmed hadrons is a useful tool to extract information on charm quark thermalization in the hot medium. Greco, Ko and Rapp [91] used a coalescence model to extract predictions on D mesons elliptic flow for Au–Au collisions at $\sqrt{s_{NN}} = 200$ GeV in two extreme scenarios:

- no charm quark rescattering in the medium occurs (spectra are taken from PHYTHIA)
- complete thermalization including transverse expansion of the bulk matter

The results are shown in Figure 2.14. The red line is obtained in the no thermalization scenario (solid line: D-meson, diamonds: heavy quarks decay electron), the blue one is for thermalization and transverse expansion. The D-meson elliptic flow in the case of complete thermalization deviates from the no-thermalization scenario by about a factor 2 for $p_T > 1.5$ GeV/c. However also if thermalization is not considered, D meson elliptic flow is non-zero even at low p_T , since D mesons are also composed of light quarks that carry a fraction of v_2 , independently from charm quarks degree of thermalization.

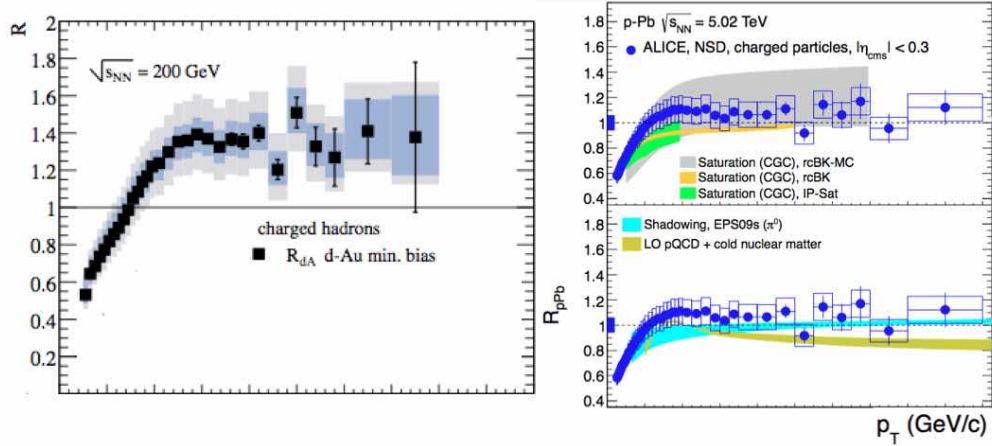


FIGURE 2.15: Left: charged hadron R_{dAu} measured by the PHENIX Collaboration in minimum bias d-Au collisions at $\sqrt{s_{NN}} = 200$ GeV [92]. Right: R_{pPb} of charged hadrons measured by the ALICE Collaboration compared to models in p-Pb collisions at $\sqrt{s_{NN}} = 5.02$ TeV [93].

2.2.4 Some results from pA collisions

We will now show some experimental results obtained in pA collisions and compare them to models taking into account the cold nuclear matter effects described so far. The measurements relative to open charm production in p-Pb collisions at LHC energies will not be presented in this chapter, since they are the main topic of this thesis. They will be discussed after the analysis procedure is described in detail.

We first show some results not directly related to charm quark production. Figure 2.15 (left) shows the nuclear modification factor of charged hadrons in minimum bias d-Au collisions at $\sqrt{s_{NN}} = 200$ GeV measured by the PHENIX collaboration [92]. The measurement is performed at mid-rapidity and shows an enhancement in inclusive charged particle production for $p_T > 2$ GeV/c that can be attributed to Cronin effect. The right

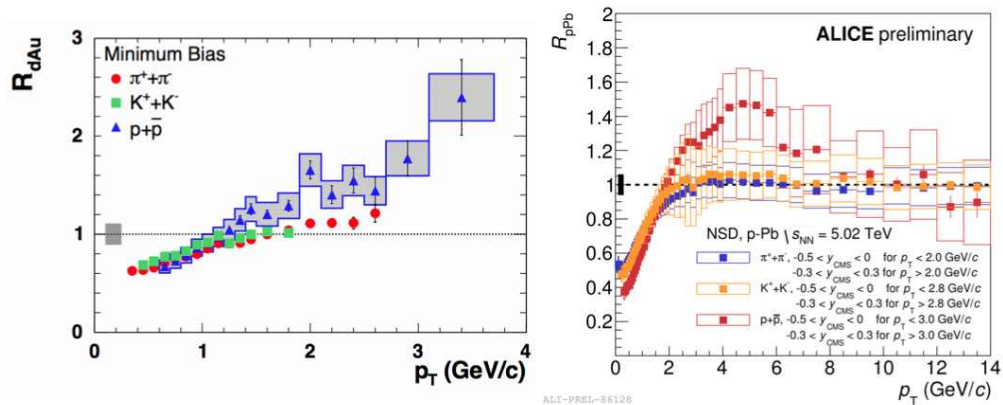


FIGURE 2.16: Left: nuclear modification factor of identified pions, kaons and protons in minimum bias d-Au collisions at $\sqrt{s_{NN}} = 200$ GeV measured by the PHENIX Collaboration [30]. Right: nuclear modification factor of identified pions, kaons and protons in minimum bias p-Pb collisions at $\sqrt{s_{NN}} = 5.02$ TeV measured by the ALICE Collaboration

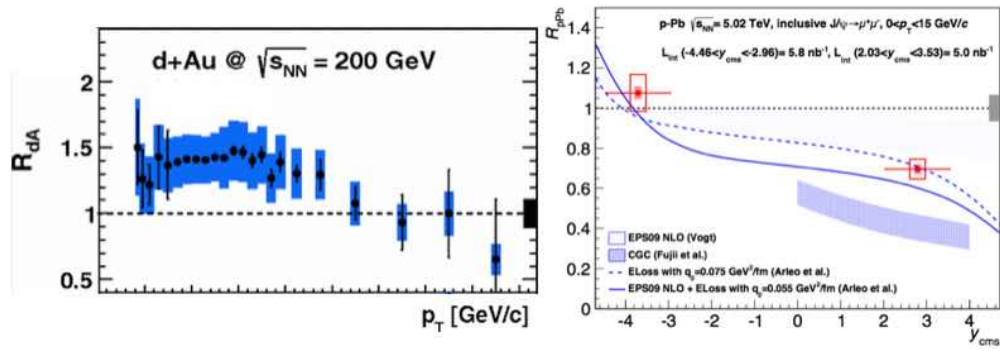


FIGURE 2.17: Left: heavy-flavour decay electrons R_{dAu} measured at mid-rapidity by the PHENIX Collaboration in minimum-bias d-Au collisions at $\sqrt{s_{NN}} = 200$ GeV [94]. Right: J/Ψ R_{pPb} at forward and backward rapidity measured by the ALICE Collaboration in p-Pb collisions at $\sqrt{s_{NN}} = 5.02$ TeV [95]

panel of the same figure shows the same measurement performed by the ALICE Collaboration at mid-rapidity in p-Pb collisions at $\sqrt{s_{NN}} = 5.02$ TeV [93], where a smaller magnitude of the Cronin effect is seen at higher energies. The top panel of this figure shows a comparison with CGC models (Section 2.2.1), that are consistent with the data. The bottom panel shows the comparison to two different predictions. NLO pQCD calculations with EPS09 parametrization of the nuclear PDFs (Section 2.2.1) show good agreement with data.

Figure 2.16 shows the nuclear modification factor of identified pions, kaons and protons in minimum bias d-Au collisions at $\sqrt{s_{NN}} = 200$ GeV measured by the PHENIX Collaboration [30] (left) and in minimum bias p-Pb collisions at $\sqrt{s_{NN}} = 5.02$ TeV measured by the ALICE Collaboration (left¹⁰). PHENIX results show a species dependence in the Cronin effect. The Cronin effect for charged pions is small, while the nuclear enhancement for protons and antiprotons is considerably larger. The kaon measurement has a more limited kinematic range, but the R_{dA} is in agreement with that of the pions at comparable p_T . ALICE results show no enhancement for pions and kaons and a pronounced peak for protons. Models including initial state multiple scattering as well as geometrical shadowing do not predict a species dependent Cronin effect, as initial state parton scattering precedes fragmentation into the different hadronic species. This might point to relevant final state effects in p-A collisions.

Figure 2.17 (left) shows the nuclear modification factor of electrons from open heavy-flavour decays measured by the PHENIX collaboration in minimum-bias d-Au collisions at $\sqrt{s_{NN}} = 200$ GeV [94]. The R_{dAu} shows an enhancement above unity up to $p_T = 5$ GeV/c while at higher p_T results are compatible with unity within uncertainties.

The right panel of Figure 2.17 shows the nuclear modification factor of inclusive J/Ψ in p-Pb collisions at $\sqrt{s_{NN}} = 5.02$ TeV measured by the ALICE collaboration [95]. The measurement is performed in two different regions of rapidity measured in the centre-of-mass system: positive rapidity ($2.03 < y_{cms} < 3.53$) corresponds to the p-going direction, negative rapidity ($-4.46 < y_{cms} < -2.96$) corresponds to the Pb-going direction. From Equation 2.15 we obtain that the x value of the partons in the Pb nucleus involved in the $c\bar{c}$ pair production is $\sim 10^{-5}$ for the positive y_{cms} interval and $\sim 10^{-2}$ for the negative interval. At forward rapidity the inclusive J/Ψ production is suppressed with respect to the one in binary-scaled pp collisions, whereas it is unchanged at backward rapidity. Four different models are superimposed to data. A CGC-based model overpredicts the

¹⁰ALICE Physics Preliminary, not yet published in a paper

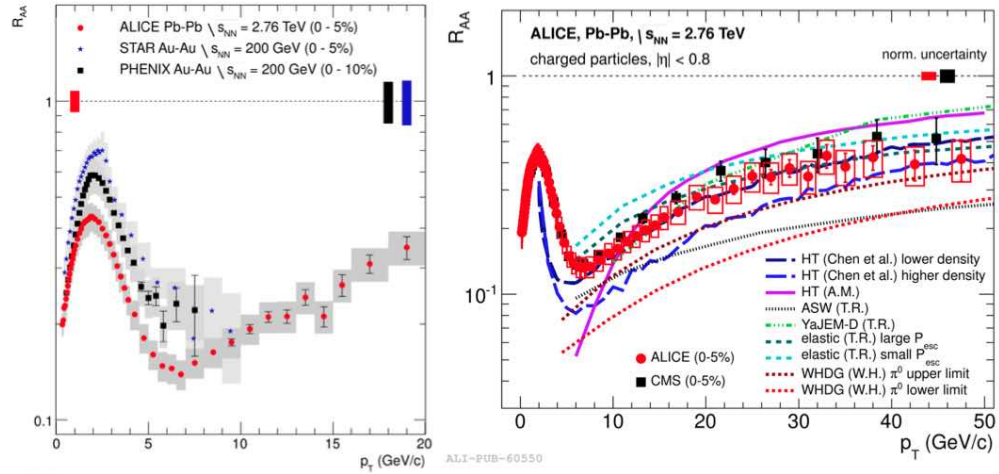


FIGURE 2.18: Left: charged-hadron nuclear modification factor measured in central Pb–Pb collisions at $\sqrt{s_{NN}} = 2.76$ TeV by the ALICE Collaboration [96]. The results of charged-hadron nuclear modification factor measured in central Au–Au collisions at $\sqrt{s_{NN}} = 200$ GeV by the PHENIX and STAR [97] Collaborations at RHIC are superimposed. Right: charged-hadron nuclear modification factor measured in central Pb–Pb collisions at $\sqrt{s_{NN}} = 2.76$ TeV by the ALICE Collaboration [96] and CMS Collaboration [98]. Predictions of different theoretical calculations based on in-medium energy loss are superimposed.

observed suppression. A model based on NLO pQCD calculations with EPS09 nuclear PDFs parametrization qualitatively reproduces the results. The last two models also include a partonic energy loss in cold nuclear matter. The \hat{q} values used are shown in the legend, and both models are able to describe the data.

2.2.5 Some results from AA collisions

The nuclear modification factor defined in Equations 2.9 and 2.10 is sensitive to possible energy loss mechanisms that could play a major role in A–A collisions. Before discussing results relative to heavy-flavour, results on charged hadron R_{AA} will be discussed.

The left panel of Figure 2.18 shows charged-hadron nuclear modification factor measured in central Pb–Pb collisions at $\sqrt{s_{NN}} = 2.76$ TeV by the ALICE Collaboration [96]. The results of charged-hadron nuclear modification factor measured in central Au–Au collisions at $\sqrt{s_{NN}} = 200$ GeV by the PHENIX and STAR [97] Collaborations at RHIC are superimposed. The peak structure centred at $p_T \approx 2$ GeV/c has been interpreted in terms of different hadronization mechanisms (quark coalescence) in AA collisions with respect to pp collisions, or as a consequence of radial flow. At higher p_T , in which the effects of in-medium energy loss start to be dominant, we can summarize the results as follows:

- STAR and PHENIX results show that hadron production in $6 < p_T < 10$ GeV/c is suppressed by a factor $4 \div 5$ with respect to pp collisions. This suppression cannot be reproduced by models taking into account Cronin enhancement and shadowing alone, but it is reproduced if partonic energy loss in dense matter is included [97].

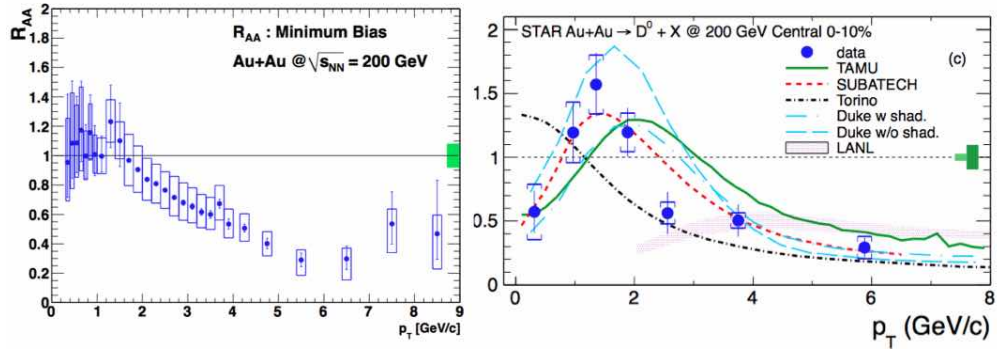


FIGURE 2.19: Left: heavy-flavour decay electron R_{AA} measured by PHENIX from Au–Au collisions at $\sqrt{s_{NN}} = 200$ GeV in the 0–10% centrality class [99]. Right: D^0 R_{AA} measured by STAR from Au–Au collisions at $\sqrt{s_{NN}} = 200$ GeV in the 0–10% centrality class [100]. The SUBATECH curve correspond to the MC@sHQ+EPOS model. The TORINO curve corresponds to POWLANG. The DUKE curve corresponds to Cao,Qinn,Bass. The LANL curve corresponds to Vitev.

- ALICE results show that R_{AA} reaches a minimum of $R_{AA} \approx 0.14$ at $p_T = 6-7$ GeV/c. A significant rise of R_{AA} by about a factor of two is observed for $7 < p_T < 20$ GeV/c

At the larger LHC energy the density of the medium is expected to be higher than at RHIC, leading to a larger energy loss of high p_T partons. On the other hand, the less steeply falling spectrum at the higher energy would lead to a smaller suppression in the p_T spectrum of charged particles, for a given magnitude of partonic energy loss. The measurement of Figure 2.18 show that the nuclear modification factor measured by ALICE in $6 < p_T < 7$ GeV/c is smaller than at RHIC. This suggests an enhanced energy loss at LHC and therefore a denser medium. It can also indicate a more relevant fraction of high- p_T hadrons which originate from fragmentation of gluons, that according to Equation 2.21 loose more energy in the medium.

Figure 2.18 (right) shows the same ALICE results of the left panel together with the corresponding CMS results [98]. CMS result is fully in agreement with the ALICE measurement within the uncertainties. Predictions of different theoretical calculations based on in-medium energy loss are superimposed. All selected models use RHIC data to calibrate the medium density. A variety of energy loss formalisms is used. An increase of R_{AA} due to a decrease of the relative energy loss with increasing p_T is seen for all the models.

We now switch to the heavy-flavour sector. Figure 2.19 shows two measurements performed at RHIC in Au–Au collisions at $\sqrt{s_{NN}} = 200$ GeV. The left panel shows heavy-flavour decay electron R_{AA} measured by PHENIX Collaboration in the 0–10% centrality class [99]. The measurement is inclusive (i.e. both charm and bottom hadrons decay electrons are included) and shows that heavy-flavour electron production is compatible to binary scaling of pp cross-section up to $p_T \sim 2$ GeV/c, while above this p_T value a suppression is clearly seen, reaching a value ~ 4 at $p_T = 6$ GeV/c.

The right panel of Figure 2.19 shows the p_T differential nuclear modification factor of D^0 mesons measured by STAR in the 0–10% centrality class [100]. A suppression of

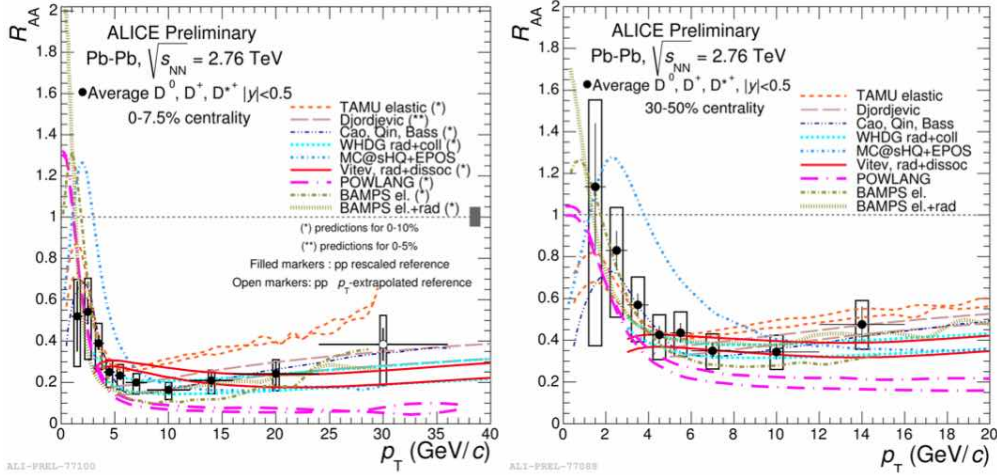


FIGURE 2.20: D-meson R_{AA} (average of D^0 , D^+ and D^{*+}) measured by the ALICE Collaboration in Pb–Pb collisions at $\sqrt{s_{NN}} = 2.76$ TeV in the 0-7.5% (left) and 30-50% (right) centrality classes.

D^0 meson yield is observed for $p_T > 2.5$ GeV/c, and different predictions are superimposed¹¹. POWLANG calculation misses the intermediate- p_T enhancement structure for $p_T < 3$ GeV/c, indicating that a coalescence type hadronization mechanism is important in modeling charm-quark hadronization at low and intermediate p_T .

Figure 2.20 (left) shows the p_T differential prompt D-meson nuclear modification factor measured by the ALICE collaboration in the 0-7.5% centrality class in Pb–Pb collisions at $\sqrt{s_{NN}} = 2.76$ TeV. This measurement is obtained from the weighted average of D^0 , D^+ and D^{*+} results. It shows a strong (factor 4÷5) suppression of D mesons transverse momentum spectra with respect to pp collisions for $p_T > 5$ GeV/c, comparable to the one seen for charged particles at the same energy in Figure 2.18. This big suppression indicates a large energy loss of charm quarks, similar to the one of light quarks and gluon and in contrast to what would be expected considering the radiative energy loss discussed in Section 2.2.2.2.

Several theoretical model are superimposed in the plot, briefly:

- **TAMU** [101] [102] predictions take into account elastic scattering with medium constituents. In the hypothesis that the typical momentum transfer in a single elastic interaction with a light partons is small compared to the heavy quark energy, the diffusion process can be simulated using relativistic Fokker-Planck dynamics for elastic scattering in a hydrodynamic background

$$dx = \frac{\mathbf{p}}{E} dt \quad d\mathbf{p} = -\Gamma(\mathbf{p})\mathbf{p}dt + \sqrt{2\Gamma(\mathbf{p}+d\mathbf{p})E(\mathbf{p}+d\mathbf{p})T}d\mathbf{t}\rho \quad (2.26)$$

where \mathbf{x} , \mathbf{p} and E are the position, momentum and energy of the heavy quark, Γ is the drag coefficient, and ρ a noise term. The evolution is constrained by light-flavour hadron spectra and elliptic flow data. The heavy-quark transport coefficients in the medium are obtained from non-perturbative T -matrix interactions which build up resonant correlations close to the transition temperature. The latter also form the basis for hadronization of heavy quarks into heavy-flavor mesons via

¹¹they are the same theoretical models of the ALICE measurement in Figure 2.20, but they are tagged in a different way in the figure - as explained in the caption

recombination with light quarks from the medium. Hadronization via coalescence (fragmentation) is found to dominate at low (high) p_T .

- **Djordjevic** predictions [103] compute an energy loss probability which includes both radiative and collisional processes in a realistic finite size dynamical QCD medium. The quenched spectra of partons and hadrons are calculated from the following convolution

$$\frac{E_f d^3\sigma(H_Q)}{dp_f^3} = \frac{E_i d^3\sigma(Q)}{dp_i^3} \otimes P(E_i \rightarrow E_f) \otimes D(Q \rightarrow H_Q) \quad (2.27)$$

where Q denotes quarks and gluons, H_Q heavy-flavour hadrons, $P(E_i \rightarrow E_f)$ is the energy loss probability and $D(Q \rightarrow H_Q)$ is the fragmentation function. The initial heavy quark spectrum $\frac{E_i d^3\sigma(Q)}{dp_i^3}$ is computed at next-to-leading order with FONLL, using CTEQ5M PDFs with collinear factorization. The $P(E_i \rightarrow E_f)$ term takes into account path-length fluctuations, multigluon fluctuations (i.e. the fact that energy loss is a distribution), magnetic mass of QGP constituents and running coupling in the assumption of large E_f , so that the Eikonal approximation can be employed. This model does not simulate the hydrodynamic evolution of heavy-quark in the medium.

- **Cao, Qinn, Bass** is based on a modified version of the Langevin equation that also takes into account radiative energy loss, and was discussed in Section 2.2.2.2 (Equation 2.25).
- **WHDG** approach [104] is based on Equation 2.27, with the initial heavy quark spectrum computed as in Djordjevic predictions. A realistic collision geometry based on the Glauber model is used, without hydrodynamical expansion, and anisotropy results from path-length dependent energy loss. The $P(E_i \rightarrow E_f)$ term takes into account path length and energy loss fluctuations. The collisional contribution to energy loss for a parton with Casimir factor C_R in an ideal ultra-relativistic QGP with n_f active flavours and temperature T is

$$\frac{dE^{el}}{dx} = C_R \pi \alpha_s^2 T^2 (1 + n_f/6) \log B_c \quad (2.28)$$

where the parameter B_c takes into account minimum and maximum momentum transfers. The radiative energy loss is given by the DGLV formula that can be found in [105].

- **MC@sHQ+EPOS** [106] is based on Monte-Carlo propagation of heavy quarks in the medium. The medium fluid dynamical expansion is based on the EPOS model, including initial conditions obtained from a flux tube approach [107] and according to the equations of ideal hydrodynamics within a 3 + 1 D fluid dynamically expanding plasma, namely the local energy-momentum conservation and the conservation of baryon number, strangeness, and electric charge. The elastic cross sections are obtained from pQCD matrix elements in Born approximation including a running coupling α_s . The incoherent emission of bremsstrahlung gluons is included via matrix elements from scalar QCD, while the coherent emission of gluons, i.e., the

QCD generalization of the Landau-Pomeranchuk-Migdal (LPM¹²) effect is included via an effective reduction of the spectrum. The hadronization of the heavy quarks takes place at the transition temperature via coalescence (fragmentation) for low (high) p_T heavy quarks.

- **Vitev** [108] is a perturbative QCD description of heavy flavor dynamics in the thermal medium that combines D and B meson in-medium formation and dissociation with parton-level charm and beauty quark radiative energy loss. Heavy-quarks initial distributions are taken from FONLL predictions and the model also takes into account bound state formation above the deconfinement temperature T_c
- **POWLANG** [109] uses the relativistic Langevin equation,

$$\frac{d\vec{p}}{dt} = -\nu_D(p)\vec{p} + \vec{\xi} \quad (2.29)$$

Only collisional energy loss is considered. A sample of c and b quarks is generated using POWHEG [110], a code which implements pQCD at NLO accuracy, and CTEQ6M PDFs with EPS09 nuclear corrections. Heavy quarks are initially distributed in the transverse plane according to the nuclear overlap function corresponding to the selected impact parameter \mathbf{b} . At a given equilibrium time τ_0 an iterative procedure is started to follow the stochastic evolution of the heavy quarks in the plasma until hadronization: the Langevin transport coefficients are evaluated at each step according to the local 4-velocity and temperature $T(x)$ of the expanding background medium. Hadronization only happens via fragmentation.

- **BAMPS** [111] is a 3+1 dimensional partonic transport model that solves the Boltzmann equation

$$\left(\frac{\partial}{\partial t} + \frac{\mathbf{p}_i}{E_i} \frac{\partial}{\partial r} \right) f_i(\mathbf{r}, \mathbf{p}_i, t) = C_i^{2 \rightarrow 2} + C_i^{2 \rightarrow 3} + \dots \quad (2.30)$$

for on-shell partons and allows elastic interactions among gluons, light quarks and heavy quarks. C_i are the relevant collision integrals, and $f_i(\mathbf{r}, \mathbf{p}_i, t)$ the one-particle distribution function of partons. Heavy quarks, in particular, interact with the rest of the medium via binary scatterings with a running coupling and a Debye screening length. The lack of radiative processes in the heavy flavor sector is accounted for by scaling the binary cross section with a phenomenological factor $K = 3.5$, which describes well the elliptic flow v_2 and nuclear modification factor R_{AA} at RHIC.

The right panel of Figure 2.20 shows the same measurement in the 30-50% centrality class. The modification of D meson transverse momentum spectra with respect to pp collisions is still present but of smaller magnitude, as expected from the smaller size of the system created.

Figure 2.21 (left) shows a comparison of D-meson and charged π R_{AA} as a function of

¹²A high energy particle undergoing multiple soft scatterings from a medium will experience interference effects between adjacent scattering sites. As the longitudinal momentum transfer gets small the particles wavelength will increase, and if the wavelength becomes longer than the mean free path in the medium (the average distance between scattering sites) then the scatterings can no longer be treated as independent events. This is the LPM effect. The Bethe-Heitler spectrum for multiple scattering induced radiation (Equation 2.20) assumes that the scatterings are independent, the quantum interference between successive scatterings caused by the LPM effect leads to suppression of the radiation spectrum relative to that predicted by Bethe-Heitler.

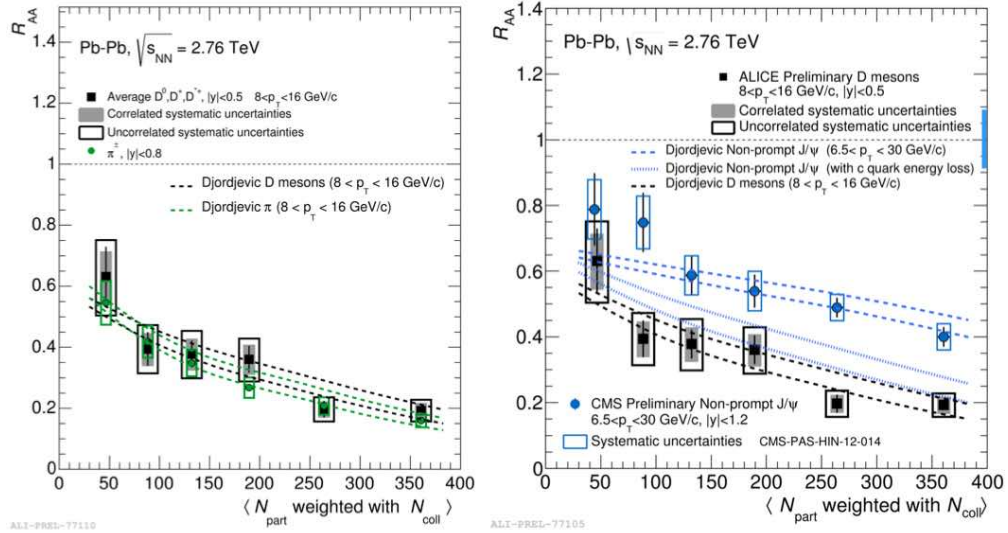


FIGURE 2.21: Comparison of D-meson R_{AA} as a function of average N_{part} to the one of π (left) and non-prompt J/Ψ (right) measured by the ALICE and CMS Collaborations. Predictions from [103] are superimposed, in particular in the right plot the non-prompt J/Ψ R_{AA} is computed considering c (blue dotted line) and b (blue dashed line) energy loss.

centrality expressed in terms of number of participant nucleons. D-meson and charged π R_{AA} are measured in the $8 < p_T < 16$ GeV/c range. The two measurements are compatible within uncertainties and with Djordjevic [103] model that takes into account energy loss hierarchy due to color charge and quark mass. The calculation closely describes the similarity of the D meson and charged π R_{AA} over the entire centrality range. In this calculation the colour-charge dependence of energy loss introduces a sizeable difference in the suppression of the gluon and c quark production. The softer fragmentation and p_T spectrum of gluons with respect to those of c quarks, together with the increase of the parton-level R_{AA} with increasing p_T , lead to a compensation effect that results in very similar R_{AA} for D mesons and pions.

Figure 2.21 (right) shows a comparison of D-meson and non-prompt J/Ψ (measured by CMS [112]) R_{AA} as a function of centrality expressed in terms of number of participant nucleons. D-meson R_{AA} is measured in the $8 < p_T < 16$ GeV/c range, in the $6.5 < p_T < 30$ GeV/c range for non-prompt J/Ψ , which means that the p_T of the B meson originating the non-prompt J/Ψ and that of the D mesons are comparable. Djordjevic model [103] predicts a difference between the D-meson and non-prompt J/Ψ R_{AA} similar to that observed in the data. In order to study the origin of this large difference in the calculation, the result for a test case with the energy loss of b quarks calculated using the c quark mass was considered. In this case the R_{AA} of non-prompt J/Ψ was found to be quite close to that of D mesons, indicating that the difference between D-meson and non-prompt J/Ψ R_{AA} observed in Djordjevic model is mainly due to the quark mass dependence of parton energy loss.

To conclude this section we will discuss some measurement on the elliptic flow of heavy-flavour decay electrons and D mesons, which are sensitive to the degree of thermalization of charm quarks in the medium:

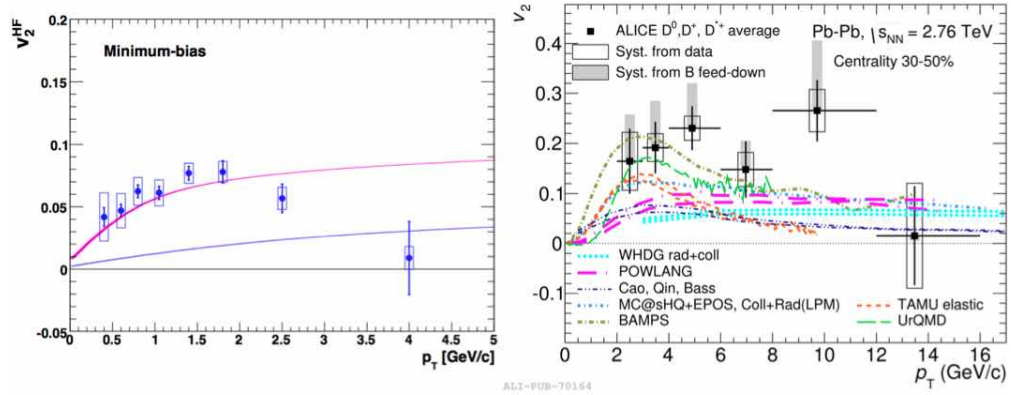


FIGURE 2.22: Left: p_T differential v_2 in minimum bias Au–Au collisions at $\sqrt{s_{\text{NN}}} = 200$ GeV [99]. Right: D-meson p_T differential v_2 in Pb–Pb collisions at $\sqrt{s_{\text{NN}}} = 2.76$ TeV for the 0-10%, 10-30% and 30-50% centrality class [113].

- PHENIX Collaboration measured the heavy-flavour decay electrons p_T differential v_2 in minimum bias Au–Au collisions at $\sqrt{s_{\text{NN}}} = 200$ GeV [99]. The resulting v_2 is large ($v_2 \sim 0.05 \div 0.1$, not compatible with zero within uncertainties) in the range $0.5 < p_T < 3$ GeV/c. This result is shown in the left panel of Figure 2.22.
- the ALICE Collaboration measured the D-meson p_T differential v_2 in Pb–Pb collisions at $\sqrt{s_{\text{NN}}} = 2.76$ TeV for the 0-10%, 10-30% and 30-50% centrality class [113]. A positive v_2 is observed in mid-central collisions (30-50% centrality class) with a mean value of $0.204^{+0.099}_{-0.036}$ (tot. unc.) in the interval $2 < p_T < 6$ GeV/c, which decreases towards more central collisions. Figure 2.22 (right) shows the p_T differential v_2 in the 30-50% centrality class. This measurement is obtained from the weighted average of D^0, D^+ and D^{*+} results. The measured v_2 of D mesons is comparable in magnitude to that of light-flavour hadrons shown in previous chapter.

The right panel of Figure 2.22 also shows the theoretical predictions of v_2 based on the same models used in Figure 2.20 for R_{AA} . Models including both charm quark energy loss in a geometrically anisotropic medium and mechanisms that transfer to charm quarks the elliptic flow induced during the system expansion qualitatively describe the observed anisotropy. Models that do not include a collective expansion of the medium or lack a contribution to the hadronization of charm quarks from recombination with light quarks from the medium predict in general a smaller anisotropy than observed in the data. The comparison for R_{AA} and v_2 shows that it is challenging to simultaneously describe the large suppression of D mesons in central collisions and their anisotropy in non-central collisions. In general, the models that are best in describing R_{AA} tend to underestimate v_2 and the models that describe v_2 tend to underestimate the measured R_{AA} at high p_T . In conclusion, it is challenging for models to describe simultaneously the large suppression of D mesons in central collisions and their anisotropy in non-central collisions. The higher statistic expected for LHC Run 2 will help restricting the experimental uncertainties allowing a better discrimination between models.

Chapter 3

p–Pb collisions with the ALICE detector

Even if it was not mentioned in the initial LHC Design Report (2004), the ALICE Collaboration asked for a p–Pb data taking period in 2011, and after some feasibility tests (2011) and pilot runs (2012), p–Pb runs took place at the beginning of 2013.

Since the LHC is mainly conceived as a particle-particle collider, the two beams can not be accelerated in a single ring. The super-conducting magnet design adopted is a "two in one" dipole as in Figure 3.1 (left). The identical bending field in both apertures of the dipole fixes the relation between the momenta of the beams in the two rings

$$p_{\text{Pb}} = Z p_p \quad (3.1)$$

As seen in the previous chapter, circulating particles with charges Z_1 and Z_2 in the rings with the magnetic field set to accelerate protons with momentum p_p will result in:

$$\sqrt{s_{\text{NN}}} = \sqrt{s_p} \sqrt{\frac{Z_1 Z_2}{A_1 A_2}} \quad y_{\text{NN}} = \frac{1}{2} \log \frac{Z_1 A_2}{Z_2 A_1} \quad (3.2)$$

For the proton beam energy of 4 TeV as in the 2012 pp runs one gets $\sqrt{s_{\text{NN}}} = 5.02$ TeV. The centre-of-mass of the p–Pb system in the laboratory frame has a rapidity $y_{\text{cms}} =$

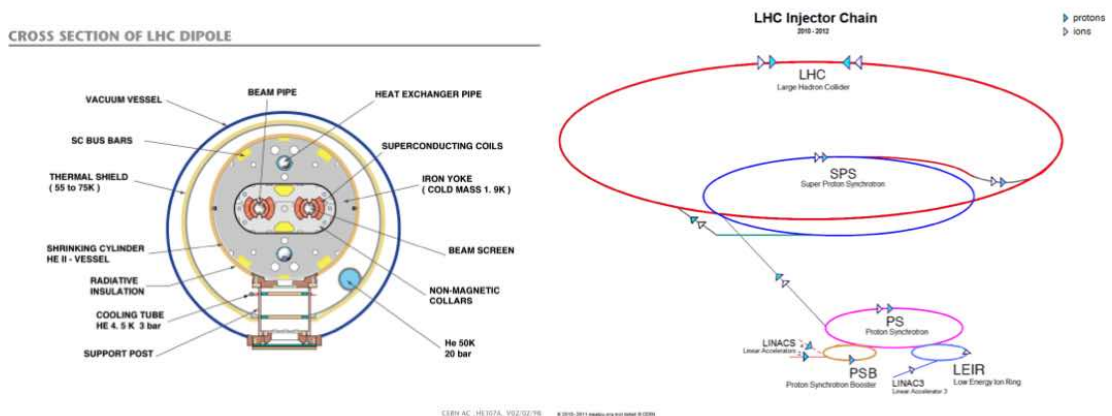


FIGURE 3.1: Left: Section of the LHC two-in-one accelerating dipole. Right: LHC injection scheme

0.465 in the proton direction.

The acceleration chain (Figure 3.1 - right) at the LHC begins with a linear accelerator (LINAC2) accelerating proton beams to 50 MeV, followed by the Proton Synchrotron Booster (PSB) that further accelerates them to 1.4 GeV. Proton beams are then extracted from PSB and sent to the Proton Synchrotron (PS) reaching an energy of 25 GeV and finally to the Super Proton Synchrotron (SPS) that accelerates them to 450 GeV. At this point protons are ready to be injected to the LHC where they are further accelerated and finally collided.

The accelerating chain differs for Pb ions in the first two steps, since Pb ions are first accelerated in the LINAC3 at 4.5 MeV per nucleon and then in the Low Energy Ion Ring (LEAR) which delivers them to the PS. The complete ionization of Pb atoms is more complex than ^1H ionization. The process begins before the injection in the LINAC3, where an electron-cyclotron resonance source ionize them to Pb^{28+} . Full ionization is then achieved sending the beam through two different copper stripper foils, one after LINAC3 and one after the PS. Once p and Pb beams reach the LHC, they are further accelerated and finally collided in the four interaction points.

The ALICE detector is located at Interaction Point 2 of the LHC and an overview of its components is shown in Figure 3.2. ALICE consists of a central barrel, a forward muon arm and several detectors for trigger and event characterization.

The direction of the p and Pb beams were reversed during the 2013 data taking to allow the muon arm to study p-Pb collisions in two different rapidity regions, allowing measurements like the one shown in Figure 2.17 of Chapter 2¹. The muon arm consists of an absorber, a large dipole magnet and tracking stations; a second muon filter at the end of the spectrometer and four planes of RPC which are used for muon identification

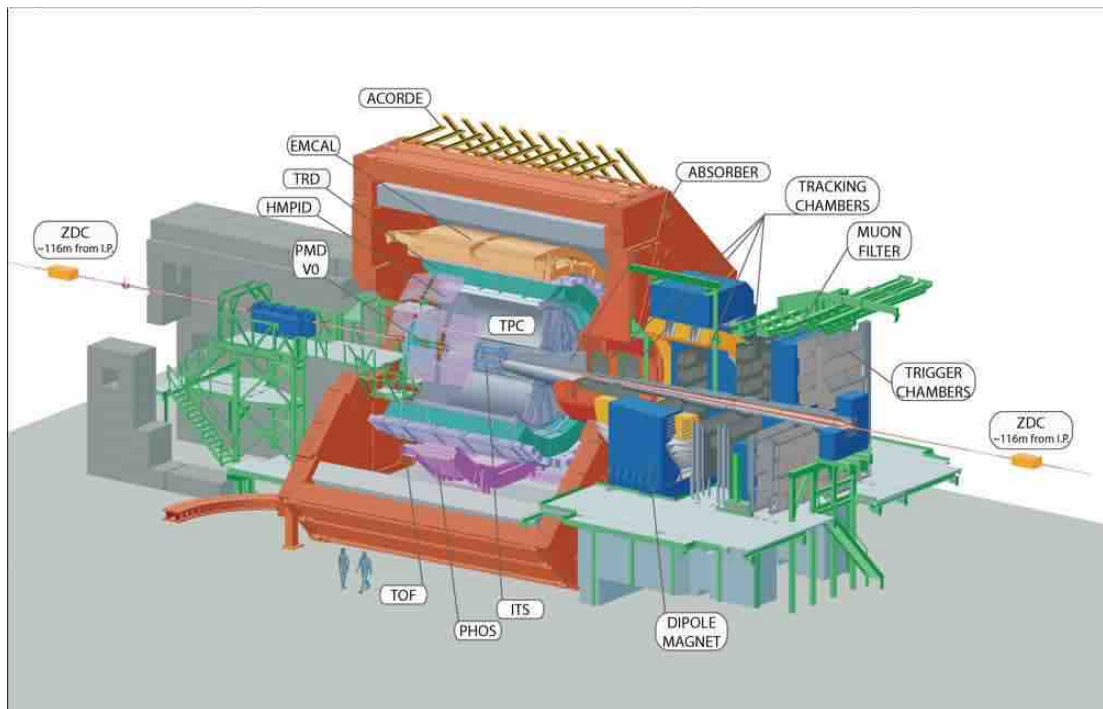


FIGURE 3.2: ALICE Detector

¹During the first part of 2013 data taking, the proton beam was directed towards the muon spectrometer: this will be referred as the p-Pb data taking. Then the beam configuration was reversed with the Pb beam directed towards the muon spectrometer: this is the Pb-p configuration.

and triggering. This part of the ALICE detector is not used for the analysis presented in this thesis and won't be discussed further.

In this chapter I will describe the central barrel detectors used in the reconstruction of D-meson hadronic decays, concentrating in particular on the vertexing and tracking capabilities of the ALICE detector. The determination of centrality in both Pb-Pb and p-Pb collisions will also be discussed.

3.1 ALICE Detector

The ALICE detector has been designed as a high-energy nuclear experiment able to analyze the complex systems emerging from Pb-Pb collisions at several TeV of centre-of-mass energy. This requires good performance in:

- measuring and identifying hadrons, electrons and photons in the central rapidity region
- tracking particles in broad range of transverse momentum (0.1-100 GeV/c)
- reconstructing primary and secondary vertices with a good spatial resolution
- operate in a high-multiplicity environment

The multiplicity in the 5% most central Pb-Pb events was measured during the first Pb-Pb runs in November 2010 [114]

$$\frac{dN_{ch}}{d\eta} = 1584 \pm 4(stat) \pm 76(syst) \quad (3.3)$$

from which we can extract an average multiplicity per participant pair of 8.3, a factor of 2.2 larger than that found at highest RHIC energies (200 GeV per nucleon pair).

Having a good tracking performance in such a high multiplicity environment requires the use of high granularity detectors which can only operate at a reduced luminosity in pp interactions. Luminosity reduction is obtained by beam defocusing (the bunches are broadened near the interaction point and refocused after it) and beam displacing (the two colliding bunches do not collide in their central regions but in their tails).

After three years of operation at the LHC, experience has shown that the maximum pp interaction rate at which all ALICE detectors can be safely operated is around 700 kHz, corresponding to a luminosity of $\mathcal{L} = 10^{29} \text{ s}^{-1}\text{cm}^{-2}$ for minimum bias triggers [115]. In Pb-Pb collisions the highest luminosity was achieved in 2011 ($\mathcal{L} = 10^{26} \text{ s}^{-1}\text{cm}^{-2}$) while the maximum manageable interaction rate for p-Pb collisions was 200 kHz, roughly corresponding to a luminosity $\mathcal{L} = 10^{29} \text{ s}^{-1}\text{cm}^{-2}$.

The value of the magnetic field B (0.5 T) has been chosen in order to find a compromise between two requirements: tracking of low p_T hadrons and momentum resolution at high p_T . In fact a 200 MeV/c pion has a curvature radius $R \approx \frac{70}{B}$ cm, expressing the magnetic field in Tesla, which for CMS magnetic field (4 T) would result in $R \approx 18$ cm. The lower magnetic field value of 0.5 T allows the same pion to reach the ALICE Time Projection Chamber (Section 3.1.2), which is located at 90 cm from the beam pipe. However the lower the magnetic field, the smaller the curvature of high p_T tracks, which results in a worse p_T resolution.

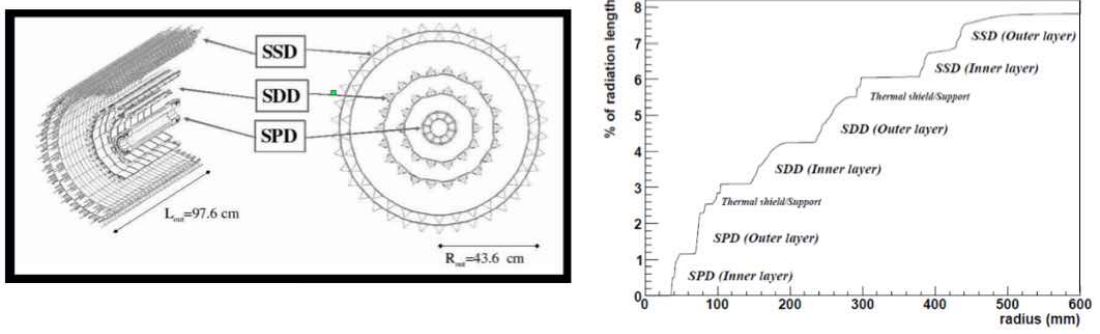


FIGURE 3.3: Left: transverse and side view of the ITS. Right: % of radiation length traversed by a particle crossing ITS as a function of the radial distance from the beam axis.

The next paragraphs are dedicated to the detectors used in the analysis presented in this thesis. For information on the other detectors more details can be found in [116] can be consulted.

3.1.1 Inner Tracking System (ITS)

The ITS surrounds the beam pipe and consists of six cylindrical layers of silicon detectors, located at radial distances from the beam line between 4 and 43 cm. The whole detector covers a pseudorapidity range of $|\eta| < 0.9$ for all vertices located within 5.3 cm along the beam axis from the detector center, but the innermost layers have a wider rapidity range that can contribute to multiplicity measurements.

The main tasks of this detector are:

- localize primary and secondary vertices
- track and identify particles with momentum below 200 MeV/c
- contribute to the Minimum Bias (MB) trigger
- improve momentum and angle resolution for particles reconstructed in the TPC (main tracking device in ALICE)
- reconstruct particles passing through dead regions of the TPC

To satisfy these requirements in the high-multiplicity environment of heavy-ion collisions at the LHC the detector has been designed as follows:

- the two innermost layers are based on silicon pixel technology (SPD)
- the two intermediate layers are Silicon Drift Detectors (SDD) equipped with analogue read-out of charge deposition
- the two outer layers have double-sided Silicon Strip Detectors (SSD) with analogue read-out of charge deposition

The four outer layers (SPD and SDD) can provide dE/dx measurement for Particle Identification (PID) in the non-relativistic ($dE/dx \propto 1/\beta^2$) region of the Bethe-Block curve. Since track momentum and impact parameter resolution are dominated by multiple scattering effects at low momentum, the material budget of ITS has been kept to a minimum using thin silicon layers ($\sim 300\mu\text{m}$) and taking care of the total material budget of support, cables and cooling system. The support consists of lightweight carbon-fibre structures. For particles crossing ITS in the radial direction the material budget is about 8% of a radiation length (Figure 3.3). This value slightly depends on the azimuthal angle. The design parameters of the different layers are summarized in table 3.1.

The Silicon Pixel Detector (SPD) is based on a two dimensional silicon matrix of reverse biased silicon detectors diodes bump-bonded to readout chips. The sensor matrix includes 256×160 cells measuring $50 \mu\text{m}$ ($r\varphi^2$) by $425 \mu\text{m}$ (z) with a thickness of $200 \mu\text{m}$.

The inner SPD layer is located at an average distance of 3.9 cm from the beam axis, while the outer one at an average distance of 7.6 cm. SPD are used to reconstruct **tracklets**, obtained aligning clusters in the two SPD layers with the interaction vertex.

The third and fourth layers of the ITS (Silicon Drift Detector - SDD) provide 2D position measurement and dE/dx of incident particles via measurements of drift time (for $r\varphi$ coordinate) and charge deposition. The electrons produced by ionizing particles crossing the detectors (Figure 3.4 - left) drift in an electric field produced by an array of cathode strips connected by resistors to form a detector voltage divider kept at -1.8 kV and are collected by 512 anodes divided in two rows located at the two opposite edges of the sensor. The inner SDD layer is located at an average radial distance of 15 cm from the beam axis, while the outer one at an average radius of 23.9 cm.

The two outer layers which are fundamental for the matching of tracks from the TPC to the ITS consist of double-sided Silicon Strip Detectors (SSD) mounted on carbon-fibre support structures identical to the ones which support the SDD. Each module (Figure 3.4 - right) is a double sided silicon sensor with 768 p-type strips on one side and 768 n-type strips on the other side. The spacing between adjacent strips is $95 \mu\text{m}$ and the strips are oriented with an angle of 7.5 mrad with respect to the short edge of the sensor on the p-side and with an angle of 27.5 mrad on the n-side. This configuration allows 2D position measurement on the surface of the module.

Parameter	Silicon Pixel	Silicon Drift	Silicon Strip
Spatial precision $r\varphi$ (μm)	12	35	20
Spatial precision z (μm)	100	25	830
Two track resolution $r\varphi$ (μm)	100	200	300
Two track resolution z (μm)	850	600	2400
Active area per module (mm^2)	12.8×69.6	72.5×75.3	73×40
Readout channels per module	40960	2×256	2×768
Total number of modules	240	260	1698
Total number of readout channels (k)	9835	133	2608
Total number of cells (M)	9.84	23	2.6

TABLE 3.1: Main characteristics of the ALICE ITS; maximum occupancy is referred to central Pb-Pb collisions

²The z axis is parallel to the mean beam direction at ALICE interaction point and points along the LHC anticlockwise direction. The $r\varphi$ direction is tangent to a circumference perpendicular to the beam and centred on the interaction point

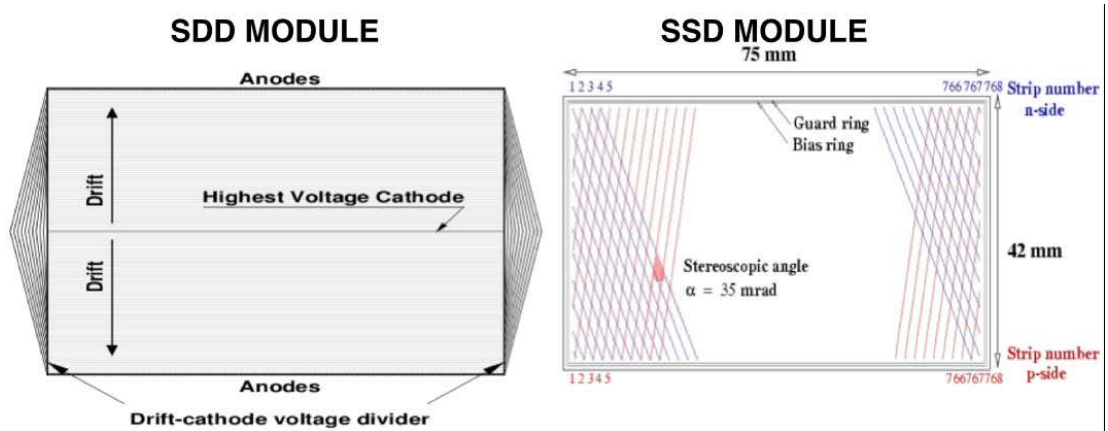


FIGURE 3.4: Left: SDD sensor. Right: SSD sensor

The spatial resolutions in both z and $r\varphi$ direction depend on the layer and are summarized in Table 3.1. The dE/dx resolution achieved in Pb–Pb collisions combining SDD and SSD signals is $\sigma(dE/dx) \approx 10\text{--}15\%$.

3.1.2 Time Projection Chamber (TPC)

The TPC (Figure 3.5 - left) is the main tracking detector of the ALICE central barrel. The phase space covered by this detector is:

- pseudo-rapidity $|\eta| < 0.9$ for tracks that also match ITS, TOF and TRD; for reduced track length an acceptance up to about $|\eta| < 1.5$ is accessible
- full azimuthal coverage, except for dead zones between the sectors
- p_T range covered from about 0.2 GeV/c to 100 GeV/c with a p_T resolution $\sigma(p_T)/p_T \sim 1\%$ at 1 GeV/c, $\sigma(p_T)/p_T \sim 10\%$ at 50 GeV/c

The TPC consists of a cylindrical volume with an inner radius of 85 cm, an outer radius of 250 cm and an overall length along the beam direction of 5 m filled with 90 m³ of Ne/CO₂/N₂ gas mixture. A central high voltage (100 kV) electrode creates a highly uniform electrostatic field (~ 400 V/cm) in which electrons and ions produced by the particles traversing the gas drift along the beam direction. The maximum drift time in the volume is ~ 92 μ s. The readout system is located at the two edges of the cylinder and is based on multi-wire proportional chambers with cathode pad read-out. There are about 560000 readout pads of size ranging from 4×7.5 mm² to 6×15 mm², since the inner region has a higher occupancy and finer segmentation is needed. The read-out pads provide space as well as dE/dx and drift time measurements, from which energy loss and 3D track reconstruction can be extracted. The relative dE/dx resolution was measured to be about 6% for tracks that cross the entire detector, the spatial resolution is 1 mm in both z and $r\varphi$ directions.

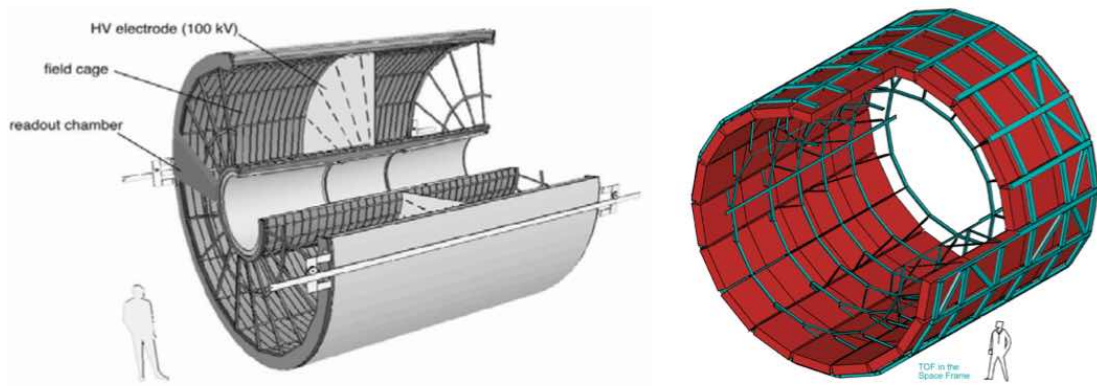


FIGURE 3.5: Left: structure of the ALICE TPC. Right: schematic view of the ALICE TOF

3.1.3 Time of Flight Detector (TOF)

The TOF (Figure 3.5 - right) is located at a radial distance of about 4 m from the beam pipe and it is separated from the TPC by the Transition Radiation Detector (TRD). It is a large area array of Multi-gap Resistive Plate Chambers (MRPCs) covering the full azimuth in the central rapidity region ($|\eta| < 0.9$). Unlike standard RPCs, in MRPCs the gas gap between the electrodes is divided by means of internal plates which are physical barriers stopping the avalanche from growing too much; in this way it is possible to apply a very intense electric field that provokes the avalanche process immediately after primary ionization occurs in the gas volume. The MRPCs are designed as double-stack strips each having 5 gas gaps of 250 μm width. The resistive plates between the gaps are made of high-resistivity glass of 0.4 mm thickness. The two stacks are placed on each side of a central anode. On the outer surface of the external plates a very intense electric field (~ 100 kV/cm) is applied.

A time-of-flight measurement is based on the quantity $\mathbf{t}_{hit} - \mathbf{t}_0$, where \mathbf{t}_{hit} is the time measured by the TOF detector while \mathbf{t}_0 is the time of the interaction that can be measured with the ALICE T0 subdetector. However, due to the detector acceptance, especially in pp collisions, no signals are observed by the T0 for a fraction of the events and an alternative method was developed where the TOF information itself is used to determine the event time when at least three tracks have an associated TOF signal. This is done by means of a combinatorial algorithm which compares the measured TOF times to the expected times of the tracks, assuming a common event time \mathbf{t}_0 . This latter quantity is obtained from a χ^2 minimization procedure. The overall time resolution of the TOF detector is given by $\sigma_{tot}^2 = \sigma_{TOF}^2 + \sigma_{t_0}^2$, where σ_{TOF}^2 is the intrinsic TOF time resolution and $\sigma_{t_0}^2$ is the resolution on the event time. Both σ_{TOF}^2 and $\sigma_{t_0}^2$ depend on the number of tracks matched to TOF: for $n_{tracks} = 30$, $\sigma_{TOF}^2 \approx 80$ ps and $\sigma_{t_0}^2 \approx 25$ ps [117].

3.1.4 V0 detector

The V0 detector (Figure 3.6 - left) consists of two arrays of scintillator counters, called V0A and V0C, which are installed on either side of the ALICE interaction point. The V0A detector is located 340 cm from the detector centre on the side opposite to the muon spectrometer whereas V0C is located on the muon spectrometer side at 90 cm distance

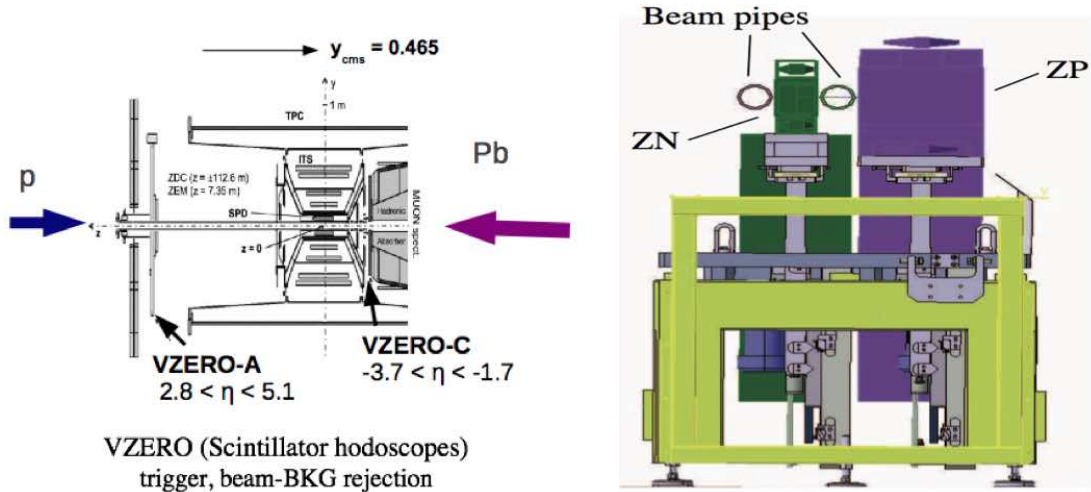


FIGURE 3.6: Left: location of the two V0 scintillators along the beam line. Right: location of the ZDC detectors, transverse view

from the detector centre. They cover the pseudo-rapidity ranges $2.8 < \eta < 5.1$ (V0A) and $-3.7 < \eta < -1.7$ (V0C) and each one is segmented into 32 individual counters distributed in four rings. The scintillation light deposited by particles in each counter is collected by optical fibers and then guided to photo-multipliers. This detector has several functions:

- triggering
- background rejection
- luminosity measurements
- centrality and multiplicity measurements

3.1.5 Zero Degree Calorimeter (ZDC)

Two sets of hadronic calorimeters are located at 112.5 m (114 m until 2011) from the detector centre on either side of the Interaction Point (IP) to detect spectator nucleons. Since spectator protons and nuclear fragments are deflected by the magnetic field of LHC while neutrons are undeflected, each ZDC set is composed of two elements: one for spectator neutrons (ZN) placed between the two beam pipes at 0 degrees relative to the LHC axis, and one for spectator protons (ZP) placed outside the beam pipe on the side where positive particles are deflected (Figure 3.6 - right). Nuclear fragments with $Z/A \approx 1/2$ (like Pb nuclei) are not detected since they remain inside the beam pipe.

The ZN dimensions are $7.04 \times 7.04 \times 100 \text{ cm}^3$, the ZP dimensions are $12 \times 22.4 \times 150 \text{ cm}^3$. They are hadronic sampling calorimeters using W-alloy (ZN) and brass (ZP) as passive material. The shower generated by incident particles produces Cherenkov radiation in quartz fibers interspersed in the passive material. The fibre spacing is smaller than the radiation length of the passive material in order to avoid electron absorption. The Cherenkov light is then sent to photomultipliers.

As will be discussed in next sections, ZDC is used for event selection (Section 3.2.2) and centrality measurements (Section 3.3).

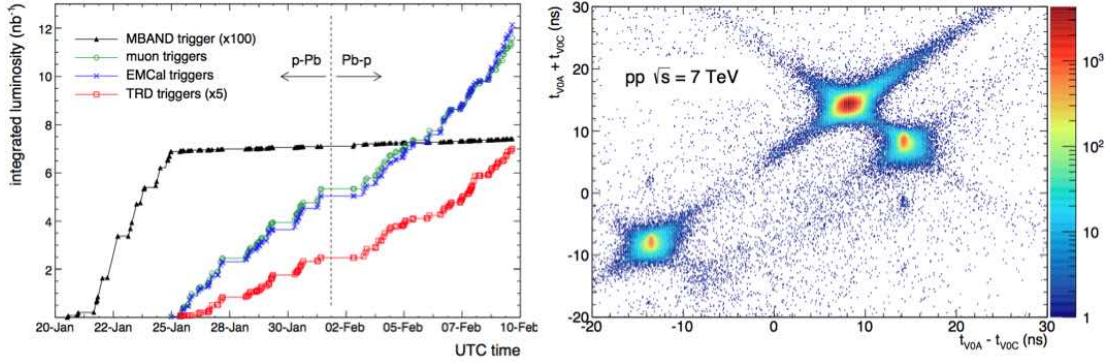


FIGURE 3.7: Left: integrated luminosity per trigger type in the 2013 p-Pb run. Right: Correlation between the sum and difference of signal times in V0A and V0C.

3.2 ALICE Performance

3.2.1 Trigger

During the data taking the trigger decision is generated by the Central Trigger Processor (CTP) based on detector signals and information about the LHC bunch filling scheme. The CTP evaluates trigger inputs from the trigger detectors every LHC machine clock cycle (~ 25 ns). The Level 0 trigger decision (L0) is made $\sim 0.9 \mu\text{s}$ after the collision and is delivered to the detectors with a latency of about 300 ns. The events accepted at L0 are further evaluated by the Level 1 (L1) trigger algorithm in the CTP. The L1 trigger decision is made $\sim 6.5 \mu\text{s}$ after L0. This delay is caused by the computation time (TRD and EMCal) and propagation times (ZDC, located at 112.5 m from IP2). The L0 and L1 decisions, trigger the buffering of the event data in the detector front-end electronics. The trigger decisions is complemented by the information as to whether there are bunches coming from both A-side and C-side, or one of them, or neither, with a resolution of 25 ns.

ALICE operates with minimum-bias (MB) triggers, mainly based on V0 and SPD, and with rare triggers that are optimized to select particular classes of events such as events containing jets or muons or high-multiplicity events. In Pb-Pb collisions the V0 information has been used for triggering central and semicentral events. The decision in this case depended on the summed-up amplitude of the signals coming from both scintillators.

Figure 3.7 (right) shows the integrated luminosity collected with the different triggers used in the 2013 p-Pb runs as a function of time. In this thesis events selected with the **MBAND** trigger are used. This minimum bias trigger requires the presence of signal from both V0A and V0C detectors. From Figure 3.7 (left) we see that an integrated luminosity of more than 7 nb^{-1} has been collected using this trigger.

3.2.2 Background rejection

During the operation of the LHC a significant amount of background events arises from interactions of the beams with the residual gas present in the beam vacuum tubes. The most relevant component of beam background in ALICE is produced close to the experimental region by inelastic beam-gas (BG) interactions occurring within the first 40 m on either side of the detector centre. Given the requirement of a reduced luminosity,

in pp running the background rate in ALICE can be of the same order of magnitude as the interaction rate.

ALICE background rejection consists of an online and an offline procedure. During the data taking the signal from either sides of the V0 detector is used. Since the background caused by beam-gas interactions is produced upstream of the V0 in the side from which the beam arrives, it produces an “early” signal in the corresponding V0 scintillator when compared with the time corresponding to a collision in the nominal interaction point. The difference between the expected beam and background signals is on average 22.6 ns in the A side and 6 ns in the C side. As shown in Figure 3.7 (right), background events accumulate mainly in two peaks in the time sum-difference plane, well separated from the main peak that corresponds to events occurring in the interaction point. Background from Beam 1 concentrates at (-14.3 ns, -8.3 ns), background from Beam 2 concentrates at (14.3 ns, 8.3 ns). Events are not rejected only if their timing signal from both V0A and V0C detectors is within a fiducial window.

The offline background rejection is based on a cut on the correlation between clusters and tracklets reconstructed in the SPD (Figure 3.8 - left). Background particles usually cross the pixel layers in a direction parallel to the beam axis. Therefore, only random combinations of BG hits can build a reconstructed track pointing to a fake vertex. In the cluster-tracklet plane of Figure 3.8 (left) background events which have many clusters and only few tracklets populate the region above the green dashed line, which is the cut used offline to exclude BG events from data analysis. Only a very small fraction of background events (0.02%) survive the above-mentioned cuts in Pb-Pb collisions while in pp collisions the amount of background surviving the cuts is strongly dependent on the running conditions and on the specific trigger configuration under study, reaching a value of 17% in some of the 2012 runs. In p-Pb the fraction of background events surviving the physics selection cuts is $\sim 0.11\%$.

Collisions of main bunches and satellite bunches³ located at short distance from the main bunch are also a source of background. These satellite events are rejected using the correlation between the sum and the difference of times measured in the ZDC, as shown in Figure 3.8 (right) for Pb-Pb collisions. The large cluster in the middle corresponds to

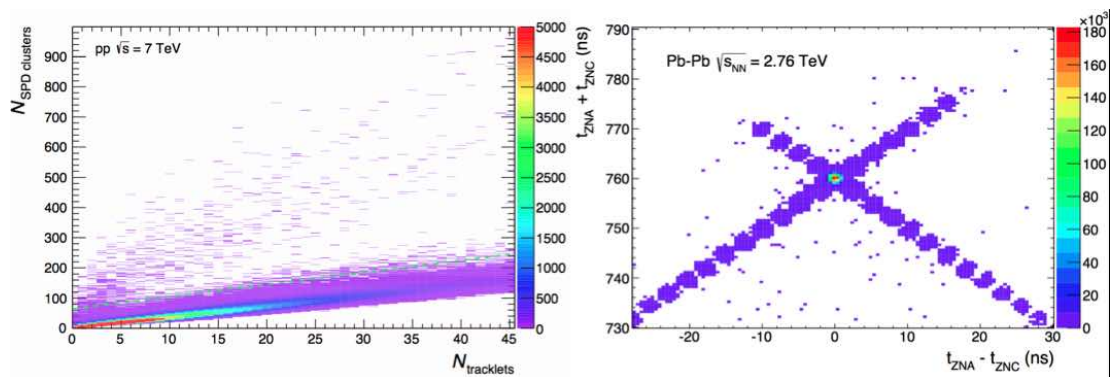


FIGURE 3.8: Left: correlation between reconstructed SPD clusters and tracklets. Two bands corresponding to physics collisions and background are visible. The dashed cyan line represents the cut used in the offline selection: events lying in the region above the line are tagged as BG and rejected. Left: correlation between the sum and the difference of times recorded by the neutron ZDCs on either side (ZNA and ZNC) in Pb-Pb collisions.

³The RF operations involved in the delivery of proton and lead ion bunches to the LHC can result in satellite bunches of varying intensity occupying the nominally empty RF buckets

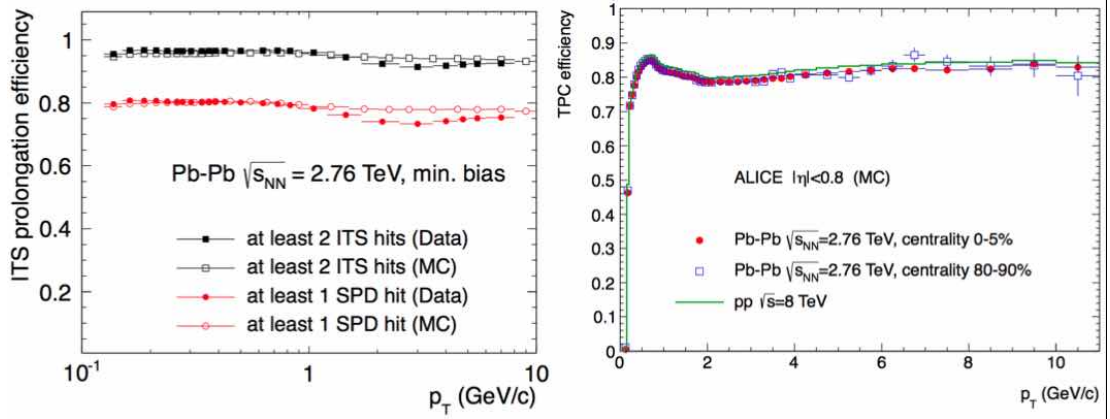


FIGURE 3.9: Left: ITS-To-TPC matching efficiency as a function of p_T for data and MC in minimum bias Pb–Pb collisions. Tracks used in the evaluation of the matching efficiency are required to have at least 2 ITS hits or at least 1 SPD hit. Right: TPC track finding efficiency from MC simulations for pp collisions at $\sqrt{s} = 8$ TeV, central and peripheral Pb–Pb collisions at $\sqrt{s_{NN}} = 2.76$ TeV.

collisions between ions in the nominal RF bucket on both sides, while the small clusters along the diagonals (spaced by 2.5 ns in time difference) correspond to collisions in which one of the ions is displaced from the main bucket by one or more RF buckets.

3.2.3 Track and vertex reconstruction

Tracking in ALICE is performed offline and consists of the following steps:

- the clusters in the two layers of SPD are used to reconstruct the primary vertex, defined as the space point to which a maximum number of tracklets (Section 3.1.1) converge. When a 3D reconstruction of the primary vertex is not feasible (essentially in very low-multiplicity events) the algorithm performs a minimization using

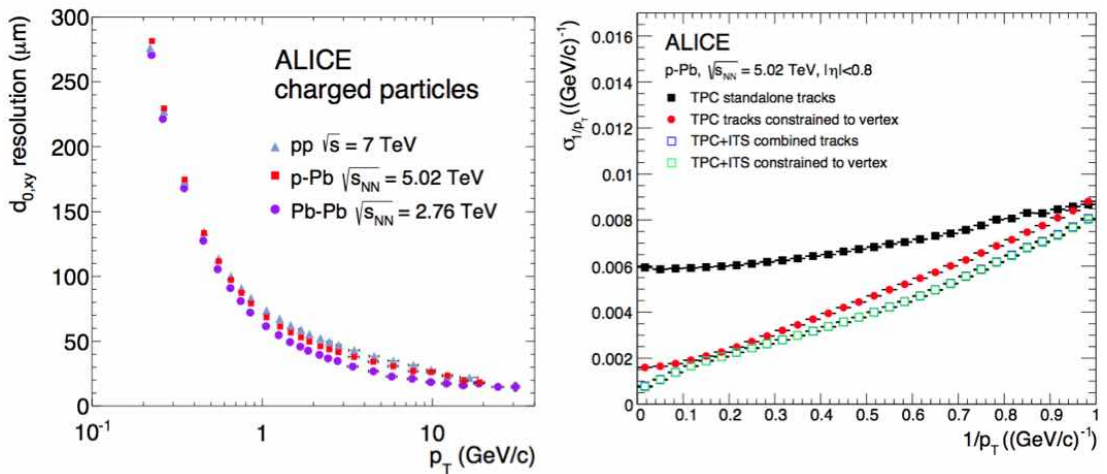


FIGURE 3.10: Left: resolution on the projection of the impact parameter in the transverse plane for charged particles in pp, Pb–Pb and p–Pb collisions as a function of p_T . Right: inverse- p_T resolution σ_{1/p_T} as a function of p_T in p–Pb collisions, for TPC and ITS-TPC tracks without and with vertex constrain

information from the distance of closest approach (DCA) of tracklets to the beam axis. This method only gives access to the z coordinate of the vertex

- tracking starts at the TPC outer radius. Track seeds are built first with two TPC clusters and the vertex point, then with three clusters and without the vertex constraint. The seeds are propagated inward and, at each step, updated with the nearest cluster found by the algorithm (Kalman filter [118]) until the inner radius of the TPC is reached.
- tracks are then propagated to the outermost ITS layer and become the seeds for track finding in the ITS. Each TPC track produces a tree of track hypotheses in the ITS and the candidates are selected according to their reduced χ^2 . The matching efficiency of this step, defined as the ratio of the fraction of TPC tracks that have a prolongation in the ITS, is shown in Figure 3.9 (left) for data and simulations and different requirements on the ITS hits attached to the track
- the ITS clusters not used in the TPC-ITS reconstruction are used to perform an ITS stand-alone reconstruction. In fact the TPC track finding efficiency drops at low p_T (Fig 3.9 - right) whereas the ITS still has a good performance in this p_T region. This ITS stand-alone reconstruction also allows to reconstruct track traversing dead regions of the TPC or decaying before the inner TPC radius
- once the reconstruction in the ITS is complete, all tracks are extrapolated to their point of closest approach to the interaction vertex, and the outward propagation starts. Once the track reaches the TRD an attempt is made to match it with a TRD tracklet (track segment within a TRD layer) in each of the six TRD layers. Tracks reaching the TOF detector are matched to TOF clusters. The tracks are then propagated further for matching with signals in EMCal, PHOS, and HMPID.
- at the final stage of the track reconstruction, all tracks are propagated inwards starting from the outer radius of the TPC. In each detector (TPC and ITS), the tracks are refitted with the previously found clusters. The track position, direction, inverse curvature, and its associated covariance matrix are determined. The vertex position is recomputed using these tracks.

The left panel of Figure 3.10 shows the resolution on the transverse distance of closest approach of the track to the primary vertex (defined as impact parameter) for all charged particle tracks in pp, Pb-Pb and p-Pb collisions. One can notice an improvement of the

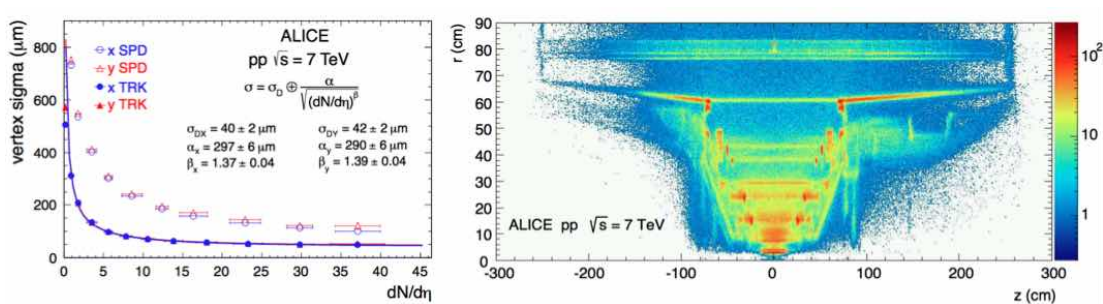


FIGURE 3.11: Left: transverse resolution of the preliminary interaction vertices found with SPD and with global tracks. Right: Distribution of secondary vertices from hadronic interactions in the ALICE material.

resolution in p-Pb and Pb-Pb collisions thanks to the more precise determination of the primary vertex for higher multiplicities.

The absolute resolution on $1/p_T$ for TPC standalone tracks and ITS-TPC combined tracks for p-Pb collisions, is shown in Figure 3.10 (right). The effect of constraining the tracks to the primary vertex is shown as well. The absolute inverse- p_T resolution σ_{1/p_T} , plotted in this figure, is connected to the relative transverse momentum resolution via $\sigma_{p_T}/p_T = p_T \sigma_{1/p_T}$.

The resolution on the position in the transverse plane of the interaction vertex reconstructed with SPD and with global tracks are shown as a function of multiplicity in Figure 3.11 for the case of pp collisions at $\sqrt{s}=7$ TeV. Both resolutions scale with the square root of the number of tracklets/tracks used in the vertex determination.

Once the tracks and the interaction vertex have been found and reconstructed, a search for photon conversions and secondary vertices from strange particle decays is performed. Tracks with a distance of closest approach to the interaction vertex exceeding a certain minimum value (0.5 mm in pp and 1 mm in Pb-Pb) are selected and their point of closest approach is calculated. Figure 3.11 shows the 2D distribution of such vertices that mostly come from photon conversion in the material. The ITS layers, the inner TPC containment vessel, and the inner TPC field cage are visible.

3.2.4 Particle Identification

Many of the ALICE subdetectors have particle identification capabilities:

- ITS: The outer four layers of the Inner Tracking System have an analog readout to measure the deposited charge, thereby providing a dE/dx measurement. For each track, the dE/dx is calculated using a truncated mean: the average of the lowest two points if four points are measured, or a weighted sum of the lowest (weight 1) and the second-lowest points (weight 1/2), if only three points are measured. The dE/dx resolution achieved in Pb-Pb collisions combining SDD and SSD signals is $\sigma(dE/dx) \approx 10\text{-}15\%$.
- TPC measures the charge deposited on up to 159 pad rows. A truncated mean dE/dx (40% highest-charge clusters discarded) is calculated and used for a wide range of momenta. The relative dE/dx resolution was measured to be about 6% for tracks that cross the entire detector.
- TOF measures the arrival time of particles with a resolution of ~ 100 ps
- the High Momentum Particle Identification Detector (HMPID) is a ring-imaging Cherenkov detector that covers $|\eta| < 0.6$ in pseudorapidity and 57.6 degrees in azimuth, corresponding to 5% acceptance of the central barrel, and provides proton/kaon separation up to $p_T = 5$ GeV/c.
- The Transition Radiation Detector (TRD) identifies electrons based on their specific energy loss and transition radiation (TR) and covers the full azimuth for $|\eta| < 0.9$.
- The Electromagnetic Calorimeter (EMCal) identifies electrons by measuring their energy deposition and comparing it to the measured track momentum (E/p).
- The Photon Spectrometer (PHOS) is a high-granularity electromagnetic calorimeter that can also identify electrons using the E/p method.

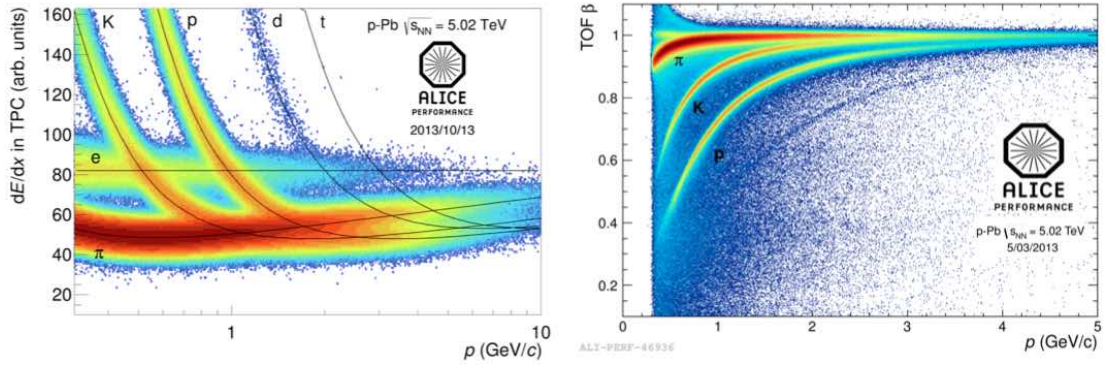


FIGURE 3.12: Left: Specific energy loss (dE/dx) in the TPC vs. particle momentum in p -Pb collisions. The lines show the ALEPH parametrizations of the expected mean energy loss. Right: TOF measured velocity β distribution as a function of momentum.

In the analysis that will be exposed in this thesis, particle identification is exploited to identify the pions and kaons coming from D^+ mesons decay. To do this, PID information from TPC and TOF is used.

In the TPC particle identification is performed by simultaneously measuring the specific energy loss (dE/dx), the charge, and the momentum of each particle traversing the detector gas. The energy loss, described by the Bethe-Bloch formula, is parametrized by a function originally proposed by the ALEPH collaboration

$$f(\beta\gamma) = \frac{P_1}{\beta P_4} (P_2 - \beta P_4 - \ln(P_3 + \frac{1}{(\beta\gamma)^{P_5}})) \quad (3.4)$$

where β is the particle velocity, γ is the Lorentz factor, and P_{1-5} are fit parameters. The energy loss is also reproduced by parametrizations developed by the ALICE Collaboration that are periodically tuned on the data. Figure 3.12 (left) shows the measured dE/dx vs. particle momentum in the TPC, demonstrating the clear separation between the different particle species. The lines correspond to the ALEPH parametrization. While at low momenta ($p < 1$ GeV/c) particles can be identified on a track-by-track basis, at higher momenta particles can still be separated on a statistical basis via multi-Gaussian fits. Indeed, for long tracks (~ 130 dE/dx samples) and with the truncated-mean method the resulting dE/dx distribution is Gaussian down to at least 3 orders of magnitude from the peak.

The TOF particle identification performance depends on its intrinsic resolution and on the start time measurement. The start time for the TOF measurement is provided by the T0 detector, which consists of two arrays of Cherenkov counters T0C and T0A, positioned at opposite sides of the interaction point (IP) at $-3.28 < \eta < -2.97$ and $-4.61 < \eta < -4.92$, respectively. However, due to the detector acceptance, especially in pp collisions, no signals are observed by the T0 for a fraction of the events and an alternative method was developed where the TOF information itself is used to determine the event time when at least three tracks have an associated TOF signal. This is done by means of a combinatorial algorithm which compares the measured TOF times to the expected times of the tracks, assuming a common event time t_0 . This latter quantity is obtained from a χ^2 minimization procedure. Figure 3.12 (right) illustrates the performance of the TOF detector by showing the measured velocity β distribution as a function of track momentum (measured by the TPC and ITS). The bands relative to electrons, muon, pions, kaons, protons and deuterons are visible. The background is due to tracks that

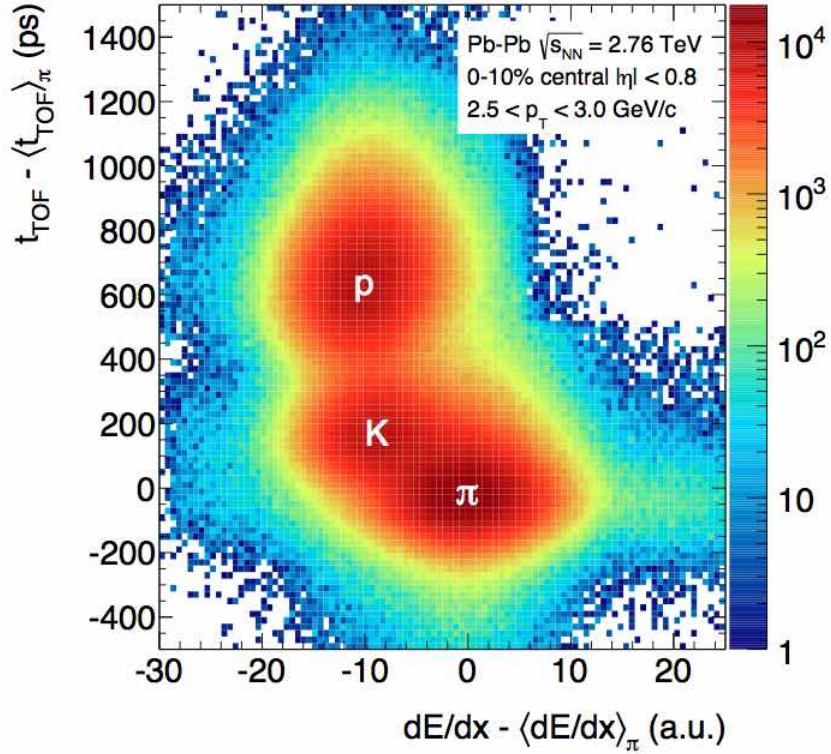


FIGURE 3.13: Combined pion, kaon and proton identification with TOF and dE/dx in the TPC for central Pb–Pb collisions

are incorrectly matched to TOF hits in high-multiplicity p–Pb collisions.

The separation of hadron species can be improved by combining information from TOF and TPC, thus allowing a further extension of the momentum range for identified particle measurements. In Figure 3.13 the difference between the measured and expected PID signals for TPC and TOF are represented in the pion mass hypothesis. It is evident that cuts or fits using a combination of the variables provide a better separation than just considering their projections. This can improve the PID performance in the identification of kaon and pions from D^+ meson decays.

3.3 Centrality determination with ALICE

For spherical nuclei, the geometry of heavy-ion collisions is characterized by the impact parameter, which is the vector \vec{b} connecting the centers of the two colliding nuclei in the plane transverse to the beam direction. It is usual to express the centrality of nuclear collisions not in terms of the impact parameter b but via a percentage of the total hadronic interaction cross section σ_{AA} . The centrality percentile c of an AA collision with impact parameter $0 < b < b_{max}$ is defined as

$$c(b) = \frac{\int_0^{b'} \frac{d\sigma}{db'} db'}{\int_0^\infty \frac{d\sigma}{db'} db'} = \frac{1}{\sigma_{AA}} \int_0^{b_{max}} \frac{d\sigma}{db'} db' \quad (3.5)$$

Experimentally, the centrality is defined as the fraction of cross section with the largest detected charged-particle multiplicity N_{ch} or the smallest zero-degree energy E_{ZDC}

$$c \approx \frac{1}{\sigma_{AA}} \int_{N_{ch}}^{\infty} \frac{d\sigma}{dN'_{ch}} dN'_{ch} \approx \frac{1}{\sigma_{AA}} \int_0^{E_{ZDC}} \frac{d\sigma}{dE'_{ZDC}} dE'_{ZDC} \quad (3.6)$$

The cross section may be replaced with the number of observed events n (corrected for the trigger efficiency and for the non-hadronic interaction background)

$$c \approx \frac{1}{N_{ev}} \int_{N_{ch}}^{\infty} \frac{dn}{dN'_{ch}} dN'_{ch} \approx \frac{1}{N_{ev}} \int_0^{E_{ZDC}} \frac{dn}{dE'_{ZDC}} dE'_{ZDC} \quad (3.7)$$

We are assuming that, on average,

- the particle multiplicity at midrapidity increases monotonically with centrality.
- the zero-degree energy decreases monotonically with centrality.

For the zero-degree energy measurement, this assumption holds only for central collisions because nuclear fragments emitted in peripheral collisions may be deflected out of the acceptance of the zero-degree calorimeter, leading to low signals indistinguishable from those seen in central collisions.

3.3.1 Centrality determination in Pb–Pb collisions

The Glauber MC introduced in Section 1.3.2 is used to simulate Pb–Pb collisions. The impact parameter b is randomly selected from the geometrical distribution $dP/db \propto b$ up to a maximum $b_{max} \approx 20\text{fm} > 2R_{Pb}$. The maximum value of the impact parameter b_{max} is chosen large enough to simulate collisions until the interaction probability becomes zero.

The number of collisions N_{coll} and the number of participants N_{part} are determined by counting, respectively, the binary nucleon collisions and the nucleons that experience at least one collision. The geometric nuclear overlap function T_{AA} is then calculated as $T_{AA} = N_{coll}/\sigma_{inel}$ where σ_{inel} is the nucleon-nucleon inelastic cross-section. For nuclear collisions at $\sqrt{s_{NN}} = 2.76$ TeV, $\sigma_{inel} = (64 \pm 5)$ mb is used, estimated by interpolation of pp data at different center-of-mass energies and from cosmic rays, and subtracting the elastic scattering cross section from the total cross section. The impact parameter and N_{part} distributions are shown in Figure 3.14. The centrality classes are defined by sharp cuts on the the impact parameter distribution, the corresponding N_{part} distributions are shown in Figure 3.14 (right).

To divide the events collected by ALICE in centrality classes, a connection between the impact parameter and an experimental observable has to be established. This can be done using the Glauber MC to generate N_{part} and N_{coll} and parametrizing the particle multiplicity per nucleon-nucleon collision with a Negative Binomial Distribution with parameters μ and k :

$$P_{\mu,k}(n) = \frac{\Gamma(n+k)}{\Gamma(n+1)\Gamma(k)} \cdot \frac{(\mu/k)^n}{(\mu/k+1)^{n+k}} \quad (3.8)$$

To apply this model to any collision with a given N_{part} and N_{coll} one has to introduce the concept of “ancestors”, i.e. independently emitting sources of particles. We assume

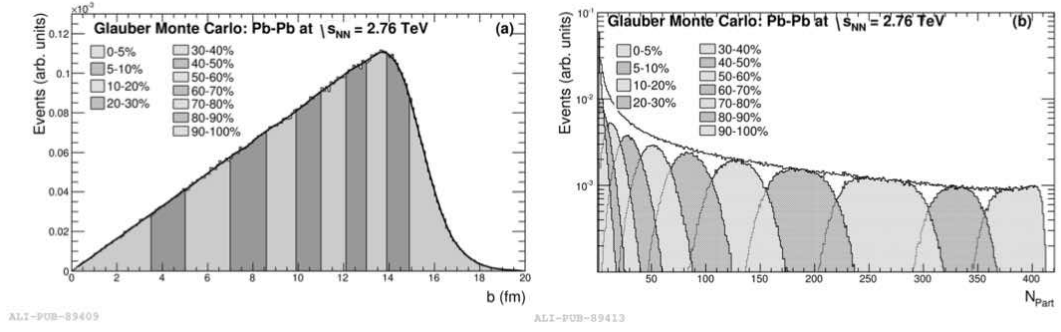


FIGURE 3.14: Left: impact parameter distribution obtained from Glauber MC simulations for Pb-Pb collisions at $\sqrt{s_{NN}} = 2.76$ TeV. Right: the corresponding N_{part} distributions for different intervals of impact parameter values.

that the number of ancestors $N_{ancestors}$ can be parameterized by $N_{ancestors} = f \cdot N_{part} + (1-f) \cdot N_{coll}$. This is inspired by two-component models which decompose nucleus-nucleus collisions into soft and hard interactions, where the soft interactions produce particles with an average multiplicity proportional to N_{part} , and the probability for hard interactions to occur is proportional to N_{coll} . Experimentally this framework is used to fit different observables:

- the sum of the signal amplitudes of the V0A and V0C scintillators, which is proportional to the number of particles hitting them
- the number of clusters in the second layer of the SPD
- the number of tracks reconstructed in the TPC

Figure 3.15 (left) shows the distribution of the sum of amplitudes in the V0 scintillators. The distribution is fitted with a parametrization based on the Glauber MC and the NBD distribution (NBD-Glauber fit in the following) and the parameters extracted are shown: f is the parameter that appears in the definition of $N_{ancestors}$, while μ and k are the parameters of the NBD distribution.

Another way to determine the centrality is to measure the energy deposited by the

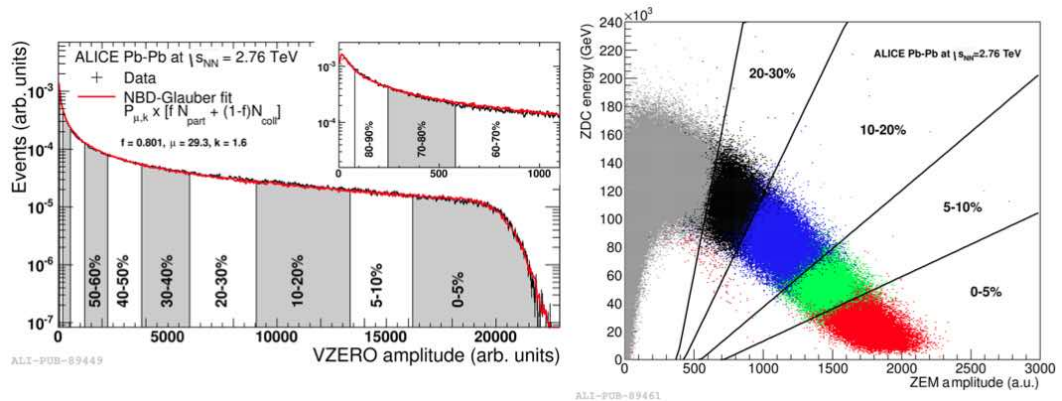


FIGURE 3.15: Left: sum of amplitudes in the V0 scintillators for Pb-Pb collisions at $\sqrt{s_{NN}} = 2.76$ TeV. The distribution is fitted with the NBD-Glauber distribution. Right: two dimensional distribution for ZEM amplitude and ZDC energy.

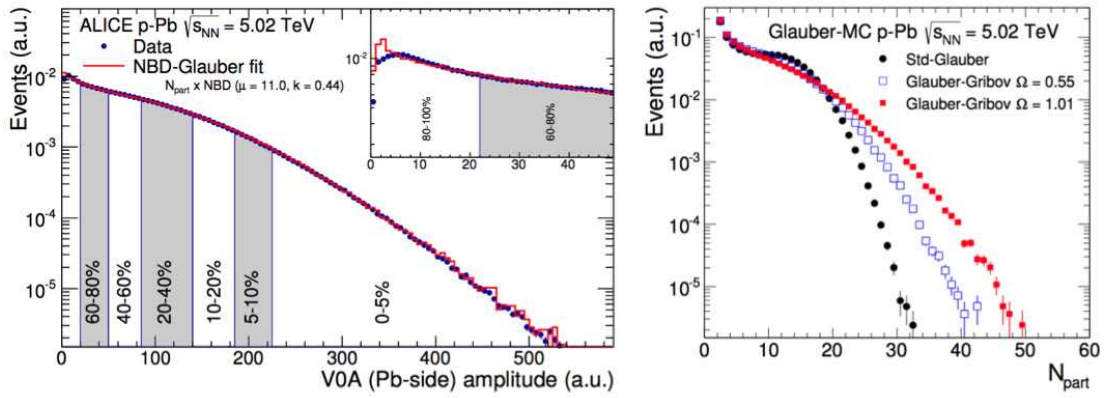


FIGURE 3.16: Left: distribution of amplitudes in the V0A scintillators during the p -Pb runs. Right: N_{part} distributions obtained from standard Glauber MC and from Glauber MC coupled to Glauber-Gribov fluctuations.

spectator nucleons in the ZDC. In theory this would easily relate to N_{part} via

$$N_{\text{part}} = 2A - E_{ZDC}/E_A \quad (3.9)$$

where E_{ZDC} is the energy measured by the ZDC and E_A is the beam energy per nucleon. In practice however some nuclear fragments have charge over mass ratio similar to the lead ions in the beam and remain inside the beam pipe. A quantity that has a monotonic increasing behaviour with N_{part} is the energy deposited in the ZEM detectors, a set of two electromagnetic calorimeters placed close to the beam pipe at 7.5 m from the interaction point covering a region $4.8 < |\eta| < 5.7$. Figure 3.15 (right) shows the two dimensional distribution of ZEM amplitude and ZDC energy. The centrality here is defined by cutting the plane into regions defined by straight lines. As one can see from the figure, the slope of these straight lines increases going to peripheral collisions, where the correlation between ZEM amplitude and ZDC energy is partially lost, making this measurement trustable in 0-30% centrality region only.

The accuracy of the experimental determination of centrality with the different methods was evaluated in [119] and turned out to depend in the rapidity coverage of the detector used. The best centrality resolution is achieved when combining V0A and V0C detectors (Figure 3.15-left), due to 4.3 units of rapidity coverage, and ranges from 0.5% resolution for central collisions to 2% for peripheral collisions.

The standard method typically used in ALICE physics analyses to extract N_{part} and N_{coll} per centrality class in Pb-Pb collisions is the NBD-Glauber fit to the sum of V0A and V0C amplitudes. The other methods described are used to asses the systematic uncertainty on the centrality determination.

3.3.2 Centrality determination in p -Pb collisions

In Figure 3.16 (left) the distribution of amplitudes in the V0A scintillator array during the p -Pb runs (the V0A is thus in the Pb-going direction) is shown together with the NBD-Glauber fit and with the centrality classes indicated by the vertical lines. The NBD-Glauber approach used in p -Pb collisions is similar to the one described in the previous section, but here $N_{\text{ancestors}}$ is assumed to be equal to N_{part} and the final multiplicity distributions scales with a $NDB \times N_{\text{part}}$ law. Furthermore in hadron-nucleus collisions

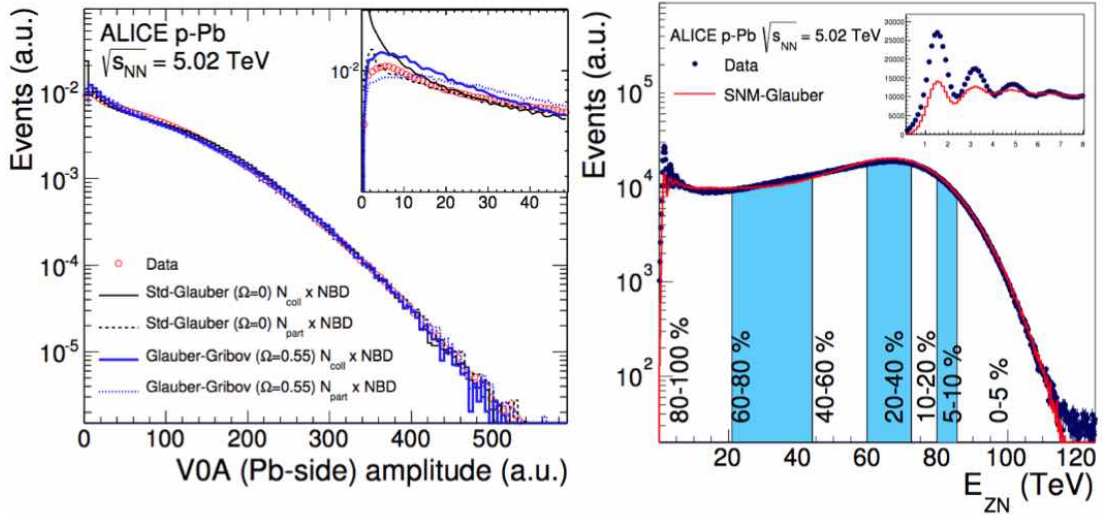


FIGURE 3.17: Left: distribution of amplitudes in the V0A hodoscopes during the p-Pb runs with standard Glauber and Glauber-Gribov fits. Right: distribution of the neutron energy spectrum measured in the ALICE neutron calorimeter (ZN) on the A-side.

one has to take into account the particular quark-gluon configuration of the hadron, which is frozen during the collision leading to a different interaction strength compared to $\sigma_{\text{NN}}^{\text{inel}}$. This leads to fluctuations of the number of collisions which are significantly larger than in the standard Glauber MC approach [120]. In the Glauber MC shown in Figure 3.16 (left) these fluctuations are implemented by an effective scattering cross-section.

Another approach taking into account these fluctuations is the Glauber-Gribov model, which includes event-by-event variations of $\sigma_{\text{NN}}^{\text{inel}}$. The width of the variations in $\sigma_{\text{NN}}^{\text{inel}}$ is controlled by the parameter Ω . The N_{part} distributions obtained from standard Glauber MC and from Glauber MC coupled to Glauber-Gribov fluctuations is shown in Figure 3.16 (right), where the Glauber-Gribov computations have been performed for $\Omega=0.55$ and $\Omega=1.01$. One can see that the N_{part} distribution becomes broader when considering Glauber-Gribov fluctuations. I recall that in p-Pb collisions $N_{\text{part}}=N_{\text{coll}}+1$.

In Figure 3.17 (left) the same V0A distribution of Figure 3.16 (left) is shown together with the standard NBD-Glauber fit and with a Glauber-Gribov ($\Omega=0.55$) fit. Both methods have been repeated with different assumptions on the multiplicity scaling law: $\text{NDB} \times N_{\text{part}}$ and $\text{NDB} \times N_{\text{coll}}$. The standard NBD-Glauber fits yield satisfactory results using either the N_{part} or the N_{coll} scaling, which result in similar average number of collisions $\langle N_{\text{coll}} \rangle$ evaluated for each of the centrality intervals as shown in Table 3.2. The Glauber-Gribov fits with $\Omega=0.55$ provide an equally good description of the measured V0A distribution as the standard Glauber, indicating that the fits cannot discriminate between the models. As expected, the Glauber-Gribov values of $\langle N_{\text{coll}} \rangle$ also shown in Table 3.2 are larger (smaller) for central (peripheral) collisions than those obtained from the standard Glauber, as a consequence of the different shapes of the N_{part} distributions in these models.

Another estimator used for centrality determination in p-Pb is the so-called **CL1**, which is given by the number of clusters in the outer layer of the SPD in the range $|\eta| < 1.4$. A NBD-Glauber fit on the CL1 signal similar to the one performed on V0A amplitude, performed assuming N_{part} scaling, gives the CL1 N_{coll} values that are also shown in Table 3.2.

Centrality (%)	V0A NBD-Glauber		V0A Glauber-Gribov		ZNA SNM-Glauber	CL1 NBD-Glauber
	$N_{\text{part}} \times \text{NBD}$	$N_{\text{coll}} \times \text{NBD}$	$N_{\text{part}} \times \text{NBD}$	$N_{\text{coll}} \times \text{NBD}$		
0-5	14.8	15.3	17.8	19.2	15.7	15.6
5-10	13.0	13.4	14.4	15.2	13.9	13.6
10-20	11.7	12.0	12.0	12.5	12.4	12.0
20-40	9.36	9.62	8.82	9.04	9.99	9.49
40-60	6.42	6.40	5.68	5.56	6.53	6.18
60-80	3.81	3.42	3.33	2.89	3.04	3.40
80-100	1.94	1.85	1.72	1.43	1.24	1.76

TABLE 3.2: N_{coll} values obtained from various fits to V0A, CL1 and ZNA distributions.

The ZDC detects the slow nucleons emitted during the proton-nucleus interaction that can give information on the centrality of the collision. Emitted nucleons are classified as “black” or “grey”. This terminology originates from emulsion experiments:

- black particles, typically defined to have velocity $\beta \lesssim 0.25$ in the nucleus rest frame, are produced by nuclear evaporation processes
- gray particles, $0.25 \lesssim \beta \lesssim 0.7$, are mainly nucleons knocked out from the nucleus

These slow nucleons have been studied at lower energies. The similarities in their emission found at different energies suggested the idea that their production is dictated by nuclear geometry only [121]. Therefore one can expect that slow nucleon emission at LHC can be described by the same models used at lower energy after an appropriate scaling of the parameters.

In Figure 3.17 (right) the distribution of the neutron energy spectrum measured in the ALICE neutron calorimeter (ZN) on the A-side (Pb-going direction) is shown. In the following this variable will be called ZNA energy. The distribution is fitted using the Glauber MC coupled to a slow nucleon emission model (Slow Nucleon Model - SNM) obtained based on the parametrization of experimental results at lower energies (E910 at BNL, Cooler Synchrotron COSY). The average $\langle N_{\text{coll}} \rangle$ values obtained with this method are also shown in Table 3.2.

3.3.3 Biases on centrality in p -Pb collisions

I will now discuss three different sources of bias that have been observed in p -Pb collisions.

3.3.3.1 Multiplicity bias

The left panels of Figure 3.18 show the scatter plot of N_{part} as a function of the impact parameter \mathbf{b} of the collision (top) and of the particle multiplicity as a function of N_{part} (bottom) in the case of a Glauber MC simulation of p -Pb collisions at $\sqrt{s_{\text{NN}}} = 5.02$ TeV. The right panels are the same plots obtained with the Glauber MC for Pb-Pb collisions at $\sqrt{s_{\text{NN}}} = 2.76$ TeV. Looking at the top left plot, it can be observed that the range of N_{part} values generated by the Glauber MC for a given value of \mathbf{b} is large and it is comparable in size to the full range of N_{part} values that appear in the plot, except for \mathbf{b} values exceeding $7 \div 8$ fm. This is not the case in the top right plot, corresponding to Pb-Pb collisions.

Also the multiplicity fluctuations present in p -Pb collisions for a given N_{part} are large.

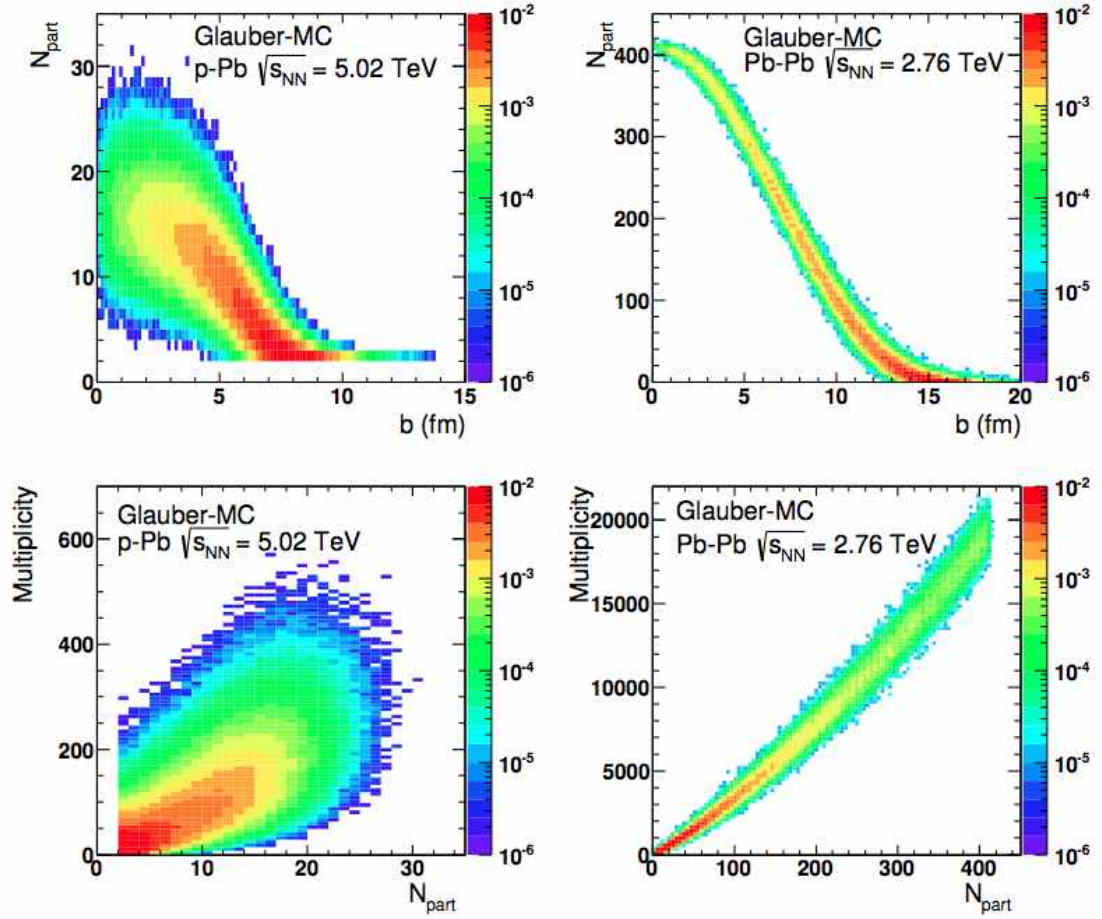


FIGURE 3.18: Top: Scatter plot of number of participating nucleons versus impact parameter. Bottom: Scatter plot of multiplicity versus the number of participating nucleons from the Glauber fit to V0A amplitudes. The quantities are calculated with a Glauber Monte Carlo of p-Pb (left) and Pb-Pb (right) collisions.

For instance let's consider the bottom right plot for Pb-Pb and concentrate on $N_{\text{part}} = 100$ and $N_{\text{part}} = 300$: the ranges of multiplicity values generated by the Glauber-NBD simulation are about 2000-400 and 10000-13000, respectively, and do not overlap. Considering the same scatter plot for p-Pb collisions (bottom left) at $N_{\text{part}} = 10$ and $N_{\text{part}} = 20$, the ranges of multiplicity values generated largely overlap.

These fluctuations lead to the fact that in p-Pb collisions a centrality classification of events based on multiplicity may select a sample with an average number on N-N collisions which is biased compared to a sample defined by cuts in the impact parameter b .

The left panel of Figure 3.19 shows the ratio between the average multiplicity per ancestor and the average multiplicity of the NBD mean multiplicity μ as a function of centrality for different estimators based on multiplicity (V0M is the sum of the V0A and V0C amplitudes). In Pb-Pb collisions, where the width of the plateau of the N_{part} distribution is large with respect to multiplicity fluctuations, the ratio (estimated for the V0M centrality estimator) deviates from unity only for the most peripheral collisions. As expected, in p-Pb collisions the ratio differs from unity for all centralities and all estimators with large deviations for the most central and most peripheral collisions; the most central (peripheral) collisions have on average much higher (lower) multiplicity per participant. When selecting event classes using impact parameter b intervals, there is no deviation from unity, as expected.

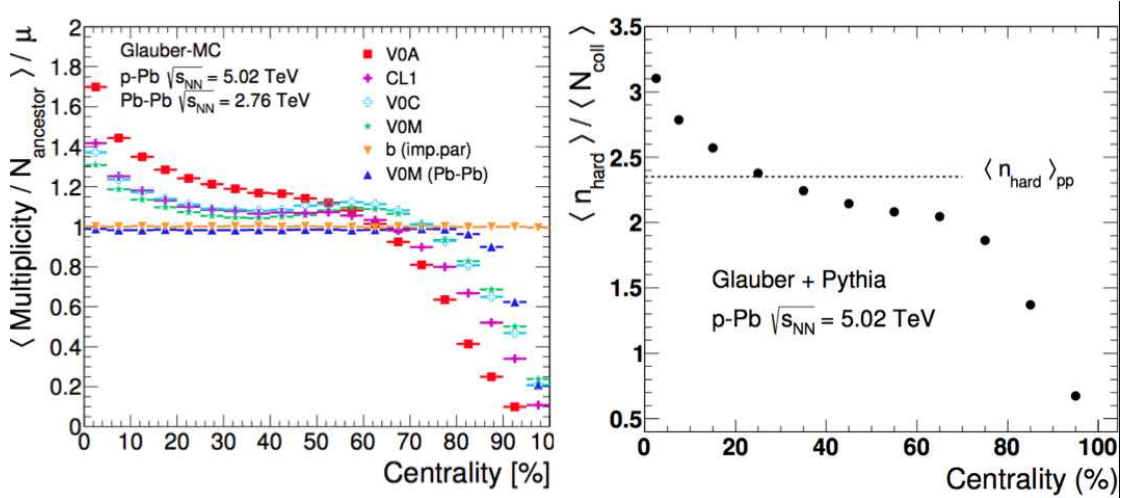


FIGURE 3.19: Top: ratio between the average multiplicity per ancestor and the average multiplicity of the NBD mean multiplicity μ as a function of centrality for different estimators based on multiplicity in p-Pb collisions at $\sqrt{s_{NN}} = 5.02$ TeV and for V0M estimator in Pb-Pb collisions at $\sqrt{s_{NN}} = 2.76$ TeV. Bottom: $\langle n_{\text{hard}} \rangle / \langle N_{\text{coll}} \rangle$ in the different centrality classes for a p-Pb data sample at $\sqrt{s_{NN}} = 5.02$ TeV generated with Glauber MC + PHYTHIA.

The bias on multiplicity also corresponds to a bias on the average number of hard scatterings N_{hard} with respect to the number of binary nucleon-nucleon collisions N_{coll} estimated with Glauber MC. Figure 3.19 (right) shows the results obtained using Glauber MC to generate a sample of p-Pb events at $\sqrt{s_{NN}} = 5.02$ TeV, each having N_{coll} binary collisions. For each generated event, PHYTHIA is used N_{coll} times to generate N_{coll} independent pp collisions at $\sqrt{s} = 5.02$ TeV. The average number of hard scattering per event in pp collisions at this energy in PHYTHIA is $\langle N_{\text{hard}}^{pp} \rangle \approx 2.4$. Dividing the p-Pb data sample generated with Glauber MC + PHYTHIA in centrality classes based on multiplicity, and

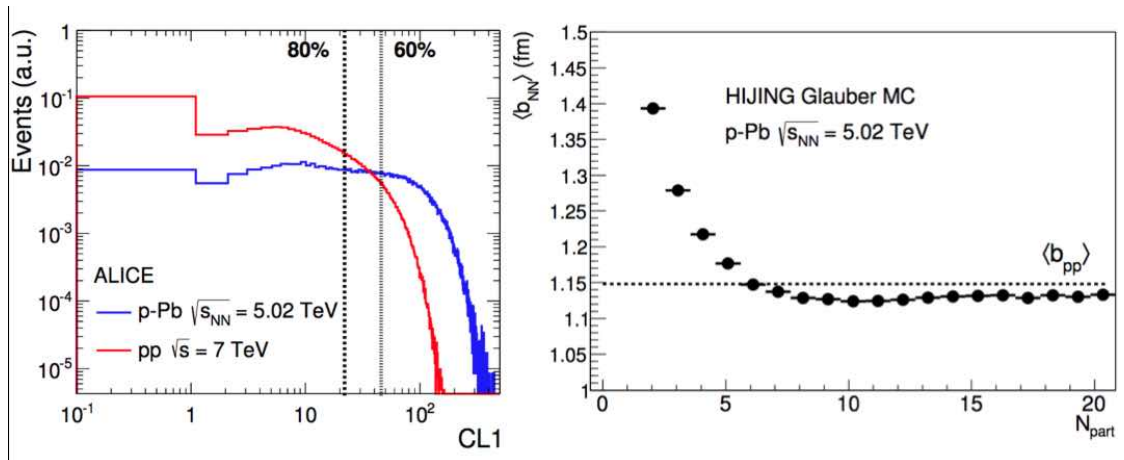


FIGURE 3.20: Top: CL1 multiplicity distribution used as centrality estimator in p-Pb collision at $\sqrt{s_{NN}} = 5.02$ TeV, compared to the distribution in pp collisions at $\sqrt{s} = 7$ TeV. The dashed lines mark the 80% and the 60% percentile of the p-Pb cross-section respectively. Bottom: average impact parameter between the proton and each wounded nucleon of the Pb-nucleus ($\langle b_{NN} \rangle$), calculated from a Glauber MC simulation implemented in HIJING as a function of N_{part} .

calculating $\langle N_{\text{hard}} \rangle / \langle N_{\text{coll}} \rangle$ in the different centrality classes, a bias is observed as shown in Figure 3.19 (right). Central collisions tend to have on average a higher number of hard scatterings per binary collision.

3.3.3.2 Jet-veto bias

High p_T particles contribute to the overall event multiplicity rising with parton energy and can thus introduce a correlation between the centrality estimator and the presence of a high p_T particle in the event. Figure 3.20 (left) shows the distribution of the number of clusters in the outer layer of SPD (CL1) for *p*-Pb collisions, compared to the same distribution in *pp* collisions at $\sqrt{s} = 7$ TeV. The dashed lines mark the 80% and the 60% percentile of the *p*-Pb cross-section. The fraction of the cross collisions having a multiplicity in the range defined by the 80- 100% (60-100%) CL1 multiplicity class in *p*-Pb collisions is 0.8 (0.97). This means that the 80-10% *p*-Pb multiplicity class includes events with multiplicity values lower than those reached in the 20% of *pp* events with the highest multiplicities. This represent an effective veto on hard processes, leading to a $R_{\text{pPb}} < 1$ for low multiplicity *p*-Pb collisions.

3.3.3.3 Geometrical bias

Another source of bias arises from the geometric configuration of *p*-Pb interactions: Figure 3.20 (right) shows the average impact parameter between the projectile proton and each wounded nucleon of the Pb-nucleus ($\langle \mathbf{b}_{\text{NN}} \rangle$), calculated from a Glauber MC simulation implemented in HIJING as a function of N_{part} . $\langle \mathbf{b}_{\text{NN}} \rangle$ is almost constant for central collisions, but rises significantly for $N_{\text{part}} < 6$. This reduces the average number of interactions for most peripheral events.

All the elements discussed above introduce a bias in the determination of N_{coll} for a given centrality class. Similarly to R_{pPb} , we define Q_{pPb} as

$$Q_{\text{pPb}}^{\text{est.}}(p_T, \text{centr}) = \frac{dN_{\text{cent}}^{\text{pPb}}/dp_T}{\langle N_{\text{coll}}^{\text{est.}} \rangle dN^{\text{pp}}/dp_T} = \frac{dN_{\text{cent}}^{\text{pPb}}/dp_T}{\langle T_{\text{pA}}^{\text{est.}} \rangle d\sigma^{\text{pp}}/dp_T} \quad (3.10)$$

for a given centrality percentile according to a particular centrality estimator "est." (in our case N_{coll} is estimated using V0A or CL1 signals with Glauber-NBD fit or ZNA signal with SNM fit). The Q_{pPb} is different from R_{pPb} because it is influenced by potential biases due to the centrality estimator which are not related to nuclear effects. Hence Q_{pPb} can differ from unity even in the absence of nuclear effects. Figure 3.21 shows the Q_{pPb} of charged particles in $|\eta| < 3$ measured by the ALICE collaboration in *p*-Pb collisions at $\sqrt{s_{\text{NN}}} = 5.02$ TeV as a function of p_T [122]. Data are divided in seven centrality classes by mean of Glauber-NBD fit applied to V0A amplitude ($Q_{\text{pPb}}^{\text{V0A}}$ - left) or CL1 distribution ($Q_{\text{pPb}}^{\text{CL1}}$ - right). The N_{coll} values used are reported in Table 3.2. Q_{pPb} strongly deviates from unity at high p_T in all centrality classes, with values well above unity for central collisions and below unity for peripheral collisions. These

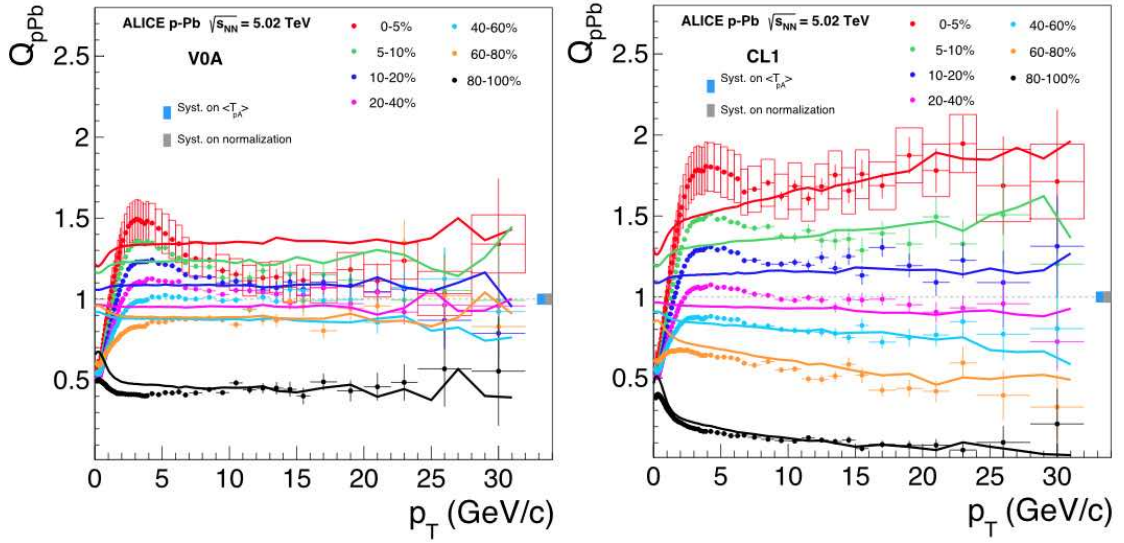


FIGURE 3.21: Left: Q_{pPb}^{V0A} measured by the ALICE Collaboration in p -Pb collisions at $\sqrt{s_{NN}} = 5.02$ TeV [122]. Right: Q_{pPb}^{CL1} measured by the ALICE Collaboration in p -Pb collisions at $\sqrt{s_{NN}} = 5.02$ TeV [122].

results reflect all biases discussed above. However, the spread of Q_{pPb} values between centrality classes reduces with increasing rapidity gap between the tracking region and the centrality estimation region, i.e. going from CL1 to V0A results. The classes selected by the ZNA (Figure 3.22 - left) present Q_{pPb}^{ZNA} values much more similar to each other and close to unity than those of CL1 and V0A estimators, except for peripheral collisions (60-80% and 80-100%). In fact the ZNA does not measure multiplicity and should not be sensitive to the bias sources described above except for the geometrical bias on $\langle b_{NN} \rangle$. The behaviour of Q_{pPb}^{ZNA} in 60-100% is rather due to a limit in the Slow Nucleon Model to correctly describe the most peripheral events.

The Q_{pPb} results show that the bias in the determination of N_{coll} depends on the rapidity gap between the regions where centrality is estimated and the regions in which the charged particles production is measured. We will now discuss this rapidity dependence in more detail.

To provide an unbiased centrality estimator, the ALICE Collaboration has developed a method (**hybrid** method in the following) that relies on two main assumptions:

- a centrality event selection based on ZN does not introduce any bias on the bulk of particle production at mid-rapidity and on high- p_T particle production
- charged-particle multiplicity measured at mid-rapidity scales with N_{part}

The first step is to study the scaling law of particle production in different pseudorapidity regions. To do this we divide the events in seven centrality classes using the energy deposition in the Zero-Degree Neutron Calorimeter in the A side (ZNA), as shown in Figure 3.17. For each centrality class i , the average value of the following signals $\langle s_i \rangle$ is considered

- charged-particle density $dN_{ch}/d\eta$ in $-1 < |\eta| < 0$, measured with SPD tracklets (Section 3.1.1)

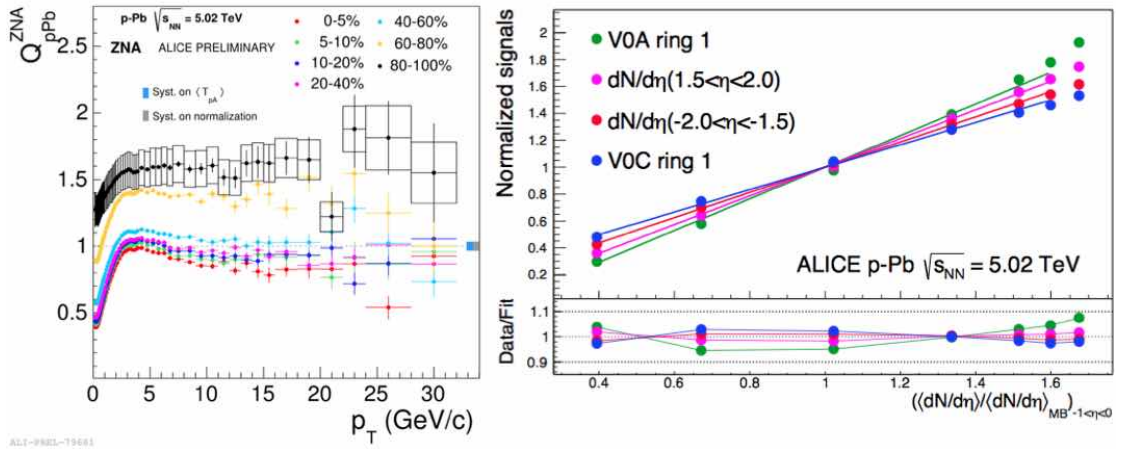


FIGURE 3.22: Left: Q_{pPb}^{ZNA} measured by the ALICE Collaboration in p -Pb collisions at $\sqrt{s_{NN}} = 5.02$ TeV [122]. Right: normalized signals $\langle s_i \rangle / \langle s_{MB} \rangle$ for V0A and V0C (inner ring) and charged particle density in $-2 < |\eta| < -1.5$ and $1.5 < |\eta| < 2$ measured with SPD, vs normalized signals for charged particle density in $-1 < |\eta| < 0$ measured with SPD. Each set of data points is relative to one of the centrality classes measured with ZNA defined in Figure 3.17. Centrality increases from left to right.

- charged-particle density $dN_{ch}/d\eta$ in $-2 < |\eta| < -1.5$, measured with SPD tracklets (Section 3.1.1)
- charged-particle density $dN_{ch}/d\eta$ in $1.5 < |\eta| < 2$, measured with SPD tracklets (Section 3.1.1)
- raw signal in the inner ring of the V0A detector
- raw signal in the inner ring of the V0C detector

The average values $\langle s_i \rangle$ are then compared to the average signal in minimum bias collisions to get the normalized signals $\langle s_i \rangle / \langle s_{MB} \rangle$. Figure 3.22 (right) shows the correlation of these ratios for the seven ZNA centrality classes considered (centrality decreasing from left to right). One can note that the correlation exhibits a clear dependence on the pseudorapidity region in which the normalized signal has been measured. Using the assumption that charged-particle multiplicity measured at mid-rapidity scales with N_{part} , $dN_{ch}/d\eta|_{-1 < |\eta| < 0} \propto N_{part}$, we look for a relation between the other observables in Figure 3.22 (right) and N_{part} , assuming a linear dependence.

The linear dependence can be parameterized as $\langle s_i \rangle \propto N_{part} - \alpha$, so that $\alpha=0$ is equivalent to $\langle s_i \rangle \propto N_{part}$ and $\alpha=1$ is equivalent to $\langle s_i \rangle \propto N_{coll}$. The normalized signals can then be expressed as

$$\begin{aligned} \langle s_i \rangle / \langle s_{MB} \rangle &= \frac{(\langle N_{part} \rangle_i - \alpha)}{(\langle N_{part} \rangle_{MB} - \alpha)} = \\ &= \frac{\langle N_{part} \rangle_{MB}}{(\langle N_{part} \rangle_{MB} - \alpha)} \cdot \left(\frac{\langle dN_{ch}/d\eta \rangle_i}{\langle dN_{ch}/d\eta \rangle_{MB}} \right)_{-1 < \eta < 0} - \frac{\alpha}{(\langle N_{part} \rangle_{MB} - \alpha)} \quad (3.11) \end{aligned}$$

where $\langle N_{part} \rangle_{MB} = 7.9$ is the average number of participating nucleons in minimum bias collisions. The relation is used to find α for each of the normalized signals by a fit to the data. The ratio of the data and the fit results are shown in the lower panel of Figure 3.17 (left).

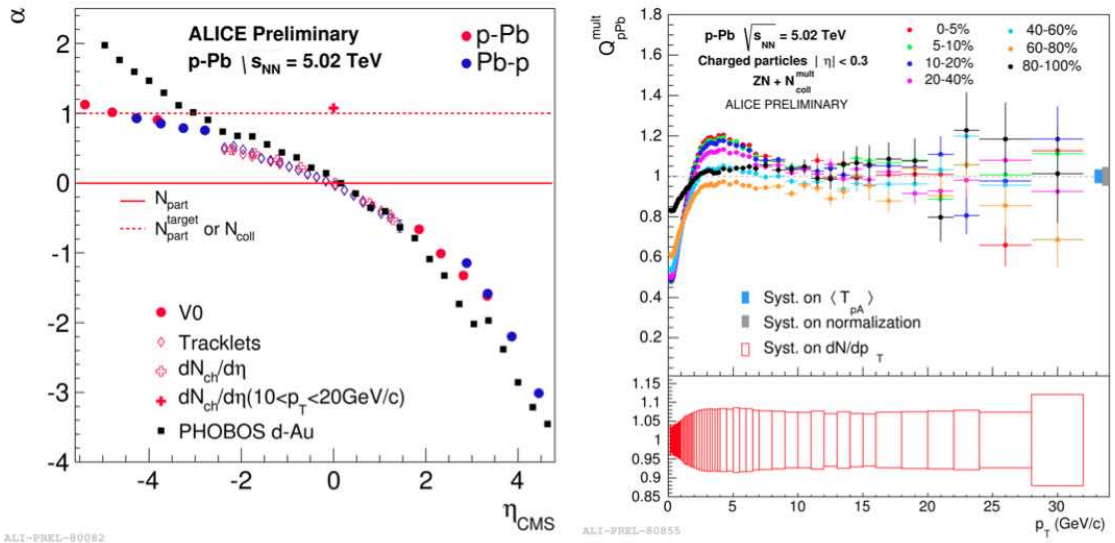


FIGURE 3.23: Left: results for α as a function of the pseudorapidity in the centre-of-mass frame, η_{cms} . Data from both p -Pb and Pb - p collisions are used. Negative pseudorapidity values in the c.m.s. correspond to the Pb going direction in both configurations. At mid-rapidity, the fit is also performed for high- p_T particles (red cross). Right: Q_{pPb}^{mult} measured by the ALICE Collaboration in p -Pb collisions at $\sqrt{s_{\text{NN}}} = 5.02$ TeV [122]. Hybrid method is used to estimate N_{coll} .

Figure 3.23 shows the results for α as a function of the pseudorapidity in the centre-of-mass frame, η_{cms} . To increase the pseudorapidity coverage, data from both p -Pb and Pb - p collisions have been used. Negative pseudorapidity values in the c.m.s. correspond to the Pb going direction in both configurations. At mid-rapidity, the fit is also performed for high- p_T particles (red cross in Figure 3.23).

The result of the fits indicates a smooth and continuous change of the scaling behaviour for charged particle production with pseudorapidity. High p_T particle production at midrapidity scales almost proportionally to N_{coll} ($\alpha \approx 1$), as already observed when discussing the Q_{pPb}^{ZNA} in 0-60% centrality. At large negative pseudorapidity (Pb-going direction) the value of the parameter α obtained from fits to V0 normalized signals gets close to unity, indicating that the scaling behaviour approaches N_{coll} scaling.

The evolution of the fit parameter α reported in Figure 3.23 (left) gives an explanation of the bigger bias observed for CL1: under the assumption that the ZNA signal is unbiased, Figure 3.23 demonstrates that the signals of V0A and CL1 centrality estimators do not scale with N_{coll} , and that the signal of CL1 deviates more from the N_{coll} scaling law than that of V0A.

We can then easily extract the $\langle N_{\text{coll}} \rangle_i$ relative to each ZNA centrality class i in the hybrid approach as

$$\langle N_{\text{coll}} \rangle_i^{\text{mult}} = \langle N_{\text{part}} \rangle_i - 1 = \langle N_{\text{part}} \rangle_{\text{MB}} \cdot \left(\frac{\langle dN_{\text{ch}}/d\eta \rangle_i}{\langle dN_{\text{ch}}/d\eta \rangle_{\text{MB}}} \right)_{-1 < \eta < 0} - 1 \quad (3.12)$$

The $\langle N_{\text{coll}} \rangle_i^{\text{mult}}$ obtained with this method are shown in Table 3.3. These values agree within 15% with those obtained with the SNM approach applied to ZNA signal, except for the most peripheral regions where the Slow Neutron Model is inaccurate. We can now use these $\langle N_{\text{coll}} \rangle_i^{\text{mult}}$ values to compute Q_{pPb}^{mult} in ZNA centrality classes.

The results of Q_{pPb}^{mult} in the hybrid approach are shown in Figure 3.23 (right) and remain

consistent with unity at high- p_T for all centrality classes. This confirms the absence of initial state effects, already observed for minimum bias collisions. The Cronin enhancement, which has already been noted in minimum bias collisions, is observed to be stronger in central collisions and nearly absent in peripheral collisions. The geometry bias is still present and uncorrected, even with this method. Its effect is limited to peripheral classes only, resulting in $Q_{pPb}^{\text{mult}} < 1$ for 80-100%.

In summary, we have seen how the determination of centrality classes in p-Pb collisions is affected by several sources of bias on the extraction of $\langle N_{\text{coll}} \rangle$. This forces us to question the usage of the word "centrality", therefore we will use instead the term "event activity" or "multiplicity" in the next chapters.

Centrality (%)	$N_{\text{coll}}^{\text{mult}}$
0-5	12.2
5-10	11.6
10-20	11.0
20-40	9.56
40-60	7.08
60-80	4.30
80-100	2.11

TABLE 3.3: $\langle N_{\text{coll}} \rangle_i^{\text{mult}}$ values obtained in the hybrid approach.

Chapter 4

Reconstruction of prompt D^+ mesons in p–Pb collisions

In this chapter I describe the general strategy used to extract the prompt D^+ meson signal from the data sample of p–Pb collisions at $\sqrt{s_{NN}}=5.02$ TeV shown in Chapter 3. In the analysis I consider the hadronic decay of D^+ into $K^-\pi^+\pi^+$ and its charge conjugate (D^- into $K^+\pi^-\pi^-$). The relevant quantities that characterize this meson are shown in Table 4.1¹. The same informations are given for the other D-meson species reconstructed up to now with the ALICE detector (D^0 , D^{*+} , D_s^+). The branching ratio² is relatively high, compared to the other decays shown in Table 4.1, and the mean life assures an average decay length of few hundreds μm .

Looking at the D^- decay sketch in Figure 4.1 we define few quantities that will be used in the following:

- **Pointing angle** θ_{pointing} : the angle between the D-meson flight line (joining the primary and the secondary vertices) and the direction of the reconstructed D-meson momentum. Usually the cosine of this quantity is used
- **d_0** : the impact parameter of the D-meson
- **decay length**: the distance between the primary and the decay vertex

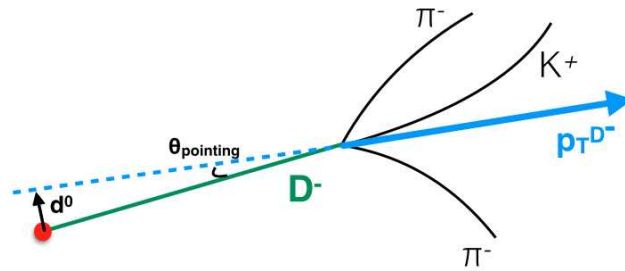


FIGURE 4.1: Sketch of D^+ to $K^-\pi^+\pi^+$ hadronic decay.

¹PDG average [123]

²About 20% of this branching ratio is given by resonance decays, namely $D^+ \rightarrow \bar{K}_0^*(1430)\pi^+ \rightarrow K^-\pi^+\pi^+$ (BR=1.21%), $D^+ \rightarrow \bar{K}^*(892)\pi^+ \rightarrow K^-\pi^+\pi^+$ (BR=1.01%), $D^+ \rightarrow \bar{K}^*(1680)\pi^+ \rightarrow K^-\pi^+\pi^+$ (BR=2.1 10^{-4} %) and $D^+ \rightarrow \bar{K}_2^*(1430)\pi^+ \rightarrow K^-\pi^+\pi^+$ (BR=2.2 10^{-4} %)

Particle	Mass (MeV/ c^2)	Decay Channel	Branching Ratio (%)	Mean Life (s)
D^0	1864.84 ± 0.07	$K^- \pi^+$	(3.88 ± 0.05)	$(410.1 \pm 1.5) 10^{-15}$
D^+	1869.5 ± 0.4	$K^- \pi^+ \pi^+$	(9.13 ± 0.19)	$(1040 \pm 7) 10^{-15}$
D^{*+}	2010.26 ± 0.07	$D^0 \pi^+ \rightarrow K^- \pi^+ \pi^+$	(67.7 ± 0.5)	strong decay
D_s^+	1969.0 ± 1.4	$\Phi \pi^+ \rightarrow K^+ k^- \pi^+$	(2.32 ± 0.14)	$(500 \pm 7) 10^{-15}$

TABLE 4.1: Characteristics of D mesons hadronic decays reconstructed with the ALICE detector

It is also interesting to estimate the momentum of the three daughters: considering the 3-body decay in the rest frame of the mother meson, kinematic calculations give

$$\begin{aligned}
 p_{K,max} &= \frac{1}{2M_{D^+}} \sqrt{[M_{D^+}^2 - (m_K + 2m_\pi)^2][M_{D^+}^2 - (2m_\pi - m_K)^2]} \\
 p_{\pi,max} &= \frac{1}{2M_{D^+}} \sqrt{[M_{D^+}^2 - (2m_\pi + m_K)^2][M_{D^+}^2 - (m_\pi + m_K - m_\pi)^2]}
 \end{aligned}
 \tag{4.1}$$

where M is the mass of the mother particle and $m_{\pi/K}$ the mass of the daughters. Figure 4.3 shows the scatter plot of the D^+ mesons p_T vs the p_T of its daughters and the p_T of the daughter with the lowest momentum. These simulations are obtained with PYTHIA 6.

Also important is the word "prompt" appearing in the title of this chapter. Prompt D^+ mesons are those coming from the hadronization of a c -quark, or from the decay of an excited D-meson state such as $D^{*+}(2010)$. Figure 4.2 shows the decay sketch for a prompt D^- meson (right) and a feed-down D^- meson. The latter comes from the decay of a B hadron, in this case a semi-leptonic decay of B^0 -meson³ and is on average more displaced from the primary vertex, given the typical mean lives of B mesons ($\sim 10^{-12}$ s). In this chapter we will show the strategy used to extract the D meson signal from the 2013 p-Pb data sample.

4.1 D^+ meson signal in p-Pb collisions

The signal coming from D^+ mesons is obtained via an invariant mass analysis of $K^- \pi^+ \pi^+$ decay topologies.

The first step of this analysis is the identification, for each event, of secondary vertices from triplets of tracks with the proper sign combination: two positive tracks and one negative in the case of D^+ candidates and the opposite to obtain D^- candidates. Tracks

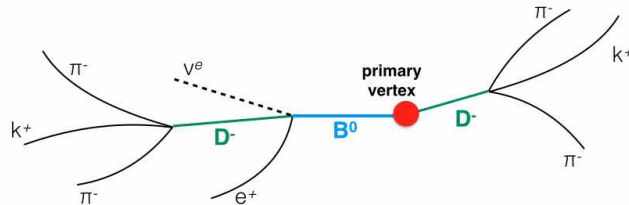


FIGURE 4.2: Sketch of prompt and feed-down D^+ to $K^- \pi^+ \pi^+$ hadronic decay

³all B meson states have significant inclusive branching fraction into D-meson

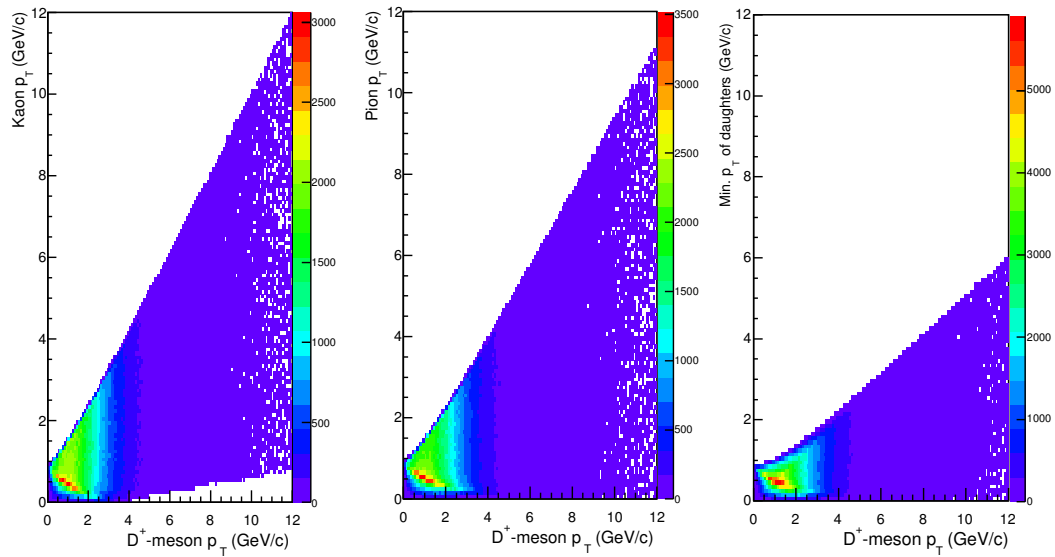


FIGURE 4.3: Left: scatter plot of D^+ mesons p_T vs the p_T of the decay kaons. Centre: scatter plot of D^+ mesons p_T vs the p_T of the decay pion with the highest momentum. Right: scatter plot of D^+ mesons p_T vs the p_T of the decay particle with the lowest momentum.

are approximated as straight lines in the vicinity of the primary vertex and the coordinates of the primary vertex are given by finding the point of minimum distance among the tracks. The resolution on the secondary vertex position was estimated in [124] for pp collisions and is shown in Figure 4.4. For low p_T D^+ , the daughter particles have low

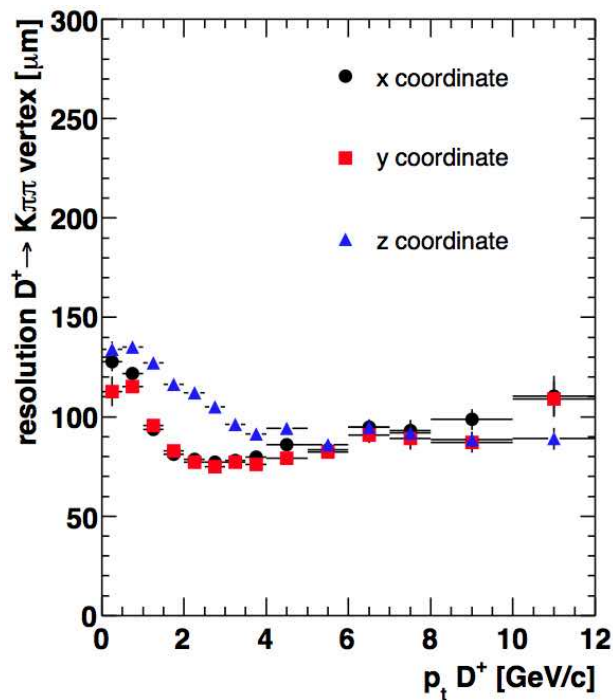


FIGURE 4.4: x , y and z resolution on secondary vertex position as a function of D^+ p_T [124].

momentum and suffer multiple scattering, resulting in a poorer resolution on the secondary vertex position. At high p_T , an improvement of the resolution would be expected since tracks have large momentum and are less affected by multiple scattering, however the decay particles are more collinear with the direction of the parent D^+ momentum and this makes the determination of the vertex position less precise.

For each vertex the invariant mass is obtained as

$$M_{\text{inv}} = \sqrt{(E_K + E_{\pi_1} + E_{\pi_2})^2 - (p_{\vec{K}} + p_{\vec{\pi}_1} + p_{\vec{\pi}_2})^2} \quad (4.2)$$

where the energy values $E_K, E_{\pi_1}, E_{\pi_2}$ are the energies of the kaon and of the pions, respectively. The D^+ candidates p_T is obtained as

$$p_T^{D^+} = p_T^K + p_T^{\pi_1} + p_T^{\pi_2} \quad (4.3)$$

Very important in the D^+ case is the fact that the decay configuration allows only one possible value for the invariant mass, since the kaon mass in Equation 4.2 is always assigned to the track with opposite charge sign with respect to the other two. This is not the case e.g. in the $D^0 \rightarrow K^-\pi^+$, where each candidate vertex has two values of the invariant mass.

4.1.1 Event Selection

The analysis is performed on $\sim 110 \cdot 10^6$ p-Pb collisions collected with a minimum bias trigger requiring signal in both V0 scintillators (Section 3.2.1 - Figure 3.7). Only events that are not rejected by the physics selection cuts described in Section 3.2.2 are selected for the analysis.

A further selection is performed on the basis of the reconstructed vertex. From this point of view events can be divided in four groups:

- events where no vertex has been reconstructed
- events where the vertex has been reconstructed with global (ITS+TPC and TPC only) tracks (Section 3.2.3)
- events where the vertex has been reconstructed only with SPD tracklets and the 3D (x, y, z) coordinates have been determined (Section 3.2.3)
- events where the vertex has been reconstructed only with SPD tracklets and only the z coordinate has been determined (this happens in case the 3D SPD vertexing algorithm fails, e.g. at low multiplicity) (Section 3.2.3)

The reconstruction of the vertex with SPD has higher efficiency due to the wider η coverage of the SPD and of the less stringent request applied to tracklets w.r.t. tracks in the vertex calculations. The efficiency of vertex reconstruction ϵ^{vertex} was estimated in minimum bias pp collisions at $\sqrt{s} = 7$ TeV. For the SPD vertex reconstruction (3D+z) $\epsilon_{\text{SPD}}^{\text{vertex}} \approx 96\%$, while the reconstruction based on tracks has $\epsilon_{\text{TRK}}^{\text{vertex}} \approx 81\%$.

In the analysis we only keep events with vertex reconstructed using global tracks. The reason for this choice is that this class of vertices has a better resolution in the transverse plane compared to vertices reconstructed with the SPD tracklets, as it can be seen in

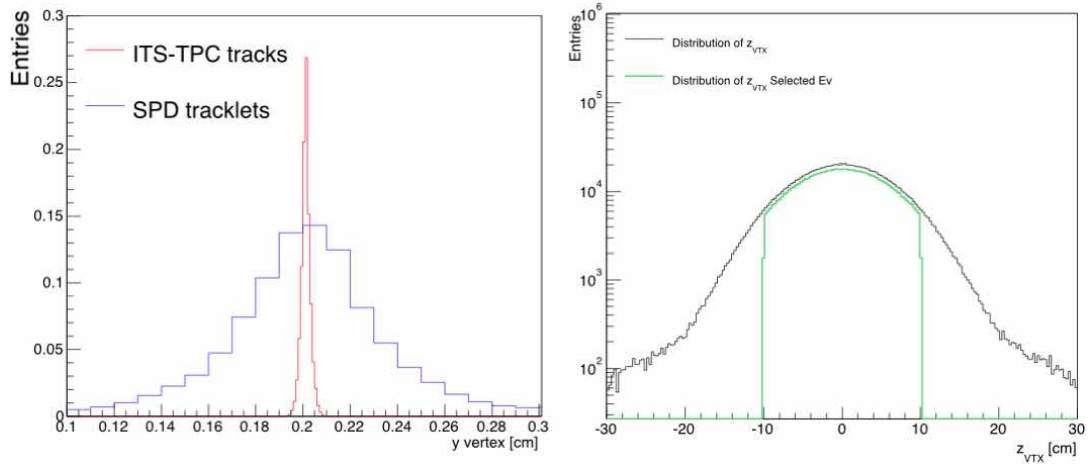


FIGURE 4.5: Left: distribution of the y coordinate of vertices reconstructed with SPD(blue) and global tracks (red). Right: distribution of the z coordinate of vertices reconstructed with global tracks before (black) and after (green) the selection used in this analysis.

Figure 4.5 (left) that shows the distribution of the y position of the reconstructed vertices with SPD and global tracks. This better resolution is crucial in the reconstruction of D^+ -meson, since as we will see in the next section, the topological selections applied rely on a precise measurement of the primary and secondary vertex position.

Only vertices in a $|z| < 10$ cm window are used in the analysis, this to keep a uniform acceptance on the tracks reconstructed by ITS and TPC in $|\eta| < 0.8$.

Figure 4.5 (right) shows the distribution of the z coordinates for vertices reconstructed with global tracks before and after the event selection. The sharp cut at 10 cm is visible in the distribution of selected events.

The inclusion of the D^+ -meson decay tracks introduces a bias in the calculation of the primary vertex position and covariance matrix. For this reason, in this analysis for each D^+ -meson candidate the primary vertex was recomputed excluding its decay tracks.

In the p -Pb minimum bias data sample used in this analysis the amount of pile-up events still present after the background rejection described in Section 3.2.2 is low, below the per cent level. Events are identified as pile-up and rejected if the SPD vertexer has reconstructed two vertices at a minimum distance of 0.8 cm, the lower multiplicity vertex having at least 5 contributors.

Figure 4.6 (left) shows the percentage of events rejected at the different selection steps mentioned above. The most important contribution comes from the vertex position cut, rejecting $\sim 12\%$ of the events.

4.1.2 Track Selection

The secondary vertices of D meson candidates are reconstructed using ITS-TPC tracks with $|\eta| < 0.8$, $p_T > 0.3$ GeV/c. Selected tracks are required to have been successfully fitted by the Kalman Filter algorithm during the final inward propagation (from outer detectors to inner ones - see Section 3.2.3) both in the ITS and TPC; these conditions in ALICE software framework are called `kITSrefit` and `kTPCrefit`.

Furthermore, selected tracks have at least 70 (out of a maximum of 159) associated clusters in the TPC, and a $\chi^2/ndf < 2$ for the track momentum fit in the TPC.

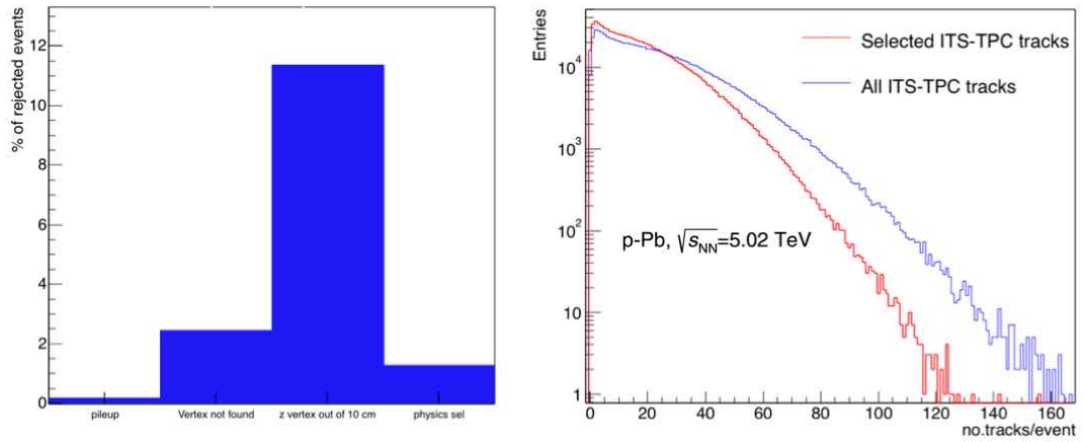


FIGURE 4.6: Left: fractions of events rejected during vertex and physics selection. Right: distribution of tracks per event before (blue) and after (red) the single track selections, for events passing the selections described in Section 4.1.1.

Tracks are also required to have at least one associated cluster in the SPD layers. This condition improves the impact parameter resolution of the daughter tracks and of the secondary vertex, since it ensures a spatial measurement as close as possible to the primary and secondary decay vertices.

Figure 4.6 (right) shows the distribution of number of the ITS-TPC tracks per selected event before and after the track selection cuts. After track selections on average ~ 18 tracks per selected event are kept for further analysis.

The black histogram in Figure 4.7 shows the invariant mass distribution for D^+ and D^- candidates in the p_T bin $2 < p_T^{D^+} < 3$ GeV/c obtained after applying the event and track selection cuts discussed so far. No peak is visible in the D^+ mass region. In fact, a number of selections has to be performed on D^+ -meson candidates to sufficiently reduce the background and make the signal peak emerge, as in the red histogram of the same figure, also corresponding to D^+ and D^- candidates in the p_T bin $2 < p_T^{D^+} < 3$ GeV/c. These selections will be discussed in the following paragraphs.

4.1.3 Kinematical and topological selection

In this section we will describe all selections that are performed at the level of D^+ candidate, based on the kinematical and topological characteristics of the reconstructed decay. This selections exploit the different distribution of topological and kinematic variables for signal and background candidates.

Figure 4.8 (left) shows the y -differential fraction of D^+ that have all daughters in $|\eta| < 0.8$, obtained from the same MC simulations that will be described in detail in Section 4.2. One can see that low p_T D^+ mesons have a lower acceptance, since decay tracks have a larger dispersion around the D^+ meson flight direction. The acceptance further decreases towards higher absolute values of D^+ meson rapidity ($|y| > 0.5$), where the D^+ meson flight line approaches the borders of the tracking region. D^+ -meson candidates kept for the analysis have a p_T dependent fiducial cut on their rapidity values. The cut values ranges from $|y| < 0.5$ at low p_T ($1 < p_T < 2$) to $|y| < 0.8$ above 4 GeV/c and is visualized by the red lines in the right panel of Figure 4.8.

Figure 4.9 (left) shows the distributions (normalized to their area) of transverse momentum of kaons coming from D^+ meson decays from MC simulations for three different

intervals of D^+ mesons p_T . One observes that at higher p_T of the parent D^+ the distribution becomes harder and peaks at higher values of kaon p_T . The right panel of Figure 4.9 shows the same p_T distributions (normalized to their area) for signal and background candidates for D^+ with $5 < p_T < 6$ GeV/c from MC simulations. The background distribution is softer, so that a lower cut on the kaon transverse momentum can help excluding a significant fraction of background keeping most of the signal candidates.

The situation for the pion transverse momentum distributions is similar if one considers the pion emitted with the highest momentum, which distribution is shown in Figure 4.10 (left). When looking at the pion emitted with lowest momentum, the distribution is softer and more similar to the background distribution (Figure 4.10 - left).

Figure 4.11 (left) shows the distributions (normalized to their area) of the decay length, measured as the 3D distance of the primary and secondary vertices, for three different prompt D^+ meson p_T intervals. The decay length in the different p_T intervals is governed by the mean proper decay length and by the Lorentz boost: $\gamma * c\tau$. In the case shown here, $\gamma \sim 1.4$ for $1 < p_T < 2$, $\gamma \sim 3$ for $5 < p_T < 6$, $\gamma \sim 6$ for $8 < p_T < 12$. The comparison with the decay length distributions of background D^+ meson candidates, shown in the right panel of Figure 4.11, shows that a cut on the decay length can be useful to reject a significant amount of background. However this cut has to be handled carefully if the purpose is to select prompt D^+ mesons, since the distribution of feed-down candidates extends to even larger decay lengths, as seen in the left panel of Figure 4.12. In fact in the feed-down case the total distance between the primary and secondary vertices of the D^+ mesons includes also the B-meson decay length, which is typically of the order of several hundreds of μm ($B^+ c\tau=491 \mu\text{m}$, $B^0 c\tau=457 \mu\text{m}$).

As seen in Table 3.1, the spatial resolution on the ITS points is higher in the $r\phi$ direction than in the z direction. This results in a better resolution on the vertex position in the transverse plane. Thus a better resolution is achieved for the decay length projection on xy plane with respect to the decay length in 3D. The decay length in the transverse plane divided by its uncertainty, obtained from the secondary vertex covariance matrix,

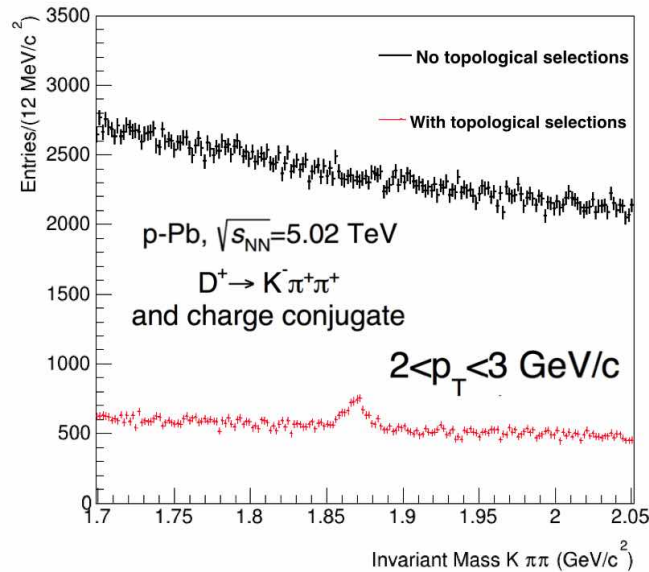


FIGURE 4.7: Invariant mass spectrum of D^+ candidates before and after applying topological selections.

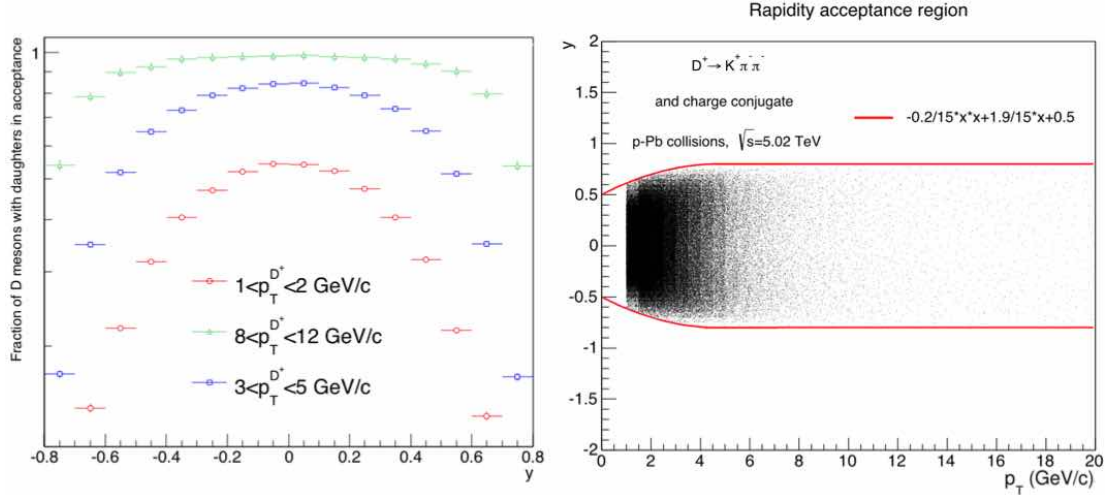


FIGURE 4.8: Left: fraction of D^+ mesons with daughters in $|\eta| < 0.8$ and $p_T > 0.1$ acceptance region vs D^+ meson rapidity. Right: p_T dependent y fiducial cut.

is therefore used in the selection of D^+ signal candidates

$$L_{xy} = \frac{DecayLength_{xy}}{\Delta_{DecayLength_{xy}}} \quad (4.4)$$

The distribution of this variable for prompt D^+ mesons and background is shown in Figure 4.12 (right) for candidates in $2 < p_T < 5$ GeV/c. The background distribution shows a peak at $L_{xy} = 1 \div 2$, and a negligible part of the distribution is found at L_{xy} values higher than 5. On the contrary signal candidates distribution are characterized by higher values of L_{xy} . This is due to the fact that signal candidates truly coming from a secondary vertex have on average a smaller error on vertex position, which combined with the different decay length distribution of prompt and background D^+ mesons shown in Figure 4.11 results in these distributions.

A selection on the quality of the D^+ decay vertex was also applied looking at the daughter

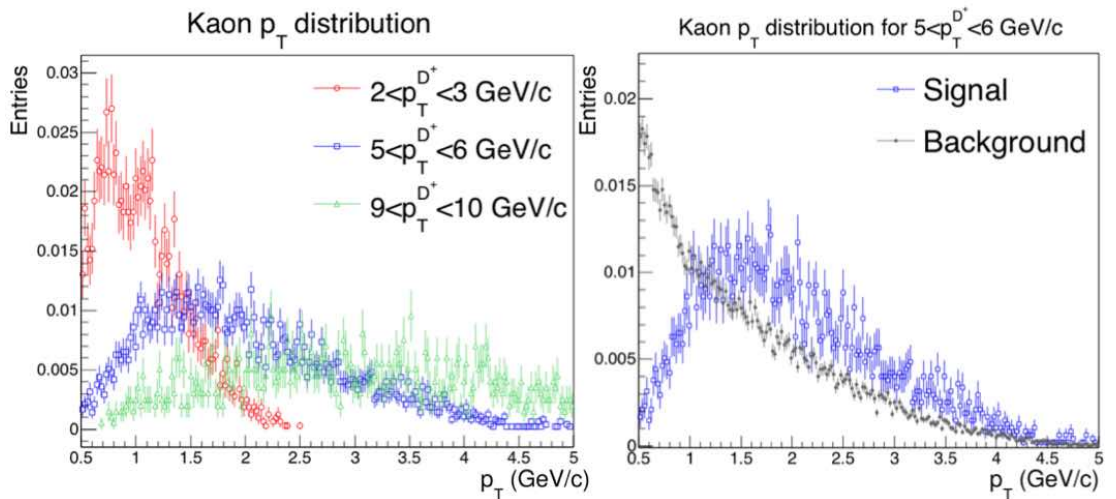


FIGURE 4.9: Distributions of the decay kaon transverse momentum

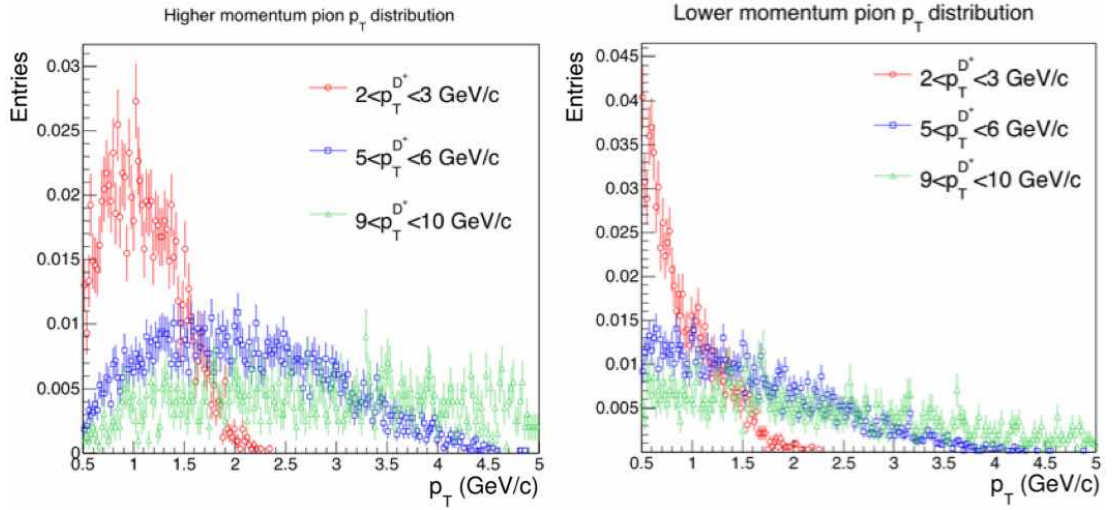
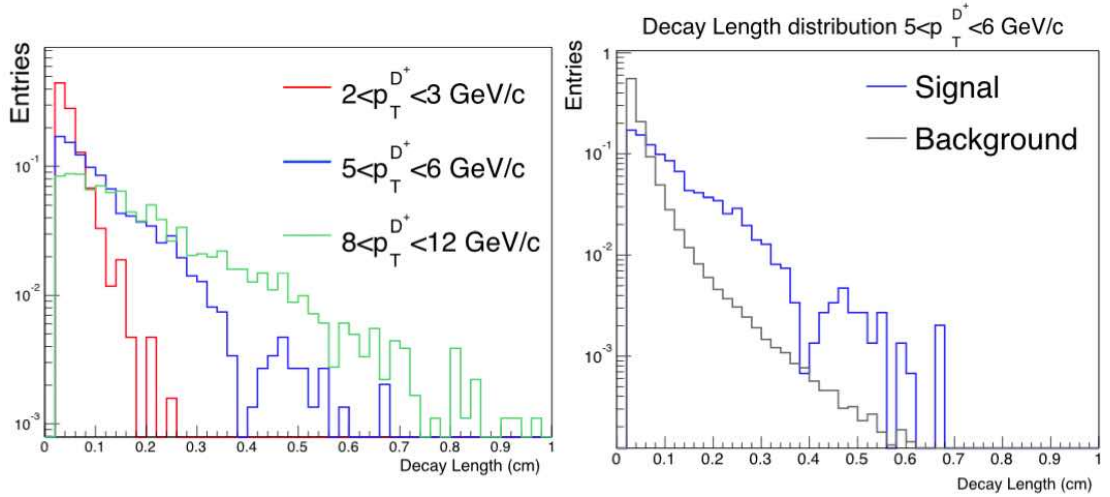


FIGURE 4.10: Distributions of the decay pion transverse momentum

FIGURE 4.11: Distributions of the decay length of D^+ mesons.

track dispersion around the secondary decay vertex. The selection variable is defined as

$$\sigma_{\text{vertex}} = \sqrt{d_1^2 + d_2^2 + d_3^2} \quad (4.5)$$

where d_i is the distance of minimal approach between the decay track i and the position of the secondary vertex. For signal candidates, all daughters are coming from the same vertex and this dispersion should be close to 0 with a distribution whose width is determined by the resolution on the track parameters. On the contrary the background, as visible in Figure 4.13, has a broader distribution peaked at larger values. An upper cut on the value of σ_{vertex} is therefore applied.

Finally the cosine of the pointing angle defined at the beginning of this chapter can be used as a selection variable. In fact if the reconstructed secondary vertex does not correspond to a real D^+ meson, the directions of the reconstructed D^+ momentum and of its flight line will be less correlated and the cosine of the pointing angle will deviate from unity. The distributions for signal and background D^+ -meson candidates (normalized to their area) are shown in Figure 4.13 (right). The lower panel shows the distributions

of the cosine of the pointing angle in the transverse plane for signal and background. Thanks to the better resolution on the vertex coordinates in the transverse plane, the signal peak is narrower (the entries are more concentrated close to $\cos\theta_{\text{pointing}}^{xy}=1$). For the xy component, however, the background distribution is also more peaked at 1. For this reason a lower cut is applied on both $\cos\theta_{\text{pointing}}$ and $\cos\theta_{\text{pointing}}^{xy}$ with the aim of optimizing the amount of background candidates rejected and the amount of signal kept.

Convenient values of cut variables result in invariant mass spectra that clearly reveal the D^+ meson peak around its PDG mass value of $1.869 \text{ GeV}/c^2$. To extract the convenient values of the cut variables a cut optimization strategy has been adopted. This strategy, performed separately for different p_T regions, can be better explained with the help of Figure 4.14 which represent a 3 dimensional array of cut values (cells), each dimension corresponding to a different variable, in this case the kaon p_T , the cosine of the pointing angle and the decay length. Each element of this array is characterized by three cut values, one for each quantity, and has a corresponding invariant mass histogram filled with the candidates passing the selection cuts of the considered cell.

In the case of Figure 4.14, we focus on two particular cells, one with looser selections (red) and one with tighter selections (blue). Once all candidates in the data sample have been analyzed, a fit is performed on each cell:

- an exponential function is used to fit the invariant mass region on the two sides of the peak. The output of this fit is the red function in Figure 4.16
- the total distribution is then fitted with the sum of an exponential and a gaussian. The exponential is initialized using the parameters obtained in the previous step and the gaussian is initially centred on the D^+ mass value from PDG
- the D^+ meson signal is then extracted as the integral of the fitted gaussian

The signal yields are shown for each of the two invariant mass distributions of Figure 4.14 together with their statistical error. The significance, defined as $\frac{S}{\sqrt{S+B}}$ is also shown. A significance higher than 5 indicates that the probability for the peak being a fluctuation of the exponential background is lower than $2.87 \times 10^{-7}\%$.

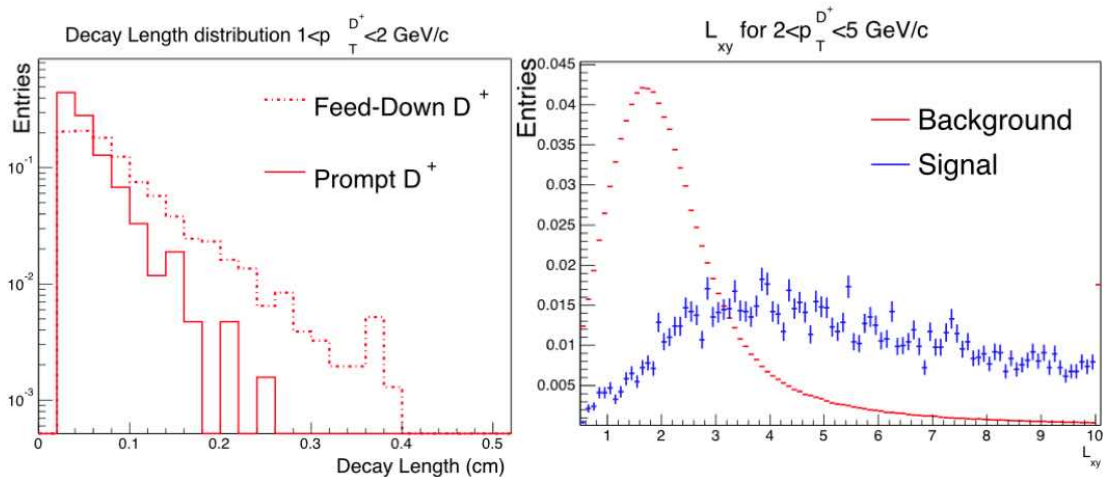


FIGURE 4.12: Left: Distributions of the decay length of prompt and feed-down D^+ mesons. Right: Distributions of the L_{xy} variable.

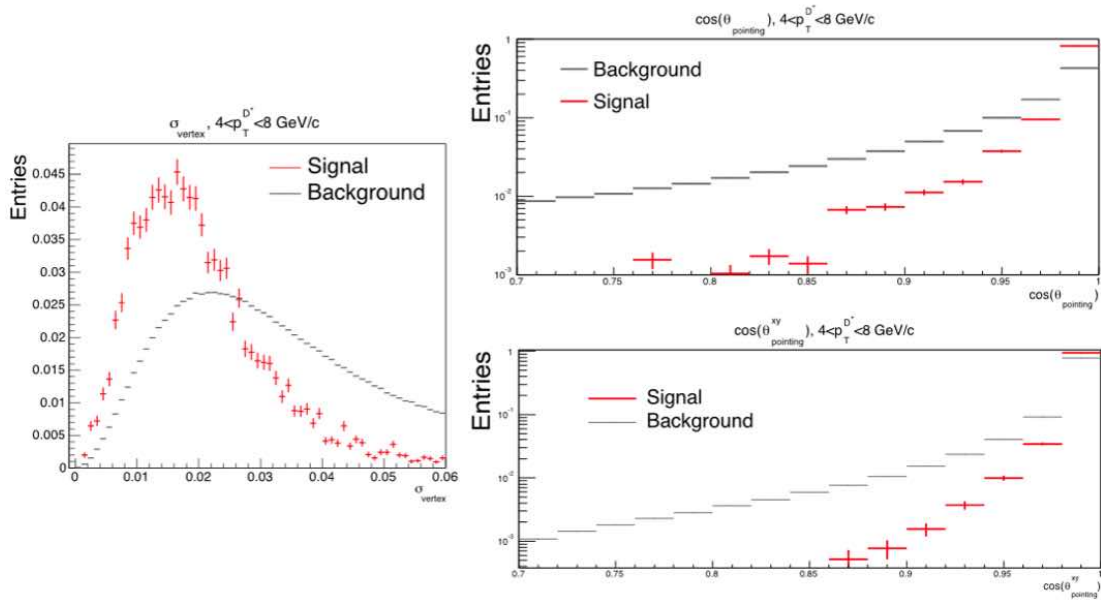


FIGURE 4.13: Left: Distributions of σ_{vertex} . Right: Distributions relative to the cosine of the pointing angle (top) and its projection on the transverse plane (bottom).

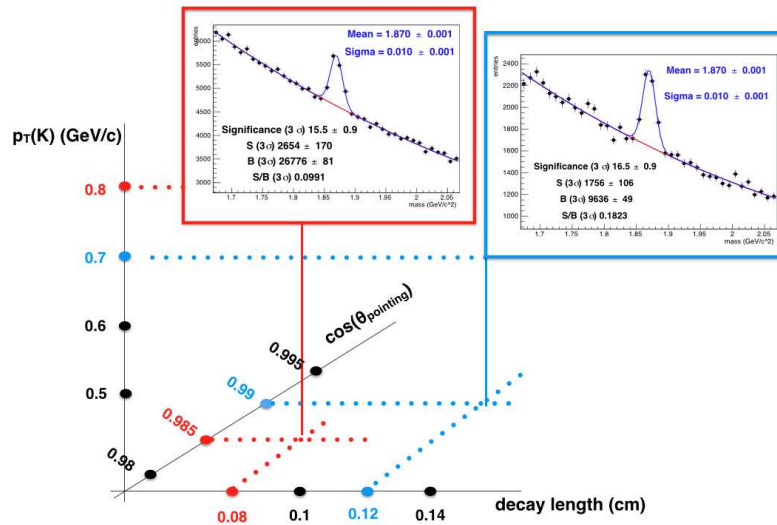


FIGURE 4.14: Schematization of the cut optimization procedure

As an example Figure 4.15 shows the values of significance extracted from the fit described above as a function of two cut variables, namely the decay length and the cosine of the pointing angle, for $8 < p_T^{D^+} < 12$ GeV/c. All other cut variables are fixed in this example. The significance shows maximum values for intermediate decay length cut values, while the highest significance values in the plot are found for the tightest cut value on pointing angle. However the choice of the central cut values has to be performed considering

- the stability of the fit parameters (mean, sigma of the gaussian)
- the amount of signal and its statistical error

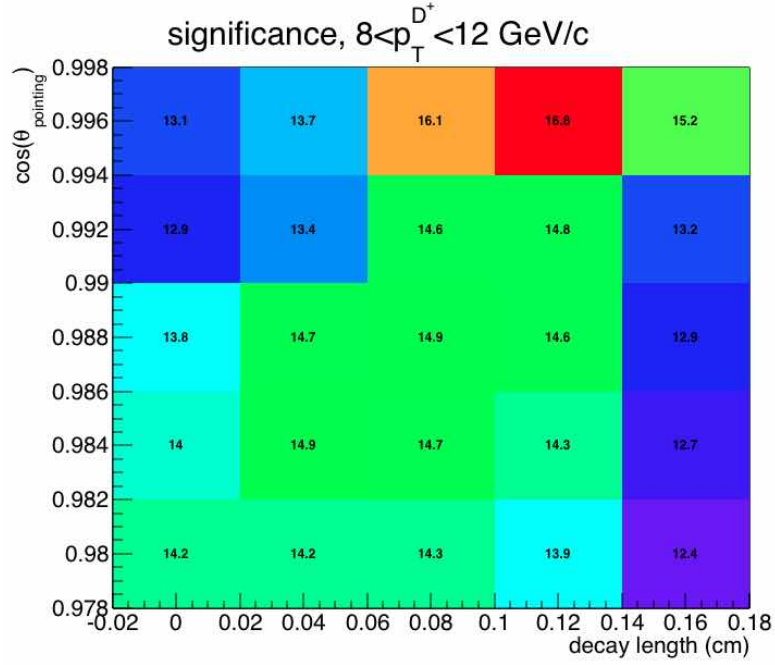


FIGURE 4.15: Significance extracted from the fit described above as a function of decay length and the cosine of the pointing angle, for $8 < p_T^{D^+} < 12$ GeV/c. All other cut variables are fixed in this example.

- the fraction of prompt D^+ mesons that is being selected. As an example, the tighter the cuts on decay length, the higher the fraction of D^+ mesons from B-hadron decays that is being selected

The procedure described is a simplification of what is done, since the cut variables used are 7 and so a 7 dimensional array is used. Note that using e.g. 5 intervals for each variables results in 80k cells, which is not an easily manageable number in terms of computing costs. It is thus more convenient to start with a limited number of variables, identify a convenient working point for their cut values, and further optimize the rest of them.

The results of the cut optimization performed on the minimum bias data p-Pb sample are shown in Table 4.2, and will be used as topological cut values in next section. They allow to extract the invariant mass spectrum of 4.16. The fit described above is applied to extract signal, significance, signal over background ratio. The mean and width of the fitted gaussian are also shown. The mean value is compatible with the D^+ meson PDG

p_T (GeV/c)	[1,2]	[2,8]	[8,9]	[9,10]	[10,11]	[11,12]	[12,14]	[14,16]	[16,24]
$ \Delta M_{D^+} $ (GeV/c ²)	0.2	0.2	0.2	0.2	0.2	0.2	0.2	0.2	0.2
σ_{vertex} (cm)	0.03	0.03	0.035	0.035	0.035	0.07	0.07	0.09	0.03
p_T^K (GeV/c)	0.2	0.2	0.2	0.2	0.2	0.2	0.2	0.2	0.2
p_T^π (GeV/c)	0.2	0.35	0.35	0.35	0.35	0.35	0.35	0.35	0.35
Decay Length (cm)	0.02	0.04	0.04	0.04	0.04	0.04	0.1	0.1	0.15
L_{xy}	9	8	8	8	8	6	6	9	5
$\cos(\theta_{pointing})$	0.99	0.99	0.99	0.99	0.99	0.99	0.99	0.99	0.99
$\cos(\theta_{pointing,xy})$	0.995	0.99	0.99	0.99	0.99	0.99	0.99	0.99	0.99

TABLE 4.2: Summary table of the D^+ analysis cuts optimized for the minimum bias p-Pb data sample.

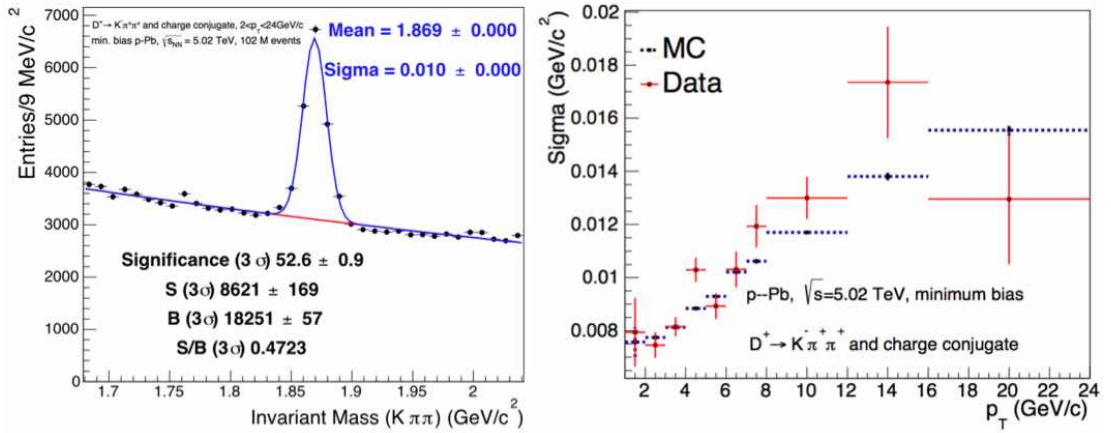


FIGURE 4.16: Left: invariant mass distribution for D^+ mesons candidates in the p_T range $1 < p_T < 24$ GeV/c extracted from minimum-bias p -Pb collisions. The fit function is superimposed. Right: width of the gaussian of the D^+ peak as a function of p_T for minimum-bias p -Pb collisions and from the MC data sample that is described in next Section.

mass value. The width of the peak is a detector resolution effect and depends on p_T . In fact, looking at Equation 4.2, we see that the invariant mass of the D^+ meson candidates depends on the measured momenta of the three daughters. Looking at Figure 3.10, we deduce that the higher the D^+ meson p_T , the harder are its daughter, and the worse the resolution on momenta will be, yielding a constant broadening of the gaussian sigma going at high p_T . The gaussian sigma from the fits applied in different p_T bins are shown in the right panel of Figure 4.16 as a function of p_T . The gaussian sigma values expected from MC simulations are superimposed. Some discrepancies are present, and they will be taken into account in the evaluation of the systematic error as will be discussed in next Chapter.

4.1.4 Particle Identification

Further background rejection is achieved using PID on the decay tracks. The rejection is based on the identification of triplets of tracks in which:

- $D^+ \rightarrow K^- \pi^+ \pi^+$: the negative track is compatible with the kaon hypothesis, the two positive tracks are compatible with the pion hypothesis
- $D^- \rightarrow K^+ \pi^- \pi^-$: the positive track is compatible with the kaon hypothesis, the two negative tracks are compatible with the pion hypothesis

As explained in Sec. 3.2.4, this PID selection is performed using the time of flight of the particles and their energy loss in the TPC.

Each particle has its own resolution σ on both time of flight and energy loss measurements, which depends on the track momentum. To each track in the triplet, four values $n\sigma_{\pi}^{\text{TOF}}$, $n\sigma_K^{\text{TOF}}$, $n\sigma_{\pi}^{\text{TPC}}$, $n\sigma_K^{\text{TPC}}$ are computed

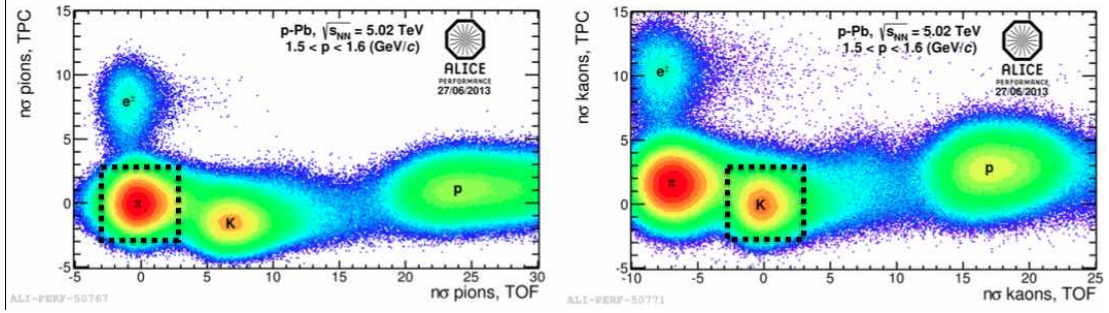


FIGURE 4.17: Left: $n\sigma_{\pi}^{\text{TOF}}$ vs $n\sigma_{\pi}^{\text{TPC}}$. Right: $n\sigma_K^{\text{TOF}}$ vs $n\sigma_K^{\text{TPC}}$

- $n\sigma_{\pi}^{\text{TOF}}$: the number of sigmas the track time of flight deviates from the pion expected time of flight
- $n\sigma_K^{\text{TOF}}$: the number of sigmas the track time of flight deviates from the kaon expected time of flight
- $n\sigma_{\pi}^{\text{TPC}}$: the number of sigmas the track dE/dx deviates from the pion expected value
- $n\sigma_K^{\text{TPC}}$: the number of sigmas the track dE/dx deviates from the kaon expected value

Figure 4.17 shows the distribution of $n\sigma_{\pi}^{\text{TOF}}$ as a function of $n\sigma_{\pi}^{\text{TPC}}$ (left) and of $n\sigma_K^{\text{TOF}}$ as a function of $n\sigma_K^{\text{TPC}}$ (right). In the left (right) panel, the dense region around (0,0) contains tracks whose signal is close to the one expected for pions (kaons) in both TPC and TOF, and are thus very likely to be real pions (kaons). Other dense regions are visible in the distribution, and they are populated by kaons (pions), protons and electrons. From this plot it is clear that a convenient cut on the number of σ for the selected tracks can help in rejecting the background.

The dE/dx and time of flight of each track are compared to their expected values in the π and K hypothesis giving a PID response. Three different cases relative to different $n\sigma$ intervals in both TPC and TOF are defined in Table 4.3

- IDENTIFIED as π , K in case of positive identification of the tracks
- COMPATIBLE with the π , K hypothesis
- REJECTED, in this case the tracks is very likely not to be a π or a K

TPC	$p_T < 0.6$ GeV/c	$0.6 < p_T < 0.8$ GeV/c	$p_T > 0.8$ GeV/c
$n\sigma < 1$	IDENTIFIED as π/K		COMPATIBLE with π/K
$1 < n\sigma_{\text{TPC}} < 2$	IDENTIFIED as π/K	COMPATIBLE with π/K	
$2 < n\sigma_{\text{TPC}} < 3$	COMPATIBLE with π/K		
$n\sigma > 3$	REJECTED		

TOF	$p_T < 1.5$ GeV/c	$p_T > 1.5$ GeV/c
$n\sigma_{\text{TOF}} < 3$	IDENTIFIED as π/K	COMPATIBLE with π/K
$n\sigma_{\text{TOF}} > 3$	REJECTED	

TABLE 4.3: PID selection regions

For instance all tracks outside the black dashed square in the left (right) panel of Figure 4.17 are rejected as pions (kaons), while all the tracks inside the box are compatible or positively identified as pions (kaons).

The information from the two detectors is collected for all three daughters in the triplet and combined to finally decide if the candidate has to be kept or rejected. In the analyses that will be presented in the next chapters, two slightly different approaches have been used. The STANDARD PID, used for candidates with $p_T > 2\text{GeV}/c$

- no track in the triplet has to be positively identified as proton while being rejected as k/π by either TOF or TPC
- the number of tracks positively identified as kaon by either TPC or TOF and rejected as pion by either TPC or TOF does not have to exceed one
- the number of tracks rejected as kaon by either TPC or TOF does not have to exceed two
- the two tracks having the same charge sign as the $D^{+/-}$ mother have to be at least compatible with the pion hypothesis in both TPC and TOF
- the track having the opposite charge sign with respect to the $D^{+/-}$ mother has to be at least compatible with the kaon hypothesis in both TPC and TOF

For $p_T < 2\text{GeV}/c$ stronger requirements are adopted (STRONG PID)

- the first three points of the STANDARD PID are unmodified
- the two tracks having the same charge sign as the $D^{+/-}$ have to be positively identified as pions by either TPC or TOF
- the track having the opposite charge sign with respect to the $D^{+/-}$ mother has to be identified as kaon by either TPC or TOF

The signal selection efficiency and background rejection power of these PID techniques have been evaluated via MC simulations and are shown in Figure 4.18 (left). The STRONG PID, which is applied in the bin $1 < p_T < 2\text{ GeV}/c$, has a lower signal selection efficiency compared STANDARD PID which is applied elsewhere. However it turns out to have a higher ($\sim 20\%$) background rejection power⁴.

The right panel of Figure 4.18 shows the fit to the D^+ invariant mass distribution obtained applying topological cuts only (top) and topological cuts plus STANDARD PID (bottom) in the p_T bin $4 < p_T < 5\text{ GeV}/c$. An increase of significance with a minor signal loss is achieved with the PID selections.

4.2 Monte Carlo simulations of $D^{+/-}$ mesons in ALICE

Reliable MC simulations are needed to extract the efficiency and acceptance values used to correct the raw yields measured in the various data samples collected with the ALICE

⁴Defined as the number of background candidates that pass the PID selection

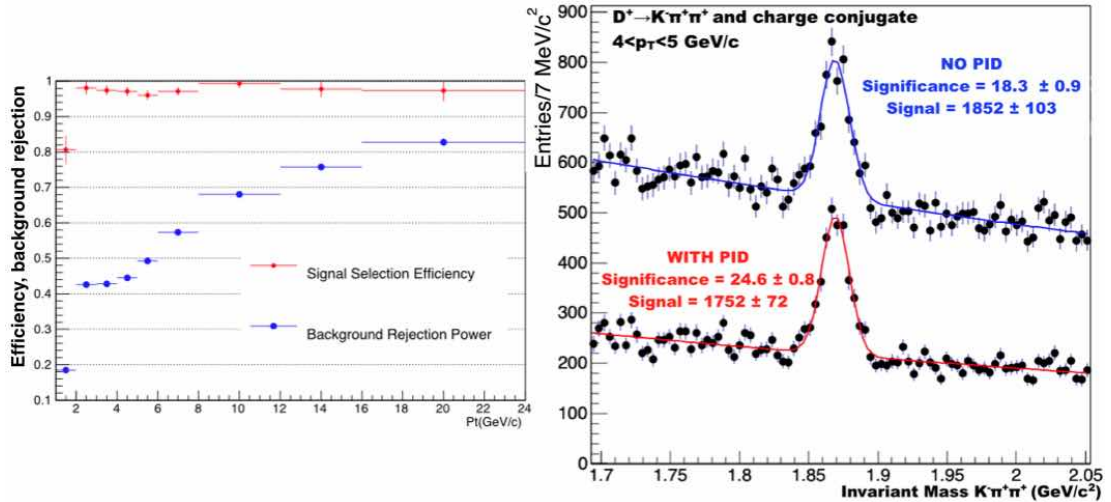


FIGURE 4.18: Left: PID signal efficiency and background rejection power as a function of p_T . STRONG PID is applied in the bin $1 < p_T < 2$ GeV/c, STANDARD PID for $p_T > 2$ GeV/c. Right: D^+ mesons invariant mass distributions with and without the use of STANDARD PID.

detector. In particular it is crucial to have a precise description of the detector conditions and of track parameter resolution, as well as of the PID performance, since they affect several parameters used in the analysis, e.g. the width of the $D^{+/-}$ peak and the distributions of the selection variables.

4.2.1 Monte Carlo data sample

The HIJING (Heavy Ion Jet INteraction Generator) Monte Carlo generator [125] has achieved a very good quantitative understanding of high-energy heavy ion interactions. However, in order to have acceptable values of the statistical uncertainties on D^+ -meson efficiencies keeping low computation costs, a charm enriched MC data sample was generated.

The MC sample was constructed starting from ~ 90 M pp events generated with PYTHIA v6.4.21, each of which had to satisfy one of the following conditions with the same probability (25 % each):

- an event which contains a $c\bar{c}$ pair with at least one of the quarks having $|y| < 1.5$. D mesons from the hadronization of c -quarks are forced to decay in the hadronic channels of Table 4.1
- an event which contains a $b\bar{b}$ pair with at least one of the quarks having $|y| < 1.5$. In this case, D mesons that are produced by the decay of a B meson are forced to decay in one of the hadronic channels of Table 4.1
- an event with at least one $c\bar{c}$ and one heavy-flavour decay electron with $y < 1.2$;
- an event with at least one $b\bar{b}$ pair and one heavy-flavour decay electron with $y < 1.2$.

For each event, a number of binary nucleon-nucleon collisions N_{coll} is extracted from a distribution obtained starting from a Glauber MC simulation of p -Pb collisions. If

the extracted number of binary collisions is larger than 1, a HIJING p -Pb event is added as underlying event to the PYTHIA pp collision. The underlying event makes the multiplicity distribution in the MC more realistic, which is crucial since the resolution on vertex position depends on multiplicity as shown in Figure 3.11. The simulations used the GEANT3 particle transport package together with a detailed description of the geometry of the apparatus and of the detector response to reconstruct the generated particles. The simulation was configured to reproduce the conditions of the luminous region and of all of the ALICE subsystems, in terms of active electronic channels, calibration level, and their time evolution within the 2013 p -Pb data taking period.

4.2.2 Acceptance and efficiency computation

The calculation of the acceptance and efficiency correction is based on the Correction Framework included in the ALICE analysis software. The Correction Framework includes classes that allow one to store in a container the number of candidates at specific stages (steps) of the generation, reconstruction or selection procedure on an N-dimensional grid (called “CF container” from now on). The containers can be filled in for prompt $D^{+/-}$ mesons only, feed-down $D^{+/-}$ only or both of them, and stores, for each D^+ -meson, the p_T , y , φ values as well as the vertex position and the multiplicity of the event. The steps used to store the candidates are:

- *kStepGenerated*: at this stage the Correction Framework container is filled with the generated $D^{+/-}$ particles, for collisions with $|z_{\text{vertex}}| < 10$ cm.
- *kStepGeneratedLimAcc*: at this stage the $D^{+/-}$ mesons generated in the rapidity range $|y| < 0.5$ are counted and stored in the CF container, for collisions with $|z_{\text{vertex}}| < 10$ cm.
- *kStepAcceptance*: at this step the CF container is filled for the $D^{+/-}$ mesons for which the 3 daughters in the final state fulfill the acceptance conditions $|\eta| < 0.9$ and $p_T > 0.1$ GeV/c of the ALICE central barrel, for collisions with $|z_{\text{vertex}}| < 10$ cm.

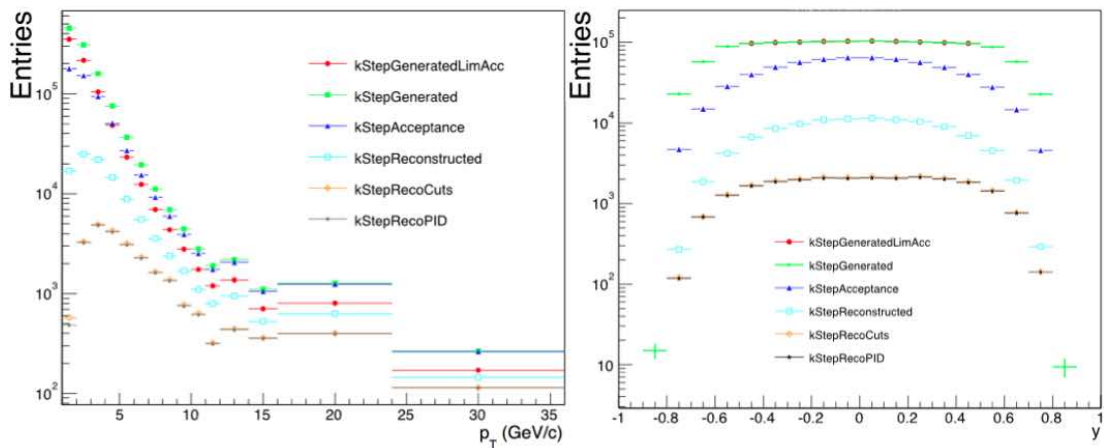


FIGURE 4.19: Left: p_T distribution of prompt $D^{+/-}$ mesons at the different step of selections defined in the CF Container. Right: rapidity distribution of prompt $D^{+/-}$ mesons at the different step of selections defined in the CF Container.

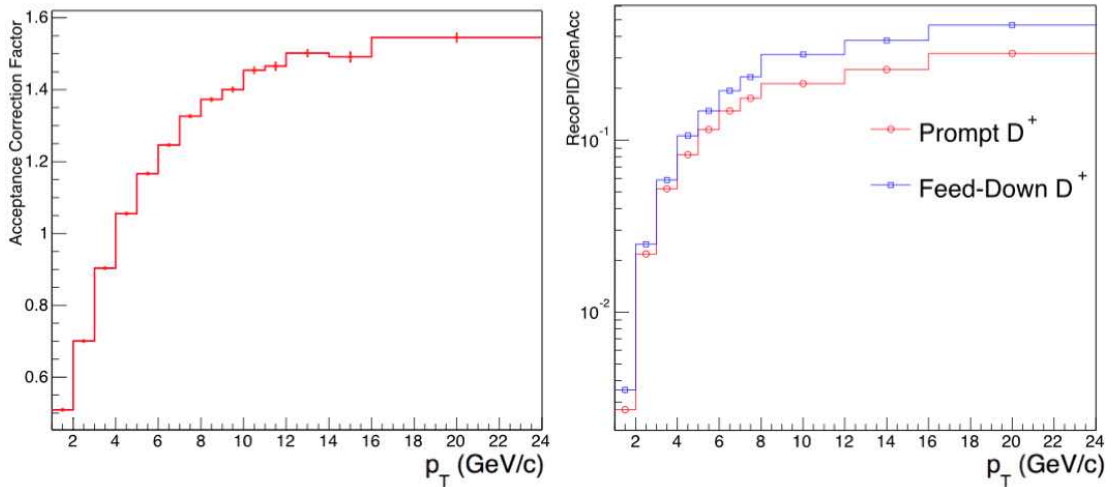


FIGURE 4.20: Left: Acceptance correction factor for prompt D^+ mesons. Right: efficiencies for prompt D^+ mesons and for D^+ coming from beauty decays for the selection cuts used for the p -Pb analysis.

- *kStepReconstructed*: the CF container is filled with reconstructed $D^{+/-}$ mesons that pass minimal cuts (called filtering cuts) on decay track quality
- *kStepRecoCuts*: at this stage the $D^{+/-}$ mesons that pass the kinematical and topological cuts used in the analysis are stored in the CF container.
- *kStepRecoPID*: in this final step, also the Particle Identification selection is applied and the $D^{+/-}$ passing also these cuts, on top of the topological ones applied in the previous RecCuts step are used to fill the CF container.

Figure 4.19 shows the p_T and rapidity distributions of prompt $D^{+/-}$ mesons at the steps listed above. It should be noted that in the plot as a function of rapidity the *kStepGenerated* and the *kStepGeneratedLimAcc* distribution coincide for $|y| < 0.5$.

The efficiencies can then be computed as a function of the variables stored in the grid for each $D^{+/-}$ and at the various selection steps by performing the ratios of the contents of the CF container. The CF container structure also allows the possibility to reweight the efficiencies as a function of different variables, e.g. of p_T or multiplicity. The weighting is used to get more realistic distributions in the MC, and will be used in next Chapter.

The acceptance correction factor is obtained as the ratio of the *kStepAcceptance* and *kStepGeneratedLimAcc* containers, and it is shown as a function of p_T in Figure 4.20 (left).

The efficiency correction factor is obtained as the ratio of the *kStepRecoPID* and *kStepAcceptance* containers. The right panel of Figure 4.20 shows the efficiencies for prompt D^+ mesons and for D^+ coming from beauty decays for the selection cuts used for the p -Pb analysis. The observed higher efficiency for the secondary D mesons is due to the fact that the D mesons coming from B feed-down are more displaced from the primary vertex and they are therefore preferentially selected by the cuts based on track/vertex displacement.

Chapter 5

Prompt D^+ -meson production in p–Pb collisions

As shown in Figure 2.20, the D-meson nuclear modification factor R_{AA} measured by the ALICE Collaboration in central Pb–Pb collisions at $\sqrt{s_{NN}} = 2.76$ TeV indicates a strong modification of the D-meson spectrum for $p_T > 2$ GeV/c with respect to the spectrum in pp collisions at the same centre-of-mass energy scaled by the average number of nucleon-nucleon collisions $\langle N_{coll} \rangle$. The suppression is interpreted as c -quark in-medium energy loss due to the presence of QGP in the final state. In semi-central Pb–Pb collisions the ALICE Collaboration also observed a positive v_2 of D mesons with $2 < p_T < 6$ GeV/c as shown in Figure 2.22, which can be interpreted as due to the interaction of c -quarks with the medium constituents, which transfer to the c -quark the anisotropy of the expanding medium and may lead to partial thermalization of c -quark.

However a complete understanding of the D-meson results in Pb–Pb collisions requires an understanding of cold nuclear matter effects in the initial and final state, which can be accessed by studying p–Pb collisions assuming that the QGP is not formed in these interactions.

As discussed in Section 2.2.1, in the initial state of the collisions several effects can influence heavy flavour production:

- the nuclear environment affects the quark and gluon PDFs, which are modified in bound nucleons with respect to free nucleons. The modification depends on the parton fractional momentum x and on the atomic mass number A . Models including parton saturation as modelled in the Color Glass Condensate theory [75] or EPS09 parametrization of the nuclear PDFs [76] are able to reproduce ALICE data of charged hadron R_{pPb} , as shown in Figure 2.15
- partons experience transverse momentum broadening due to multiple soft collisions prior to the hard scattering. This leads to an R_{pPb} higher than unity at intermediate p_T . A species dependent Cronin enhancement has been reported in both d–Au (Figure 2.16 - left) and p–Pb (Figure 2.16 - right) collisions
- partons can also lose energy in the initial stages of the collision via radiation in cold nuclear matter. In particular this modifies the effective centre-of-mass energy of the partonic system undergoing the hard scattering. Models including this effect reasonably reproduce J/Ψ production in p–Pb collisions at $\sqrt{s_{NN}} = 5.02$ TeV, as shown in Figure 2.17

Nevertheless the presence of final-state effects in small collision systems is suggested by recent studies in both d-Au and p-Pb collisions. ALICE Collaboration measured the Ψ' nuclear modification factor in p-Pb collisions at forward and backward rapidities [126], measuring a larger suppression with respect to J/Ψ which is not reproduced by models including only initial state effects such as cold nuclear matter energy loss or nuclear PDFs modification. Similar results were also obtained at RHIC [127]. Also measurements of long-range correlations of charged hadrons in p-Pb collisions have shown unexpected results: as an example, Figure 5.1 (left) shows the two-particle $(\Delta\eta, \Delta\Phi)$ correlation function¹ for p-Pb collisions at $\sqrt{s_{NN}} = 5.02$ TeV with charged particle multiplicity $N_{\text{tracks}} > 110$ [128]. The dominant features of the correlation plot are the correlation peak near $(\Delta\eta, \Delta\Phi) = (0, 0)$ for pairs of particles originating from the same jet and the elongated structure at $\Delta\Phi \approx \pi$ for pairs of particles from back-to-back jets. These two structures have also been observed in pp collisions for a wide range of centre-of-mass energies [130], however in Figure 5.1 a pronounced “ridge”-like structure emerges at $\Delta\Phi \approx 0$ extending up to $|\Delta\eta| = 4$. This additional structure is similar to the one observed by the CMS Collaboration in Pb-Pb collisions at $\sqrt{s_{NN}} = 2.76$ TeV [131]. The presence of this structure in high multiplicity p-Pb collisions was confirmed by the ALICE [132] and ATLAS [133] Collaborations and it is quantitatively predicted in models assuming a collective hydrodynamic expansion of the system [134]. Hydrodynamic calculations also give a natural interpretation to the species dependent Cronin enhancement observed by ALICE and PHENIX Collaborations.

Moreover a description in terms of hydrodynamic flow in small collision systems has been recently proposed for the results on heavy-flavour decay electrons R_{dAu} . Figure 5.1 (right) shows the heavy-flavour decay electron R_{dAu} already reported in Figure 2.17 (left) together with blast-wave calculations [129] (Section 1.4.3) implementing collective radial flow in d-Au collisions. The magnitude of R_{dAu} enhancement expected from the blast-wave calculation is in good agreement with the data.

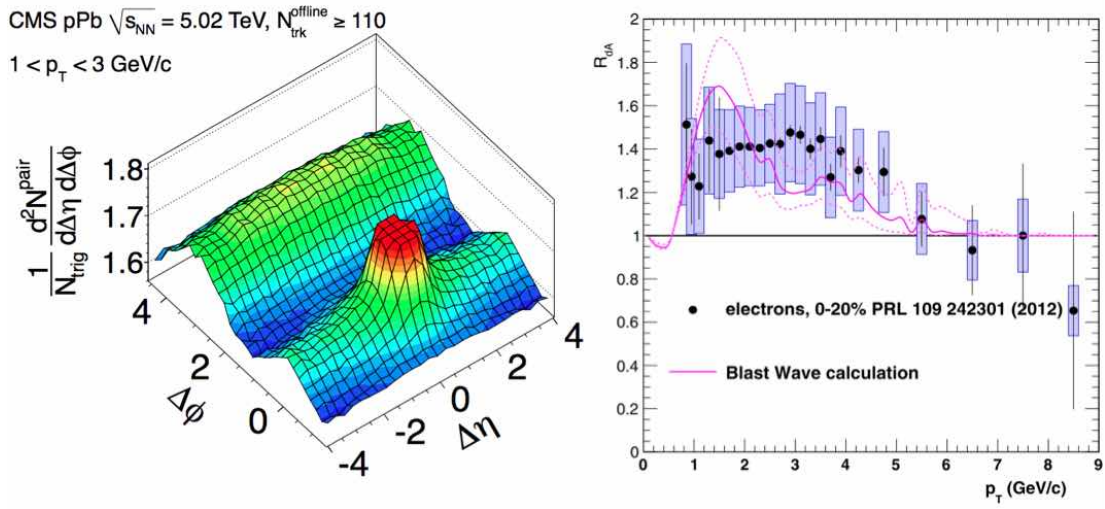


FIGURE 5.1: Left: two-particle correlation function for 5.02 TeV p-Pb collisions with charged particle multiplicity $N_{\text{tracks}} > 110$ [128]. Right: heavy-flavour decay electron R_{dAu} already reported in Figure 2.17 (left) together with blast-wave calculations (Section 1.4.3) implementing collective radial flow in d-Au collisions [129].

¹The analysis is very similar to the one described in Section 1.4.6 (Equation 1.43, Figure 1.18), except for the fact that trigger and associated particles are selected in the same p_T interval $1 < p_T < 3$ GeV/c and that the correlation is not only studied as a function of $\Delta\Phi$, but also of $\Delta\eta$.

All elements cited above suggest that the measurement of D^+ mesons production cross-section and nuclear modification factor R_{pPb} in p-Pb collision can shed light on nuclear matter effects influencing nuclear interactions and, in particular, it can clarify whether the results from Pb-Pb collisions shown in Figure 2.20 are the consequence of genuine hot QCD matter effects.

5.1 Signal Extraction

The analysis was performed using the p-Pb data sample collected in 2013 with a minimum-bias trigger that required the arrival of bunches from both directions and coincident signals in both scintillator arrays of the V0 detector (V0AND - Section 3.2.1). The integrated luminosity collected during the p-Pb beam configuration is shown in Figure 3.7. Events were selected as described in Section 4.1.1. About $110 \cdot 10^6$ events, corresponding to an integrated luminosity $L_{\text{int}} = (48.6 \pm 1.6) \mu\text{b}^{-1}$, passed the selection criteria. The secondary vertices of D^+ meson candidates are reconstructed using ITS-TPC tracks

p_T (GeV/c)	[1,2]	[2,8]	[8,9]	[9,10]	[10,11]	[11,12]	[12,14]	[14,16]	[16,24]
$ \Delta M_{D^+} $ (GeV/ c^2)	0.2	0.2	0.2	0.2	0.2	0.2	0.2	0.2	0.2
σ_{vertex} (cm)	0.03	0.03	0.035	0.035	0.035	0.07	0.07	0.09	0.03
p_T^K (GeV/c)	0.2	0.2	0.2	0.2	0.2	0.2	0.2	0.2	0.2
p_T^π (GeV/c)	0.2	0.35	0.35	0.35	0.35	0.35	0.35	0.35	0.35
Decay Length (cm)	0	0.04	0.04	0.04	0.04	0.04	0.1	0.1	0.15
L_{xy}	9	8	8	8	8	6	6	9	5
$\cos(\theta_{\text{pointing}})$	0.99	0.99	0.99	0.99	0.99	0.99	0.99	0.99	0.99
$\cos(\theta_{\text{pointing},xy})$	0.995	0.99	0.99	0.99	0.99	0.99	0.99	0.99	0.99

TABLE 5.1: Summary table of the D^+ analysis cuts.

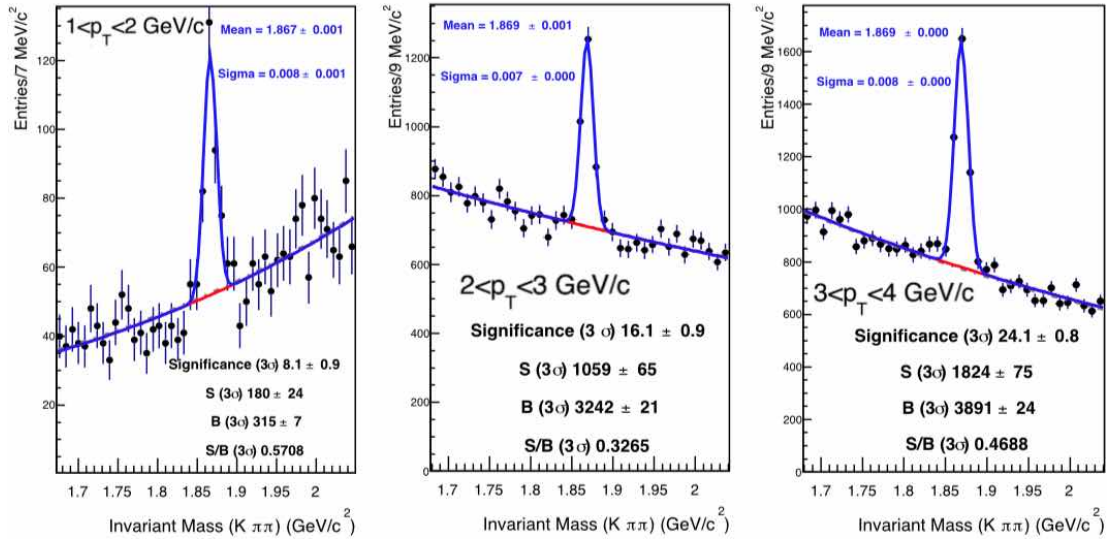


FIGURE 5.2: D^+ candidates (and charge conjugates) invariant mass distributions from minimum bias p-Pb collisions at $\sqrt{s_{NN}} = 5.02$ TeV in the p_T bins [1,2] GeV/c (left), [2,3] GeV/c (centre), [3,4] GeV/c (right).

²Computed as $N_{p-Pb,MB}/\sigma_{p-Pb,MB}$ where $N_{p-Pb,MB}$ is the number of p-Pb collisions passing the minimum-bias trigger condition and $\sigma_{p-Pb,MB} = 2.09 \text{ b} \pm 3.5\%$ (syst) is the cross section of the V0AND trigger.

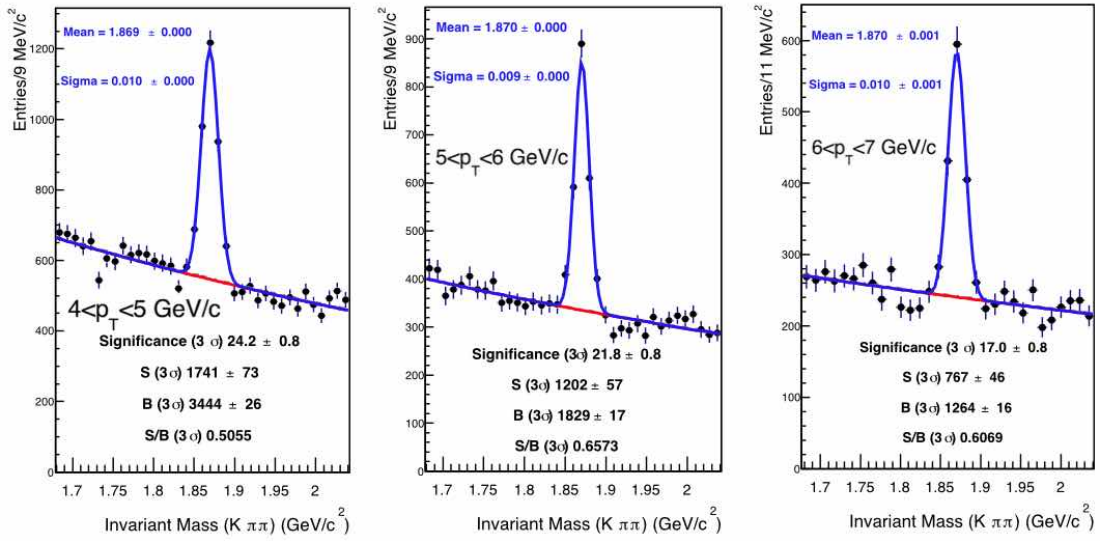


FIGURE 5.3: D^+ candidates (and charge conjugates) invariant mass distributions from minimum bias p -Pb collisions at $\sqrt{s_{NN}} = 5.02$ TeV in the p_T bins [4,5] GeV/c (left), [5,6] GeV/c (centre), [6,7] GeV/c (right).

selected as described in Section 4.1.2. The selection on D^+ -meson candidates rapidity, ranging from $|y_{lab}| < 0.5$ at low p_T ($1 < p_T < 2$) to $|y_{lab}| < 0.8$ above 4 GeV/c, is applied.

The topological cut values, optimized as described in Section 4.1.3, are shown in Table 5.1, where also the p_T bins used in the analysis are defined. The Particle Identification strategy discussed in Section 4.1.4 was applied to further reduce the background: the STANDARD PID selection was used in the p_T range $2 < p_T < 24$ GeV/c, the STRONG PID selection was used in the p_T range $1 < p_T < 2$ GeV/c.

Figures 5.2, 5.3 and 5.4 show the fit to the invariant mass distributions of D^+ meson candidates (and their charge conjugates) obtained after applying the selections described above in the ten p_T intervals used in the analysis. The fitting function is composed of

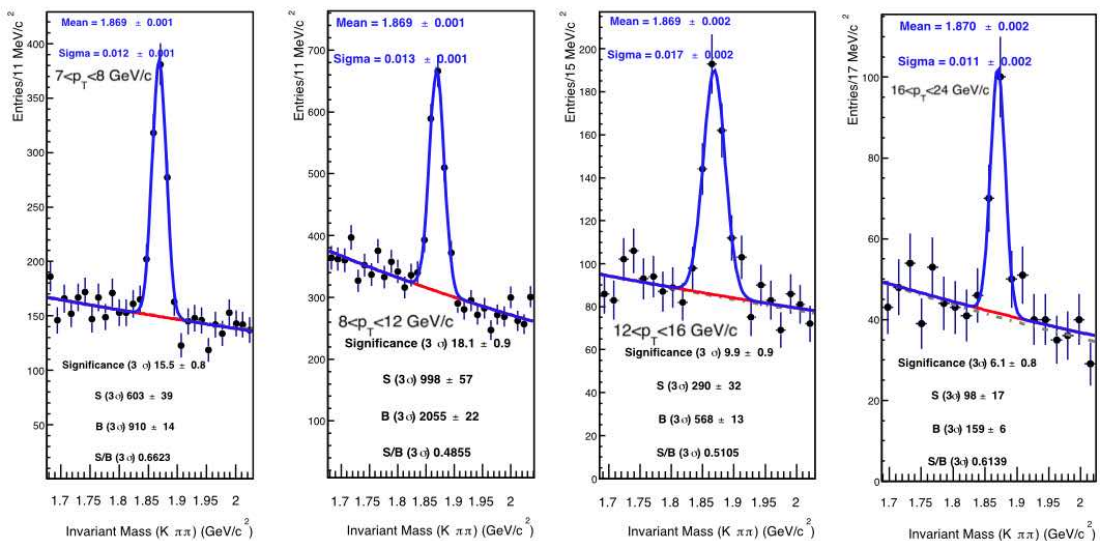
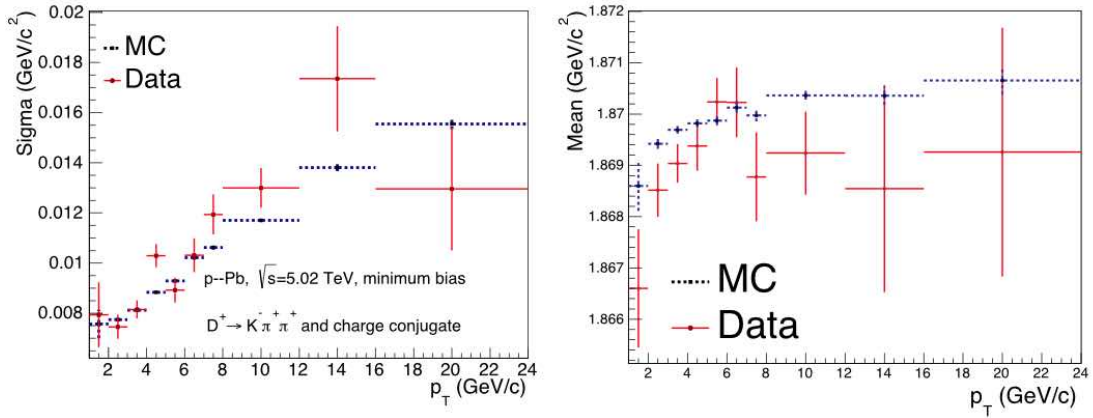


FIGURE 5.4: D^+ candidates (and charge conjugates) invariant mass distributions from minimum bias p -Pb collisions at $\sqrt{s_{NN}} = 5.02$ TeV in the p_T bins [7,8], [8,12], [12,16] and [16,24] GeV/c.

p_T (GeV/c)	D^+		
	Significance (3σ)	Signal/Background (3σ)	Signal
[1,2]	8.1 ± 0.9	0.57	180 ± 24
[2,3]	16.1 ± 0.9	0.33	1059 ± 65
[3,4]	24.8 ± 0.8	0.47	1824 ± 65
[4,5]	24.2 ± 0.8	0.51	1741 ± 73
[5,6]	21.8 ± 0.8	0.66	1202 ± 57
[6,7]	17.0 ± 0.8	0.62	767 ± 46
[7,8]	15.5 ± 0.8	0.66	603 ± 39
[8,12]	18.1 ± 0.9	0.49	998 ± 57
[12,16]	9.9 ± 0.9	0.51	290 ± 32
[16,24]	6.1 ± 0.8	0.61	98 ± 17

TABLE 5.2: Significance, signal-to-background ratios and raw yields for D^+ mesons.FIGURE 5.5: p_T differential peak width (left) and position (right) for D^+ mesons as obtained from the fit to data and to the MC data sample described in Section 4.2.1

an exponential function for the background and a Gaussian function for the signal. The peak position and width for D^+ mesons as obtained from the fit to data and to the MC data sample described in Section 4.2.1 are shown in Figure 5.5. The peak position (right panel of Figure 5.5) extracted from the data in the p_T range 1-24 GeV/c is compatible within two sigmas with the MC value in all p_T bins. It is also compatible within two sigmas with the PDG values of D^+ -meson mass in all p_T bins. The peak position (right panel of Figure 5.5) extracted from the data in the p_T range 1-24 GeV/c is compatible within two sigmas with the MC value in most p_T bins. The peak width (left panel of Figure 5.5) increases with p_T due to the worse resolution on track momentum at high- p_T . A discrepancy of more than 2 sigmas in the peak width between data and MC is present in the p_T bin $4 < p_T < 5$ GeV/c and will be taken into account in the evaluation of systematic errors.

The D^+ mesons raw yields are extracted by integrating the Gaussian fit functions over the whole invariant mass range. Table 5.2 shows the raw yields, signal-to-background ratios and significance values extracted from the fits in Figures 5.2, 5.3 and 5.4.

Applying the same selections described above, the D^+ meson signal yield has also been extracted in five rapidity sub-intervals, namely $-0.8 < y_{lab} < -0.4$, $-0.4 < y_{lab} < -0.1$, $-0.1 < y_{lab} < 0.1$, $0.1 < y_{lab} < 0.4$ and $0.4 < y_{lab} < 0.8$. The signal for each rapidity interval has been extracted in the p_T ranges $2 < p_T < 5$ GeV/c, $5 < p_T < 8$ GeV/c and $8 < p_T < 16$ GeV/c.

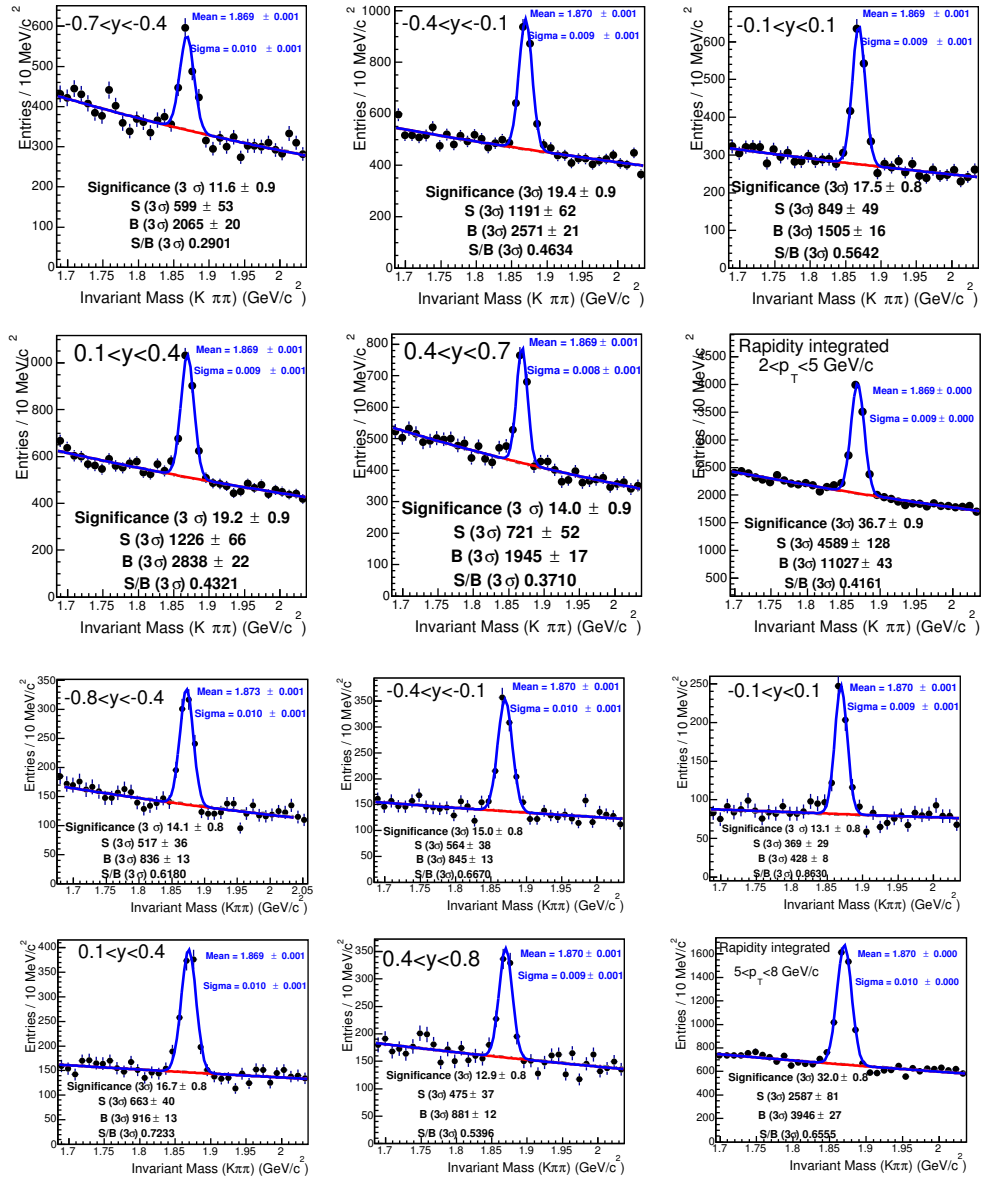
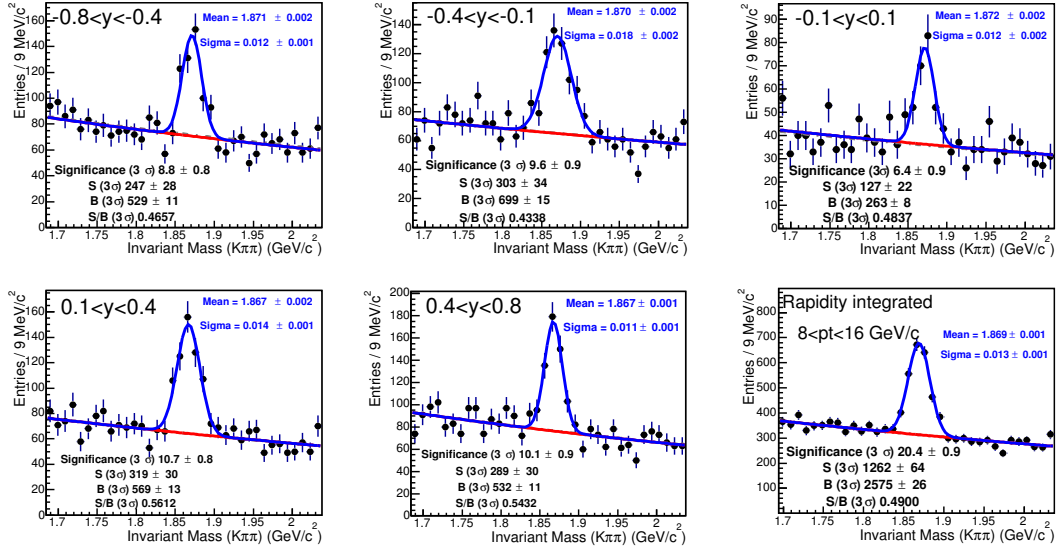


FIGURE 5.6: Two top rows: D^+ candidates (and charge conjugate) invariant mass distributions from minimum bias p - Pb collisions at $\sqrt{s_{NN}} = 5.02$ TeV for $2 < p_T < 5$ GeV/c, in the five rapidity bins considered in the analysis and in the full rapidity range $-0.7 < y_{lab} < 0.7$. Two bottom rows: D^+ candidates (and charge conjugate) invariant mass distributions from minimum bias p - Pb collisions at $\sqrt{s_{NN}} = 5.02$ TeV for $5 < p_T < 8$ GeV/c, in the five rapidity bins considered in the analysis and in the full rapidity range $-0.8 < y_{lab} < 0.8$.

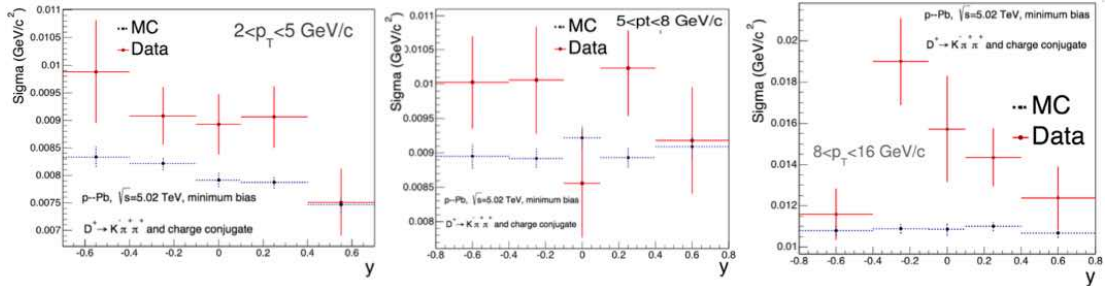
For the p_T interval $2 < p_T < 5$ GeV/c the first and last rapidity intervals are $-0.7 < y_{lab} < -0.4$ and $0.4 < y_{lab} < 0.7$ due to the fiducial acceptance cut. Figures 5.6 and 5.7 show the y_{lab} and p_T differential mass plots. The raw yields extracted from these fits are shown in Table 5.3.

A discrepancy in the peak width obtained from the fit to data (Figure 5.8) and MC is present in most of the p_T and y bins. This discrepancy is within 10-15% for $p_T < 8$ GeV/c, within 20-30% in the p_T interval $8 < p_T < 16$ GeV/c where it reaches 80% in the rapidity interval $-0.4 < y_{lab} < -0.1$. Similar deviations have been observed in the invariant

p_T (GeV/c)	Rapidity y_{lab}					
	integrated	[-0.7/-0.8, -0.4]	[-0.4, -0.1]	[-0.1, 0.1]	[0.1, 0.4]	[0.4, 0.7/0.8]
2-5	4589±128	599±53	1191±62	849±49	1226±66	721±52
5-8	2587±81	517±36	564±38	369±29	663±40	475±37
8-16	1264±64	247±28	303±34	127±22	319±30	289±30

TABLE 5.3: Summary table of the signal in 3σ per p_T and rapidity bin for D^+ .FIGURE 5.7: D^+ candidates (and charge conjugate) invariant mass distributions from minimum bias p -Pb collisions at $\sqrt{s_{NN}} = 5.02$ TeV for $8 < p_T < 16$ GeV/c, in the five rapidity bins considered in the analysis and in the full rapidity range $-0.8 < y_{lab} < 0.8$.

mass distributions of the D^0 meson candidates. These discrepancies are accounted for in the evaluation of the systematic error.

FIGURE 5.8: D^+ mesons peak width as a function of rapidity as obtained from the fit to data and to the MC data sample described in Section 4.2.1 in the p_T bins [2,5] GeV/c (left), [5,8] GeV/c (centre), [8,16] GeV/c (right).

5.2 Cross section calculation

The corrected per-event yields of prompt D^+ mesons in p -Pb collisions were obtained starting from the raw yields $N_{\text{raw}}^{D^{+/-}}|_{|y|<y_{fid}}$ as follows:

$$\frac{dN^{D^+}}{dp_T} = \frac{1}{2} \frac{1}{\Delta y \Delta p_T} \frac{f_{\text{prompt}} \cdot N_{\text{raw}}^{D^{+/-}}|_{|y|<y_{fid}}}{(\text{Acc} \times \epsilon)^{\text{prompt}} \cdot \text{BR} \cdot N_{\text{ev}}} \quad (5.1)$$

and the corrected invariant cross section as:

$$\frac{d\sigma^{D^+}}{dp_T} = \frac{1}{2} \frac{1}{\Delta y \Delta p_T} \frac{f_{\text{prompt}} \cdot N_{\text{raw}}^{D^{+/-}}|_{|y|<y_{fid}}}{(\text{Acc} \times \epsilon)^{\text{prompt}} \cdot \text{BR} \cdot L_{\text{int}}} \quad (5.2)$$

where Δy and Δp_T are the rapidity and p_T interval width, respectively. The rapidity coverage of this cross section in the laboratory frame is equivalent to a rapidity coverage $-0.96 < y_{\text{cms}} < 0.04$ due to the fact that the centre-of-mass frame moves with a rapidity $|\Delta y| = 0.465$ in the proton direction. f_{prompt} is the fraction of prompt D^+ mesons, $(\text{Acc} \times \epsilon)^{\text{prompt}}$ is the acceptance and efficiency correction for prompt D^+ mesons, BR is the branching ratio of the $D^+ \rightarrow K^- \pi^+ \pi^+$ decay channel, the factor 1/2 accounts for the fact that we are measuring the raw yields for the sum of D^+ and D^- and N_{ev} is the number of analyzed events.

It is necessary to stress that the last two equations represent a visible cross section for D^+ mesons counted in events triggered by the V0AND that pass the physics selection, the pile-up rejection and with a primary vertex reconstructed from ITS TPC tracks and $|z_{\text{RecoVert}}| < 10$ cm. Since the *kStepGenerated* step of the Correction Framework (4.2.2) requires $|z_{\text{GeneratedVert}}| < 10$ cm, the efficiency factor also corrects for those events in which $|z_{\text{GeneratedVert}}| < 10$ cm, but no vertex has been reconstructed. For this reason N_{ev} is computed as

$$\begin{aligned} N_{\text{ev}} &= N^{\text{RecoVert}}(|z_{\text{RecoVert}}| < 10\text{cm}) + N^{\text{NoVert}}(|z_{\text{RecoVert}}| < 10\text{cm}) = \\ &= N^{\text{RecoVert}}(|z_{\text{RecoVert}}| < 10\text{cm}) + N_{\text{tot}}^{\text{NoVert}} - N^{\text{NoVert}}(|z_{\text{RecoVert}}| > 10\text{cm}) = \\ &= N^{\text{RecoVert}}(|z_{\text{RecoVert}}| < 10\text{cm}) + N_{\text{tot}}^{\text{NoVert}} - N_{\text{tot}}^{\text{NoVert}} \frac{N^{\text{RecoVert}}(|z_{\text{RecoVert}}| > 10\text{cm})}{N_{\text{tot}}^{\text{RecoVert}}} \end{aligned} \quad (5.3)$$

This allows to normalize the raw yield to the number of minimum-bias interactions (V0AND triggers) with the z position of the vertex within 10 cm from the detector centre, independently from the fact that the vertex was reconstructed. The nuclear modification factor is computed as

$$R_{\text{pA}}(p_T) = \frac{d\sigma_{\text{pA}}^{D^+}/dp_T}{A d\sigma_{\text{pp}}^{D^+}/dp_T} \quad (5.4)$$

More details on this formula can be found in Appendix A. In the next sections the $(\text{Acc} \times \epsilon)$ and f_{prompt} correction factors will be discussed in more details.

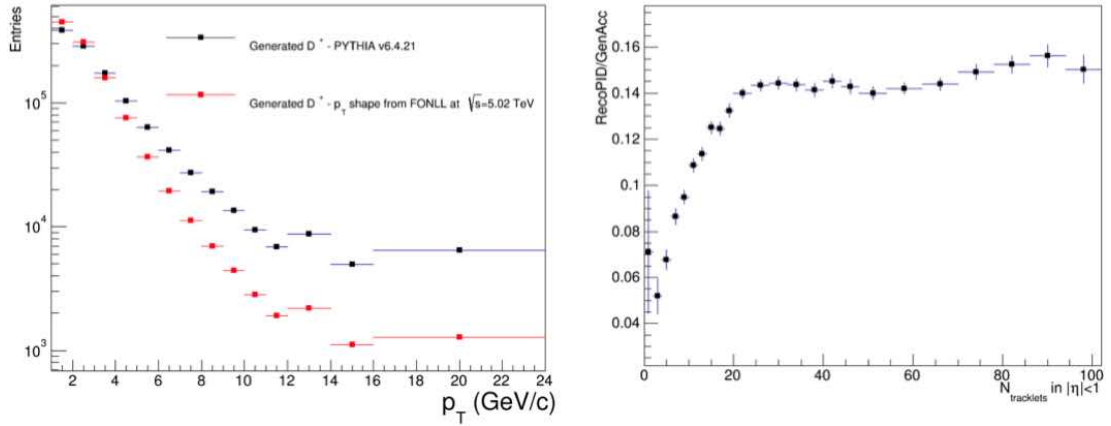


FIGURE 5.9: Left: p_T distribution of generated D^+ mesons obtained from PYTHIA v6.4.21 and from FONLL. Right: efficiency for prompt D^+ mesons selection as a function of the multiplicity, quantified by the number of SPD tracklets in $|\eta| < 1$

5.3 Acceptance and efficiency corrections

The efficiency and acceptance correction ($\text{Acc} \times \epsilon$) is obtained from the MC data sample generated using HIJING for simulating the underlying p -Pb event and PYTHIA v6.4.21 to inject a pp collision with a $c\bar{c}$ pair as described in Section 4.2.1. As discussed therein, the acceptance correction factor is obtained as the ratio of the $kStepAcceptance$ and $kStepGeneratedLimAcc$ containers (the definition of container can be found in Section 4.2.2) and the efficiency correction factor is obtained as the ratio of the $kStepRecoPID$ and $kStepAcceptance$ containers³. In both cases the statistical uncertainties on the ratio are computed as binomial errors, since in both cases the numerator is a sub-sample of the

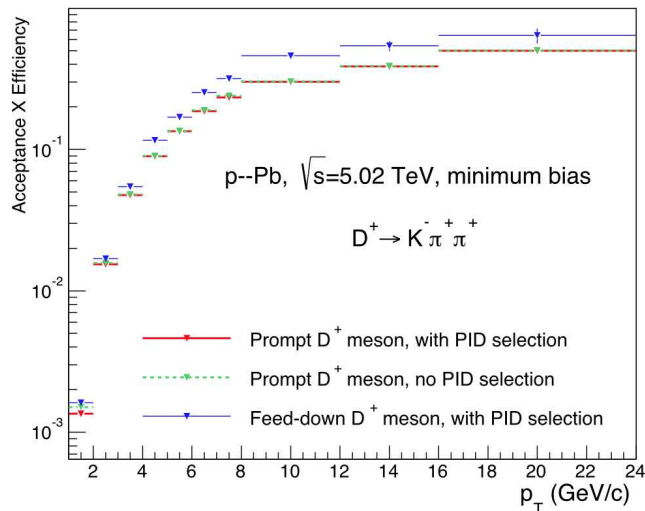


FIGURE 5.10: Left: Acceptance times efficiency correction factor for prompt (with and without PID selection) and feed-down D^+ mesons as a function of p_T , obtained after applying multiplicity and p_T shape corrections, for minimum bias p -Pb collisions at $\sqrt{s_{NN}} = 5.02$ TeV.

³Due to the definition of the $kStepGeneratedLimAcc$ and $kStepAcceptance$ in Section 4.2.2, the $\text{Acc} \times \epsilon$ discussed here actually also includes the Δy factor present in Equations 5.1 and 5.2

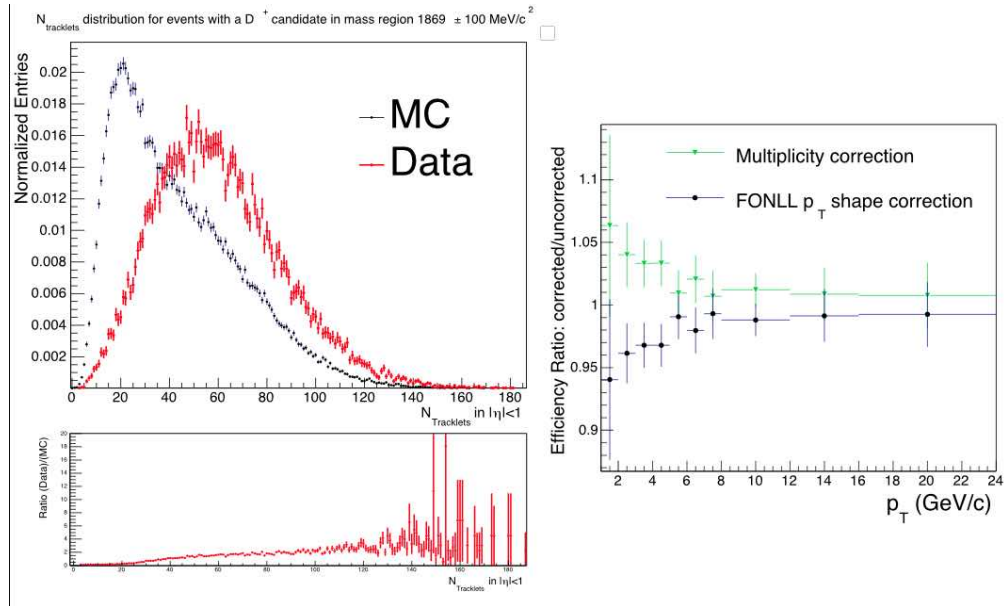


FIGURE 5.11: Left: $N_{\text{tracklets}}$ distributions for events that contain at least one D^+ candidate in the invariant mass region $1869 \pm 100 \text{ MeV}/c^2$ for data (red) and HIJING+PHYTHIA simulation (black). In the bottom panel the ratio of the two distributions is shown. Right: ratio of the efficiency values obtained applying the two corrections separately and those obtained without any correction.

denominator. We have already seen how the efficiency of D^+ meson reconstruction and selection shown in Figure 4.20 (right) varies from 0.5-1% for $p_T < 2 \text{ GeV}/c$ to 20-30% for $p_T > 12 \text{ GeV}/c$ because of the larger displacement of the decay vertex of high- p_T candidates due to the Lorentz boost. The efficiency of feed-down D^+ meson selection is also higher than the one for prompt D^+ meson because at the same p_T , feed-down D^+ are on average more displaced from the primary vertex. The efficiencies of Figure 4.20 (right) are directly obtained from the MC data sample without any further correction. However we will now discuss two corrections that one has to take into account to get the appropriate values of the efficiencies:

- corrections for the p_T shape of the generated D^+ mesons
- corrections for the different event multiplicity distributions in data and simulations

In order to avoid a bias in the efficiency values due to a difference in the generated p_T shape between data and MC, the D^+ meson spectrum used to calculate the efficiencies was re-weighted to reproduce the shape given by FONLL calculations at $\sqrt{s} = 5.02 \text{ TeV}$. The difference in the p_T spectrum of generated D^+ meson obtained from PYTHIA v6.4.21 and from FONLL is shown in Figure 5.9.

The efficiency also depends on the multiplicity of charged particles produced in the collision since the primary vertex resolution, and consequently the resolution of the topological selection variables, improves with increasing multiplicity. As an example, the selection efficiency for D^+ mesons as a function of the multiplicity, quantified by the number of SPD tracklets in $|\eta| < 1$, is shown in the right panel of Figure 5.9. Due to its multiplicity dependence, the efficiency has to be estimated using a Monte Carlo sample that reproduces the multiplicity distribution observed in data. The $N_{\text{tracklets}}$ distributions for events that contain at least one D^+ candidate in the invariant mass region

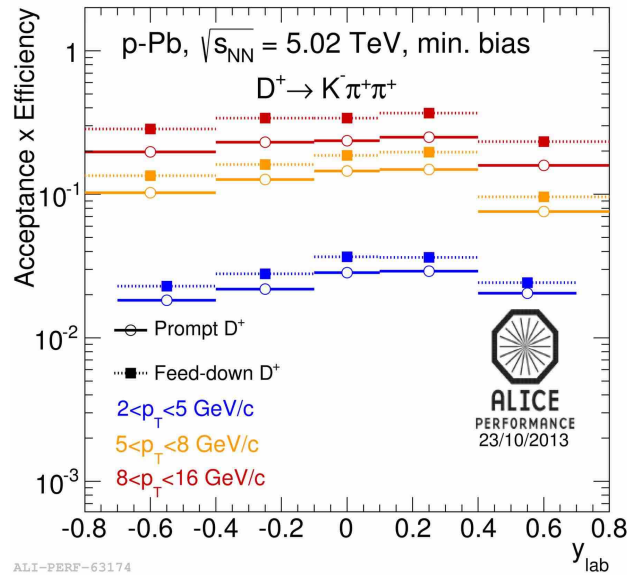


FIGURE 5.12: Left: Acceptance times efficiency correction factor for prompt and feed-down D^+ mesons as a function of rapidity measured in the laboratory frame y_{lab} , obtained in three p_T bins after applying multiplicity and p_T shape corrections, for minimum bias p -Pb collisions at $\sqrt{s_{NN}} = 5.02$ TeV.

1869 ± 100 MeV/ c^2 are shown in the top panel of Figure 5.11 (left) for data and simulated events. The distribution for data is plotted in red, that from the HIJING+PHYTHIA simulation in black. The ratio of the two distributions is shown in the bottom panel of Figure 5.11 (left). This ratio can be used to re-weight the multiplicity distribution of generated and reconstructed obtained from the MC data sample, in order to reproduce the multiplicity distribution of the data. To do this, the output of the correction framework was projected, for each p_T interval, on the $N_{tracklets}$ variable for the steps relevant for the efficiency calculation, namely $kStepRecoPID$ and $kStepAcceptance$. The two $N_{tracklets}$ distributions were then multiplied, bin by bin, by the weight function, and the efficiencies were evaluated as the ratio of the $kStepRecoPID$ and $kStepAcceptance$ containers after the re-weighting.

To quantify the effect of the two corrections described above, Figure 5.11 (right) shows the ratio of the efficiency values obtained applying the two corrections separately (namely the MC p_T shape correction and the multiplicity correction) and those obtained without any correction. The vertical bars represent the statistical errors. The effect of the multiplicity weights is at the level of +4% at low p_T and about +2% at high p_T . The effect of the p_T shape correction is at the level of -4% at low p_T and about -2% at high p_T . The final values of the acceptance times efficiency correction are shown in Figure 5.10 as a function of p_T for prompt and feed-down D^+ mesons. The acceptance times efficiency correction factor for prompt D^+ mesons without PID selections is also shown. For $p_T > 2$ GeV/ c , the efficiency is almost identical ($\sim 2\%$ higher in the NO PID case). For $p_T < 2$ GeV/ c the efficiency is 15% lower if PID is applied, because in this p_T range the STRONG PID strategy (Section 4.1.4) has to be applied in order to get a satisfactory significance.

Figure 5.12 shows the acceptance times efficiency correction as a function of rapidity for the three p_T intervals considered in Table 5.3. There is a slight difference in the extraction of this correction factor with respect to the rapidity integrated one, since as shown in

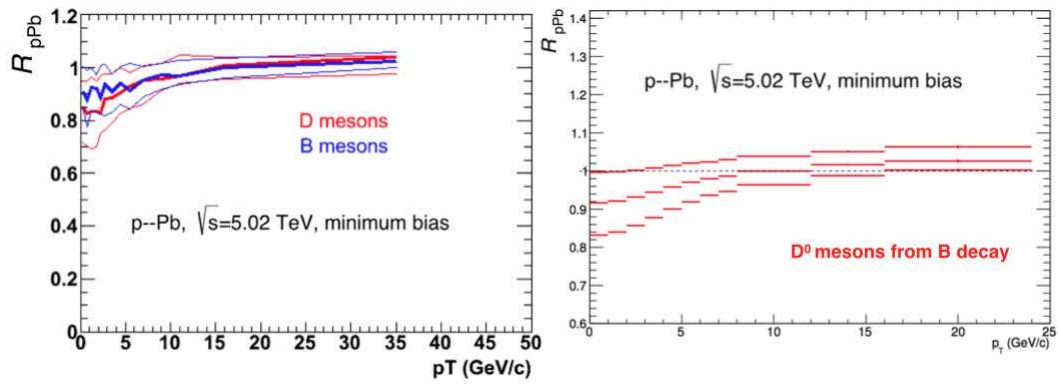


FIGURE 5.13: Left: R_{pA} of prompt D and B mesons from NLO pQCD calculations including EPS09 shadowing modification of nuclear PDFs. Right: R_{pPb} of D^0 mesons from B decays.

Figure 4.19 the $kStepGeneratedLimAcc$ is by definition empty for $|y| > 0.5$ (4.2.2) and the acceptance correction factor here is obtained as $kStepAcceptance$ over $kStepGenerated$. The same multiplicity and p_T shape corrections described above are applied to get the efficiency correction factor.

5.4 Beauty Feed-down subtraction

The D^+ meson raw yields $N_{raw}^{D^{+/-}}$ contain the contribution of both prompt ($c \rightarrow D^+$, $c \rightarrow D^{*+}(2010) \rightarrow D^+$ and other resonant decays cited in Chapter 4) and feed-down ($b \rightarrow B \rightarrow D^+$) yields. As seen in the previous section, prompt and feed-down contributions to the total raw yield have different reconstruction and selection efficiencies. Since the aim of this chapter is the extraction of the nuclear modification factor of prompt D^+ mesons, the feed-down contribution has to be subtracted.

FONLL calculations are used to estimate the expected B-hadron production cross section, varying the theoretical parameters within the following ranges

- $0.5 < \mu_F / \mu_0 < 2$ (central value: 1, $0.5 < \mu_R / \mu_0 < 2$ (central value: 1), with the constraint $0.5 < \mu_F / \mu_R < 2$)
- $4.5 < m_b < 5.0$ GeV/ c^2 (central value: 4.75 GeV/ c^2)

where $\mu_0 = \sqrt{m_b^2 + p_{T,Q}^2}$, with m_b is the mass of the heavy quark.

The $B \rightarrow D^+ + X$ decay kinematic is simulated using the EvtGen⁴ [135] generator to get the cross-section of D^+ mesons from B hadron decays $(\frac{d\sigma}{dp_T dy})_{feed-down}^{FONLL}$. The production cross section of D^+ mesons from B-hadron decays were corrected by their acceptances and efficiencies ($Acc \times \epsilon$)^{feed-down} in each p_T bin, in order to evaluate the expected raw yields of D^+ mesons originating from B hadron decays. The fraction of prompt D^+

⁴The EvtGen package is a framework for the implementation of physics processes relevant to decays of B mesons and other resonances

mesons f_{prompt} is then calculated according to

$$f_{\text{prompt}} = 1 - \langle T_{\text{pA}} \rangle \cdot \left(\frac{d\sigma}{dp_T dy} \right)_{\text{feed-down}}^{\text{FONLL}} \cdot R_{\text{pA}}^{\text{feed-down}}(p_T) \cdot \frac{(\text{Acc} \times \epsilon)^{\text{feed-down}} \cdot \Delta y \Delta p_T \cdot BR \cdot N_{\text{events}}}{N_{\text{raw}}^{D^+}/2} \quad (5.5)$$

that in the following will be called N_b subtraction method. The $\langle T_{\text{pA}} \rangle = 0.098 \pm 0.007 \text{ mb}^{-1}$ is the minimum bias average nuclear overlap function and is calculated as $\langle T_{\text{pA}} \rangle = \langle N_{\text{coll}} \rangle / \sigma_{\text{inel}}^{NN}$. The nuclear modification factor of feed-down D^+ mesons $R_{\text{pA}}^{\text{feed-down}}(p_T)$ is unknown, since it has never been measured, so an assumption on its value has to be made. For the computation of the central value of f_{prompt} we will assume $R_{\text{pA}}^{\text{feed-down}}(p_T) = R_{\text{pA}}^{\text{prompt D}}(p_T)$. The latter assumption is equivalent to $R_{\text{pA}}^{\text{feed-down}}(p_T) / R_{\text{pA}}^{\text{prompt D}}(p_T) = 1$, which is used in an alternative method to compute f_{prompt} , according to the following equation

$$f_{\text{prompt}} = \left(1 + \frac{\frac{d\sigma}{dp_T dy}^{\text{FONLL}}_{B \rightarrow D} \cdot (\text{Acc} \times \epsilon)^{\text{feed-down}} \cdot R_{\text{pA}}^{\text{feed-down}}(p_T)}{\frac{d\sigma}{dp_T dy}^{\text{FONLL}}_{\text{prompt D}} \cdot (\text{Acc} \times \epsilon)^{\text{prompt D}} \cdot R_{\text{pA}}^{\text{prompt D}}(p_T)} \right)^{-1} \quad (5.6)$$

that in the following will be called f_c subtraction method and relies on the ratio between the prompt and feed-down FONLL predictions for D^+ meson cross-section, instead that on the value of $(\frac{d\sigma}{dp_T dy})_{\text{feed-down}}^{\text{FONLL}}$ like in the N_b method⁵.

The choice $R_{\text{pA}}^{\text{feed-down}}(p_T) = R_{\text{pA}}^{\text{prompt D}}(p_T)$ has been done considering an estimate on the influence of shadowing effects on the production of prompt and feed-down D mesons, performed using NLO pQCD calculations, which included EPS09 modification of nuclear PDFs. The resulting R_{pPb} of prompt D and B mesons can be seen in Figure 5.13 (left). The EvtGen decayer is used in order to extract the expected R_{pPb} of D^0 mesons from B decays (Figure 5.13 (right)) from that of B hadrons, which results to be similar to that of prompt D mesons.

The hypothesis is varied in the range $0.9 < R_{\text{pA}}^{\text{feed-down}}(p_T) / R_{\text{pA}}^{\text{prompt D}}(p_T) < 1.3$ to evaluate the systematic uncertainty, as will be discussed in Section 5.6.

5.5 The pp reference at 5.02 TeV

A pp reference at $\sqrt{s} = 5.02 \text{ TeV}$ is required in order to compare heavy flavour production in p -Pb and pp collisions via the nuclear modification factor R_{pPb} . However a pp data sample at $\sqrt{s} = 5.02 \text{ TeV}$ does not exist yet, and the pp reference is extracted from pQCD calculations that allow us to extrapolate to lower energies the p_T -differential cross sections of D^+ meson measured at 7 TeV and shown in Chapter 2 (Figure 2.8 - left).

This procedure was already used in the evaluation of the D-meson nuclear modification factor in Pb-Pb collisions at $\sqrt{s_{\text{NN}}} = 2.76 \text{ TeV}$, shown in Chapter 2 (Figure 2.20), and is described in the following.

⁵One difference between the N_b and f_c method is that in the latter the central value for the $R_{\text{pA}}^{\text{prompt D}}(p_T)$ follows directly from the assumption $R_{\text{pA}}^{\text{feed-down}}(p_T) / R_{\text{pA}}^{\text{prompt D}}(p_T) = 1$. In the N_b method the central value of $R_{\text{pA}}^{\text{prompt D}}(p_T)$ is obtained generating f_{prompt} for a range of $R_{\text{pA}}^{\text{feed-down}}(p_T)$ values, and calculating $R_{\text{pA}}^{\text{prompt D}}(p_T)$.

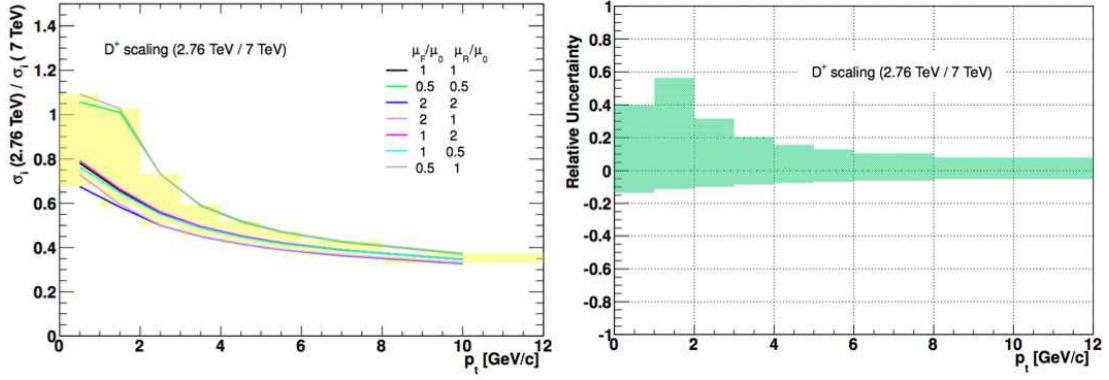


FIGURE 5.14: Left: FONLL scaling factor for D^+ mesons from $\sqrt{s} = 7$ TeV to $\sqrt{s} = 2.76$ TeV. Right: relative uncertainty on the scaling factor.

The results of prompt D^+ meson p_T -differential production cross section in pp collisions at $\sqrt{s} = 7$ TeV are shown in Figure 2.8 together with FONLL and GM-VFNS predictions. The uncertainty band of the FONLL predictions is obtained considering a parameter variation as follows:

- $0.5 < \mu_F / \mu_0 < 2$ (central value: 1)
- $0.5 < \mu_R / \mu_0 < 2$ (central value: 1)
- with the constraint $0.5 < \mu_F / \mu_R < 2$
- $1.3 < m_c < 1.7$ GeV/ c^2 (central value: 1.5 GeV/ c^2) and $4.5 < m_b < 5.0$ GeV/ c^2 (central value: 4.75 GeV/ c^2)

where $\mu_0 = \sqrt{m_Q^2 + p_{T,Q}^2}$, with m_Q is the mass of the heavy quark.

In order to compute the scaling factor from 7 TeV to a given energy α TeV:

- the FONLL predictions at 7 TeV $\sigma(7)$ and at α TeV $\sigma(\alpha)$ are rebinned according to the results of prompt D^+ meson production in pp collisions at $\sqrt{s} = 7$ TeV shown in Figure 2.8
- the ratio $\sigma(\alpha)/\sigma(7)$ is calculated considering that
 - the central value is the ratio of the central predictions at both energies
 - its uncertainty is defined by the envelope of the ratio of the calculations for the different sets of parameter. The theoretical calculation parameters are correlated (equal) at different energies
- multiply the cross-section measured at 7 TeV by the FONLL $\sigma(\alpha)/\sigma(7)$ binned ratio
- propagate the uncertainties:
 - on the FONLL ratios
 - on the uncertainties of the 7 TeV measurement
 - combine these uncertainties summing them in quadrature

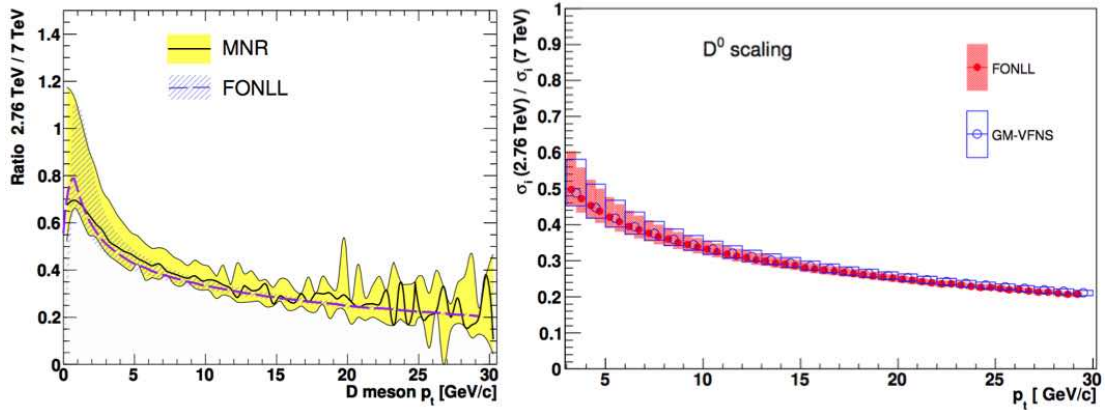


FIGURE 5.15: Left: Scaling factor from $\sqrt{s} = 7$ TeV to $\sqrt{s} = 2.76$ TeV for D^0 mesons obtained from FONLL and POWHEG. Right: Scaling factor from $\sqrt{s} = 7$ TeV to $\sqrt{s} = 2.76$ TeV for D^0 mesons obtained from FONLL and GM-VFNS.

5.5.1 pp reference at $\sqrt{s} = 2.76$ TeV

I will first show some results on the scaling performed to get the pp reference at $\sqrt{s} = 2.76$ TeV, in order to prove the stability of the method. The FONLL scaling factor for D^+ from $\sqrt{s} = 7$ TeV to $\sqrt{s} = 2.76$ TeV is shown in Figure 5.14 (left) as a function of p_T . The scaling factor obtained with the different sets of scales are drawn with solid lines, while the resulting global scaling envelope is depicted by a yellow filled band. The central value (black dashed line) of the scaling is obtained with $\mu_F/\mu_0 = \mu_R/\mu_0 = 1$ and $m_c = 1.5$ GeV/ c^2 . The values of the scales for the other sets are reported in the legend $(\mu_F/\mu_0, \mu_R/\mu_0)$. The scaling factor depends mainly on the value of the factorization scale μ_F , since for the same charm quark p_T , different Bjorken x ranges are probed at 2.76 TeV and at 7 TeV, and changing the factorization scale affects the x dependence of the parton distribution functions (PDFs). The right panel of Figure 5.14 shows the relative uncertainty of the scaling factor, obtained from the envelope of the different computations in the left panel. The relative uncertainty is larger ($40 \div 50\%$) at low p_T , and decreases to about 8% for $p_T > 8$ GeV/ c . The scaling factor does not show a significant dependence on the value used for the charm quark mass in the calculation as shown in [136].

Figure 5.15 shows the scaling factor from $\sqrt{s} = 7$ TeV to $\sqrt{s} = 2.76$ TeV obtained for D^0 with FONLL calculations and its uncertainties together with:

- the scaling factor obtained with MNR calculations ([110] - Section 2.2.5) cross-sections and their uncertainties (left). The scaling factors agree with each other, however the uncertainties are larger for the MNR case
- the scaling factor obtained with GM-VFNS cross-sections ([55] - Section 2.1.2) and its uncertainties (right). In the GM-VFNS case the parameters that are varied within the calculations to obtain the uncertainties are the renormalization scale, the factorization scale for initial state singularities and the factorization scale for final state singularities. In this case the scaling central values and their uncertainties agree very well with those given by FONLL

Figure 5.15 (left) shows the ALICE pp data at $\sqrt{s} = 7$ TeV scaled with FONLL calculations to $\sqrt{s} = 1.96$ TeV compared to the D^+ meson cross-section measured by the CDF

Collaboration in $p\bar{p}$ collisions at $\sqrt{s} = 1.96$ TeV [66]. The CDF measurements and the ALICE rescaled data agree within uncertainties.

Figure 5.15 (left) compares the ALICE pp data at $\sqrt{s} = 7$ TeV scaled with FONLL calculations to $\sqrt{s} = 2.76$ TeV with the D^+ meson cross-section measured by the ALICE Collaboration in pp collisions at $\sqrt{s} = 2.76$ TeV [66]. The integrated luminosity used to compute the D^+ meson cross-section at $\sqrt{s} = 2.76$ TeV is 1.1 nb^{-1} . The measurements at $\sqrt{s} = 7$ TeV were rebinned to match the p_T binning used at $\sqrt{s} = 2.76$ TeV. The ALICE data scaled from $\sqrt{s} = 7$ TeV agree with the ones measured at $\sqrt{s} = 2.76$ TeV within uncertainties in all p_T bins. The results are compatible within statistical uncertainties only, and their central values coincide within 5–10% in almost all p_T bins, confirming the stability and appropriateness of the energy scaling procedure.

5.5.2 pp reference at $\sqrt{s} = 5.02$ TeV

As seen in the previous paragraph, the FONLL scaling factors agree very well with those obtained with other pQCD calculations, so only the approach based on FONLL will be shown for the case of scaling to $\sqrt{s} = 5.02$ TeV. The scaling factor obtained with the FONLL approach is the one that will be used to compute the R_{pPb} that will be shown in the end of this chapter.

The FONLL calculations were performed using the CTEQ 6.6 PDFs parametrization (Section 2.1.1), and varying the factorisation and renormalisation scales within the same ranges quoted in the previous paragraph. The resulting scaling factor is shown in Figure

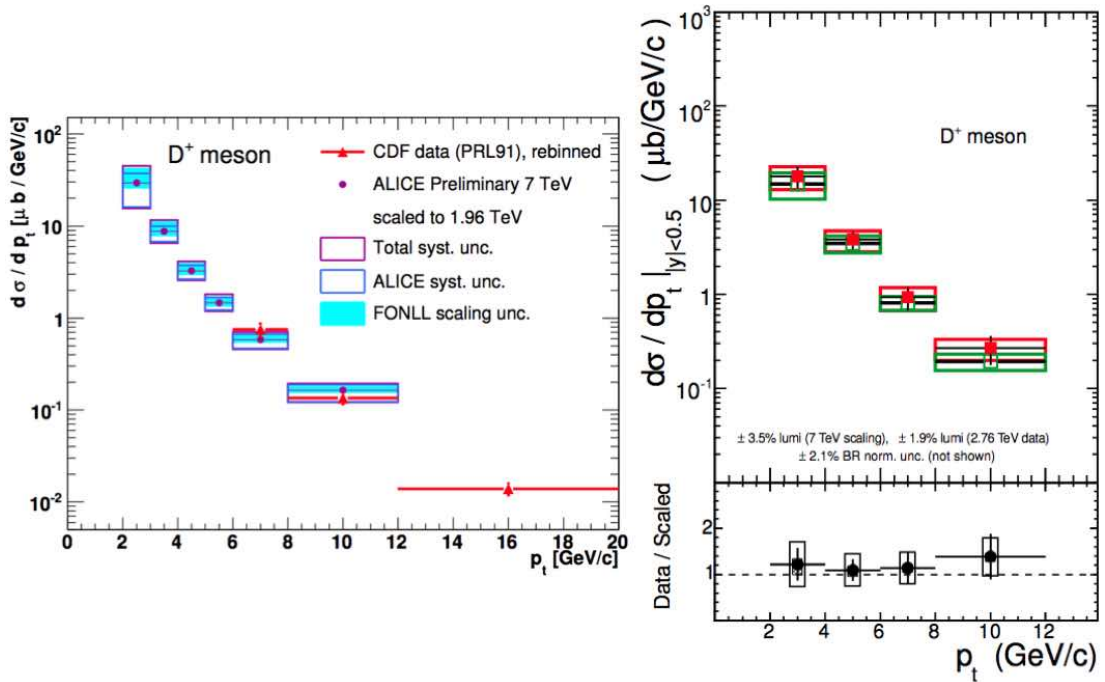


FIGURE 5.16: Left: ALICE pp data at $\sqrt{s} = 7$ TeV scaled with FONLL calculations to $\sqrt{s} = 1.96$ TeV and D^+ meson cross-section measured by the CDF Collaboration in $p\bar{p}$ collisions at $\sqrt{s} = 1.96$ TeV [66]. Right: ALICE pp data at $\sqrt{s} = 7$ TeV scaled with FONLL calculations to $\sqrt{s} = 1.96$ TeV and D^+ meson cross-section measured by the ALICE Collaboration in pp collisions at $\sqrt{s} = 2.76$ TeV [66].

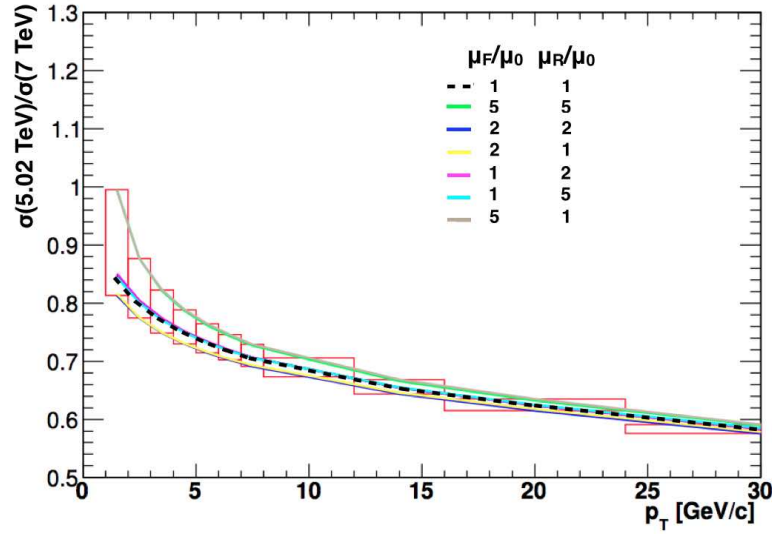


FIGURE 5.17: FONLL scaling factor for D^+ mesons from $\sqrt{s} = 7$ TeV to $\sqrt{s} = 5.02$ TeV

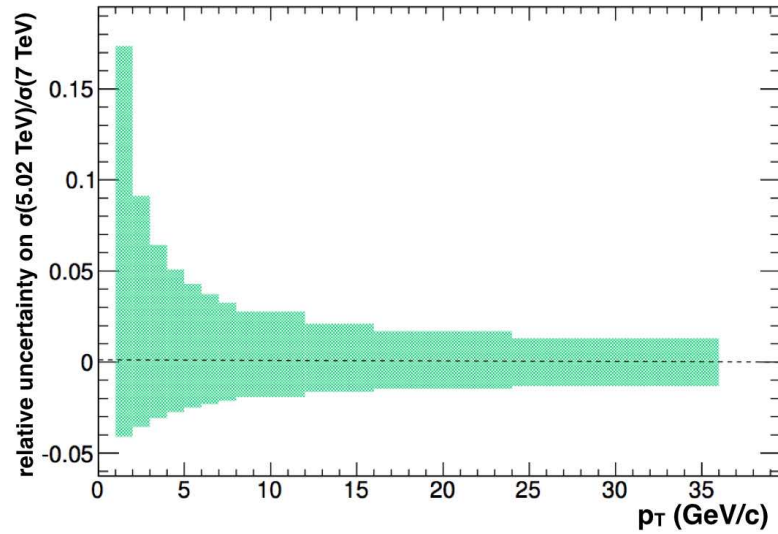


FIGURE 5.18: Relative uncertainties on the FONLL scaling factor for D^+ mesons from $\sqrt{s} = 7$ TeV to $\sqrt{s} = 2.76$ TeV.

5.17. As in the case of the scaling to $\sqrt{s} = 2.76$ TeV, it depends mainly on the value of the factorization scale due to its effect on the x dependence of PDFs. The uncertainties on the scaling factor are shown in Figure 5.18. The relative uncertainty is larger (15%) at low p_T , and decreases to about 2% for $p_T > 8$ GeV/c. The uncertainties are smaller with respect to the scaling from $\sqrt{s} = 7$ TeV to $\sqrt{s} = 2.76$ TeV, as expected due to the smaller energy gap.

5.6 Systematic uncertainties

The sources of systematic uncertainty considered in this analysis are as follows:

1. systematic uncertainty on the extraction of the raw yields from the invariant mass distributions;
2. systematic uncertainty on the efficiency determination due to the imperfect description of the cut variables in the MC;
3. systematic uncertainty on the PID selection efficiency;
4. systematic uncertainty on the efficiency due to the p_T shape of the generated D^+ ;
5. systematic uncertainty on the tracking efficiency.
6. systematic uncertainty on the beauty feed-down subtraction
7. systematic uncertainty on the pp reference at $\sqrt{s} = 5.02$ TeV
8. systematic uncertainty on the integrated luminosity and branching ratio

5.6.1 Systematic uncertainty due to the yield extraction

The systematic error on the yield extraction was estimated by comparing the extracted raw yields when the invariant mass fit parameters and constraints were varied. In particular, the following tests were made:

- extending and reducing the invariant mass range used in the fit;
- using a different bin width for the invariant mass distribution (twice the bin width and half of the bin width);
- fixing the peak width to that extracted from MC;
- using a parabolic background fit function instead of the exponential one;
- using a bin counting method based on counting the entries in the invariant mass histogram within 3σ from the peak centre after subtracting the background estimated via the fit;

As an example, Figure 5.19 shows the fit to the invariant distribution in $3 < p_T < 4$ GeV/c for the cases:

- using half the bin width (left)
- restricting the fit range (right)

The ratio between the raw yields obtained with these variations and the ones of the default configuration was evaluated to estimate the systematics. The ratios are reported in Figure 5.20 in the rapidity integrated case (left) and as a function of rapidity in $5 < p_T < 8$ GeV/c. The statistical errors on the extracted raw yields are treated as uncorrelated in the ratio. However some degree of correlation is present among the raw yields extracted with different fit techniques, so the errors of Figure 5.20 are slightly overestimated. The systematic uncertainties were assigned so as to obtain the best estimate of an RMS uncertainty by removing the "pathological" cases in which the values of mean and sigma

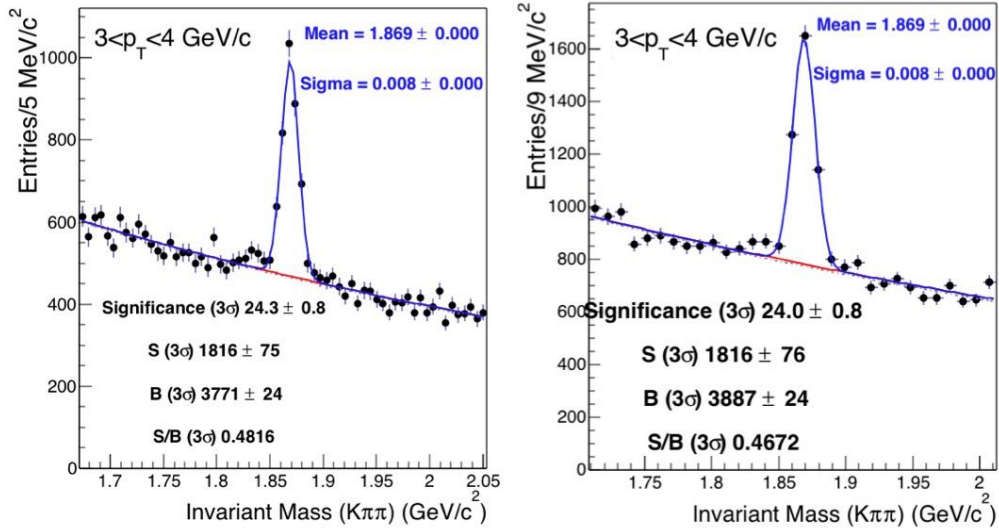


FIGURE 5.19: Invariant mass fit in $3 < p_T < 4$ GeV/c for the multiplicity integrated case using half the bin width (left) and restricting the fit range (right).

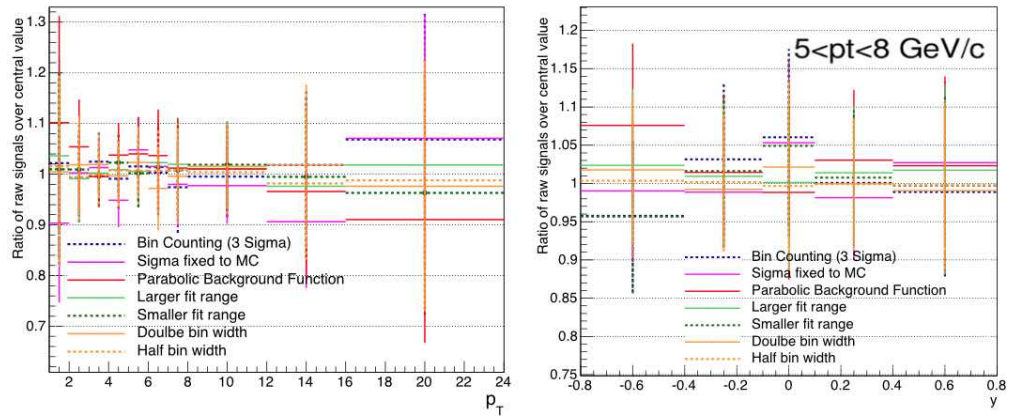


FIGURE 5.20: Left: relative variation of the raw yield obtained with the different fit strategies with respect to the central values of Figures 5.2, 5.3 and 5.4 as a function of transverse momentum. Right: the same in the p_T bin [5,8] GeV/c as a function of rapidity.

of the invariant mass fit deviate from the expected values, and by trying not to include effects of statistical fluctuations in the estimated systematic uncertainty. The resulting values of systematic uncertainties are summarized in Table 5.4 for the rapidity integrated case and for the five rapidity intervals.

The systematic uncertainties increase at low p_T is due to the lower significance. At high p_T the higher systematic uncertainties are due to the discrepancy in the Gaussian σ observed between data and MC.

5.6.2 Systematic uncertainty due to topological cut efficiency

The systematic uncertainty due to the imperfect description in the Monte Carlo of the variable used in the topological selection was evaluated by repeating the analysis with four different sets of cuts and looking at the relative variations of the corrected yield in

p_T (GeV/c)	1-2	2-3	3-4	4-5	5-6	6-7	7-8	8-12	12-16	16-24
rapidity integrated	10%	8%	5%	5%	5%	5%	5%	5%	8%	8%
$-0.8/-0.7 < y_{lab} < -0.4$	x		7%			5%		10%		x
$-0.4 < y_{lab} < -0.1$	x		5%			5%		10%		x
$-0.1 < y_{lab} < 0.1$	x		5%			5%		5%		x
$0.1 < y_{lab} < 0.4$	x		5%			5%		5%		x
$0.4 < y_{lab} < 0.7/0.8$	x		7%			5%		7%		x

TABLE 5.4: Systematic uncertainty on the extraction of raw yields from the D^+ meson invariant mass distributions

each p_T and rapidity interval. Two of the set of cuts adopted are looser (i.e. have higher selection efficiencies) with respect to those reported in Table 5.1, while the other two are tighter (i.e. have lower selection efficiencies). In the plots of Figure 5.21 they are labeled according to the cut value used on the cosine of the pointing angle (central value = 0.99). The variation of the corrected spectra with the modified sets of cuts relative to the one obtained with the cuts of Table 5.1, shown in Figure 5.21, is used to assign the systematic uncertainty as a best estimate of an RMS uncertainty. This was done, for example, checking that the values of mean and sigma of the invariant mass fit are stable for each set of cuts, and that the extracted significance is reasonably high (>3 in all cases). In addition, at high p_T the full spread of the ratios shown in Figure 5.21 has to be disentangled from the high statistical uncertainty arising from the limited statistics. The statistical errors on the computed corrected spectra are treated as correlated in the ratio. Some degree of correlation is present among the raw yields extracted with different fit techniques, so the errors of Figure 5.20 are slightly overestimated.

The assigned values of relative systematic uncertainties due to topological cut efficiencies are reported in Table 5.5.

p_T (GeV/c)	1-2	2-3	3-4	4-5	5-6	6-7	7-8	8-12	12-16	16-24
rapidity integrated	10%	10%	6%	6%	6%	5%	5%	5%	5%	5%
$-0.8/-0.7 < y < -0.4$	x		7%			7%		8%		x
$-0.4 < y < -0.1$	x		7%			7%		8%		x
$-0.1 < y < 0.1$	x		7%			7%		8%		x
$0.1 < y < 0.4$	x		7%			7%		8%		x
$0.4 < y < 0.7/0.8$	x		7%			7%		8%		x

TABLE 5.5: Systematic uncertainty due to topological cut efficiency

5.6.3 Systematic uncertainty due to PID

The possible systematic effects due to the PID selection were studied by comparing the corrected D^+ meson yields (Equation 5.1) obtained with and without applying the PID selections to the decay tracks. The ratios of the corrected yields with and without PID as a function of p_T for the rapidity integrated analysis are reported in Figure 5.22. The statistical errors on the extracted corrected spectra are treated as correlated in the ratio. The ratios are compatible with unity, and the highest discrepancy is found in the p_T interval $1 < p_T < 2$ GeV/c, where the STRONG PID is applied. No PID systematic uncertainty is assigned in the range $2 < p_T < 24$. For $p_T < 2$ GeV/c a 10% uncertainty

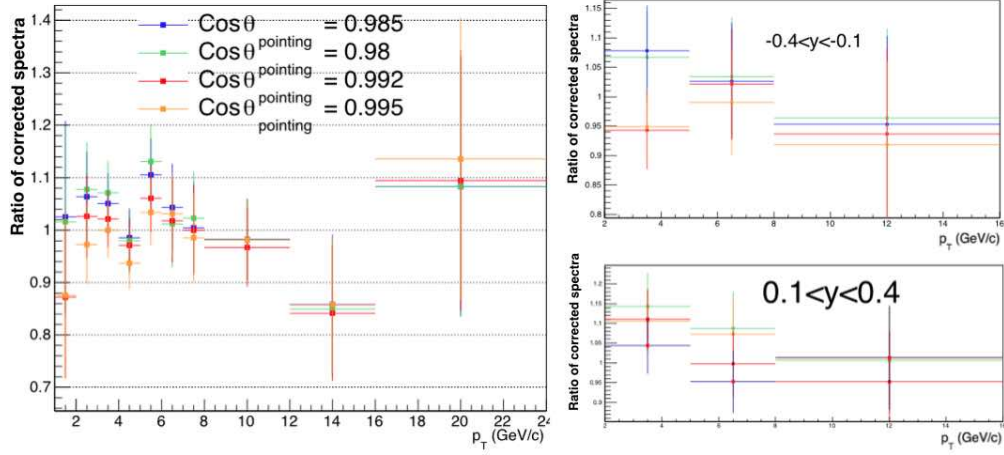


FIGURE 5.21: Left: relative variation of the corrected spectra obtained with different sets of cuts as a function of p_T . Right: the same in the p_T bin [5,8] GeV/c as a function of rapidity.

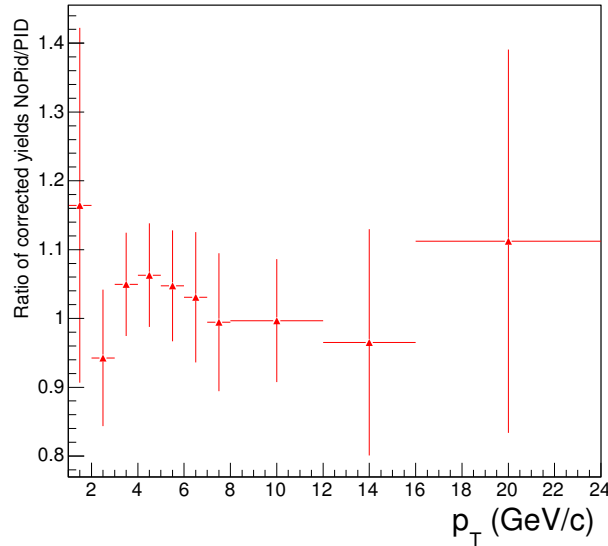


FIGURE 5.22: Relative variation of the corrected D^+ meson yields obtained with and without applying PID.

is estimated from Figure 5.22. Since no rapidity dependence of the PID response is expected, and after checking that the y_{lab} differential results are compatible with the y_{lab} integrated ones, no PID uncertainty is assigned to the y_{lab} differential analysis.

5.6.4 Systematic due to the p_T shape of generated D^+ mesons

The p_T distribution of the generated D^+ mesons within the p_T intervals affects the efficiency, since the efficiency depends on p_T (see Figures 5.10 and 5.12) and is estimated from the relative variation of the efficiencies obtained using p_T shapes from FONLL and those of the MC data sample described in Section 4.2.1. This relative variation has been shown in Figure 5.11. The rapidity integrated uncertainty values are shown in Table 5.6. The efficiency variations due to the generated p_T shape have also been evaluated in the

y_{lab} differential analysis. The uncertainties are reported in Table 5.6. They are larger than in the rapidity integrated analysis, because here the p_T intervals are larger.

p_T (GeV/c)	1-2	2-3	3-4	4-5	5-6	6-7	7-8	8-12	12-16	16-24
rapidity integrated	3%	0%	0%	0%	0%	0%	0%	4%	4%	4%
$-0.8/-0.7 < y < -0.4$	x		10%			5%		5%		x
$-0.4 < y < -0.1$	x		10%			5%		5%		x
$-0.1 < y < 0.1$	x		10%			5%		5%		x
$0.1 < y < 0.4$	x		10%			5%		5%		x
$0.4 < y < 0.7/0.8$	x		10%			5%		5%		x

TABLE 5.6: Systematic uncertainty due to the p_T shape of generated D^+ mesons.

5.6.5 Systematic uncertainty due to track reconstruction efficiency

The systematic uncertainty related to the tracking efficiency was estimated by varying the track quality selection criteria, such as the minimum number of TPC clusters for analyzed tracks (default value = 70, systematic checks with 50 TPC clusters). The resulting uncertainty is estimated to be 3% per track, independent of p_T and y . Therefore, the uncertainty from tracking efficiency is 9% for the 3-body decay of D^+ considered in this analysis in all p_T and rapidity intervals.

5.6.6 Systematic uncertainty due to beauty feed-down subtraction

The beauty feed-down subtraction procedure described in Section 5.4 contains two sources of systematics.

The first source of systematic uncertainty is given by the uncertainties on the FONLL predictions used in Equations 5.5 and 5.6. In fact, the FONLL predictions used in this

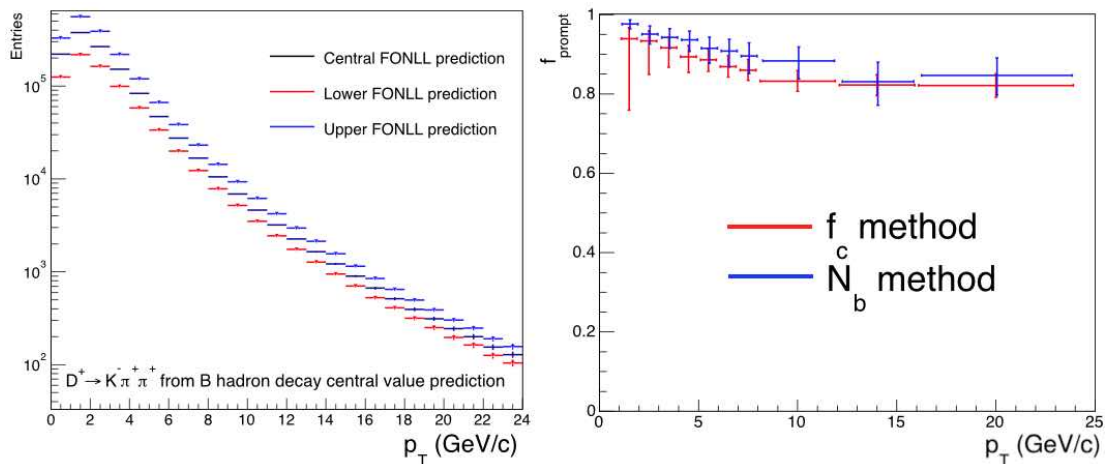


FIGURE 5.23: Left: FONLL predictions for D^+ from B decays cross section at $\sqrt{s} = 5.02$ TeV. Central, upper and lower values are shown. Right: f_{prompt} values obtained with the f_c and N_b methods taking into account the FONLL prediction uncertainties.

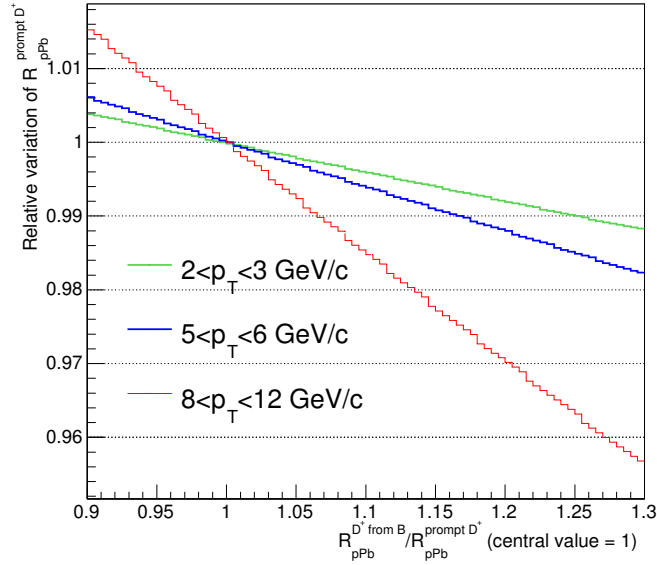


FIGURE 5.24: Relative variation of prompt D^+ -meson R_{pPb} as a function of the hypothesis on $R_{pA}^{\text{feed-down}}(p_T)/R_{pA}^{\text{prompt } D^+}(p_T)$ for three p_T intervals.

analysis for prompt and feed-down D^+ meson cross section at $\sqrt{s} = 5.02$ TeV are composed of a central, an upper and a lower value, shown for D^+ mesons from B decays in Figure 5.23 (left). This means that f_{prompt} is evaluated for both methods f_c and N_b three times, yielding a central, a maximum and a minimum value for f_{prompt} . Note that in the f_c case, where the ratio of FONLL predictions for feed-down and prompt D^+ mesons are needed, a "conservative approach" is used, which means that the two extreme values of f_{prompt} are obtained from Equation 5.6 using the ratio of the upper (lower) FONLL predictions for feed-down D^+ -meson to the upper (lower) FONLL predictions for prompt D^+ -meson: the extreme case obtained from the ratio of the upper FONLL predictions for feed-down D^+ -meson to the lower FONLL predictions for prompt D^+ -meson is not considered. The two histograms in Figure 5.23 (right) show the f_{prompt} values obtained with the f_c and N_b methods: the central values are those obtained with the central FONLL predictions, the asymmetric error bars represent the f_{prompt} variation obtained using the upper/lower values of the FONLL predictions.

The second source of systematic uncertainty is the hypothesis on the nuclear modification factor of feed-down D^+ mesons $R_{pPb}^{\text{feed-down}}$. This contribution is evaluated varying the ratio of feed-down and prompt D^+ mesons R_{pPb} in the range $0.9 < R_{pA}^{\text{feed-down}}(p_T)/R_{pA}^{\text{prompt } D^+}(p_T) < 1.3$, and evaluating the corresponding variation of prompt D^+ R_{pPb} . This range is chosen for the reasons discussed in Section 5.4. Figure 5.24 shows the relative variation of prompt D^+ mesons R_{pPb} as a function of the hypothesis on $R_{pA}^{\text{feed-down}}(p_T)/R_{pA}^{\text{prompt } D^+}(p_T)$.

For both methods f_c and N_b , the two sources of systematic are summed in quadrature. The total systematic uncertainty due to beauty feed-down is defined as the full envelope of the uncertainties of the two methods N_b and f_c . The central points for both prompt D^+ R_{pPb} and cross section are taken as those obtained with the N_b method using the central FONLL predictions.

Table 5.7 summarizes the total systematic uncertainties due to feed-down subtraction. For what concerns the rapidity dependence of this sources of systematic uncertainty, it

was considered that FONLL calculations for prompt and feed-down D^+ meson production predicts the cross section as a function of y to be flat within 4% in the rapidity range considered, and that the ratio $R_{pA}^{\text{feed-down}}(p_T)/R_{pA}^{\text{prompt } D}(p_T)$ to vary within 3-4% in $|y_{\text{lab}}| < 1$. Therefore the systematic uncertainty due to beauty feed-down in the rapidity differential analysis is evaluated as in the rapidity integrated case.

p_T (GeV/c)	1-2	2-3	3-4	4-5	5-6	6-7	7-8	8-12	12-16	16-24
rapidity integrated	+2% -31%	+3% -11%	-3% -7%	+3% -5%	+3% -4%	+3% -4%	+3% -3%	+4% -3%	+5% -3%	+4% -3%
-0.8/-0.7 < y < -0.4	x		+3% -10%			+3% -8%		+4% -10%		x
-0.4 < y < -0.1	x		+3% -10%			+3% -8%		+4% -10%		x
-0.1 < y < 0.1	x		+3% -10%			+3% -8%		+4% -10%		x
0.1 < y < 0.4	x		+3% -10%			+3% -8%		+4% -10%		x
0.4 < y < 0.7/0.8	x		+3% -10%			+3% -8%		+4% -10%		x

TABLE 5.7: Systematic uncertainty due to beauty feed-down subtraction.

5.6.7 Systematic uncertainty on pp reference (only for measurement)

The pp reference in the denominator of the R_{pPb} formula is also affected by systematic uncertainties. In particular:

- the measured D^+ meson cross section at $\sqrt{s} = 7$ TeV is affected by the same sources of systematic uncertainties discussed for the p–Pb data sample: yield extraction, cut efficiency, PID, tracking efficiency and p_T shape in the MC.
- the uncertainty on the scaling factor from $\sqrt{s} = 7$ TeV to $\sqrt{s} = 5.02$ TeV, shown in Figure 5.18
- the uncertainty on the beauty feed-down subtraction, which in pp collisions does not include the contribution of beauty energy loss hypothesis

In the calculation of R_{pPb} these contributions are summed in quadrature to the systematic uncertainties on the p–Pb cross section, with two exceptions: the systematic errors relative to tracking efficiency and those relative to the FONLL scale on beauty feed-down subtraction are considered as completely correlated. The systematic uncertainty values due to the pp reference are reported in Table 5.8.

p_T (GeV/c)	[1,2]	[2,3]	[3,4]	[4,5]	[5,6]	[6,7]	[7,8]	[8,12]	[12,16]	[16,24]
Uncertainty (%)	+33 -37	+33 -34	+30 -30	+19 -19	+19 -19	+17 -17	+17 -17	+17 -17	+21 -21	+19 -19

TABLE 5.8: Summary table of systematics on pp reference (data+scaling).

5.6.8 Luminosity and branching ratio

The integrated luminosity was evaluated as the ratio between the number of events passing the V0AND (3.2.1) trigger selection with $|z_{\text{vertex}}| < 10$ cm and the corresponding trigger cross section in p–Pb collisions at $\sqrt{s_{NN}} = 5.02$ TeV, σ_{V0AND} . The V0A trigger is 100%

efficient for D^+ mesons with $p_T > 1$ GeV/ c and $|y_{\text{lab}}| < 0.5$. The value of the V0AND trigger cross section was estimated with van der Meer scans as $\sigma_{\text{V0AND}} = 2.09 \pm 3.5\%$ (syst) b with negligible statistical uncertainty [137]. The luminosity is measured via the V0 trigger counts, corrected for pileup and for background contamination, divided by the corresponding cross sections. Since fluctuations of the order of 1% were observed in the run-by-run integrated luminosity, an additional 1% systematic is assigned, yielding a total systematic error on L_{int} of 3.7%.

The systematic uncertainty on the branching ratio is 2.1%, as shown in table 4.1.

5.7 Results

5.7.1 D^+ -meson cross section

The p_T differential production cross section of prompt D^+ mesons in p -Pb collisions at $\sqrt{s_{\text{NN}}} = 5.02$ TeV is shown in Figure 5.25 (left) together with the pp reference at $\sqrt{s} = 5.02$ TeV multiplied by the mass number ($A=208$) of Pb nuclei. The p_T range covered is $1 < p_T < 24$ GeV/ c . The vertical bars represent the statistical error. The empty boxes represent the systematic uncertainties on data, i.e. yield extraction, cut efficiency, tracking efficiency, PID, p_T shape of generated D^+ mesons and in the pp case those arising from the scaling factor. The filled boxes represent the systematic uncertainties on beauty feed-down.

The right panel of Figure 5.25 shows the p_T differential production cross sections of prompt D^+ mesons together with those of D^0 , D^{*+} and D_s^+ mesons measured in the hadronic decay channels listed in Table 4.1 [1]. Due to the limited statistics, the D_s^+ measurement has a different p_T binning. The relative abundances of D mesons in p -Pb collisions are compatible within uncertainties with those measured in pp, ep , and e^+e^- collisions at different energies [138].

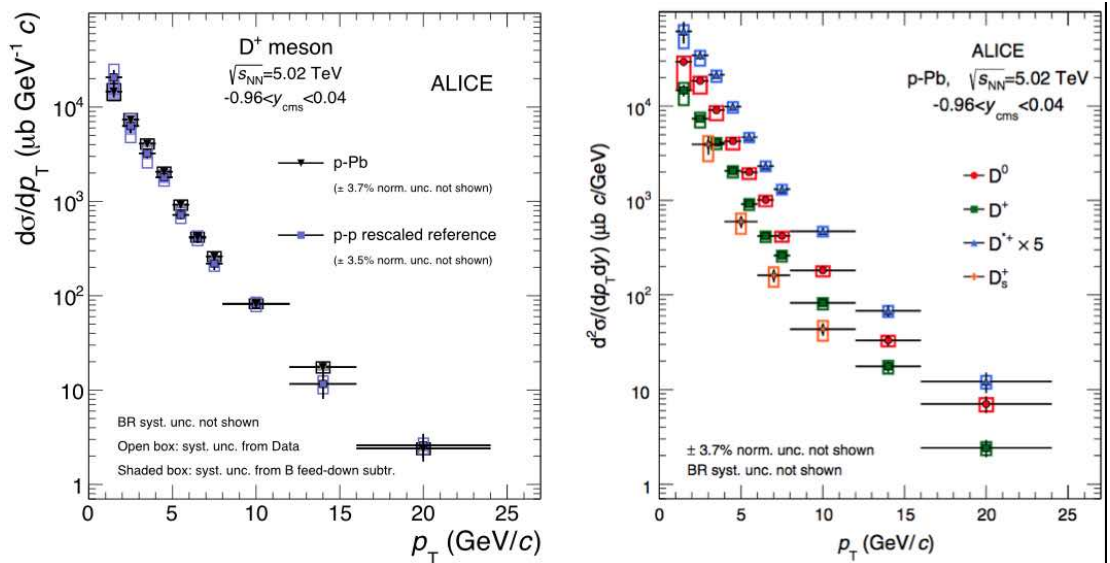


FIGURE 5.25: Left: p_T differential production cross section of prompt D^+ mesons together with the pp reference at $\sqrt{s} = 5.02$ TeV multiplied by the mass number ($A=208$) of Pb nuclei. Right: p_T differential production cross section of prompt D^+ mesons together with those of D^0 , D^{*+} and D_s^+ mesons [1].

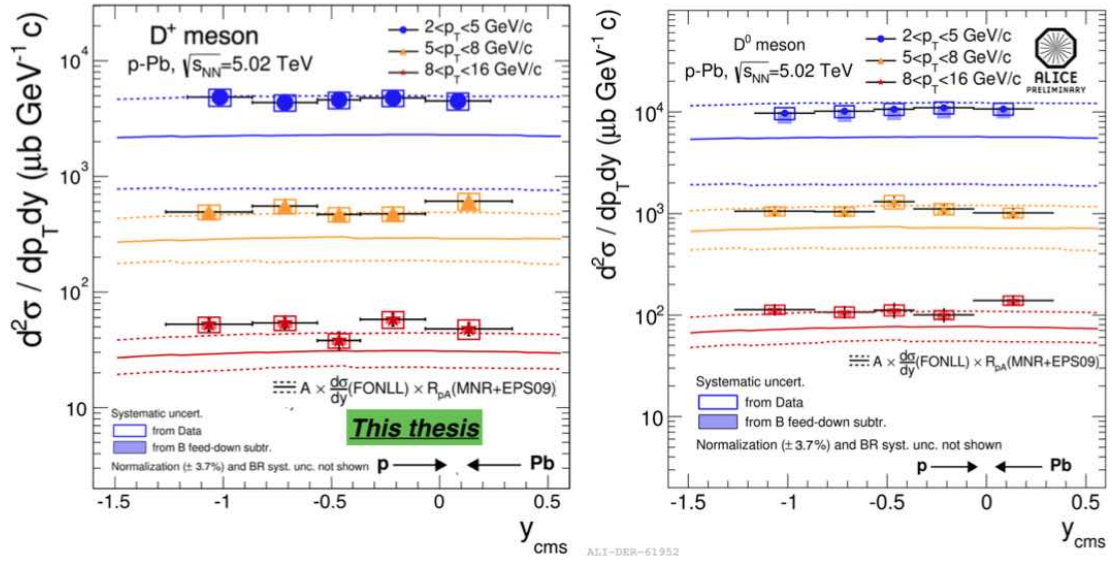


FIGURE 5.26: Left: D^+ -meson cross section as a function of y_{cms} in the three p_T intervals considered in this analysis compared to FONLL predictions taking into account EPS09 parametrization of PDFs. Right: D^0 -meson cross section as a function of y_{cms} in the three p_T intervals considered for this analysis.

Figure 5.26 (left) shows the D^+ -meson cross section as a function of y_{cms} in the three p_T intervals considered for this analysis. The empty boxes represent the systematic uncertainties on data, the filled boxes represent the systematic uncertainties on beauty feed-down. Systematic errors on branching ratio and normalization are not shown. The sketch on the p and Pb beams configuration present in the bottom right corner of Figure 5.26 shows that the positive rapidity values are those in the direction of the p beam. No significant rapidity dependence of the D^+ meson cross section in the measured y_{cms} interval is present. The results are compared to the predictions obtained with FONLL pQCD calculations with EPS09 parametrization of the PDFs, and are compatible within statistical and systematics uncertainties with the upper values of the predictions. This behaviour is also observed for the y_{cms} differential cross section of D^0 mesons, shown in the right panel.

5.7.2 D^+ -meson nuclear modification factor

The $R_{p\text{Pb}}$ of D^+ mesons in p -Pb collisions at $\sqrt{s_{\text{NN}}} = 5.02$ TeV is shown in in Figure 5.27. It is compatible with unity within the statistical and systematic uncertainties in the measured p_T range, indicating that the D^+ -meson production in p -Pb collisions is consistent with the one in pp collisions scaled by the average number of binary collisions. The D^+ -meson $R_{p\text{Pb}}$ is also consistent with those of D^0 , D^{*+} and D_s^+ mesons measured in the hadronic decay channels listed in Table 4.1, as shown in Figure 5.28. In particular, the D_s^+ $R_{p\text{Pb}}$ is not only interesting to study possible modification of c -quark dynamic in p -Pb collisions, but also because the presence of a strange quark makes it more sensible to the hadronization mechanisms and to a possible enhancement of strangeness production in p -Pb collisions. Both aspects were discussed together with some results in Sections 1.4.7 and 1.4.4.

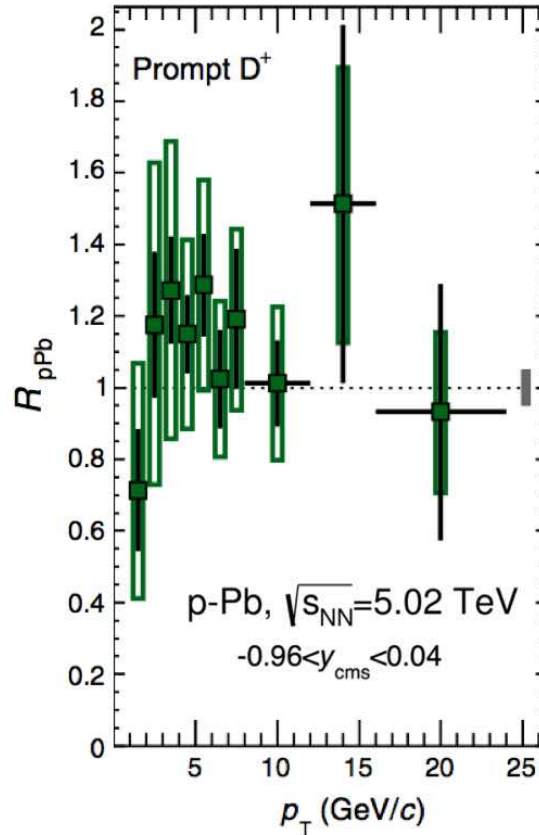


FIGURE 5.27: R_{pPb} of D^+ mesons in p -Pb collisions at $\sqrt{s_{NN}} = 5.02$ TeV as a function of p_T .

5.7.3 Comparison to model calculations

The average R_{pPb} of D^0 , D^{*+} and D^+ mesons in the p_T range $1 < p_T < 24$ GeV/c was calculated by using the relative statistical uncertainties as weights. The systematic error on the average was calculated by propagating the uncertainties through the weighted average, where the contributions from tracking efficiency, B feed-down correction, and scaling of the pp reference were taken as fully correlated among the three species. Figure 5.29 shows the average R_{pPb} compared to theoretical calculations:

- next-to-leading order pQCD calculations (Mangano, Nason, and Ridolfi (MNR) [50]) of D -meson production, including the EPS09 [76] (Section 2.2.1) nuclear modification of the CTEQ6M PDFs [53] (Section 2.1.1)
- calculations based on the color glass condensate [75] (Section 2.2.1). In this calculation gluon merging dynamic is encoded in an effective unintegrated gluon distribution (uGD) for Pb nuclei and is more prominent in the momentum region lower than the saturation scale Q_s^2 [139]
- calculations taking into account the k_T broadening of incoming partons that arises from initial-state scattering, nuclear shadowing and radiative energy loss in cold nuclear matter [140]

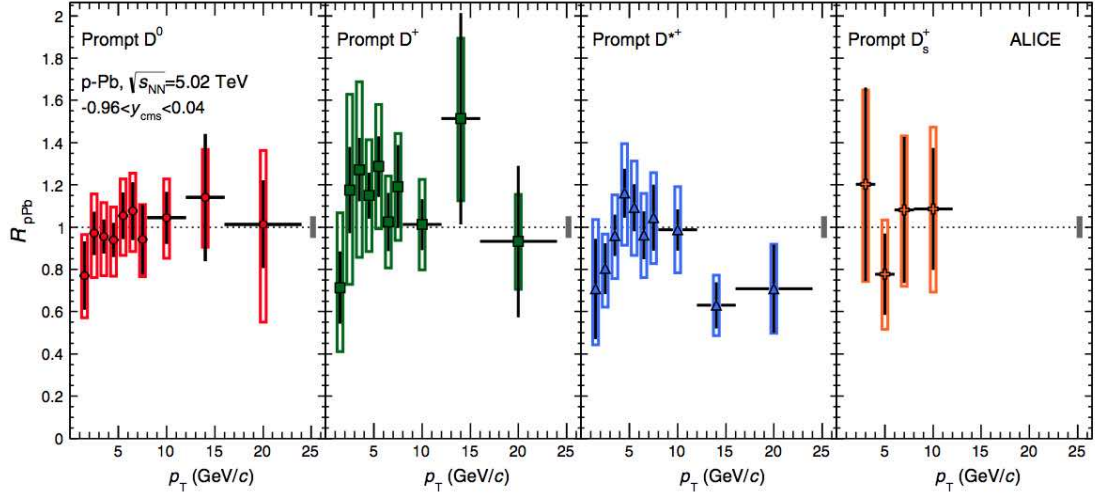


FIGURE 5.28: R_{pPb} of D mesons in p -Pb collisions at $\sqrt{s_{NN}} = 5.02$ TeV as a function of p_T : from left to right D^0 , D^+ , D^{*+} and D_s^+ mesons.

All these models only take into account initial state effects. Data are well described by all of them within statistical and systematic uncertainties, however the current uncertainties on both data and predictions do not allow to discriminate among models.

The possible effects due to the formation of a hydrodynamically expanding medium as calculated in [129] was shown in Figure 5.1 compared to R_{dAu} of heavy-flavour decay electrons. The same results from a similar calculation for D-meson R_{pPb} in p -Pb collisions at $\sqrt{s_{NN}} = 5.02$ TeV are shown in Figure 5.29 (right). The blast-wave spectra for D mesons in p -Pb collisions at $\sqrt{s} = 5.02$ TeV are divided by the p_T distributions of D mesons obtained from FONLL calculations. The blast wave curves are obtained using initial parameters (β_{\perp} and T_{kin} , Section 1.4.3) obtained from π , K and p spectra in minimum bias p -Pb collisions. With respect to the predictions for RHIC energy, here

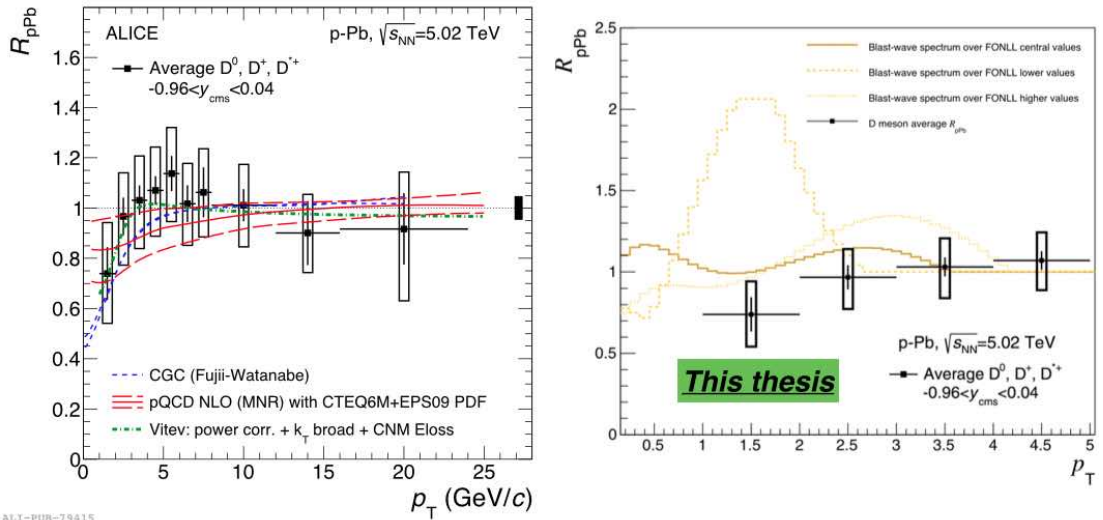


FIGURE 5.29: Left: average R_{pPb} of D^0 , D^{*+} and D^+ mesons [1] compared to models including initial state effects. Right: average R_{pPb} of D^0 , D^{*+} and D^+ mesons [1] compared to a model implementing radial expansion of the system created in the p -Pb collision [129].

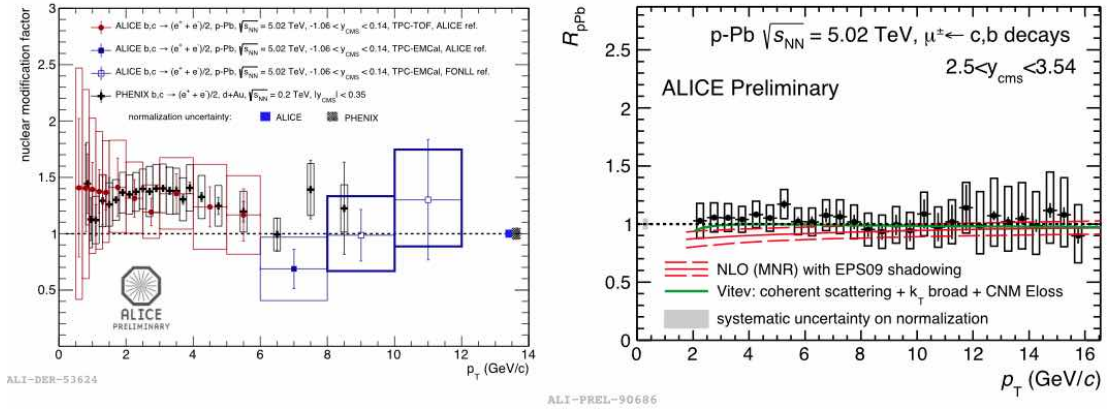


FIGURE 5.30: Left: R_{pPb} of electrons from heavy-flavour (charm + bottom) decays in p -Pb collisions at $\sqrt{s_{NN}} = 5.02$ TeV measured by the ALICE Collaboration and in d -Au collisions at $\sqrt{s_{NN}} = 200$ GeV measured by the PHENIX Collaboration. Right: R_{pPb} of muons from heavy-flavour (charm + bottom) decays in p -Pb collisions at $\sqrt{s_{NN}} = 5.02$ TeV measured by the ALICE Collaboration.

the R_{pPb} modulation expected from radial flow is smaller and confined to lower values of p_T .

With the current uncertainties on both data and blast-wave predictions it is hard to draw conclusion on possible hydrodynamic effects in p -Pb collisions.

5.7.4 Comparison to results with heavy-flavour decay electrons and muons

The preliminary R_{pPb} of electrons from heavy-flavour (charm + bottom) hadron decays in p -Pb collisions at $\sqrt{s_{NN}} = 5.02$ TeV measured by the ALICE Collaboration is shown in Figure 5.30 (right). The measurement is performed in $-1.06 < y_{lab} < 0.14$ in the p_T range 1 to 12 GeV/c. The pp reference is obtained following a strategy similar to the one described in Section 5.5.2 except for $p_T > 8$ GeV/c, where pp data at 7 TeV are not available and the reference is obtained from FONLL predictions only. The R_{pPb} of heavy-flavour decay electrons is compatible with unity within (large) uncertainties. The central values are systematically above unity of a factor ~ 0.3 up to $p_T = 8$ GeV/c.

The R_{pPb} of electrons from heavy-flavour (charm + bottom) hadron decays in d -Au collisions at $\sqrt{s_{NN}} = 200$ GeV measured by the PHENIX Collaboration⁶ is also shown in Figure 5.30 (left) and shows agreement within uncertainties with the ALICE results. However in the p_T range 1.5 to 6 GeV/c PHENIX data, which have smaller uncertainties, seem to indicate an enhancement above unity of the R_{dAu} .

The preliminary R_{pPb} of muons from heavy-flavour (charm + bottom) hadron decays in p -Pb collisions at $\sqrt{s_{NN}} = 5.02$ TeV measured by the ALICE Collaboration is shown in Figure 5.30. The measurement is performed in $2.5 < y_{lab} < 3.54$ in the p_T range 2 to 16 GeV/c. The R_{pPb} of heavy-flavour decay muon is compatible with unity within uncertainties. The measurement is compared with two of the models already compared to the D -meson R_{pPb} , namely next-to-leading order pQCD calculations including the EPS09 nuclear modification of the CTEQ6M PDFs and the Vitev calculations [140]. As in the

⁶These results are slightly different than those in Figure 5.1, since these ones are for minimum-bias d -Au collisions.

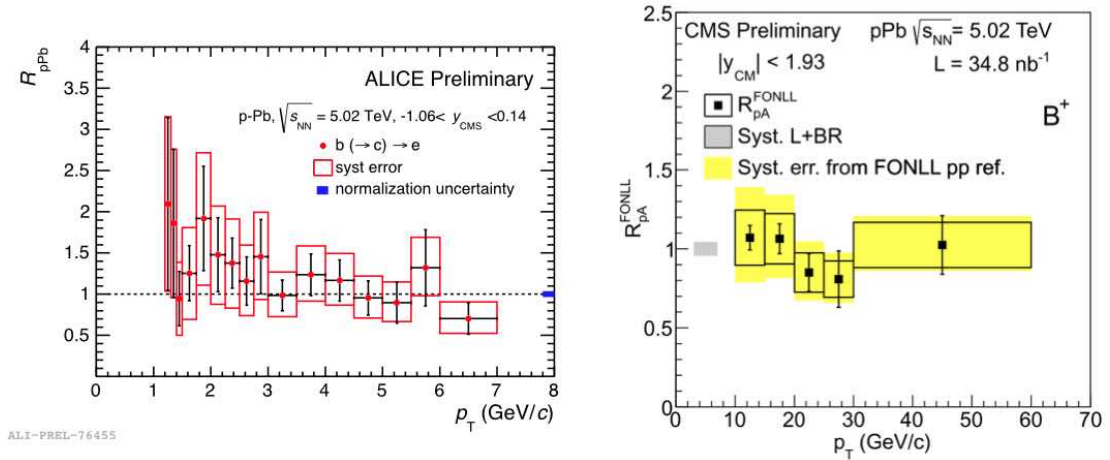


FIGURE 5.31: Left: R_{pPb} of electrons from beauty in p -Pb collisions at $\sqrt{s_{NN}} = 5.02$ TeV measured by the ALICE Collaboration. Right: R_{pPb} of B^+ hadrons measured by CMS in p -Pb collisions at $\sqrt{s_{NN}} = 5.02$ TeV [141].

case of D mesons, data and models show good agreement.

5.7.5 Comparison to some results in the beauty sector

The preliminary R_{pPb} of electrons from beauty in p -Pb collisions at $\sqrt{s_{NN}} = 5.02$ TeV measured by the ALICE Collaboration is shown in Figure 5.31. Electrons from charm and beauty are separated via a selection on their impact parameter exploiting the larger lifetime of B mesons with respect to D mesons. The R_{pPb} measurement is performed in $-1.06 < y_{lab} < 0.14$ in the p_T range 1.2 to 7 GeV/c and is consistent with unity within uncertainties.

In Figure 5.31 (right) the R_{pPb} of B^+ hadrons measured by the CMS Collaboration in p -Pb collisions at $\sqrt{s_{NN}} = 5.02$ TeV is shown [141]. B^+ mesons are reconstructed in their hadronic decay into $J/\Psi + K^+$ and their signal is extracted via an invariant mass analysis. The R_{pPb} is computed using FONLL calculations as pp reference, since no data are currently available for B^+ mesons p_T differential cross-section in pp collisions at high energies. The resulting R_{pPb} of B^+ mesons, measured in $10 < p_T < 60$ GeV/c, is compatible with unity within uncertainties. Similar results are obtained for the R_{pPb} of B^0 mesons.

5.7.6 Conclusions

The results on D meson R_{pPb} discussed in this section show that within the current uncertainties D-meson production in p -Pb collisions is consistent with the binary scaling of pp collisions. Similar conclusions come from measurements of electrons and muons from heavy-flavour hadron decays at different energies, as well as by measurements performed in the beauty sector.

We can now go back to what stated in the introduction of this Chapter about the role of p -Pb measurements in the interpretation of Pb-Pb results of D mesons nuclear modification factor, and try to draw some conclusions from Figure 5.32. The average D-meson

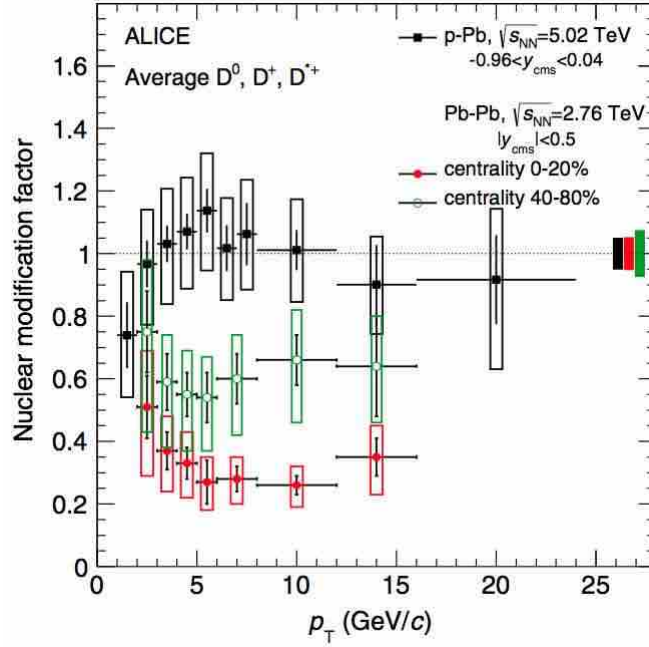


FIGURE 5.32: average D-meson R_{pPb} together with average D-meson R_{AA} measured in central (0-20%) and semiperipheral (20-40%) Pb-Pb collisions at $\sqrt{s_{NN}} = 2.76$ TeV [142].

R_{pPb} is shown together with the average D-meson R_{AA} measured in central (0-20%) and peripheral (40-80%) Pb-Pb collisions at $\sqrt{s_{NN}} = 2.76$ TeV [142].

With the caveat that Pb-Pb and p-Pb measurement are performed at different centre-of-mass energies and for different values of y_{cms} , we observe that

- R_{pPb} values are not consistent within uncertainties with R_{AA} values for central Pb-Pb collisions in the whole p_T range covered by the Pb-Pb measurement
- R_{pPb} values are consistent within uncertainties with models taking into account initial state effects only

The fact that the measured R_{AA} values can not be explained in terms of initial state effects only was already observed by comparing the R_{AA} measured in central (0-20%) Pb-Pb collisions at $\sqrt{s_{NN}} = 2.76$ TeV with calculations based on next-to-leading order pQCD calculations including EPS09 modification of nuclear PDFs⁷, as shown in Figure 5.33. This observation is now conformed by p-Pb data on D mesons production, thus reinforcing the statement that the suppression of D-meson production observed in central Pb-Pb collisions for $p_T > 2$ GeV/c is predominantly induced by final-state effects, e.g., the charm quark energy loss in the hot and dense medium.

⁷This calculations are similar to the ones shown in Figure 5.29 for R_{pPb} . The effect of shadowing is essentially at low p_T and is larger for Pb-Pb collisions were it affects both colliding nuclei

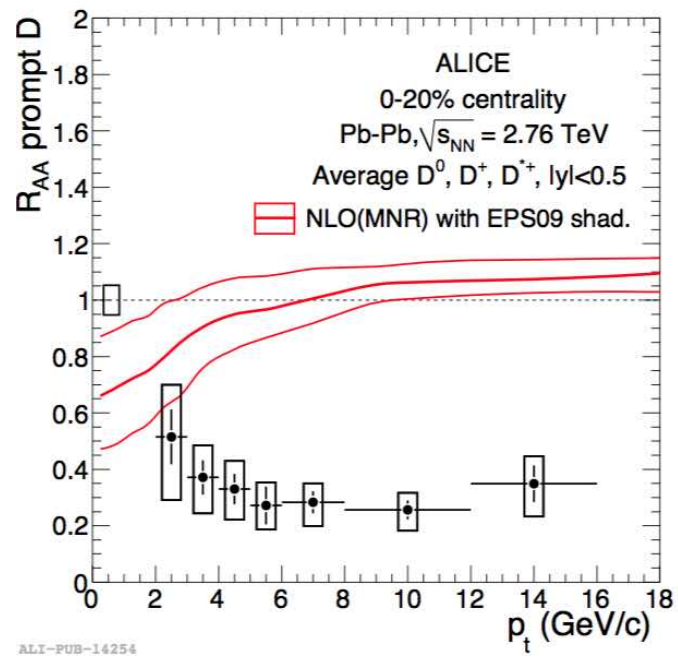


FIGURE 5.33: Average D-meson R_{AA} measured in central (0-20%) Pb-Pb collisions at $\sqrt{s_{NN}} = 2.76$ TeV compared to next-to-leading order pQCD calculations including EPS09 parametrizations of nuclear PDFs.

Chapter 6

Data-driven beauty feed-down subtraction

The results on prompt D^+ -meson cross-section and nuclear modification factor described in the previous chapter are obtained with the beauty feed-down subtraction technique described in Section 5.4. This feed-down subtraction method relies on two theoretical hypotheses: the validity of FONLL predictions on B-hadron cross sections and the energy loss of b quarks (R_{pPb} of D^+ -meson from B hadrons decay).

A data-driven approach to beauty feed-down subtraction would have the advantage of not depending on theoretical calculations and on ad-hoc assumptions on the R_{pPb} of feed-down D mesons. Moreover we have seen in Section 5.6.6 that the systematic uncertainty on theory driven feed-down subtraction is large at low p_T (30% in $1 < p_T < 2$ GeV/c). In this chapter I will present an alternative, data-driven, feed-down subtraction method based on the analysis of the impact parameter distributions of D^+ mesons passing the selection cuts described in the previous chapters. Figure 6.1 shows the sketch of the decay of a prompt D^+ -meson and of a feed-down D^+ -meson from the decay of a B^0 hadron originating from the primary vertex. I recall that the impact parameter is defined as the distance of closest approach of the D^+ -meson flight line (defined by its momentum direction) and the primary vertex.

The true impact parameter of prompt D^+ mesons is zero by definition. However the finite resolution on impact parameter of the ALICE detector shown in Figure 3.9 smears the measured values around zero. The effect of resolution on impact parameter is represented in Figure 6.1 by an orange shadowed circle.

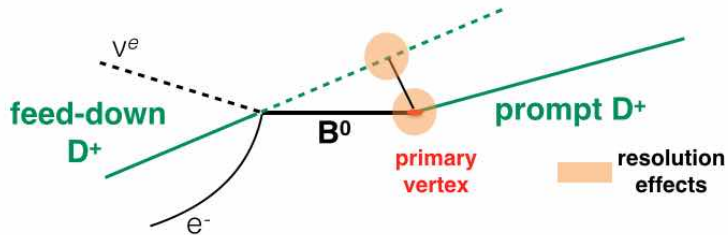


FIGURE 6.1: Sketch representing the effect of detector resolution on impact parameter measurements

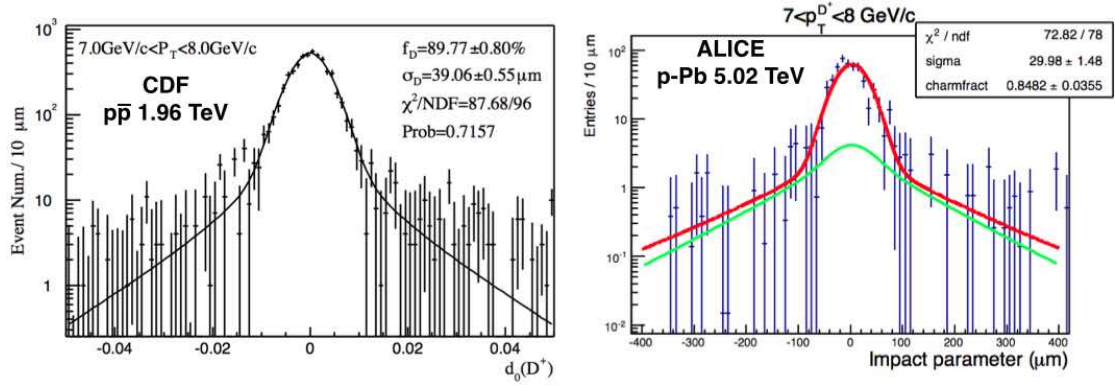


FIGURE 6.2: Impact parameter distributions of D^+ mesons used to extract f_{prompt} from the $p\bar{p}$ CDF data sample (left) and from the p-Pb ALICE data sample (right).

The true impact parameter of feed-down D^+ -meson is different from zero and depends on the B-hadron decay length and on the angle between the B-hadron and D-meson flight line, as will be discussed in next sections. Also in this case resolution effects are present. The different shapes of the impact parameter distributions of prompt and feed-down D^+ mesons can thus be used as a tool to estimate the feed-down contribution to the total D^+ -meson raw yield. The prompt fraction f_{prompt} of D^+ -meson yield can be extracted from a fit to the impact parameter distributions as discussed in next sections.

It is nonetheless worth to anticipate that this beauty feed-down subtraction method was already used by the CDF Collaboration to extract the cross sections shown in Figure 2.7. The CDF analysis, performed in the p_T range $6 < p_T < 20$ GeV/c, can count on a statistics much higher than the one presented in this thesis: the integrated luminosity $L_{\text{int}}^{\text{CDF}} \approx 60 \text{ pb}^{-1}$ results in $3 \cdot 10^{11}$ events, to be compared to the 10^8 events used in the minimum bias analysis presented in the previous Chapter: more than 3 orders of magnitude of difference. However when one compares the reconstructed D^+ -meson yields in the two analyses this difference in available statistics is strongly reduced, due to several factors: the increase of the D^+ -meson cross-section going from 1.96 TeV to 5.02 TeV of centre-of-mass energy, the N_{coll} scaling of D^+ -meson production in p-Pb collisions and the difference in selection and reconstruction efficiencies, which in the CDF analysis are about a factor 100 lower than the ones of Figure 4.20 for the minimum-bias p-Pb analysis of ALICE. As an example, in the p_T range $6 < p_T < 7$ GeV/c, $N_{\text{CDF}}^{D^{+/-}} \approx 5700$ while $N_{\text{ALICE}}^{D^{+/-}} \approx 600$, as shown by the different number of entries in the impact parameter distributions of the right and left panels of Figure 6.2. In $8 < p_T < 12$ GeV/c $N_{\text{CDF}}^{D^{+/-}} \approx 13400$ while $N_{\text{ALICE}}^{D^{+/-}} \approx 1000$.

Figure 6.2, showing the difference in available statistics between CDF and ALICE, also includes the fit function used to extract f_{prompt} that will be described in the following sections. In order to properly fit the data a minimum amount of entries is required. This minimum amount of candidates in this analysis was set to 200, so that, with respect to the analysis presented in Chapter 5, the first and the last p_T bins ($1 < p_T < 2$ GeV/c and $16 < p_T < 24$ GeV/c) will be excluded here, because the number of D^+ -meson candidates passing the selection cuts is too small.

6.1 Impact parameter distributions

In this section I will show the impact parameter distributions in the transverse plane (d_0^{xy}) expected for D^+ mesons obtained from the MC data sample described in Section 4.2.1. The impact parameter distributions obtained from the minimum-bias p–Pb data sample collected in 2013 will be also shown, together with the background subtraction method used in the analysis.

6.1.1 Prompt D^+ mesons in MC simulations

The impact parameter (d_0^{xy}) distributions in the transverse plane of prompt D^+ -meson are shown in Figure 6.3 for eight p_T intervals in the p_T range $2 < p_T < 16$ GeV/c. These distributions are obtained from the MC sample described in Section 4.2.1 after applying the same event, track quality, topological and PID selections used to extract the D^+ -meson cross-section and nuclear modification factor shown in Chapter 5.

For prompt D^+ mesons the impact parameter, defined as the distance of closest approach of the D^+ -meson trajectory to the primary vertex, is zero by definition. However resolution effects on track and primary vertex reconstruction make the distributions of Figure 6.3 symmetrically smeared around zero.

Fitting the impact parameter distributions of Figure 6.3 with a gaussian function gives reasonable results at low p_T , however at high p_T the χ^2 values of the fit indicate that a simple gaussian is not describing properly the distribution. In Figure 6.4 the same distributions are fitted with a gaussian with exponential tails, expressed by

$$F^{\text{prompt}}(d_0^{xy}) = A \left[(1-f_g) \frac{1}{2\lambda_{\text{prompt}}} e^{-\frac{|d_0^{xy}-\mu_{\text{prompt}}|}{\lambda_{\text{prompt}}}} + f_g \frac{1}{\sqrt{2\pi}\sigma_{\text{prompt}}} e^{-\frac{(d_0^{xy}-\mu_{\text{prompt}})^2}{2\sigma_{\text{prompt}}^2}} \right] \quad (6.1)$$

where A is a normalization factor, λ_{prompt} is the slope of the exponential contribution, μ_{prompt} is the common mean of the gaussian and exponential contributions and f_g is the fraction of the integral contained in the Gaussian function with width σ_{prompt} . The χ^2 values obtained with this functional form at high p_T are smaller than those obtained with a simple gaussian. For $p_T < 5$ GeV/c the situation does not vary significantly. Indeed the f_g parameters obtained at low p_T indicate that the exponential tails contribution to the total fitted function is less than 2%.

Figure 6.5 shows the σ_{prompt} values obtained with both the simple gaussian fit and the fit of Equation 6.1 as a function of p_T . In both cases the MC predicts a decreasing trend of σ_{prompt} values with increasing p_T , due to the better resolution on both impact parameter and p_T (Figure 3.10).

6.1.2 Feed-down D^+ -meson in MC simulations

Before showing the impact parameter distributions of feed-down D^+ mesons extracted from the MC data sample of Section 4.2.1, a few considerations are worth.

For feed-down D^+ mesons we expect an impact parameter different from zero. This is due to the fact that feed-down D^+ meson momenta won't in general be parallel to those of the parent B hadrons. However the shape of the distributions in the various p_T intervals is more difficult to model with respect to the ones for prompt D^+ mesons, and this is due to several reasons.

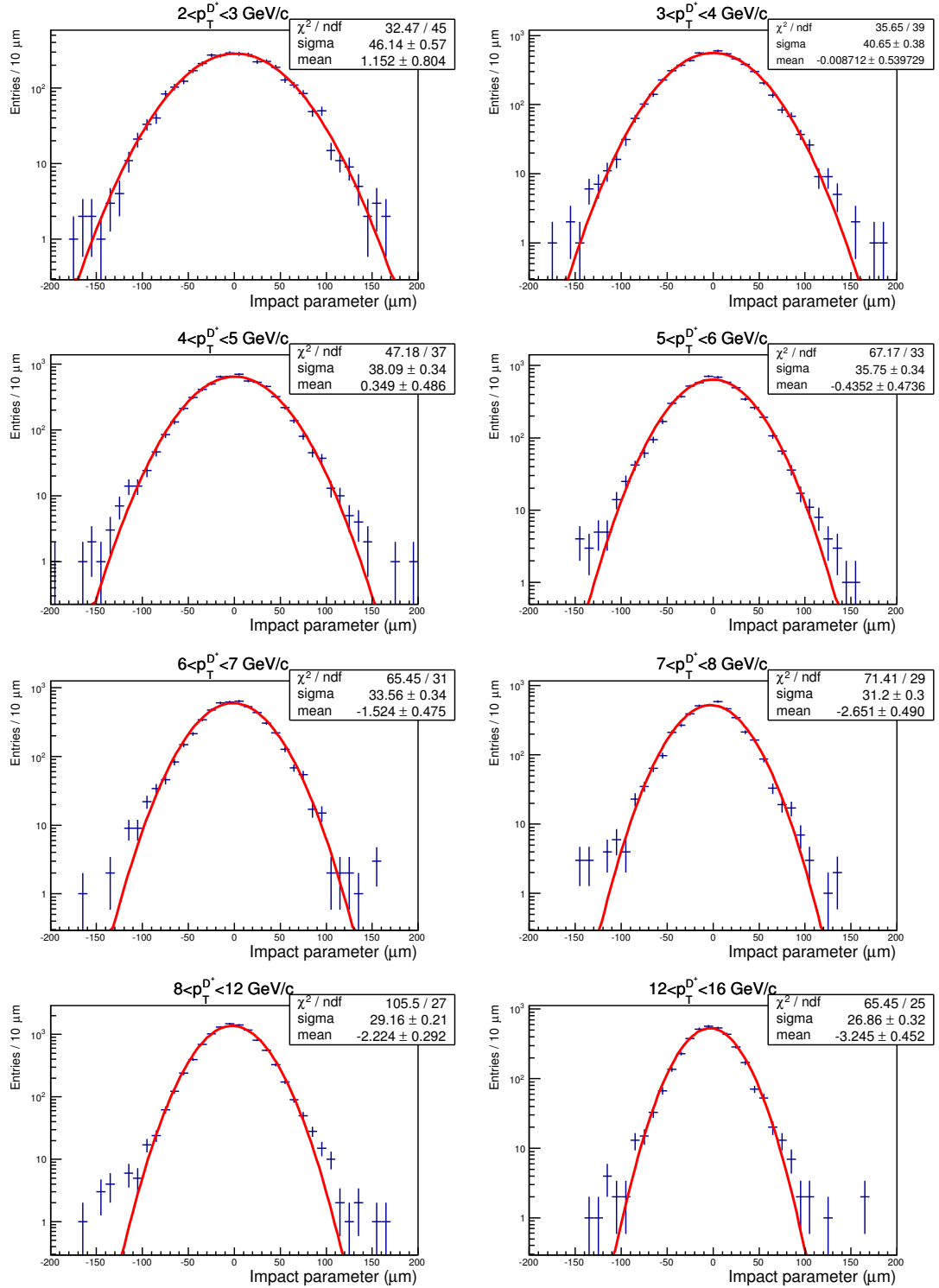


FIGURE 6.3: Impact parameter (a_0^{xy}) distribution of prompt D^+ mesons in eight p_T bins from MC simulations. The gaussian fit is also shown.

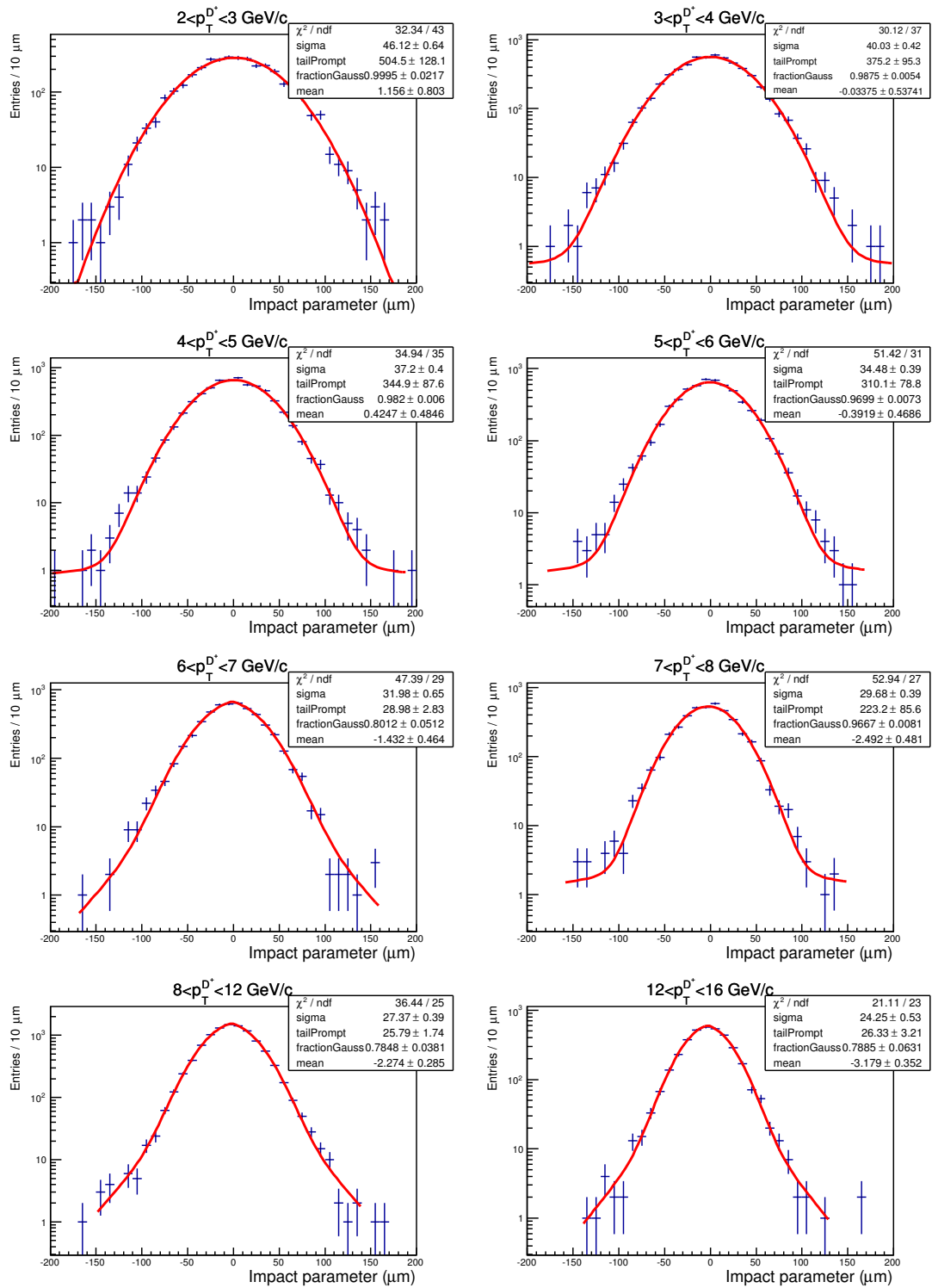


FIGURE 6.4: Impact parameter (d_0^{xy}) distribution for prompt D^+ mesons in eight p_T bins from MC simulations. The gaussian-exponential fit of Equation 6.1 is also shown.

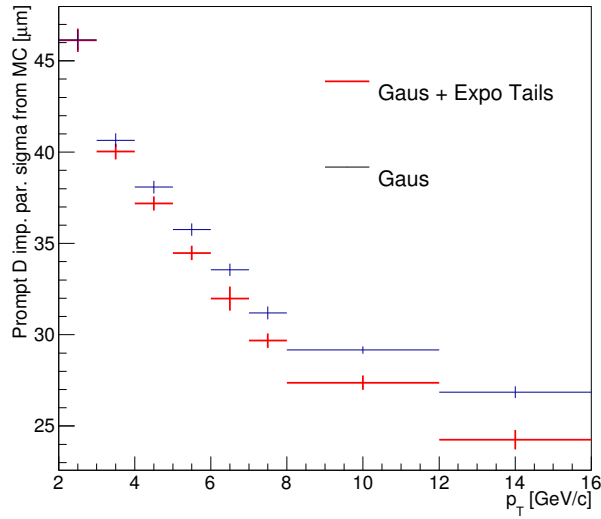


FIGURE 6.5: Gaussian width σ_{prompt} values obtained with both the simple gaussian fit and the fit of Equation 6.1 as a function of p_T .

First of all, as visible in Figure 6.6 (left), for the same angle between the B-hadron and D^+ -meson flight lines $\Delta\varphi$ (we limit ourselves to the plane transverse to the beam axis¹), the resulting D^+ -meson impact parameter depends on the distance travelled by the B-hadron L_B : $d_0^{xy} = L_B \sin \Delta\varphi$. The distribution of L_B in turn depends on the p_T of the beauty hadron due to the Lorentz boost.

Figure 6.6 (right) is obtained generating B^+ mesons with PYTHIA 6 and making them decay in channels containing a D^+ meson, and corresponds to the scatter plot of daughter D^+ p_T as a function of parent B^+ p_T . The p_T spectrum of the generated B^+ mesons is

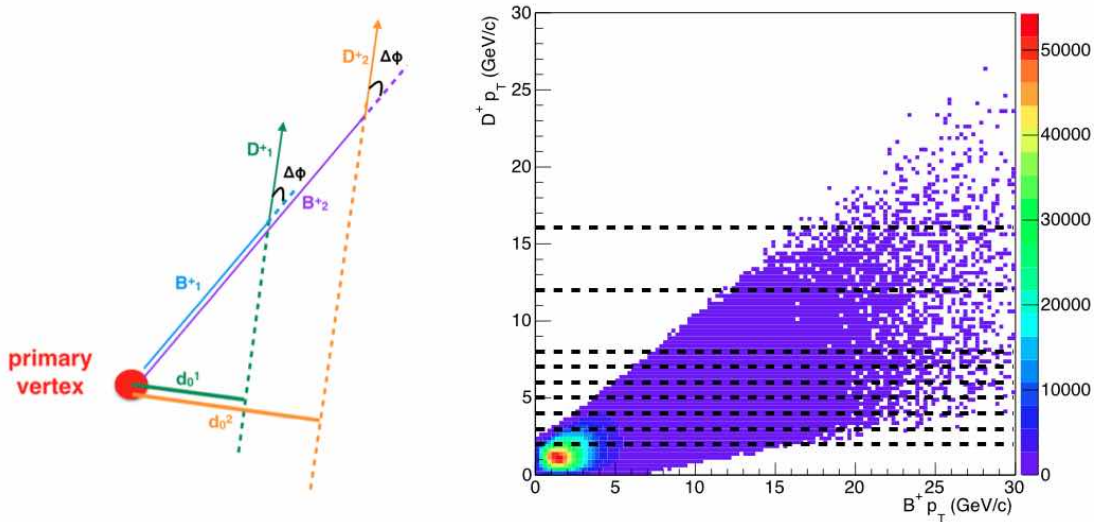


FIGURE 6.6: Left: Projection on the plane transverse to the beam axis of the decay of two B^+ mesons with different decay lengths into D^+ . Both decays have the same $\Delta\varphi$ between parents and daughters tracks. Right: scatter plot of parent B^+ p_T vs daughter D^+ p_T from PYTHIA simulations.

¹For the definition of the ALICE Coordinate System see Appendix B

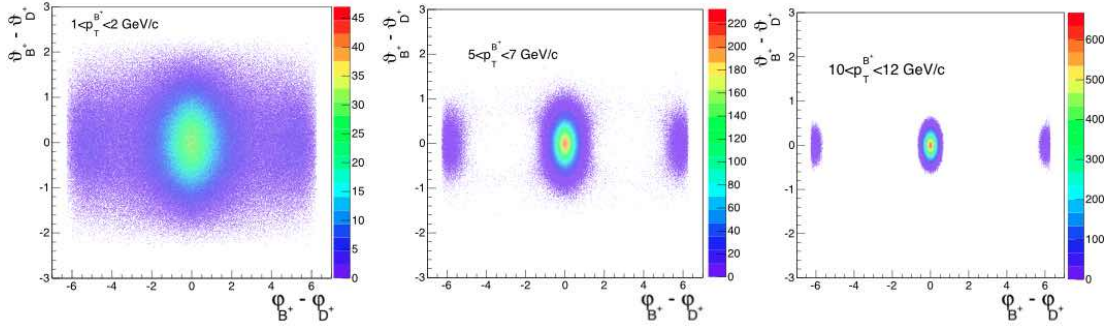


FIGURE 6.7: Scatter plot of the difference in radial angle $\Delta\varphi$ and azimuthal angle $\Delta\theta$ between the generated parent B^+ meson and the daughter D^+ meson as obtained with PYTHIA 6 in $1 < p_T^{B^+} < 2$ GeV/c, $5 < p_T^{B^+} < 7$ GeV/c, $10 < p_T^{B^+} < 12$ GeV/c.

taken from FONLL. The D^+ -meson p_T bins used in this analysis are shown as dashed lines. As one can see, for a given D^+ p_T interval the range of values for the parent B^+ meson p_T is broad (10–20 GeV/c), which results in a wide p_T distribution of B^+ -hadron decay length. We thus expect the distribution of D^+ -meson impact parameter in a given D^+ -meson transverse momentum bin to receive contributions from B^+ mesons with a wide range of decay lengths, given by the proper decay length $c\tau$ and by the γ factor of the B^+ meson.

However another aspect has to be taken into account. Figure 6.7 shows the scatter plot of the difference in polar angle² $\Delta\theta$ and azimuthal angle $\Delta\varphi$ between the generated B^+ meson and the D^+ meson from its decay as obtained with PYTHIA 6 for three B^+ p_T bins. Due to the Lorentz boost at high p_T the D^+ mesons flight line tends to be parallel to that of the parent B^+ hadron. The effect of the Lorentz boost results on average in a decrease of the feed-down D^+ -meson impact parameter.

The true impact parameter (d_0^{xy}) distributions of feed-down D^+ -meson obtained from the MC data sample described in Section 4.2.1 are shown in Figure 6.8 in the eight p_T bins considered in this analysis. Only the feed-down D^+ mesons passing the selection criteria described in Section 5.1 are included. The distributions are fitted with the sum of two exponentials

$$f_{\text{true}}^{\text{feed-down}}(d_0^{xy}) = A \left[(1 - f_{\lambda_2^{\text{FD}}}) \frac{1}{2\lambda_1^{\text{FD}}} e^{-\frac{|d_0^{xy} - \mu|}{\lambda_1^{\text{FD}}}} + f_{\lambda_2^{\text{FD}}} \frac{1}{2\lambda_2^{\text{FD}}} e^{-\frac{|d_0^{xy} - \mu|}{\lambda_2^{\text{FD}}}} \right] \quad (6.2)$$

Each exponential is governed by a slope parameter, λ_1^{FD} and λ_2^{FD} , respectively, and they have common mean value μ . The fit range considered increases with increasing p_T to take into account the broadening of the distributions with transverse momentum. The χ^2 values show that this functional form gives an acceptable description of the distributions from MC simulations.

The impact parameter distributions for D^+ mesons after the reconstruction are shown in Figure 6.9. Only the feed-down D^+ mesons passing the selection criteria described in Section 5.1 are included. The functions superimposed in Figure 6.9 are not a fit to the distributions. They are the convolution of $f_{\text{true}}^{\text{feed-down}}(d_0)$ obtained from the fit to the D^+ -meson true impact parameter distributions shown in Figure 6.8 and a Gaussian which has the same width σ_{prompt} of the prompt D^+ -meson impact parameter distribution in

²See Appendix B

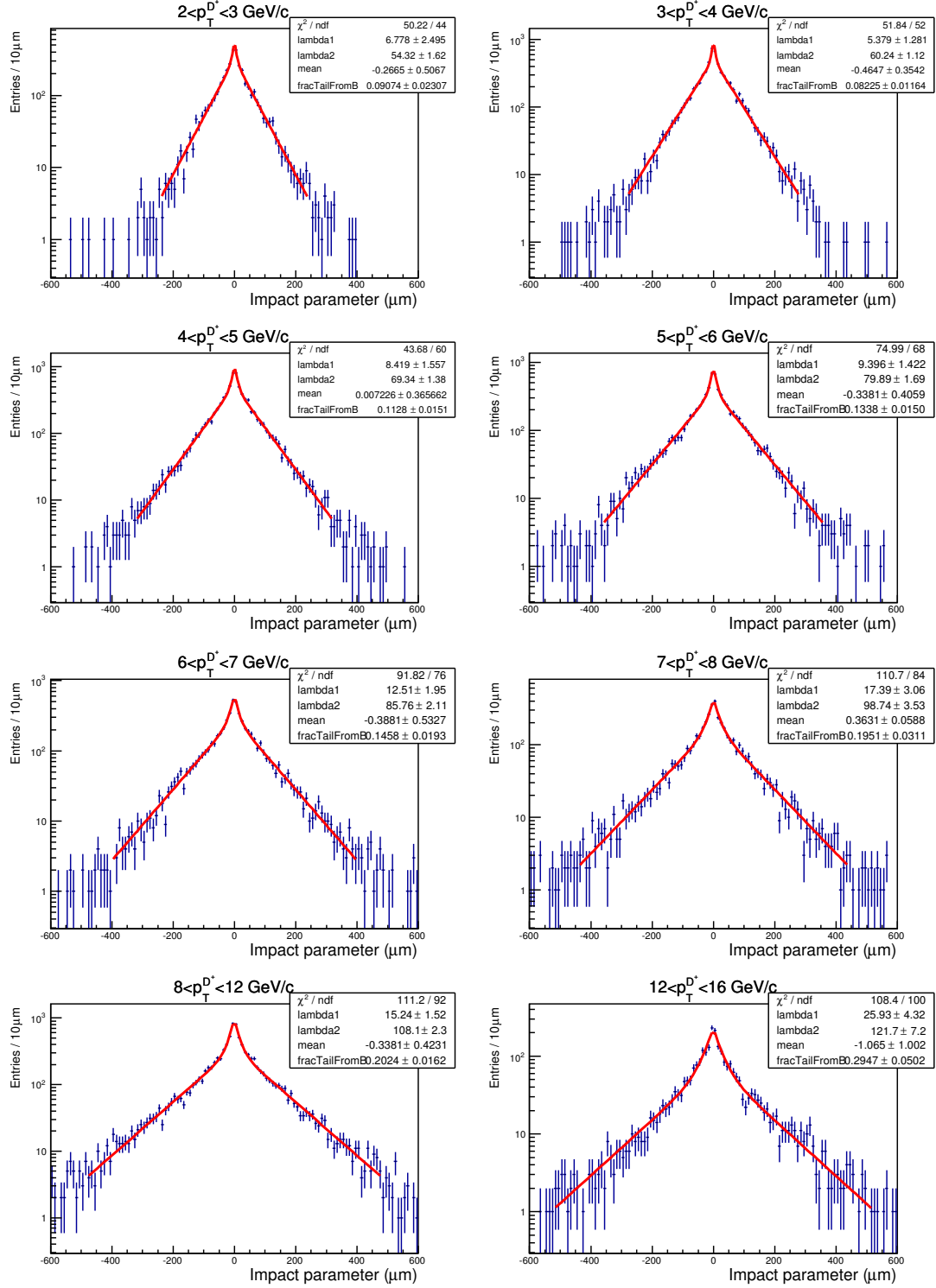


FIGURE 6.8: Impact parameter (d_0^{xy}) distributions of feed-down D^+ -meson in eight p_T bins from MC simulations, using the true value of D^+ impact parameter. The double-exponential fit of Equation 6.2 is also shown.

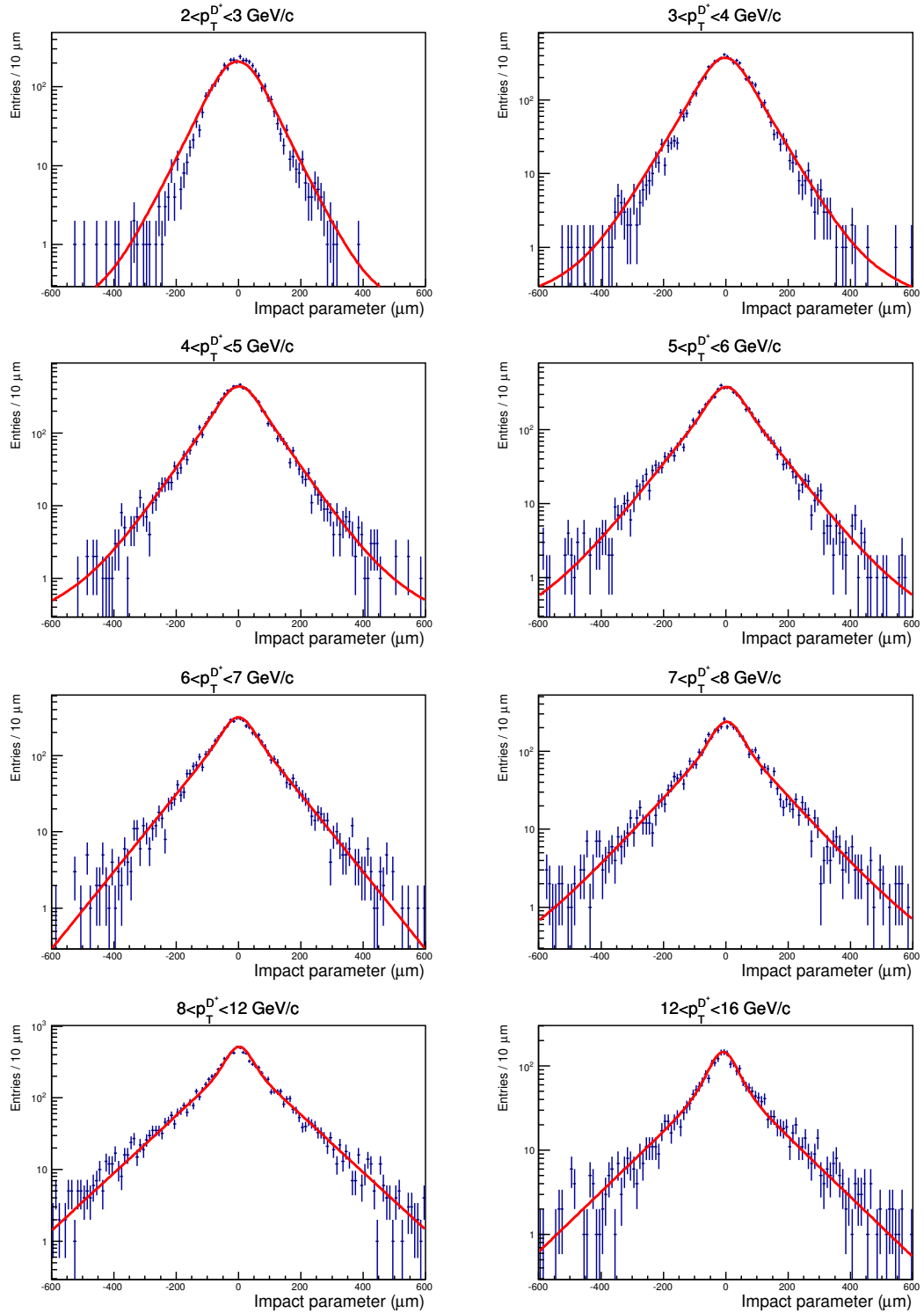


FIGURE 6.9: Impact parameter (d_0^{xy}) distributions of feed-down D^+ -meson in eight p_T bins from MC simulations, using the reconstructed value of D^+ impact parameter. The convolution of Equation 6.3 is also shown.

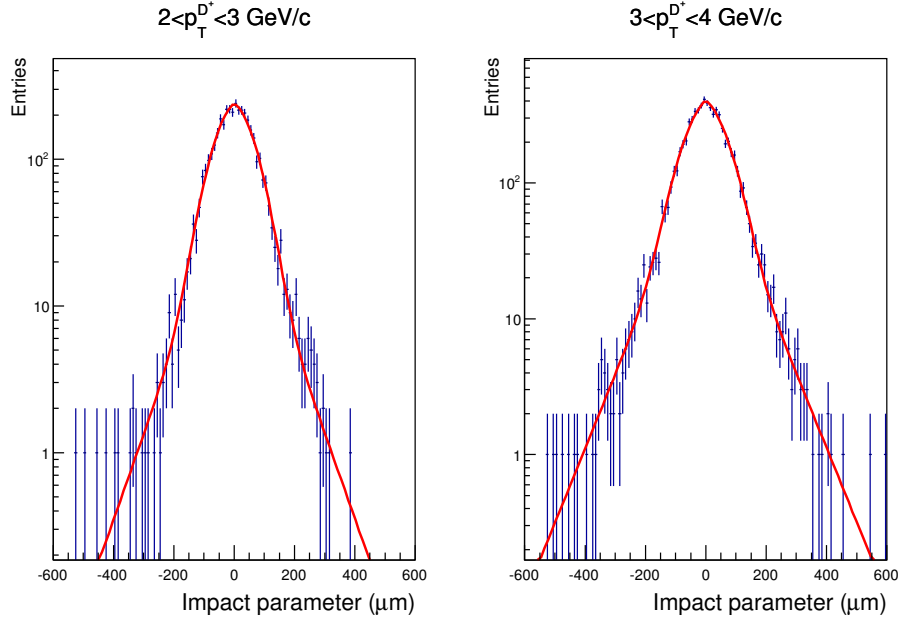


FIGURE 6.10: Impact parameter (d_0^{xy}) distributions of feed-down D^+ -meson in $2 < p_T < 3$ GeV/c (left) and $3 < p_T < 4$ GeV/c from MC simulations, using the reconstructed value of D^+ impact parameter. The distributions are fitted with the functional form of Equation 6.1.

the corresponding p_T bin

$$F^{\text{feed-down}}(d_0^{xy}) = A \int_{d_0^{\text{max}}}^{d_0^{\text{min}}} \left[f_{\text{true}}^{\text{feed-down}}(d'_0; \lambda_1^{\text{FD}}, \lambda_2^{\text{FD}}) \right] \left[\frac{1}{\sqrt{2\pi}\sigma_{\text{prompt}}} e^{-\frac{(d_0^{xy}-d'_0)^2}{2\sigma_{\text{prompt}}^2}} \right] dd'_0 \quad (6.3)$$

where A is the integral of the impact parameter distributions for D^+ mesons after the reconstruction in the corresponding p_T bin, $d_0^{\text{min}} = -600 \mu\text{m}$ and $d_0^{\text{max}} = 600 \mu\text{m}$. The functions show good agreement with the distributions except for $p_T < 4$ GeV/c. In these p_T bins a fit performed with the same functional form of Equation 6.1 gives a better description of the MC distribution as shown in Figure 6.10.

6.1.3 Impact Parameter distributions in data

The impact parameter distributions from the p-Pb data sample collected with the minimum bias trigger described in Section 4.2.1 are obtained as described in the following. I will show the procedure in the p_T bin $4 < p_T < 5$ GeV/c.

After applying the same event, track quality, topological and PID selections used to extract the D^+ -meson cross-section and nuclear modification factor shown in Chapter 5, we obtain the invariant mass (M) distribution of the selected D^+ -meson candidates as shown in Figure 6.11 (left). The impact parameter distribution for the same selected candidates in the p_T bin $4 < p_T < 5$ GeV/c is shown in Figure 6.11 (right).

The left panel of Figure 6.11 (left) also shows the fit to the invariant mass distribution, where the signal is described by a Gaussian with width $\sigma^{\text{peak}} = 10$ MeV/c and mean $M^{\text{peak}} = 1.869$ GeV/c. We define as **sideband** region the invariant mass region for which $|M - M^{\text{peak}}| > 3\sigma^{\text{peak}}$.

The method of the sideband subtraction aims at extracting the impact parameter distributions for signal candidates which are truly D^+ mesons. To achieve this goal it is necessary to eliminate the D^+ -meson background candidates under the D^+ -meson mass peak.

The starting assumption is that the impact parameter distribution of background candidates under the D^+ -meson peak are similar to the average of the same distributions of candidates in the sideband regions.

Figure 6.12 (right) shows the impact parameter distributions of candidates with $4 < p_T < 5$ GeV/c for different invariant mass intervals in the sideband regions. Each interval is characterized by a $n\sigma^{\text{peak}}$ value and has a width of $5\sigma^{\text{peak}}$ (50 MeV/c²) as indicated in the left panel of Figure 6.12. In Figure 6.13 (left) the four impact parameter distributions are normalized to their integral to see if their shape changes significantly depending on the invariant mass interval considered. This is not the case, as clearly visible in the right panel of Figure 6.13 where the ratio of the distributions at 6,8 and 10 σ^{peak} to the one obtained at $4\sigma^{\text{peak}}$ is shown. This proves the stability of the impact parameter distribution in different intervals of invariant mass. In the following I will use the impact parameter distributions of candidates with M in $5 < |M - M^{\text{peak}}| / \sigma^{\text{peak}} < 10$ to estimate the background under the D^+ peak.

Figure 6.14 (right) shows the impact parameter distribution for candidates in the signal region, defined as $|M - M^{\text{peak}}| < 1.5\sigma^{\text{peak}}$. The signal invariant mass range is the one included in the green area of Figure 6.14 (left). Within $1.5 \sigma^{\text{peak}}$ from the mass peak we expect to have 1449 signal candidates and 1582 background candidates. The impact parameter distribution of background candidates estimated from the side-bands was normalized to the number of background candidate expected in the signal region (red histogram of Figure 6.15 (left)) and was subtracted from the impact parameter distribution of candidates with $|M - M^{\text{peak}}| < 1.5\sigma^{\text{peak}}$ to obtain the impact parameter distribution of true D^+ mesons³. The result of the sideband subtraction is shown in Figure 6.15 (right)

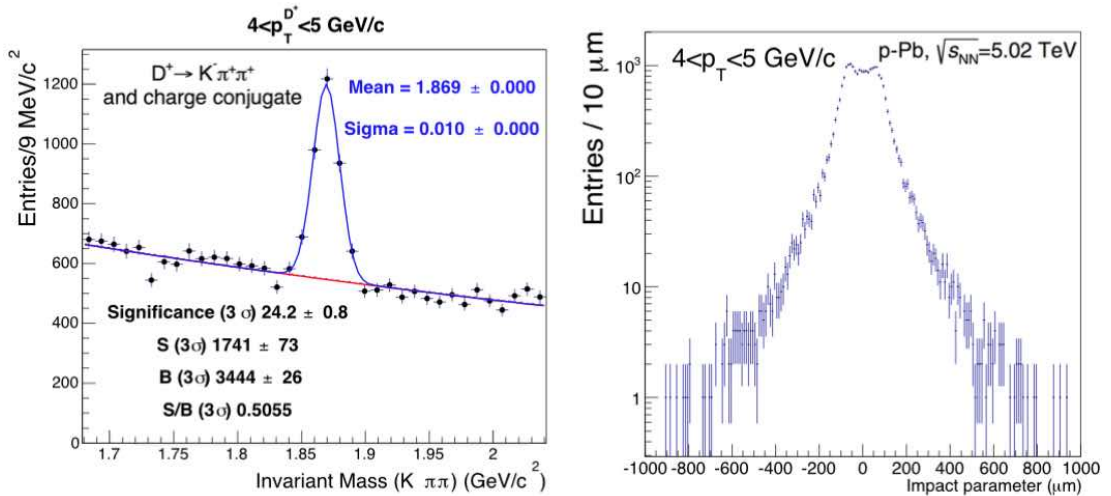


FIGURE 6.11: Left: invariant mass (M) distribution of the selected D^+ -meson candidates in the p_T interval $4 < p_T < 5$ GeV/c after applying the same event, track quality, topological and PID cuts used in Chapter 5. Right: impact parameter (d_0^{xy}) distribution of the same candidates shown in the left panel.

³One can object that the impact parameter distribution of D^+ mesons with reconstructed invariant mass M within $1.5 \sigma^{\text{peak}}$ from the mass peak does not include all the true D^+ -meson candidates in the p_T bin considered. The variation of $n\sigma^{\text{peak}}$ will be considered to evaluate the systematic.

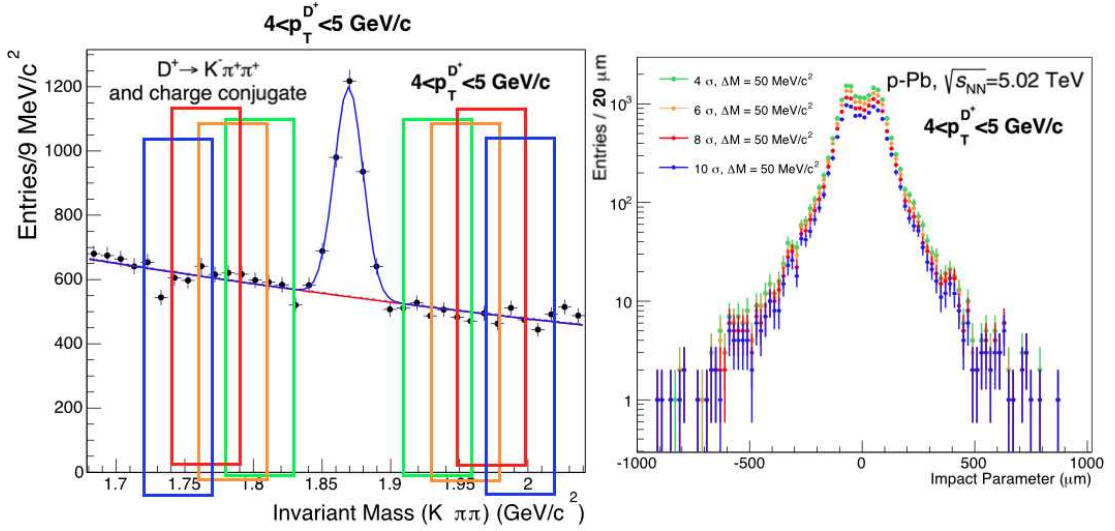


FIGURE 6.12: Left: same invariant mass distribution shown in Figure 6.11. Right: impact parameter distributions of the candidates with invariant mass lying within the four coloured boxes in the left panel.

for the p_T bin $4 < p_T < 5$ GeV/c.

The result of the sideband subtraction in the eight p_T bins considered in this analysis is shown in Figure 6.16.

6.2 Fit method

The method used to fit the impact parameter distribution of D^+ mesons to extract the fraction of prompt yield is composed of two steps: a prefit phase performed on the MC distributions, and fit phase performed on the sideband subtracted impact parameter distributions of data.

In the prefit step, the impact parameter distributions of prompt D^+ mesons from MC

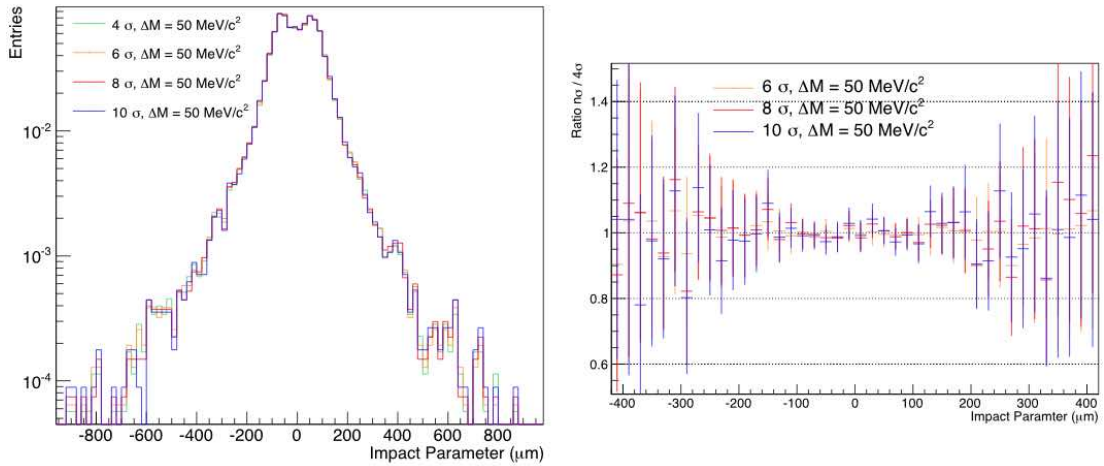


FIGURE 6.13: Left: same impact parameter distributions shown in Figure 6.12 normalized to their area. Right: ratio of the impact parameter distributions obtained at 6, 8 and 10 σ^{peak} from the invariant mass peak and that obtained at 4 σ^{peak} .

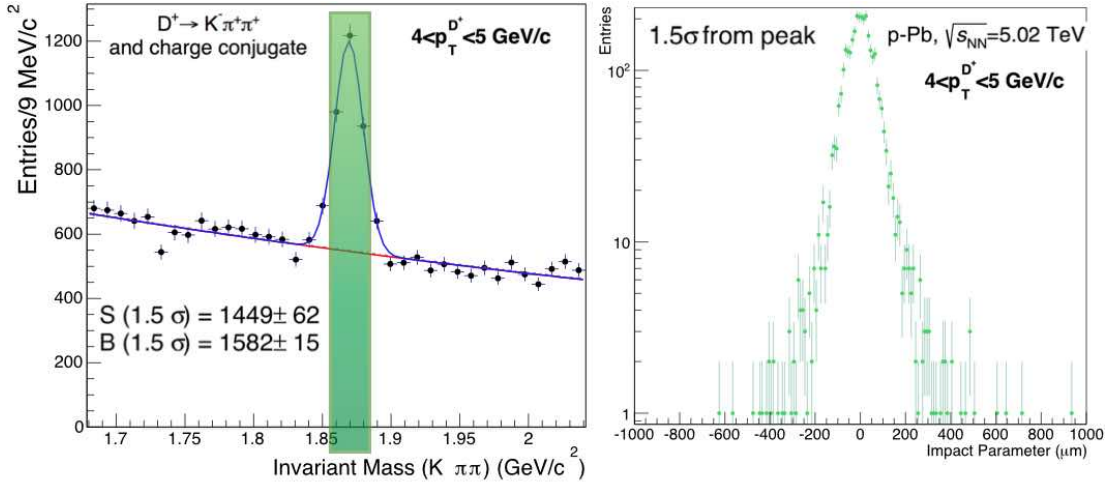


FIGURE 6.14: Left: same invariant mass distribution shown in Figure 6.11. Right: impact parameter distributions of the candidates within $1.5 \sigma^{peak}$ from the D^+ -meson peak.

simulations are fitted with the functional form of Equation 6.1, the fit results for F^{prompt} are reported in Figure 6.4. This fit yields three parameters: λ^{prompt} , σ^{prompt} and μ^{prompt} , which characterize the slope of the exponential tails and the width and mean of the Gaussian function.

Then the impact parameter distributions of true feed-down D^+ mesons from MC simulations are fitted with the functional form of Equation 6.2. The fit results are reported in Figure 6.8. This fit yields three parameters: λ_1^{FD} , λ_2^{FD} and μ^{FD} . Keeping these parameters fixed, the function obtained from the fit is convoluted with a gaussian according to Equation 6.3. The width of the convoluted gaussian is fixed to σ^{prompt} . The result of the convolution F^{FD} are shown in Figure 6.9.

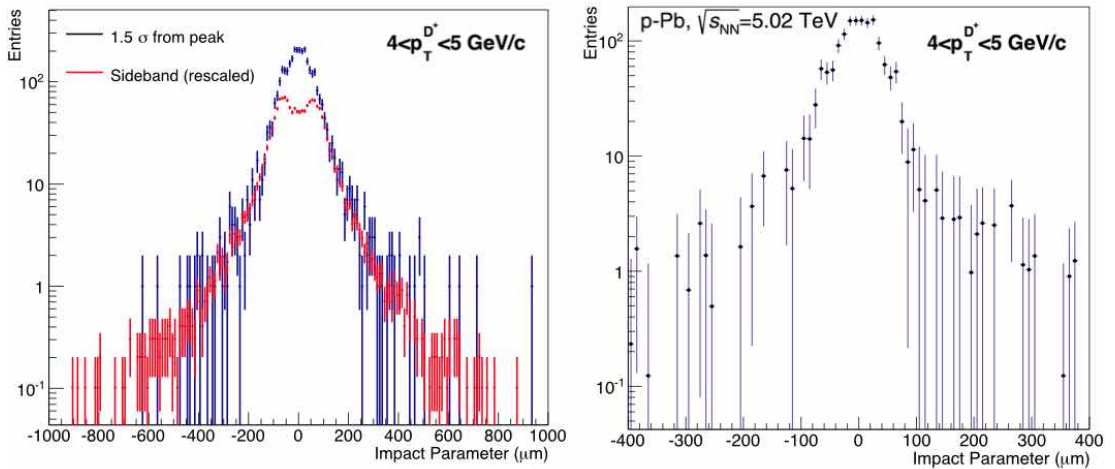


FIGURE 6.15: Left: impact parameter distributions of candidates in the signal region, i.e. within $1.5 \sigma^{peak}$ from the D^+ peak (black) together with the impact parameter distribution of the candidates in the sideband region, i.e. with $5 < |M - M_{peak}| / \sigma^{peak} < 10$ rescaled to the total amount of background present within $1.5 \sigma^{peak}$ from the invariant mass peak. Left: impact parameter distribution of candidates in the signal region after sideband subtraction.

At this point the final fit on the impact parameter distributions of data can be performed. The sideband subtracted impact parameter distribution is fitted with the following function

$$F^{D^+}(d_0) = A \left[(1 - f_{\text{prompt}}) F^{\text{FD}}(d_0) + f_{\text{prompt}} F^{\text{prompt}}(d_0) \right] \quad (6.4)$$

where A is the integral of the sideband subtracted impact parameter distribution and f_{prompt} is the fraction of prompt D^+ mesons. The fit is performed under the following conditions:

- the parameters $\lambda_1^{\text{FD}}, \lambda_2^{\text{FD}}$ and λ^{prompt} are fixed to those obtained in the prefit phase
- the parameters $\mu^{\text{Prompt}}, \mu^{\text{FD}}$ are set to 0
- the parameter A is fixed to the integral of the sideband subtracted impact parameter distribution

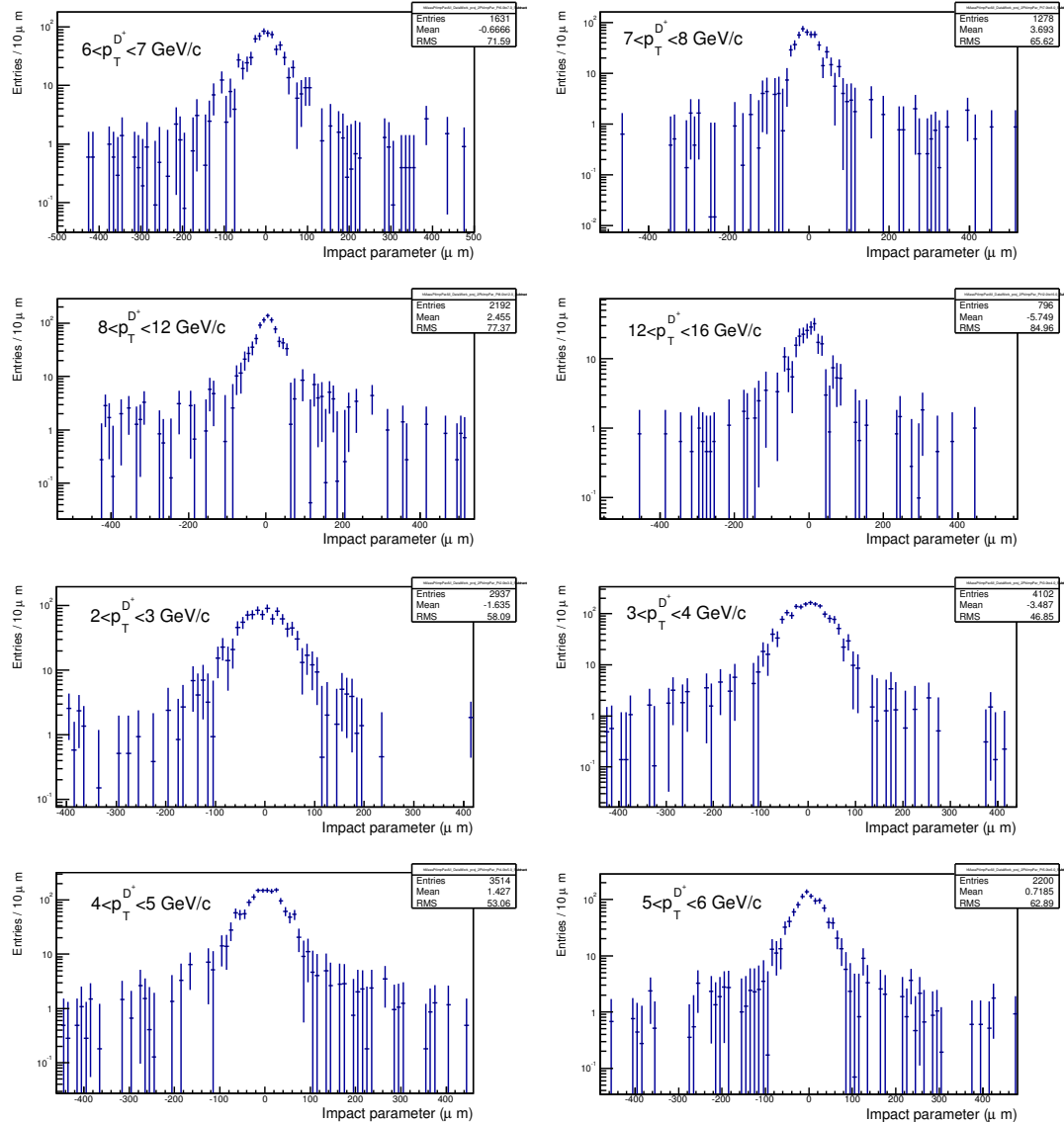


FIGURE 6.16: Data impact parameter distributions after sideband subtraction in eight p_T intervals.

- the parameter σ_{prompt} is free to vary within 20% around the value obtained in the prefit step on the prompt D^+ -meson impact parameter distribution from MC simulations
- the parameter f_{prompt} is bound between 0 and 1

The results of the fit are shown as red curves in Figure 6.17 in the eight p_T intervals considered in the analysis. The fit range gradually increases at high p_T to better account for the broadening of the distributions. The fraction of the total fit function corresponding to the feed-down component is represented by the green curves.

The values of $\chi^2/\text{n.d.f.}$ do not exceed 1.2, reaching a minimum of 0.64 in the p_T interval $12 < p_T < 16$ GeV/c where the relative statistical uncertainties of the sideband subtracted distribution become large due to the limited statistics. The values of σ_{prompt} obtained from the final fit in the different p_T bins are compared to those obtained in the prefit phase in Figure 6.18 (left). None of the final values of σ_{prompt} is at limit with respect to the 20% bound imposed in the fit.

Finally Figure 6.18 (right) shows the resulting values of f_{prompt} as a function of p_T .

6.3 Systematic uncertainties

Three sources of systematic uncertainties are considered in this analysis:

- systematic uncertainty due to the fit method used
- systematic uncertainty due to the sideband subtraction
- systematic uncertainty due to the p_T shape of generated D^+ mesons in MC

6.3.1 Systematic uncertainty on fit method

The systematic uncertainty on the fit method described in Section 6.2 was evaluated in the following way:

- the impact parameter fit range was reduced by 100 μm in each p_T interval
- the impact parameter fit range was increased by 100 μm in each p_T interval
- the bin width used for the impact parameter distribution was reduced from 10 to 5 μm
- the parameter σ_{prompt} was fixed to the one obtained in the prefit phase on MC simulations
- The function of Equation 6.1 was used to describe the feed-down contribution in the fit instead of the convolution of Equation 6.3. The function parameters were initialized fitting the impact parameter distribution for reconstructed feed-down D^+ -meson candidates, as shown in Figure 6.10

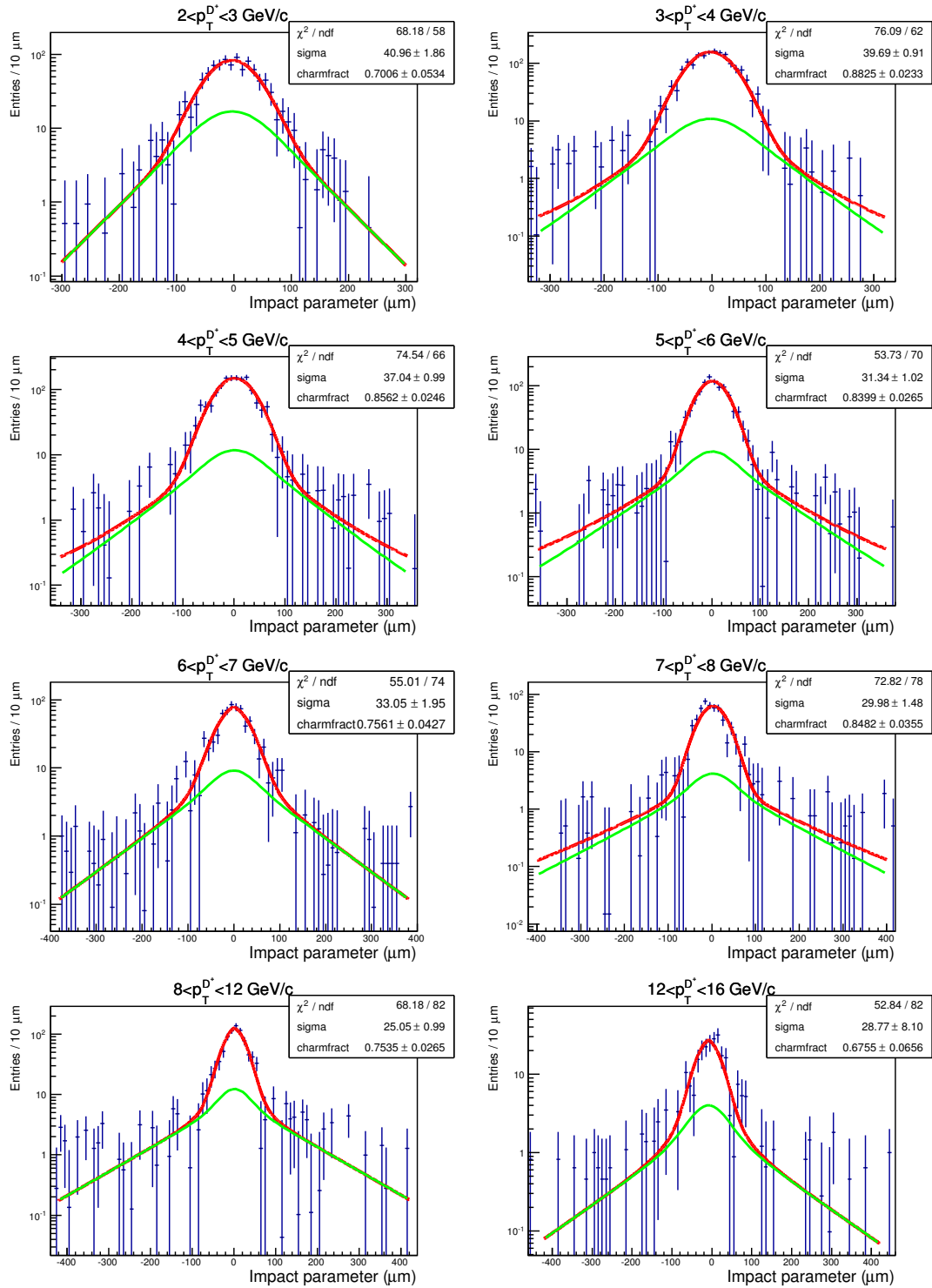


FIGURE 6.17: Fit to the sideband subtracted impact parameter distributions in eight p_T intervals. The red curves are the total fit function, the green ones represent the feed-down contribution.

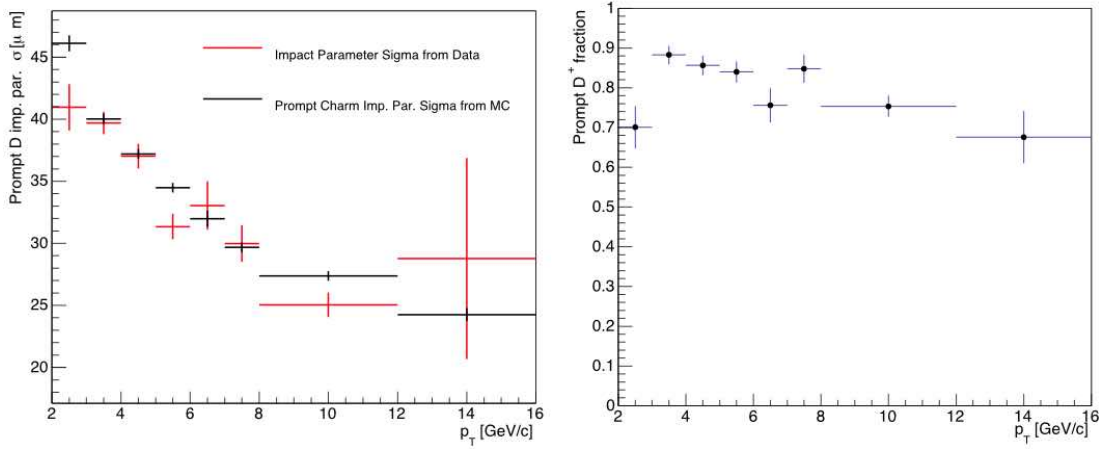


FIGURE 6.18: Left: values of σ_{prompt} obtained from the final fit to the data in the different p_T intervals compared to those obtained in the prefit phase. Right: f_{prompt} obtained from the fit as a function of p_T .

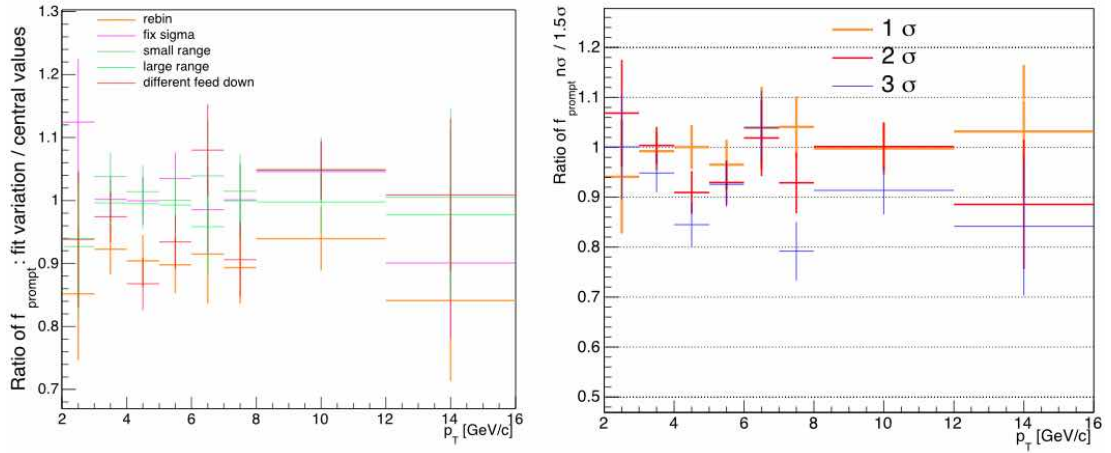


FIGURE 6.19: Left: ratio of the f_{prompt} values obtained varying the fit conditions and the central values. Right: ratio of f_{prompt} from the fit performed to D^+ mesons in the invariant mass ranges within 1, 2 and 3 σ^{peak} from the D^+ peak and the f_{prompt} central values ($1.5 \sigma^{\text{peak}}$ from the D^+ peak).

Figure 6.19 (left) shows the ratio of the f_{prompt} values obtained with the variations described above and the central values shown in Figure 6.18 (right). The systematics were assigned by the best estimate of the R.M.S. of the results as 10% for $3 < p_T < 12$ GeV/c and 15% for $p_T > 12$ GeV/c and $p_T < 3$ GeV/c.

6.3.2 Systematic uncertainty on sideband subtraction

This systematic uncertainty due to the definition of the invariant mass regions from which the signal and background impact parameter are extracted was estimated by repeating the fit described in Section 6.2 changing the number of σ from the peak in the invariant mass distribution in which the impact parameter distribution for signal is evaluated. The background distribution was proved not to change significantly in different invariant mass intervals of the sideband region.

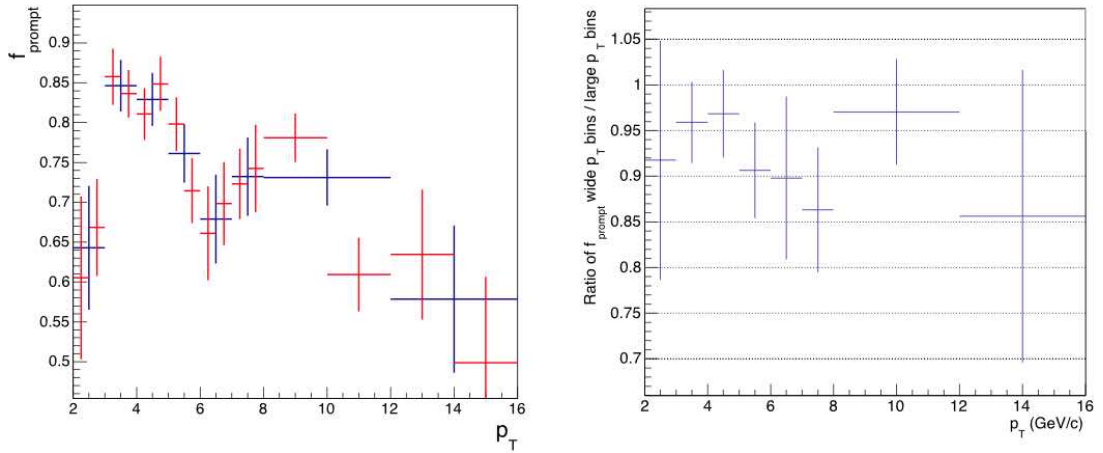


FIGURE 6.20: Left: f_{prompt} values obtained performing the analysis in finer p_T bins (red) and f_{prompt} values obtained in the standard p_T bins by combining the results in the finer bins (blue). Right: ratio of f_{prompt} values obtained combining the results in finer p_T bins to the central values

Figure 6.19 shows the ratio of the f_{prompt} values extracted from fits to impact parameter distributions of D^+ mesons measured within 1, 2 and 3 σ^{peak} from the invariant mass peak and the f_{prompt} value obtained with the standard fit performed in Section 6.2 within 1.5 σ^{peak} . The values of f_{prompt} obtained using candidates within 1 and 2 σ^{peak} seem to fluctuate around unity and do not show significant discrepancies from the central values. The values of f_{prompt} measured from D^+ candidates in a range within 3 σ^{peak} indicate a systematic shift to lower values of f_{prompt} for $p_T > 4$ GeV/c. For this reason, no systematic was assigned for $p_T < 4$ GeV/c, while a systematic uncertainty of ${}^{+0}_{-10}\%$ was assigned for $p_T > 4$ GeV/c.

6.3.3 Systematic uncertainty on the p_T shape of generated D^+ mesons in MC

The fit relies on the MC templates shown in Section 6.1, which are obtained in p_T intervals of finite size. Since the impact parameter distributions vary as a function of p_T , a discrepancy between the p_T shape of real and simulated D^+ mesons would result in a biased shape of the impact parameter distributions of the MC templates, especially in large bins like $12 < p_T < 16$ GeV/c.

To quantify this effect, the fit described in Section 6.2 was repeated in finer p_T intervals resulting in the f_{prompt} values shown by the red points in Figure 6.20 (left). The values of f_{prompt} in the fine p_T intervals were then combined together to obtain the f_{prompt} values in the wider p_T bins also shown in Figure 6.20 (blue points - left). This was done by making a weighted average of the f_{prompt} values in the corresponding fine p_T bins, using as weight the amount of signal in each of them.

The right plot of Figure 6.20 shows the ratio of f_{prompt} values obtained in this way to those obtained from the standard fit procedure (Figure 6.18). Despite the fluctuations of this ratio, all values indicate a systematic shift to lower values of f_{prompt} using finer p_T bins. This shift to lower values of f_{prompt} is smaller (${}^{+0}_{-4}\%$) for $p_T < 5$ GeV/c, and increases for $p_T > 5$ GeV/c, where a systematic of ${}^{+0}_{-10}\%$ was assigned.

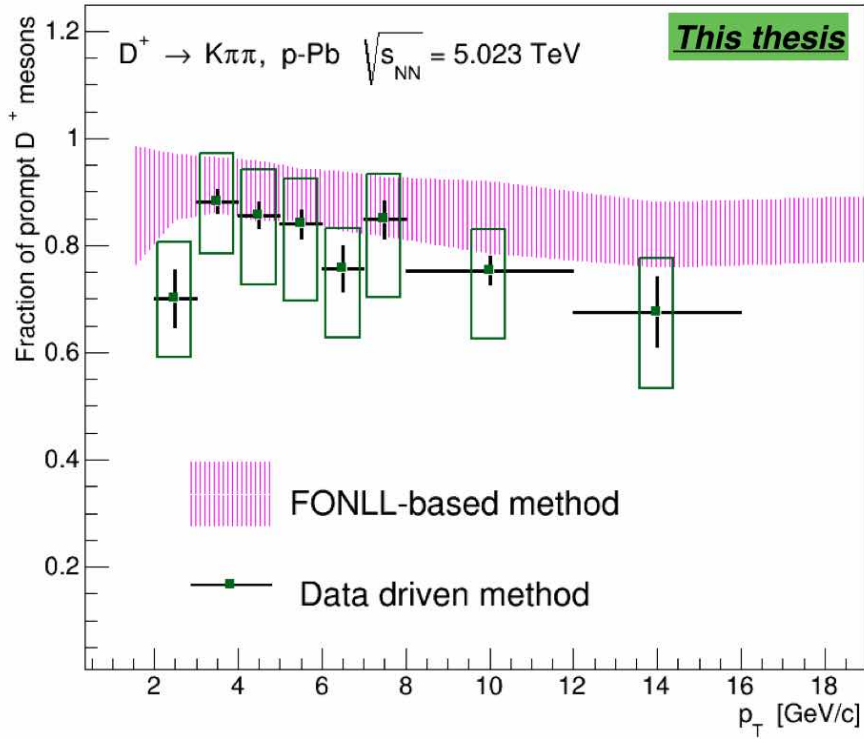


FIGURE 6.21: Results of f_{prompt} obtained from the data-driven approach. The solid bars represent the statistical errors, the green boxes the systematic errors. The FONLL predictions are represented by the pink band.

The three sources of systematic uncertainties are considered uncorrelated and summed in quadrature, as reported in Table 6.1.

p_T (GeV/c)	[2,3]	[3,4]	[4,5]	[5,6]	[6,7]	[7,8]	[8,12]	[12,16]
Fit method (%)	+15 -15	+10 -10	+10 -10	+10 -10	+10 -10	+10 -10	+10 -10	+15 -15
Sideband subtraction (%)	+0 -0	+0 -0	+0 -10	+0 -10	+0 -10	+0 -10	+0 -10	+0 -10
p_T shape (%)	+0 -4	+0 -4	+0 -4	+0 -10	+0 -10	+0 -10	+0 -10	+0 -10
Total (%)	+15 -16	+10 -11	+10 -15	+10 -17	+10 -17	+10 -17	+10 -17	+15 -21

TABLE 6.1: Summary table of the systematic uncertainties on the data-driven beauty feed-down analysis.

6.4 Results

The results for f_{prompt} obtained with the data-driven approach described in the previous sections are shown in Figure 6.21. The error bars represent the statistical uncertainties, the green boxes the systematic ones.

The f_{prompt} values obtained from the fit are compared to the FONLL ones, which were used in the previous Chapter to subtract the feed-down contribution and are represented by the magenta band. This magenta band includes the envelope of the systematic uncertainties on the f_{prompt} theory-driven calculation (pQCD FONLL parameters and feed-down D^+ energy loss hypothesis).

The two methods to determine f_{prompt} provide results which are compatible within uncertainties in all p_{T} intervals except in $2 < p_{\text{T}} < 3$ GeV/c.

The total systematic uncertainties of both methods are compared in Table 6.2. The theory-driven method shows smaller uncertainties in the whole p_{T} range considered.

p_{T} (GeV/c)	[2,3]	[3,4]	[4,5]	[5,6]	[6,7]	[7,8]	[8,12]	[12,16]
Theory-driven (%)	+3% -11%	-3% -7%	+3% -5%	+3% -4%	+3% -4%	+3% -3%	+4% -3%	+5% -3%
Data-driven (%)	+15% -16	+10% -11	+10% -15	+10% -17	+10% -17	+10% -17	+10% -17	+15% -21

TABLE 6.2: Summary table of the systematic uncertainties on the data-driven and FONLL driven beauty feed-down analysis.

However, the higher statistics expected for LHC Run II will help reduce all sources of systematic uncertainties on the data-driven measurement for the following reasons:

- the analysis could be performed in narrower p_{T} intervals, especially at high p_{T} , thus reducing the influence of the MC p_{T} shape of generated D^+ mesons on the templates
- the larger number of D^+ mesons would result in a higher population in the regions of the sideband subtracted histogram at large values of impact parameter, which are crucial in the fit since they correspond to the intervals dominated by feed-down D^+ mesons. This would give a tighter constraint to the fit and would reduce the systematic on the fit method
- a higher signal over background could be obtained since with a higher statistic tighter cuts could be used. This would reduce the amount of background to be subtracted and would lead to smaller fluctuations in the sideband subtracted impact parameter distribution

If we then consider a slightly larger timescale (~ 2018), the improvements expected from the upgrade of the ALICE Inner Tracking System will provide a substantial improvement in the tracking and vertexing performance of the ALICE detector, and consequently on the impact parameter which is crucial in the discrimination between the prompt and feed-down D^+ (and also D^0 , D^{*+} ...) mesons. This, together with the higher acquisition rate expected after the ALICE TPC upgrades, would reduce the error on the f_{prompt} measurement and could also allow a measurement of $f_{\text{feed-down}}$ with reasonable error, that in turn can be used to compute the cross section of D^+ mesons from beauty decays.

Chapter 7

D⁺-meson production as a function of multiplicity

As discussed in the introduction of Chapter 5, some of the results obtained in p–Pb collisions at the LHC may indicate the presence of final state effects: the ridge-like structure observed in the two-particle correlation function at high multiplicities [128] may be the consequence of a hydrodynamic evolution after the collision, while the Ψ' nuclear modification factor at forward and backward rapidities [126] revealed a larger suppression of this meson species with respect to J/Ψ suggesting the presence of a mechanism acting in the final state, after the formation of charmonia. In addition, also some of the initial state effects that are expected to modify charm quark production, such as nuclear shadowing and k_T broadening, are predicted to depend on the geometry of the collision, which is usually characterized in terms of centrality or impact parameter. It is thus worth to study the dependence of D⁺-meson production on multiplicity and event activity (Section 3.3.3), to verify if c -quark production and dynamics in p–Pb collisions is influenced by final state effects, such as energy loss and hydrodynamic expansion, to assess the dependence of initial state effects on the collision geometry, and to study the role of multiple hard partonic interactions occurring in a single collision.

In the first part of this chapter I will show the results of D⁺-meson $Q_{\text{pPb}}^{\text{mult}}$ (as defined in Section 3.3.3) as a function of event activity measured with the ZNA estimator. This measurement could reveal a dependence of D⁺-meson production on the event activity due to final state effects, like hydrodynamic flow or energy loss of c -quarks for high event activity values, in case the conditions to form a QGP are attained. Moreover, as discussed in Section 3.3.3, several sources of bias arise when trying to define $\langle N_{\text{coll}} \rangle$ in event activity classes in p–Pb collisions via multiplicity measurements. It is thus also interesting to study these biases using heavy flavour particles production, which is expected to scale with N_{coll} . Therefore the D⁺-meson $Q_{\text{pPb}}^{\text{V0A}}$ and $Q_{\text{pPb}}^{\text{CL1}}$ will be reported.

In the second part of this chapter, I will present a study of D⁺-meson production as a function of charged-particle multiplicity. Besides the possible presence of hydrodynamic effects at high multiplicities, this measurement is useful to assess several QCD mechanisms that have been observed in pp collisions and that will be now briefly discussed.

As discussed in Chapter 2, pQCD models describe the final state particles produced in hadronic collisions as the products of a hard partonic scattering process with large momentum transfer and an underlying event governed by energy scales below those at which pQCD is applicable. The measurement of heavy flavour production as a function of multiplicity of charge particles provides insight into the interplay between soft and

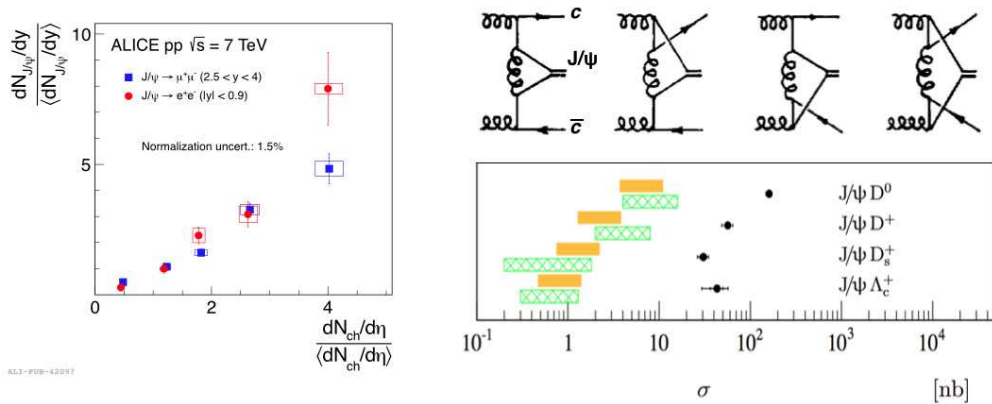


FIGURE 7.1: Left: J/Ψ yield as a function of charged particles multiplicity in pp collisions at $\sqrt{s} = 7$ TeV [145]. Right: production cross section of events with $J/\Psi + D$ mesons measured by the LHCb Collaboration, compared to predictions taking into account gluon fusion processes [146].

hard mechanisms governing particle production in hadronic collisions, which is expected to depend on the centre of mass energy and on the impact parameter of the collision. The generalized Parton Distribution Functions, corresponding to the nucleon transverse partonic structure measured at HERA via hard exclusive electroproduction of vector mesons and photoproduction of heavy quarkonia, show that gluons with $10^{-4} < x < 10^{-1}$ are localized at small transverse distances (0.4-0.5 fm) from the centre of the nucleon while gluons with lower values of Bjorken x occupy more distant regions. As shown in [143], in pp scattering this picture implies that hard processes mostly occur in central collisions, i.e. collisions with small impact parameter, where the areas occupied by partons in the relevant Bjorken x range overlap. Peripheral collisions, that constitute the dominant part of the overall inelastic cross section, are characterized by softer scales of momentum transfer.

In 1988 the NA27 Collaboration observed that events with open charm production have on average a higher charged particle multiplicity associated to a softening of the momentum spectra of produced hadrons in pp collisions at $\sqrt{s} = 28$ GeV [144]. At that time the results were interpreted as due to the fact that pp collisions in which charm is produced are on average more central than minimum-bias ones.

At LHC energies, two additional contributions to the multiplicity dependence of charm production in pp collisions have to be considered. The first is the larger amount of QCD radiation associated to the hard parton scattering processes leading to charm quark production. The second is the possible presence of Multi-Parton Interactions (MPI), i.e. several hard partonic interactions occurring in a single pp interaction. The presence of MPI constitutes a big difference with respect to the situation described in Figure 2.1, where one parton-parton scattering occurs and all other processes constitute the underlying event governed by soft energy scales.

CMS measurements of jet and underlying event properties have shown better agreement with models including MPIs [147] while ALICE studies on minijets point to an increase of MPIs with increasing charged-particle multiplicity [147].

If MPI were mainly affecting processes involving only light quarks and gluons, as implemented e.g. in PYTHIA 6.4, processes like J/Ψ and open heavy flavour production should not be influenced and their rates would be independent of the overall event multiplicity. However ALICE found an increase with approximately linear trend of J/Ψ yield as a function of multiplicity in pp collisions at $\sqrt{s} = 7$ TeV (left panel of Figure 7.1

[145]) that is not reproduced by PYTHIA 6.4. The LHCb Collaboration measured the production cross section of J/Ψ mesons accompanied by open charm, and of pairs of open charm hadrons in pp collisions at $\sqrt{s} = 7$ TeV [146]. The cross sections are shown in Figure 7.1 (right) together with predictions (yellow and green bands) from theoretical calculations taking into account gluon fusion processes ($gg \rightarrow J/\Psi + D$) only. Some examples of the gluon fusion processes leading to the production of J/Ψ mesons and open charm are shown in Figure 7.1. These predictions clearly underestimate the cross section measurements. On the other hand models taking into account double parton scattering better agree with the data.

In pA collisions we can expect a significant enhancement of MPIs. This is due to the fact that the rates of multi-parton interactions depend both on the initial-state partonic multiplicities present in the colliding system and on the density of partons in transverse space, which is higher in nuclei. However in p–Pb collisions events at high multiplicity can also be due to fluctuations in the number of binary collisions N_{coll} . It is also worth noting that in p–Pb events at $\sqrt{s_{\text{NN}}} = 5.02$ TeV the highest multiplicity values obtained are similar to the ones of Pb–Pb peripheral collisions at $\sqrt{s_{\text{NN}}} = 2.76$ TeV, keeping in mind that, as discussed in Chapter 5, the presence of final state effect such as hydrodynamic expansion is not excluded in p–Pb collisions.

It is thus interesting to verify if D^+ meson production depends on the overall event multiplicity in p–Pb collisions at $\sqrt{s_{\text{NN}}} = 5.02$ TeV, and to compare these results to those obtained in pp collisions.

7.1 D^+ -meson Q_{pPb}

In this section I will discuss the analysis aimed at the measurement of three different observables already shown and discussed in Section 3.3.3 for charged hadrons:

- $Q_{\text{pPb}}^{V0A}(p_T)$, obtained in four different intervals of event activity defined as percentiles of the V0A amplitude distribution. In this measurement the $\langle N_{\text{coll}} \rangle$ is estimated via a Glauber MC fit to the V0A amplitude distribution, as discussed in Section 3.3.2
- $Q_{\text{pPb}}^{CL1}(p_T)$, obtained in four different intervals of event activity defined as percentiles of the distribution of the number of clusters in the outer layer of the SPD in the range $|\eta| < 1.4$ (CL1). In this measurement the $\langle N_{\text{coll}} \rangle$ is estimated via a Glauber MC fit to the CL1 distribution
- $Q_{\text{pPb}}^{\text{mult}}(p_T)$, obtained in four different intervals of event activity defined as percentiles of the ZNA energy deposition distribution. In this measurement the $\langle N_{\text{coll}} \rangle$ is estimated with the hybrid method discussed in Section 3.3.3

Four event activity classes have been considered here, namely 0-20%, 20-40%, 40-60% and 60-100%. The first three classes (0-20%, 20-40%, 40-60%) contain about 20×10^6 events each, while the multiplicity class 60-100% contains about 40×10^6 events.

The corrected per-event yields of prompt D^+ mesons in p–Pb collisions were obtained starting from the raw yields $N_{\text{raw, mult. class}}^{D^{+/-}}(p_T)$ as follows:

$$\frac{dN_{\text{mult.class,est.}}^{D^+}}{dp_T} = \frac{1}{2} \frac{1}{\Delta y \Delta p_T} \frac{f_{\text{mult.class,est.}}^{\text{prompt}} \cdot N_{\text{raw, mult. class}}^{D^{+/-}} \Big|_{|y| < y_{fid}}}{(\text{Acc} \times \epsilon)_{\text{mult.class,est.}}^{\text{prompt}} \cdot BR \cdot N_{\text{ev}}^{\text{mult. class. est}}} \quad (7.1)$$

where Δy and Δp_T are the rapidity and p_T interval width, respectively; f_{prompt} is the fraction of prompt D^+ mesons, $(\text{Acc} \times \epsilon)_{\text{mult.class,est.}}^{\text{prompt}}$ is the acceptance and efficiency correction for prompt D^+ mesons in the respective event activity class, BR is the branching ratio of the $D^+ \rightarrow K^- \pi^+ \pi^+$ decay channel, the factor 1/2 accounts for the fact that we are measuring the raw yields for the sum of D^+ and D^- , $N_{\text{ev}}^{\text{mult.class.est}}$ is the number of analyzed events in the event activity class estimated with the corresponding estimator, computed as reported in Equation 5.3. The Q_{pPb} values are obtained from the corrected per-event yields as:

$$Q_{\text{pPb}}^{\text{est.}}(p_T, \text{mult. class}) = \frac{\frac{dN_{\text{mult.class,est.}}^{D^+}}{dp_T}}{\langle T_{\text{pA}}^{\text{mult.class,est.}} \rangle d\sigma^{\text{pp}}/dp_T} \quad (7.2)$$

where $d\sigma^{\text{pp}}/dp_T$ is the pp reference at $\sqrt{s_{\text{NN}}} = 5.02$ TeV and $\langle T_{\text{pA}}^{\text{mult.class,est.}} \rangle$ is the nuclear overlap function computed for the corresponding event activity class and estimator.

7.1.1 Signal Extraction

The analysis was performed using the p–Pb data sample collected in 2013 with a minimum-bias trigger (V0AND - Section 3.2.1). Events were selected as described in Section 4.1.1, rejecting beam-gas interactions and events with pile-up, and keeping only events with $|z_{\text{vert}}^{\text{reco}}| < 10$ cm. At this point events were divided in the four event activity classes according to V0A, ZNA or CL1 estimators. The secondary vertices of D^+ meson candidates are reconstructed using ITS-TPC tracks selected as described in Section 4.1.2 and the same fiducial acceptance selection on the rapidity of D^+ -meson candidates described in Chapter 5 is applied, ranging from $|y_{\text{lab}}| < 0.5$ at low p_T ($1 < p_T < 2$ GeV/c) to $|y_{\text{lab}}| < 0.8$ above 4 GeV/c.

At this point a cut optimization was performed in seven p_T intervals ranging from 1 to

p_T (GeV/c)	[1,2]	[2,4]	[4,6]	[6,8]	[8,12]	[12,16]	[16,24]
$ \Delta M_{D^+} $ (GeV/ c^2)	0.2	0.2	0.2	0.2	0.2	0.2	0.2
σ_{vertex} (cm)	0.03	0.034	0.034	0.03	0.02	0.015	0.025
p_T^K (GeV/c)	0.2	0.2	0.2	0.2	0.6	0.8	0.8
p_T^π (GeV/c)	0.2	0.35	0.35	0.35	0.35	0.35	0.35
Decay Length (cm)	0	0.04	0.04	0.05	0.08	0.1	0.1
L_{xy}	9	8	8	8	3	3	0
$\cos(\theta_{\text{pointing}})$	0.99	0.99	0.99	0.99	0.98	0.98	0.98
$\cos(\theta_{\text{pointing},xy})$	0.995	0.99	0.99	0.99	0.995	0.995	0.99

TABLE 7.1: Summary table of the D^+ cut values in the event activity classes 0-20%, 20-40% and 40-60%.

p_T (GeV/c)	[1,2]	[2,4]	[4,6]	[6,8]	[8,12]	[12,16]	[16,24]
$ \Delta M_{D^+} $ (GeV/ c^2)	0.2	0.2	0.2	0.2	0.2	0.2	0.2
σ_{vertex} (cm)	0.03	0.034	0.034	0.03	0.02	0.015	0.025
p_T^K (GeV/c)	0.2	0.2	0.2	0.2	0.6	0.8	0.8
p_T^π (GeV/c)	0.2	0.35	0.35	0.35	0.35	0.35	0.35
Decay Length (cm)	0	0.04	0.04	0.05	0.08	0.1	0.1
L_{xy}	7	6	6	6	1	1	0
$\cos(\theta_{\text{pointing}})$	0.99	0.99	0.99	0.99	0.98	0.98	0.98
$\cos(\theta_{\text{pointing},xy})$	0.99	0.985	0.985	0.985	0.99	0.99	0.988

TABLE 7.2: Summary table of the D^+ cut value in the event activity class 60-100%.

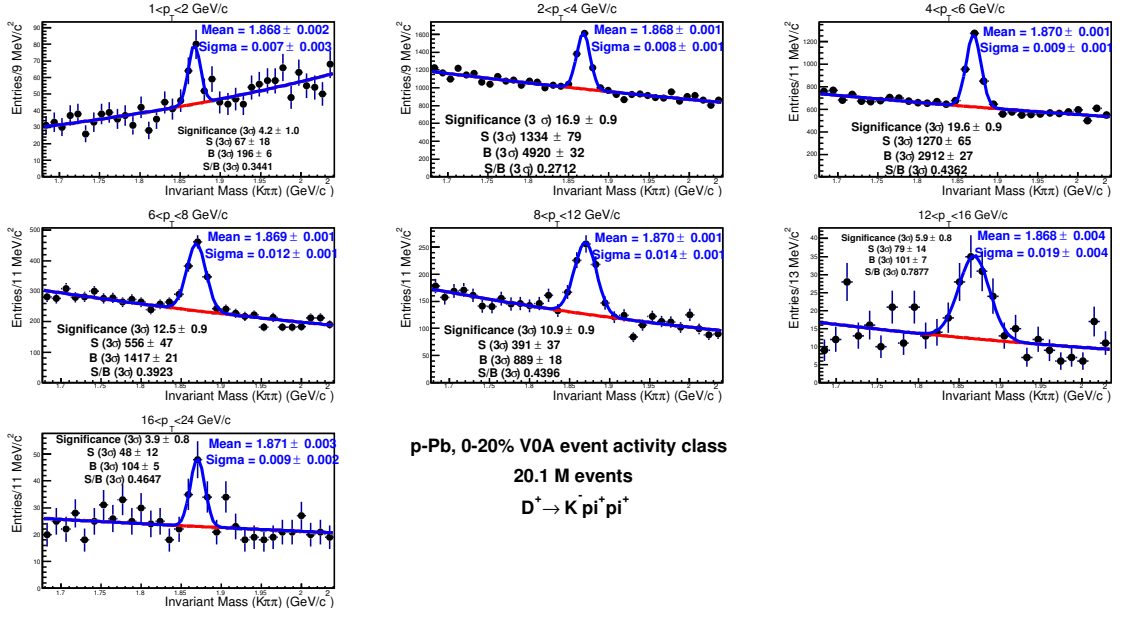


FIGURE 7.2: D^+ candidates invariant mass distributions from p-Pb collisions at $\sqrt{s_{NN}} = 5.02$ TeV in seven p_T intervals within the range $1 < p_T < 24$ GeV/c, for events in the 0-20% event activity class determined with the V0A estimator.

24 GeV/c, resulting in the cut values of Table 7.1, that also reports the p_T intervals in which the analysis is performed. The same cut values were used in the 0-20%, 20-40% and 40-60% event activity classes for all estimators, while in the 60-100% (Table 7.2) event activity class the cut values on both L_{xy} and $\cos\theta_{xy}^{\text{pointing}}$ were made looser since this event activity class corresponds on average to a lower event multiplicity and consequently to a lower combinatorial background.

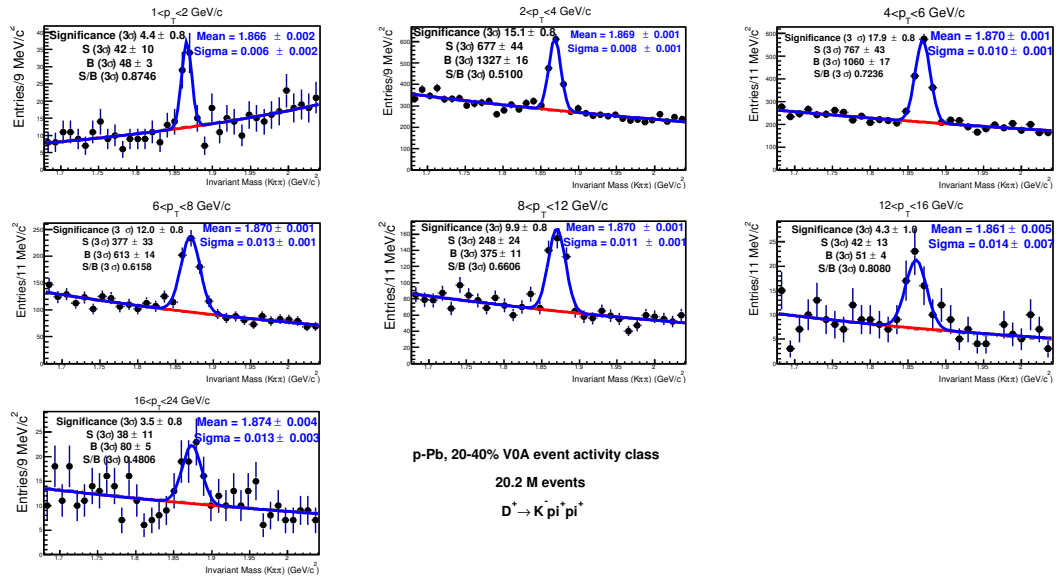


FIGURE 7.3: D^+ candidates invariant mass distributions from p-Pb collisions at $\sqrt{s_{NN}} = 5.02$ TeV in seven p_T bins within the range $1 < p_T < 24$ GeV/c, for events in the 20-40% event activity class determined with the V0A estimator.

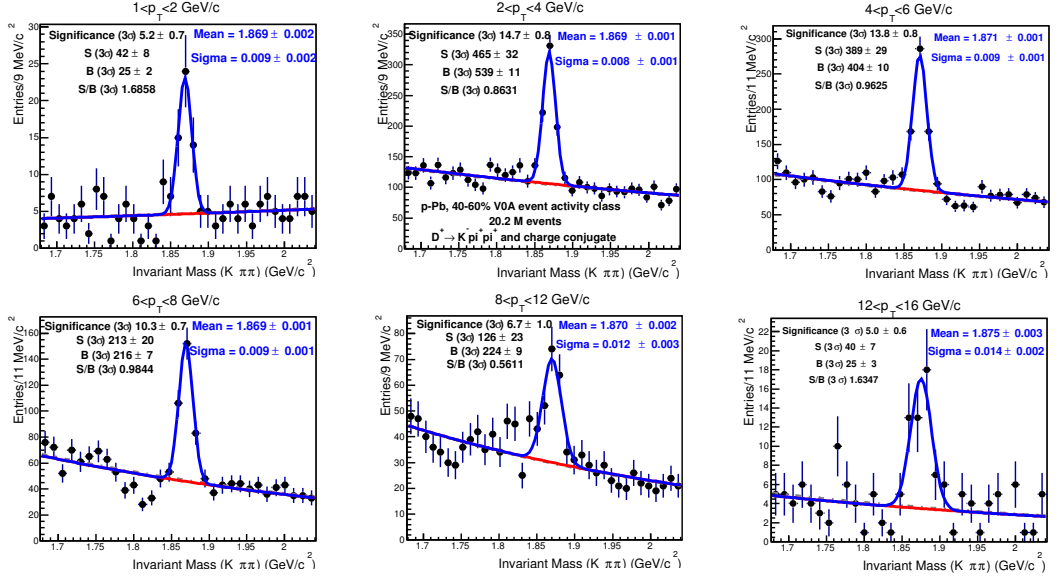


FIGURE 7.4: D^+ candidates invariant mass distributions from p-Pb collisions at $\sqrt{s_{NN}} = 5.02$ TeV in six p_T bins within the range $1 < p_T < 16$ GeV/c, for events in the 40-60% event activity class determined with the V0A estimator.

The invariant mass distributions obtained for the V0A estimator in the four event activity classes are shown in Figures 7.2, 7.3, 7.4 and 7.5, while Table 7.3 shows the extracted raw yields for all estimators and event activity classes. Due to the limited statistics the signal could not be extracted in the entire p_T range $1 < p_T < 24$ GeV/c for all event activity classes, in particular at low/high p_T and in the 60-100% event activity class.

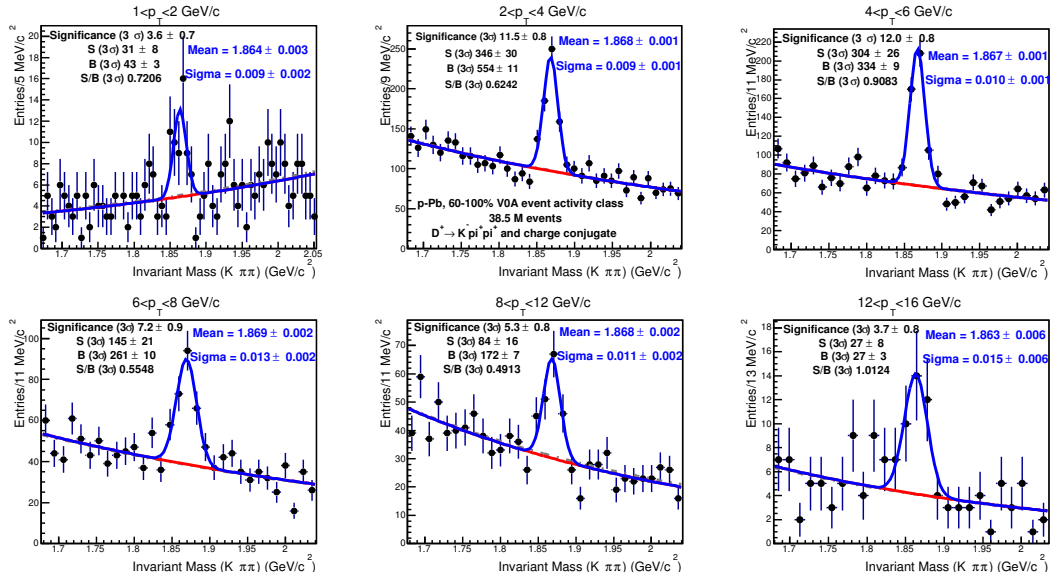


FIGURE 7.5: D^+ candidates invariant mass distributions from p-Pb collisions at $\sqrt{s_{NN}} = 5.02$ TeV in six p_T bins within the range $1 < p_T < 16$ GeV/c, for events in the 60-100% event activity class determined with the V0A estimator.

p_T (GeV/c)	1-2	2-4	4-6	6-8	8-12	12-16	16-24
Event Activity (%)	V0A						
0-20	67±18	1334±79	1270±65	556±47	391±37	79±14	48±12
20-40	42±10	677±44	767±43	377±33	248±24	42±13	38±11
40-60	42±8	465±32	389±29	213±20	126±23	40±7	X
60-100	31±8	346±30	304±26	145±21	84±16	27±8	X
Event Activity (%)	ZNA						
0-20	46±12	1020±65	969±56	501±41	272±30	68±14	X
20-40	58±12	769±55	874±49	336±33	272±29	57±11	X
40-60	27±9	557±42	485±34	253±25	165±23	33±8	X
60-100	X	472±42	457±34	243±27	120±20	34±8	30±9
Event Activity (%)	CL1						
0-20	90±21	1515±83	1537±72	687±52	494±41	98±16	66±16
20-40	40±8	724±44	720±38	345±28	218±24	41±10	45±12
40-60	18±5	389±25	335±25	175±18	96±15	31±6	X
60-100	22±6	203±19	196±16	72±12	36±10	X	X

TABLE 7.3: D^+ -meson raw yields for all estimators and event activity classes

7.1.2 Acceptance and efficiency corrections

The raw yields obtained in the previous section are corrected for the reconstruction and selection efficiency according to Equation 5.1. The D^+ -meson efficiencies as a function of p_T and N_{trk} were obtained from the MC data sample generated using HIJING for simulating the underlying p-Pb event and PYTHIA v6.4.21 to inject a pp collision with a $c\bar{c}$ pair, as described in Section 4.2.1. The efficiency correction factor is obtained as the ratio of the D^+ mesons counted at the steps *kStepRecoPID* and *kStepAcceptance*. The same reweighting on p_T shape of generated D^+ mesons discussed in Section 5.3 were applied. However in the Monte Carlo it was not possible to select events according to the event activity classes defined for V0A and ZNA since detectors at forward rapidity were not included in the simulation. Therefore, to reproduce in the Monte Carlo the

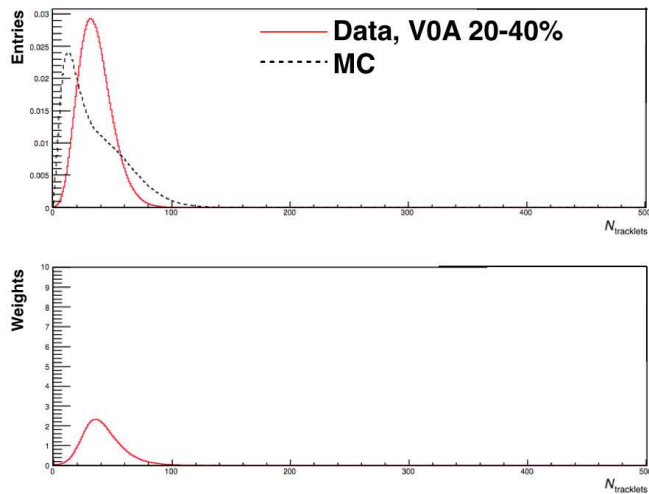


FIGURE 7.6: Top: distribution of number of tracklets in $|\eta| < 1$ from MC (multiplicity integrated - black) and from data (red) for events in the V0A 20-40% event activity class. Bottom: ratio of the black and red histograms shown in the top panel, which is used to reweight the efficiencies in the MC.

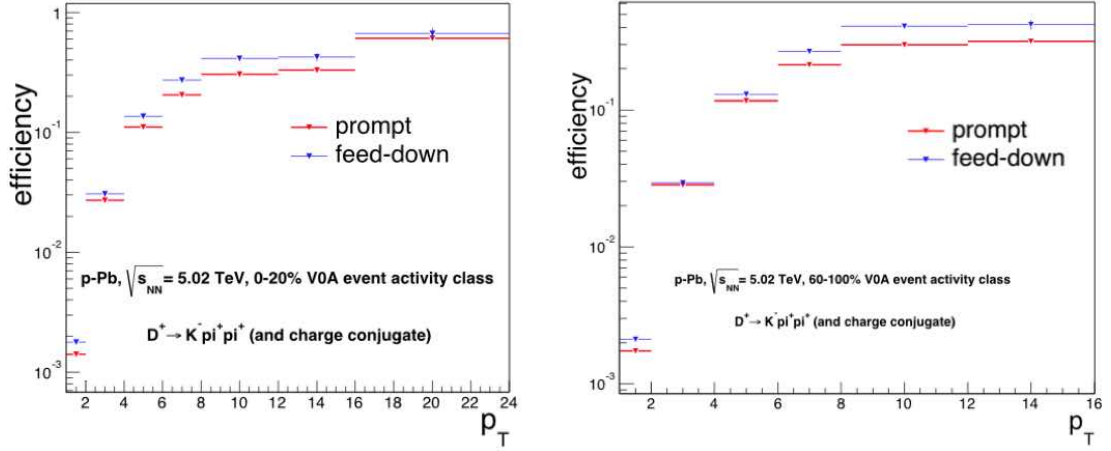


FIGURE 7.7: D^+ reconstruction and selection efficiencies in p–Pb collisions at $\sqrt{s_{\text{NN}}} = 5.02$ TeV in seven p_{T} bins in the range $1 < p_{\text{T}} < 16$ GeV/c, for prompt and feed-down D^+ mesons for events in the 0-20% (left) and 60-100% (right) event activity classes determined with the V0A estimator.

same multiplicity observed in data in each event activity class a weighting procedure was used. The distribution of the number of tracklets (N_{trk}) measured in the data in the pseudorapidity range $|\eta| < 1$ in each event activity class (estimated with V0A, ZNA and CL1) were used to calculate the weights. These distributions were divided by the distribution of the number of tracklets in $|\eta| < 1$ extracted from the Monte Carlo to get the weights used to reweight the multiplicity value of each event. As an example, the top panel of Figure 7.6 shows the N_{trk} distribution in $|\eta| < 1$ from MC (multiplicity integrated, black) and from data for events in the V0A 20-40% event activity class (red). Their ratio, which is used to reweight the efficiencies for the 20-40% V0A event class, is shown in the bottom panel.

The values of the efficiency for both prompt and feed-down D^+ mesons in the 0-20% and 60-100% V0A event activity classes obtained with this procedure are shown in Figure 7.7 as a function of p_{T} .

7.1.3 Systematic Uncertainties

The sources of systematic uncertainties are the same discussed in Section 5.6.

The systematic uncertainty on the yield extraction was evaluated using the same strategy described in Section 5.6.1 in each of the p_{T} and event activity intervals, and its values are listed in Table 7.4.

The systematic uncertainty on topological cut efficiency was evaluated following the same strategy described in Section 5.6.2, i.e. comparing the corrected yields with those obtained using two looser sets of cuts and two tighter sets of cuts. The values of the estimated uncertainties are reported in Table 7.5 and are found to be in agreement with those assigned in the different p_{T} and event activity intervals to D^0 and D^{*+} mesons. The uncertainty is larger in the p_{T} bin $1 < p_{\text{T}} < 2$ GeV/c where tighter cuts have been used.

For what concerns PID, the systematic uncertainty was evaluated comparing the corrected yields obtained in the different event activity classes with and without PID selections. The situation is similar to the one obtained in the minimum bias analysis, and no systematic uncertainty is assigned for $p_{\text{T}} > 2$ GeV/c. However, in the p_{T} bin $1 < p_{\text{T}} < 2$

	estimator	class	1-2	2-4	4-6	6-8	8-12	12-16	16-24
ls	V0A	0-20%	8%	3%	3%	6%	6%	8%	8%
	V0A	20-40%	8%	3%	3%	6%	6%	8%	8%
	V0A	40-60%	8%	3%	3%	6%	6%	8%	X
	V0A	60-100%	8%	3%	3%	6%	6%	8%	X
	CL1	0-20%	8%	3%	3%	6%	6%	8%	8%
	CL1	20-40%	8%	3%	3%	6%	6%	8%	8%
	CL1	40-60%	8%	3%	3%	6%	6%	8%	X
	CL1	60-100%	8%	3%	3%	6%	6%	X	X
	ZNA	0-20%	8%	3%	3%	6%	6%	8%	X
	ZNA	20-40%	8%	3%	3%	6%	6%	8%	X
	ZNA	40-60%	8%	3%	3%	6%	6%	8%	X
	ZNA	60-100%	X	3%	3%	6%	6%	8%	8%

TABLE 7.4: Summary table of the D^+ systematics from yield extraction for the different centrality classes defined with V0A, ZNA and CL1.

GeV/c it is impossible to extract D^+ signal without applying PID selections in the four event activity intervals for all estimators. The same systematic uncertainty from PID estimated in the minimum bias analysis (10%) was assigned in each event activity class in the p_T bin $1 < p_T < 2$ GeV/c.

The systematic uncertainty due to the p_T shape of generated D^+ mesons was evaluated following the same strategy described in Section 5.6.4. The assigned uncertainties shown in Table 7.6 and are independent of the event activity estimator. The uncertainties are larger in the 60-100% event activity class, since, despite the looser topological cut values, the lower multiplicity implies worse resolution on cut variables such as decay length, and makes the efficiency values more sensitive to the p_T shape used to generate D^+ mesons.

The systematic uncertainty assigned due to the tracking efficiency is the same as in the minimum bias analysis, i.e. 9% independently on p_T and event activity class.

The uncertainties on the beauty feed-down subtraction and the nuclear modification of the feed-down D^+ -meson (R_{pPb} of D^+ from B), evaluated as discussed in Section 5.6.6,

	estimator	class	1-2	2-4	4-6	6-8	8-12	12-16	16-24
	V0A	0-20%	10%	5%	5%	5%	5%	5%	5%
	V0A	20-40%	10%	5%	5%	5%	5%	5%	5%
	V0A	40-60%	10%	5%	5%	5%	5%	5%	X
	V0A	60-100%	10%	5%	5%	5%	5%	5%	X
	ZNA	0-20%	10%	5%	5%	5%	5%	5%	5%
	ZNA	20-40%	10%	5%	5%	5%	5%	5%	5%
	ZNA	40-60%	10%	5%	5%	5%	5%	5%	X
	ZNA	60-100%	10%	5%	5%	5%	5%	5%	X
	CL1	0-20%	10%	5%	5%	5%	5%	5%	X
	CL1	20-40%	10%	5%	5%	5%	5%	5%	X
	CL1	40-60%	10%	5%	5%	5%	5%	5%	X
	CL1	60-100%	X	5%	5%	5%	5%	5%	5%

TABLE 7.5: Summary table of the D^+ systematics from cut efficiency for the different centrality classes defined with V0A, ZNA and CL1.

p_T (GeV/c)	1-2	2-4	4-6	6-8	8-12	12-16	16-24
0-60% sys. (%)	3	2	1	1	1	1	1
60-100% sys. (%)	10	6	3	2	2	2	2

TABLE 7.6: Systematic uncertainty on the p_T shape of generated D^+ mesons

p_T (GeV/c)	1-2	2-4	4-6	6-8	8-12	12-16	16-24
Feed-down sys. (%)	+1 -30	+3 -10	+3 -6	+3 -4	+3 -4	+5 -3	+4 -3

TABLE 7.7: Systematic uncertainty on beauty feed-down subtraction.

are reported in Table 7.7.

The pp reference used as the denominator in the Q_{pPb} formulas is the same that has been discussed in Section 5.5.2, and is affected by the same systematic uncertainties reported in Table 5.8.

Since the Q_{pPb} is computed from Equations 7.1 and 7.2, the systematic on the integrated luminosity determination does not affect the measurement. The systematic on the branching ratio is 2.1%, while the systematic uncertainties on $\langle T_{pPb}^{\text{est}} \rangle$ depend on the event activity estimator and on the event activity class, and are reported in Tables 7.8 and 7.9 together with the $\langle T_{pPb}^{\text{est}} \rangle$ values used in the next section to compute the Q_{pPb} values.

Event Activity (%)	$\langle T_{pPb}^{\text{VOA}} \rangle$ (mb^{-1})	$\langle T_{pPb}^{\text{CL1}} \rangle$ (mb^{-1})	Unc. VOA, CL1 (%)
0-20	0.183	0.190	4
20-40	0.134	0.136	3.7
40-60	0.092	0.088	5.6
60-100	0.041	0.037	22.95

TABLE 7.8: $\langle T_{pPb}^{\text{VOA}} \rangle$ and $\langle T_{pPb}^{\text{CL1}} \rangle$ values used for Q_{pPb} calculation and relative uncertainties.

Event Activity (%)	$\langle T_{pPb}^{\text{mult}} \rangle$ (mb^{-1})	Unc hybrid (%)
0-20	0.164	6.6
20-40	0.137	3.9
40-60	0.101	5.9
60-100	0.046	6.34

TABLE 7.9: $\langle T_{pPb}^{\text{mult}} \rangle$ values used for Q_{pPb} calculation and relative uncertainties.

7.1.4 Results

The results of D^+ -meson $Q_{pPb}^{\text{mult}}(p_T)$, $Q_{pPb}^{\text{VOA}}(p_T)$ and $Q_{pPb}^{\text{CL1}}(p_T)$ in p-Pb collisions at $\sqrt{s_{\text{NN}}} = 5.02$ TeV are shown in the left panels of Figures 7.8, 7.9 and 7.10 as a function of p_T in the four event activity classes considered in this analysis. The vertical bars represent the statistical uncertainties, the colored boxes the systematic uncertainties. The uncertainty on $\langle T_{pPb} \rangle$ is represented by the filled boxes at $Q_{pPb} = 1$ on the right of each figure.

The right panels of Figures 7.8, 7.9 and 7.10 report the Q_{pPb} values of charged hadrons measured with the same estimators used in the D^+ -meson analysis already discussed in Section 3.3.3. The comparison of the Q_{pPb} results of D^+ mesons and charged hadrons lead to the following conclusions:

- for what concerns $Q_{\text{pPb}}^{\text{mult}}(p_T)$, the D^+ -meson results are compatible with unity for $p_T > 2$ GeV/c. This observation is in agreement with what observed for charged hadrons for $p_T > 7 \div 8$ GeV/c. In the intermediate p_T region ($3 < p_T < 7$ GeV/c) charged hadrons show a Cronin enhancement that increases with event activity, and might be due to k_T broadening and/or radial flow effects. The current systematic uncertainties on the D^+ -meson measurement do not allow to conclude on the possible presence of these effects. It is worth noting that for the D^+ measurement the p_T bin $1 < p_T < 2$ GeV/c, where for the event activity classes 0-20%, 40-60% and 60-100% the $Q_{\text{pPb}}^{\text{mult}}(p_T)$ values are systematically lower than one, at mid-rapidity corresponds to a p_T region in which Bjorken x values of the order of 10^{-3} are explored.
- for what concerns $Q_{\text{pPb}}^{\text{VOA}}(p_T)$, the D^+ -meson results in the p_T range $2 < p_T < 12$ GeV/c follow the same hierarchy with respect to the event activity class observed for charged hadrons, i.e. Q_{pPb} values from larger event activity classes are higher than those from lower event activity class. The values of D^+ -meson Q_{pPb} for different event activity classes reduce their discrepancies for $p_T > 12$ GeV/c, as observed for charged hadrons.
- for what concerns $Q_{\text{pPb}}^{\text{CL1}}(p_T)$, the D^+ -meson results for $p_T > 2$ GeV/c follow the same hierarchy with respect to event activity class observed for charged hadrons, i.e. Q_{pPb} values from higher event activity class are higher than those from lower event activity class. Focusing on the 0-20% and 60-100% event activity classes, in the first D^+ -meson Q_{pPb} is systematically higher than unity for $p_T > 2$ GeV/c, in the latter it is systematically below unity for $p_T > 2$ GeV/c

The spread among the D^+ -meson Q_{pPb} values between high and low event activity classes is reduced when going from the mid-rapidity event activity estimator (CL1) to an event activity estimator located at higher rapidity (VOA), and it is further reduced using ZNA energy to estimate event activity and the hybrid method for determining $\langle T_{\text{pPb}} \rangle$. We

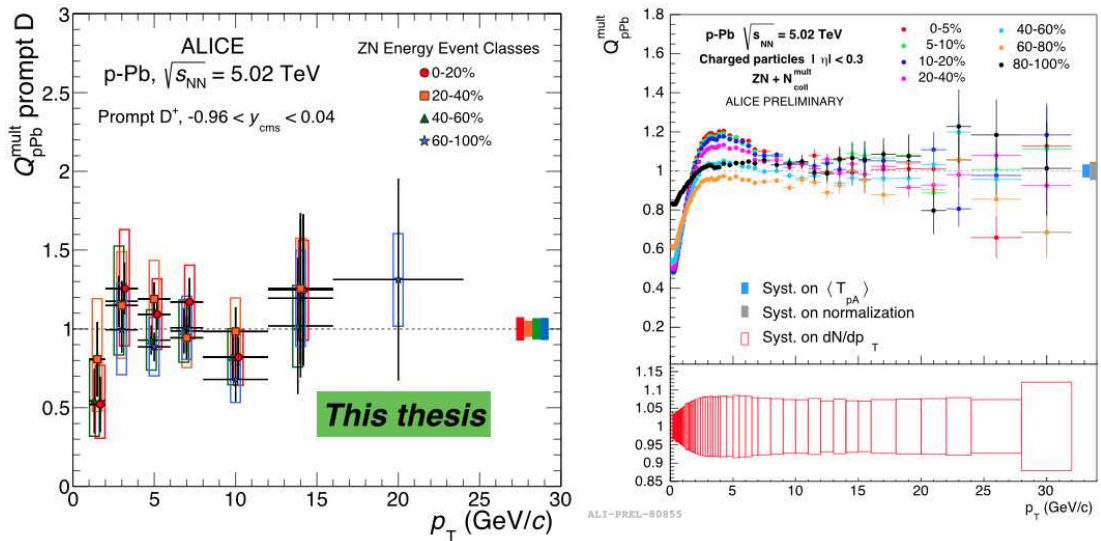


FIGURE 7.8: Left: $Q_{\text{pPb}}^{\text{mult}}(p_T)$ of D^+ -meson as a function of p_T in four ZNA event activity classes. Right: $Q_{\text{pPb}}^{\text{mult}}(p_T)$ of charged hadrons as a function of p_T in seven ZNA event activity classes

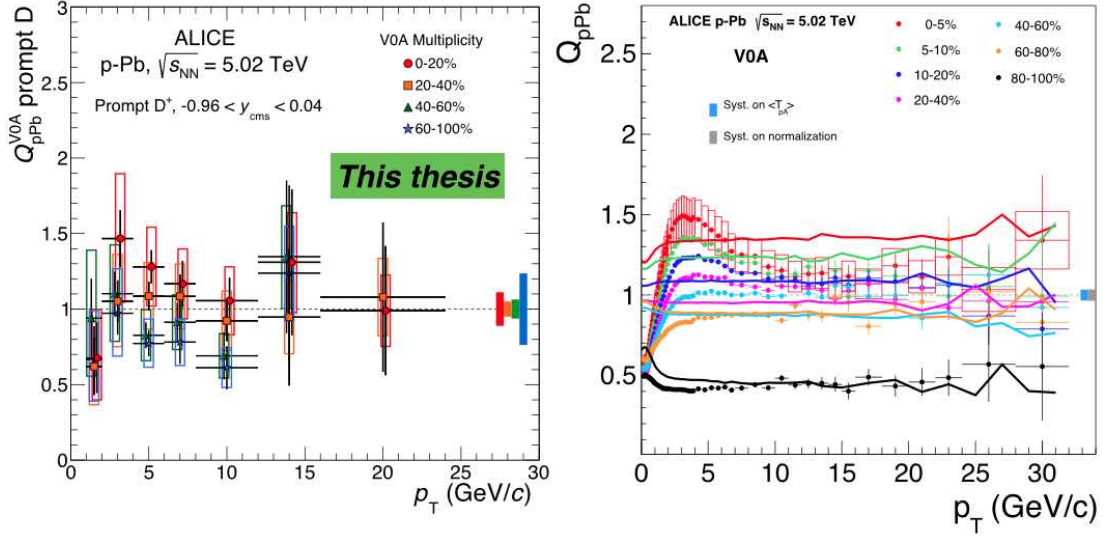


FIGURE 7.9: Left: $Q_{pPb}^{VOA}(p_T)$ of D^+ -meson as a function of p_T in four VOA event activity classes. Right: $Q_{pPb}^{VOA}(p_T)$ of charged hadrons as a function of p_T in seven VOA event activity classes

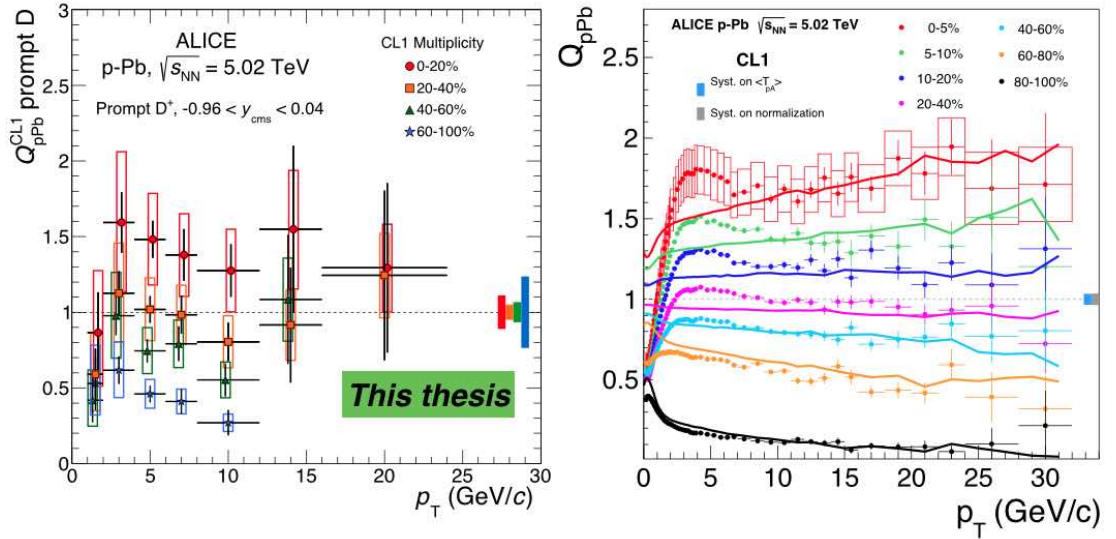


FIGURE 7.10: Left: $Q_{pPb}^{CL1}(p_T)$ of D^+ -meson as a function of p_T in four CL1 event activity classes. Right: $Q_{pPb}^{CL1}(p_T)$ of charged hadrons as a function of p_T in seven CL1 event activity classes

can conclude that the same biases in the determination of $\langle N_{coll} \rangle$ and $\langle T_{pPb} \rangle$ observed in the measurement of charged hadrons Q_{pPb} is present in measurements related to D^+ mesons. These conclusions are confirmed by the D^0 -meson $Q_{pPb}^{mult}(p_T)$, $Q_{pPb}^{VOA}(p_T)$ and $Q_{pPb}^{CL1}(p_T)$ measurements, shown in Figures 7.11 and 7.12.

For the least biased estimator, ZNA energy, the $Q_{pPb}^{mult}(p_T)$ values obtained calculating $\langle T_{pPb} \rangle$ with the hybrid method are compatible with unity within the current uncertainties and no nuclear effects are observed.

Further studies as a function of event activity in the heavy-flavour sector are currently ongoing in the ALICE Collaboration, but their results are not public yet except for those relative to J/Ψ production at forward and backward rapidity. For completeness these

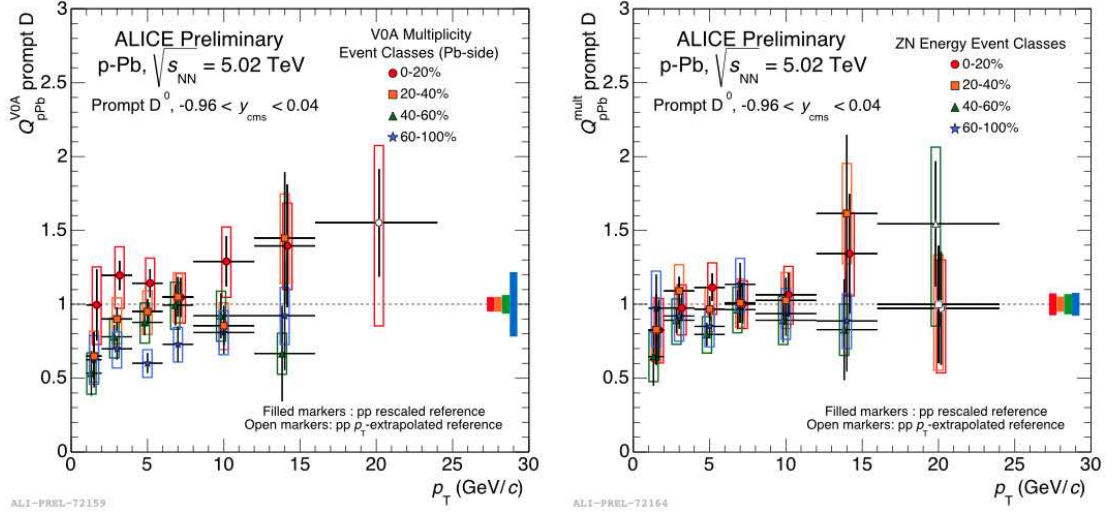


FIGURE 7.11: Left: $Q_{pPb}^{VOA}(p_T)$ of D^0 as a function of p_T in four VOA event activity classes. Right: $Q_{pPb}^{ZNA}(p_T)$ of D^0 as a function of p_T in four ZNA event activity classes.

results will be now discussed, although they can not be directly compared to those relative to D mesons because of the different rapidity coverage of the measurements.

I recall that the minimum bias nuclear modification factor of inclusive J/Ψ in p-Pb collisions at $\sqrt{s_{NN}} = 5.02$ TeV was measured by the ALICE collaboration ([95] - Section 2.2.4) at forward rapidity ($2.03 < y_{cms} < 3.53$), corresponding to the p-going direction, and negative rapidity ($-4.46 < y_{cms} < -2.96$) corresponding to the Pb-going direction. The results of this measurement showed an enhancement above unity of the nuclear modification factor of J/Ψ at backward rapidity and a suppression below unity at forward rapidity, respectively, in agreement with models taking into account nuclear shadowing of PDFs and cold nuclear matter energy loss.

Figure 7.12 shows the $Q_{pPb}^{mult}(p_T)$ values of inclusive J/Ψ at forward and backward rapidity as a function of the event activity class. At backward rapidity the inclusive J/Ψ

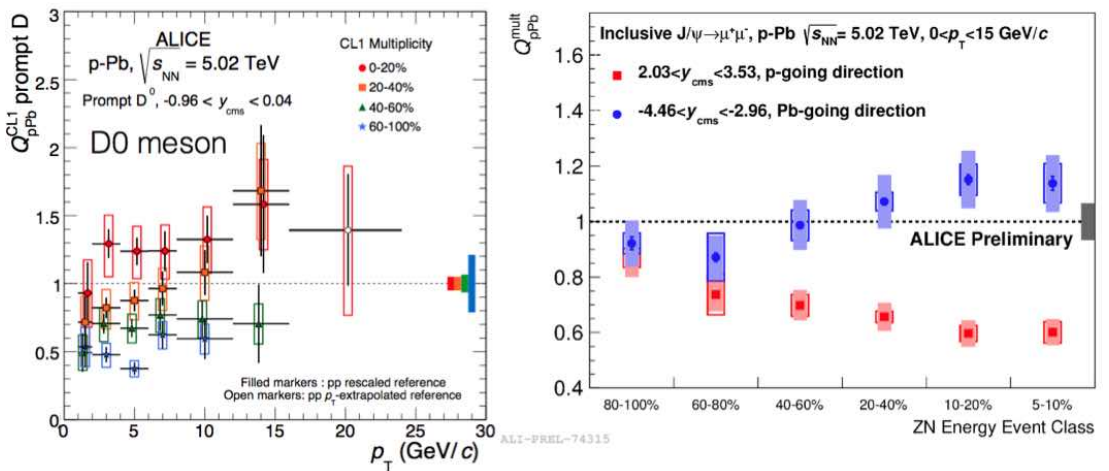


FIGURE 7.12: Left: $Q_{pPb}^{CL1}(p_T)$ of D^0 as a function of p_T in four CL1 event activity classes. Right: $Q_{pPb}^{mult}(p_T)$ of J/Ψ as a function of ZNA event activity classes in the p_T range $0 < p_T < 15$ GeV/c at forward ($2.03 < y < 3.53$) and backward ($-4.46 < y < -2.96$) rapidity.

$Q_{\text{pPb}}^{\text{mult}}(p_{\text{T}})$ shows a feeble dependence on event activity, with the higher $Q_{\text{pPb}}^{\text{mult}}(p_{\text{T}})$ values in the 5-10% event activity class. The $Q_{\text{pPb}}^{\text{mult}}(p_{\text{T}})$ of inclusive J/Ψ at forward rapidity shows a decreasing trend at backward rapidity, with all measurements below one. These results show a stronger modification (with respect to pp collisions) of J/Ψ production at forward rapidity in the highest event activity classes, that might be due to a stronger influence of effects like nuclear shadowing of PDFs and cold nuclear matter energy loss.

7.2 D^+ -meson production as a function of charged particle multiplicity

The results will be presented as a function of relative primary charged particle multiplicity at central rapidity ($|\eta| < 1$) defined as $dN_{\text{ch}}/d\eta^j / \langle dN_{\text{ch}}/d\eta \rangle$, where j is a given primary charged particle multiplicity interval, measured in $|\eta| < 1.0$, and $\langle dN_{\text{ch}}/d\eta \rangle$ is the average primary charged particle multiplicity of the minimum bias data sample. Primary charged particles are defined as prompt particles produced in the collisions, including their decay products, except those from weak decays of strange particles.

The results are presented in form of the D^+ -meson self-normalized yield in inelastic p–Pb collisions, defined as

$$\frac{(d^2 N^{D^+} / dy dp_{\text{T}})^j}{\langle d^2 N^{D^+} / dy dp_{\text{T}} \rangle} = \frac{Y^j / (\epsilon^j) f_j^{\text{prompt}}}{Y^{\text{tot}} / (\epsilon^{\text{tot}} \times \epsilon^{\text{trigger}}) f_{\text{mult int}}^{\text{prompt}}} \quad (7.3)$$

where Y^j is the D^+ -meson yield in the considered multiplicity interval, Y^{tot} the multiplicity integrated D^+ yield, ϵ^j and ϵ^{tot} are the corresponding reconstruction and selection efficiencies, f_j^{prompt} ($f_{\text{mult int}}^{\text{prompt}}$) is the fraction of prompt D^+ -meson yield in the multiplicity interval considered (multiplicity integrated data sample) and $\epsilon^{\text{trigger}}$ is the V0AND trigger efficiency for non-single diffractive events in p–Pb collisions at $\sqrt{s_{\text{NN}}} = 5.02$ TeV, which was measured to be 96.4%, with a systematic uncertainty of 3.1% [148].

7.2.1 Charged particle multiplicity determination and correction

This analysis is performed on the p–Pb data sample at $\sqrt{s_{\text{NN}}} = 5.02$ TeV collected with the V0AND trigger, after applying the physics selection and pile-up rejection criteria described in Section 4.1.1. The whole p–Pb data sample is divided in two sub-samples: the first, LHC13b, collected between 16 and 22 January 2013, the second, LHC13c, collected between 22 and 25 January 2013. The detector conditions were similar in this two periods.

Only events with vertex reconstructed with ITS-TPC tracks with $z_{\text{vtx}}^{\text{Reco}} < 10$ cm are selected for the analysis. Especially at low multiplicity, the inclusion of the D^+ -meson decay tracks introduces a bias in the calculation of the primary vertex position and

Period	$\langle N_{\text{trk}} \rangle$ before correction	$\langle N_{\text{trk}} \rangle$ after correction
LHC13b	28.29	27.87
LHC13c	27.87	27.87

TABLE 7.10: Mean multiplicity $\langle N_{\text{trk}} \rangle$ as a function of Z_{vtx} before and after correction.

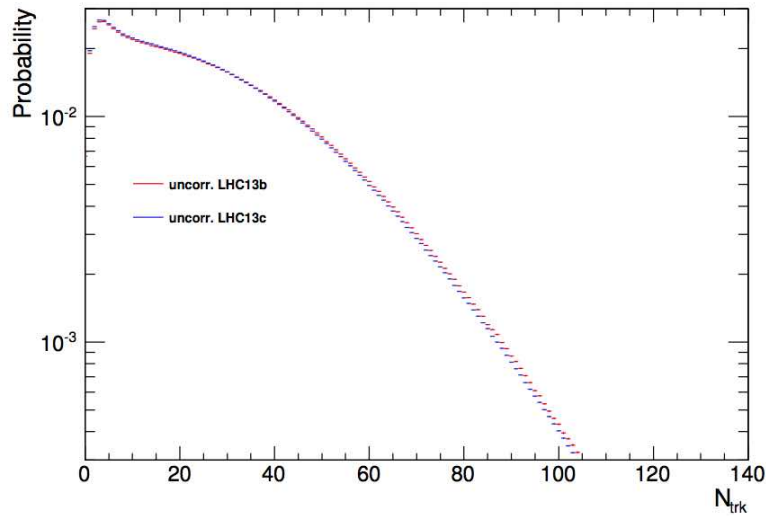


FIGURE 7.13: Distribution of uncorrected number of tracklets for LHC13b and LHC13c, normalised to their respective integrals.

covariance matrix. For this reason, in this analysis for each D^+ -meson candidate the primary vertex was recomputed excluding its decay tracks.

The multiplicity estimator used for this analysis is based on the number of tracklets reconstructed in the Silicon Pixel Detector (SPD) within a pseudorapidity range of $|\eta| < 1$, $N_{\text{trk}}|_{|\eta| < 1}$ (in the following N_{trk} for brevity). An SPD tracklet is obtained by joining hits in the two SPD layers aligned with the reconstructed primary vertex. The measured distributions of the number of tracklets (N_{trk}) for each of the periods LHC13b and LHC13c are shown in Figure 7.13. As can be seen in Table 7.10 the difference between the average multiplicities of the two periods before corrections is very small.

In order to extract a correction for the number of tracklets that account for the z_{vtx} dependence of the SPD acceptance, the uncorrected number of tracklets was studied as a function of z_{vtx} . This is shown in Figure 7.14 for LHC13b (left) and LHC13c (right). In addition, the profile of these two-dimensional histograms, defined as the mean of N_{trk}

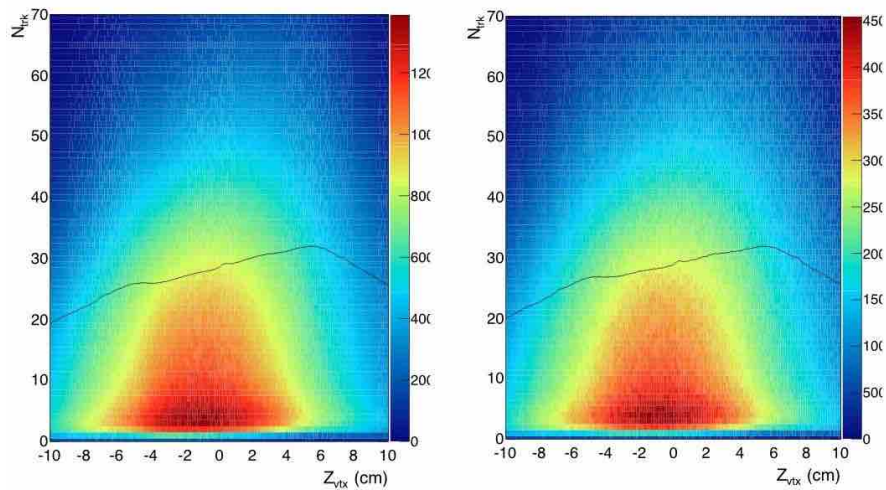


FIGURE 7.14: Distribution of number of events as a function of z_{vtx} and of the uncorrected number of tracklets N_{trk} , for LHC13b (left) and LHC13c (right).

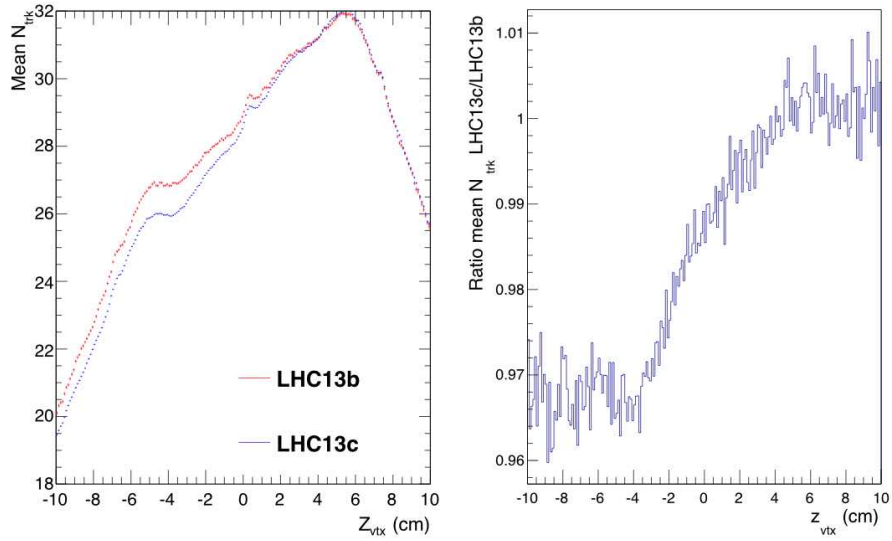


FIGURE 7.15: Left: average uncorrected number of tracklets per event as a function of z_{vtx} (left). Right: ratio of the LHC13b profile over LHC13c profile.

as a function of $z_{\text{vtx}}^{\text{Reco}}$, is drawn in Figure 7.14.

This dependence of the N_{trk} distributions on $z_{\text{vtx}}^{\text{Reco}}$ and data taking period needs to be corrected in order to define consistently the N_{trk} intervals in which the analysis is performed, otherwise a given N_{trk} interval would correspond to a different real charged particle multiplicity range depending on $z_{\text{vtx}}^{\text{Reco}}$ or data taking period. A $z_{\text{vtx}}^{\text{Reco}}$ -dependent correction factor was applied to make the N_{trk} distributions uniform in $z_{\text{vtx}}^{\text{Reco}}$. The reference multiplicity was set so that the mean of the N_{trk} distribution is 27.87 (which is the $z_{\text{vtx}}^{\text{Reco}}$ -integrated N_{trk} mean for period LHC13c, see Table 7.10) for both data taking periods and for all $z_{\text{vtx}}^{\text{Reco}}$ values. Fig. 7.16 shows the corrected z_{vtx} distribution of N_{trk} for LHC13b (left) and LHC13c (right) periods.

Once this correction is done, the events of the p–Pb minimum bias data sample are divided in six N_{trk} intervals. The intervals were chosen in order to have sufficient statistics for the D^+ -meson yield extraction, and are listed in the first column of Table 7.11, while

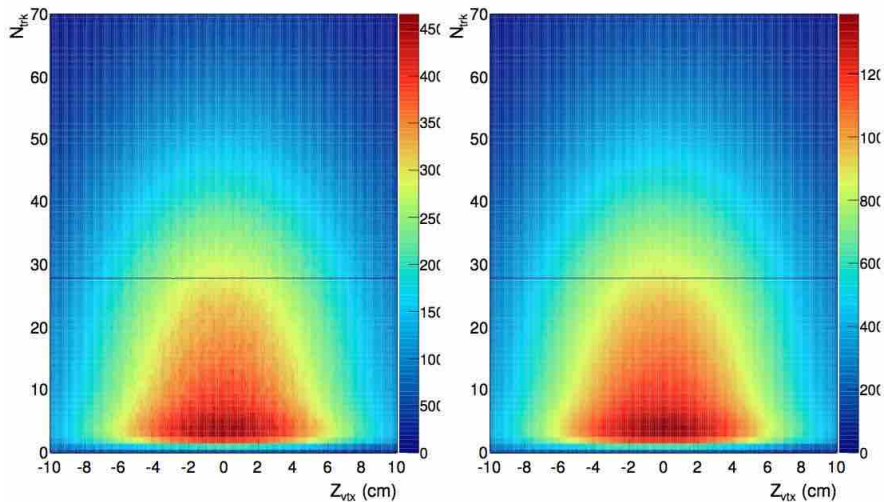


FIGURE 7.16: Distribution of corrected N_{trk} as a function of z_{vtx} , for LHC13b (left) and LHC13c (right) periods.

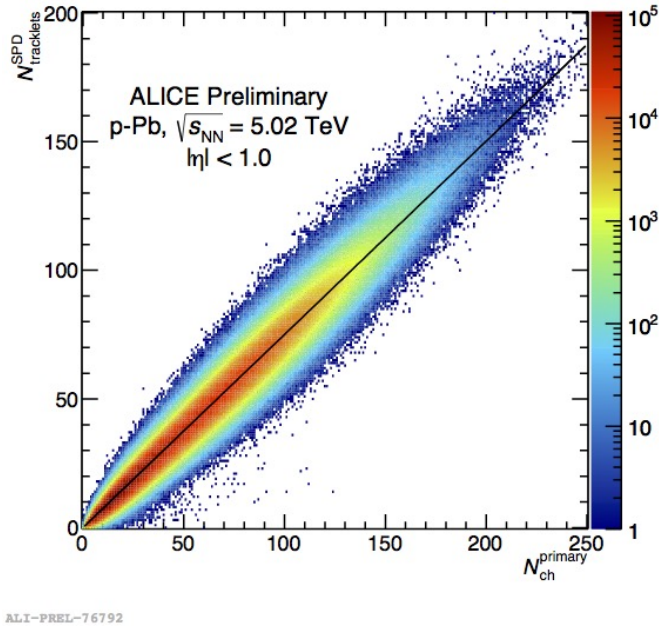


FIGURE 7.17: Scatter plot of number of tracklets $N_{\text{trk}}|_{|\eta|<1}$, as a function of the generated primary charged particle multiplicity at mid-rapidity $N_{\text{ch}}^{\text{primary}}|_{|\eta|<1}$, from MC simulations.

the second column reports the average $\langle N_{\text{trk}} \rangle$ inside each interval.

Figure 7.17 shows the scatter plot of $N_{\text{trk}}|_{|\eta|<1}$ as a function of the generated primary charged particle multiplicity at mid-rapidity $N_{\text{ch}}^{\text{primary}}|_{|\eta|<1}$ obtained from the MC data sample described in Section 4.2.1. A linear trend is observed between $N_{\text{trk}}|_{|\eta|<1}$ and $N_{\text{ch}}^{\text{primary}}|_{|\eta|<1}$, with a factor of proportionality $(N_{\text{trk}}/N_{\text{ch}}^{\text{primary}})|_{|\eta|<1}$ of 0.75 obtained from a linear fit to the average N_{trk} values as a function of $N_{\text{ch}}^{\text{primary}}$ represented by the black line. The $\langle N_{\text{trk}} \rangle$ values were divided by this value to convert them into the number of generated primary charged particles N_{ch} , and then by a factor of two (the width of the pseudorapidity range studied) to give $dN_{\text{ch}}/d\eta$. The third column of Table 7.11 shows the limits of the multiplicity intervals in terms of $dN_{\text{ch}}/d\eta$, the fourth column the average $dN_{\text{ch}}/d\eta$ within the respective multiplicity interval ($\langle dN_{\text{ch}}/d\eta \rangle$) and the fifth column reports the ratio of $\langle dN_{\text{ch}}/d\eta \rangle$ to the average $dN_{\text{ch}}/d\eta$ of the minimum bias data

N_{trk}	$\langle N_{\text{trk}} \rangle$	$dN_{\text{ch}}/d\eta$	$\langle dN_{\text{ch}}/d\eta \rangle$	$\langle dN_{\text{ch}}/d\eta \rangle / \langle dN_{\text{ch}}/d\eta \rangle_{\text{int}}^{\text{mult}}$	$N_{\text{events}} \cdot 10^6$
[1, 24]	12.11	0.7 – 16.4	8.09	0.46	50.92
[25, 44]	33.58	16.4 – 29.7	22.43	1.27	27.23
[45, 59]	51.17	29.7 – 39.8	34.19	1.94	10.83
[60, 74]	65.95	39.8 – 49.8	44.07	2.50	5.17
[75, 99]	83.54	49.8 – 66.5	55.82	3.16	2.74
[100, 199]	110.75	66.5 – 133.0	74.00	4.20	0.53
Integrated			17.64		99.26

TABLE 7.11: Summary table of the intervals of number of tracklets reconstructed in the SPD used in the analysis. The values of average number tracklets, $\langle N_{\text{trk}} \rangle$, of $dN_{\text{ch}}/d\eta$ and of $dN_{\text{ch}}/d\eta / \langle dN_{\text{ch}}/d\eta \rangle_{\text{int}}^{\text{mult}}$ for $|\eta_{\text{ab}}| < 1.0$ are reported for each interval.

sample, $\langle dN_{\text{ch}}/d\eta \rangle_{\text{int}}^{\text{mult}}$. The last column reports the number of events in each multiplicity class.

p_{T} (GeV/c)	[1,2]	[2,4]	[4,8]	[8,12]	[12,24]
$ \Delta M_{D^+} $ (GeV/ c^2)	0.2	0.2	0.2	0.2	0.2
σ_{vertex} (cm)	0.03	0.03	0.03	0.03	0.03
p_{T}^{K} (GeV/c)	0.2	0.2	0.2	0.2	0.2
p_{T}^{π} (GeV/c)	0.2	0.35	0.35	0.35	0.35
Decay Length (cm)	0	0.0	0.0	0.0	0.0
L_{xy}	9	9	9	9	9
$\cos(\theta_{\text{pointing}})$	0.99	0.99	0.99	0.99	0.99
$\cos(\theta_{\text{pointing},xy})$	0.995	0.995	0.995	0.995	0.995

TABLE 7.12: Summary table of the cut values in D^+ vs multiplicity analysis.

7.2.2 Signal Extraction

The decay vertices of D^+ meson candidates are reconstructed using ITS-TPC tracks selected as described in Section 4.1.2. The same selection on D^+ -meson candidates rapidity, ranging from $|y_{\text{lab}}| < 0.5$ at low p_{T} ($1 < p_{\text{T}} < 2$) to $|y_{\text{lab}}| < 0.8$ above 4 GeV/c, is applied.

The values of the topological cuts were optimized in six p_{T} intervals ranging from 1 to 24 GeV/c as described in Section 4.1.3. The same selections, reported in Table 7.12 were used in all multiplicity intervals in order to minimize the effect of efficiency corrections in the ratio of the yields of Equation 7.3. The Particle Identification strategy discussed in Section 4.1.4 was applied to further reduce the background: the STANDARD PID selection was used in the p_{T} range $2 < p_{\text{T}} < 24$ GeV/c, the STRONG PID selection was used in the p_{T} range $1 < p_{\text{T}} < 2$ GeV/c.

Figures 7.18, 7.19, 7.20, 7.21 and 7.22 show the fits to the invariant mass distributions of D^+ meson candidates (and their charge conjugates) obtained after applying the selections described above in the five p_{T} intervals used in the analysis. The fitting function is composed of an exponential function for the background and a Gaussian function for

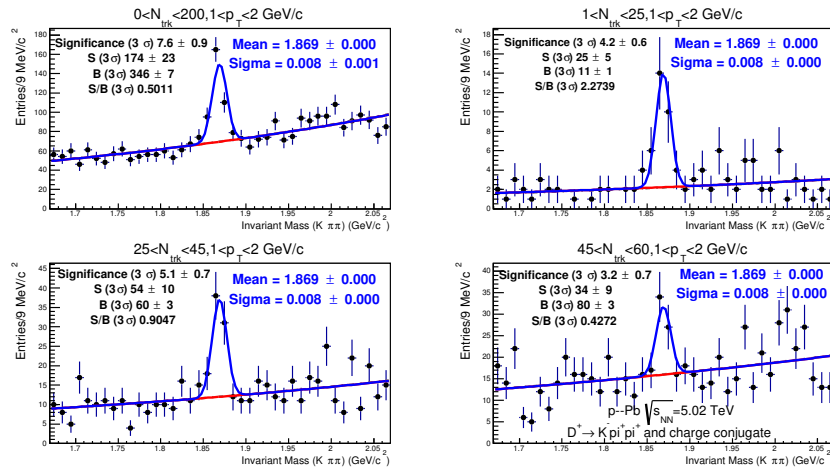


FIGURE 7.18: D^+ candidate invariant mass distributions from p–Pb collisions at $\sqrt{s_{\text{NN}}} = 5.02$ TeV in the p_{T} bin $1 < p_{\text{T}} < 2$ GeV/c integrated over multiplicity and in three multiplicity intervals ranging from 1 to 60 N_{trk} .

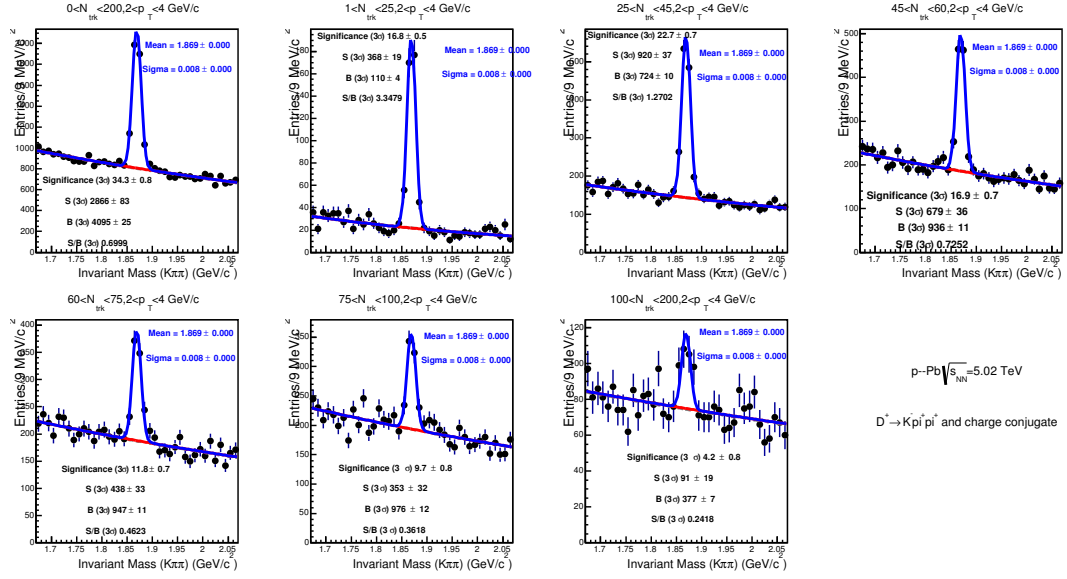


FIGURE 7.19: D^+ candidate invariant mass distributions from p–Pb collisions at $\sqrt{s_{NN}} = 5.02$ TeV in the p_T bin $2 < p_T < 4$ GeV/c integrated over multiplicity and in six multiplicity intervals ranging from 1 to 200 N_{trk} .

the signal. In order to reduce the influence of statistical fluctuations, the raw yields were determined by fixing in the fit the centroid of the signal Gaussians to the world-average D^+ mesons mass from PDG, and its width to the value obtained from a fit to the invariant mass distribution in minimum-bias events, where the signal statistical significance is larger.

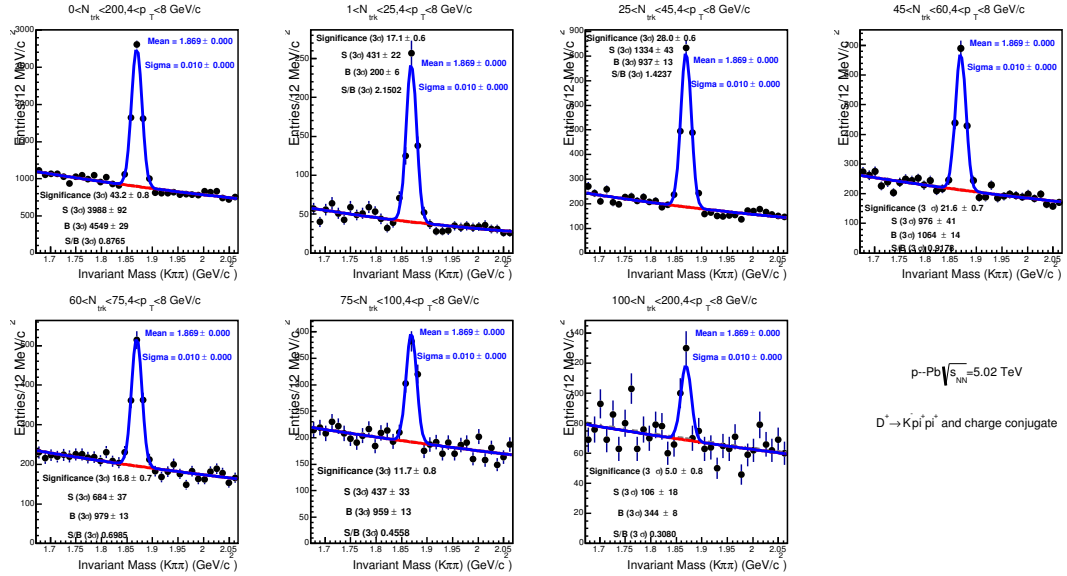


FIGURE 7.20: D^+ candidate invariant mass distributions from p–Pb collisions at $\sqrt{s_{NN}} = 5.02$ TeV in the p_T bin $4 < p_T < 8$ GeV/c integrated over multiplicity and in six multiplicity intervals ranging from 1 to 200 N_{trk} .

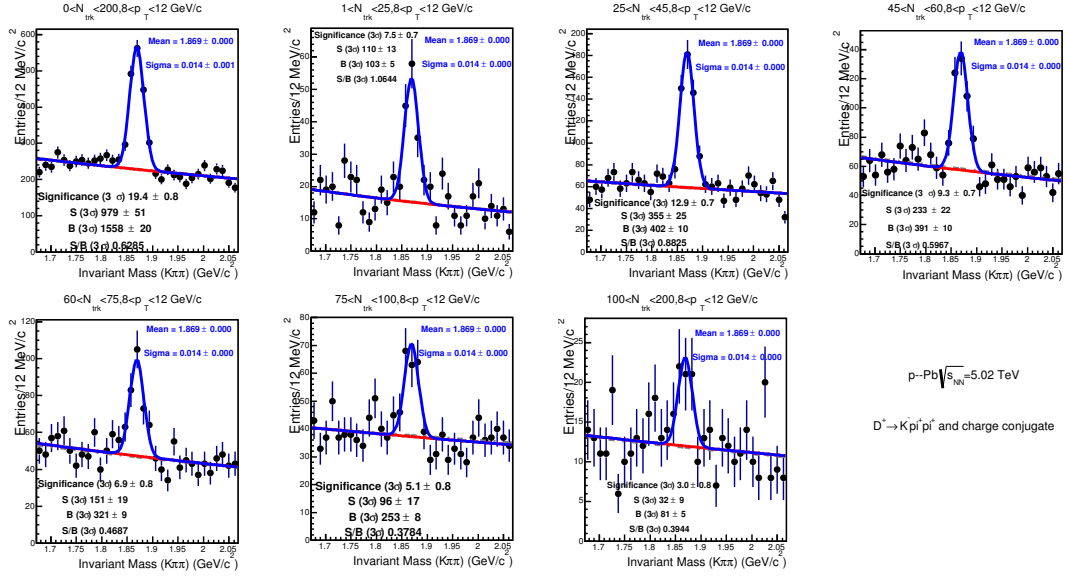


FIGURE 7.21: D^+ candidate invariant mass distributions from p–Pb collisions at $\sqrt{s_{NN}} = 5.02$ TeV in the p_T bin $8 < p_T < 12$ GeV/c integrated over multiplicity and in six multiplicity intervals ranging from 1 to 200 N_{trk} .

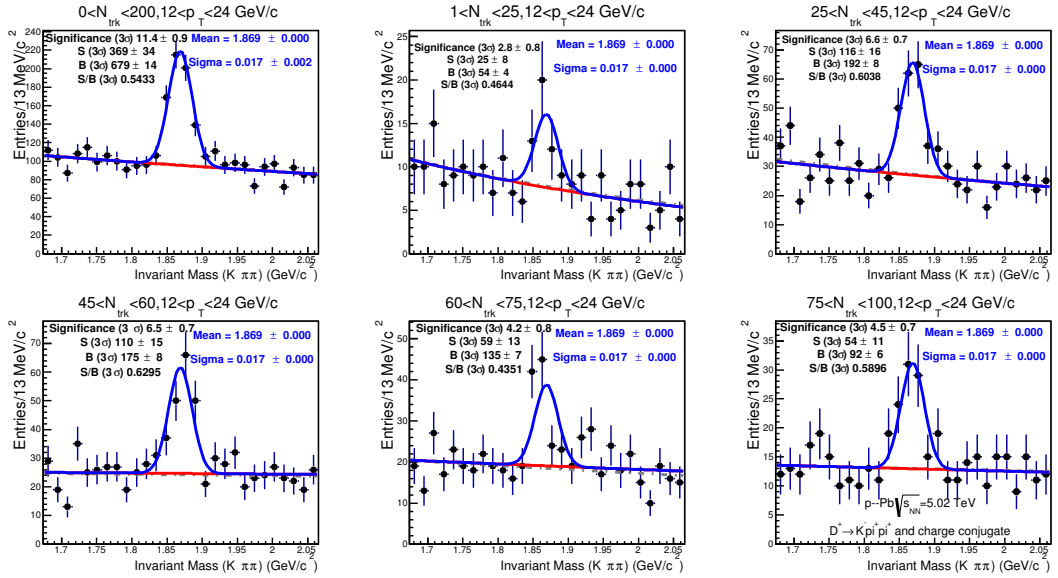


FIGURE 7.22: D^+ candidate invariant mass distributions from p–Pb collisions at $\sqrt{s_{NN}} = 5.02$ TeV in the p_T bin $12 < p_T < 24$ GeV/c integrated over multiplicity and in six multiplicity intervals ranging from 1 to 200 N_{trk} .

7.2.3 Selection efficiency correction and beauty feed-down subtraction

The raw yields obtained in the previous section are corrected for the reconstruction and selection efficiency according to Equation 7.3. The D^+ -meson efficiencies as a function of p_T and N_{trk} were obtained from the MC data sample described in Section 4.2.1. The efficiency correction factor is obtained as the ratio of the $kStepRecoPID$ and $kStepAcceptance$ containers. In Figure 7.23 the efficiency is shown as a function of N_{trk} in the five p_T intervals considered in the analysis. These efficiencies are obtained applying the same reweighting on p_T shape of generated D^+ mesons and N_{trk} distributions discussed

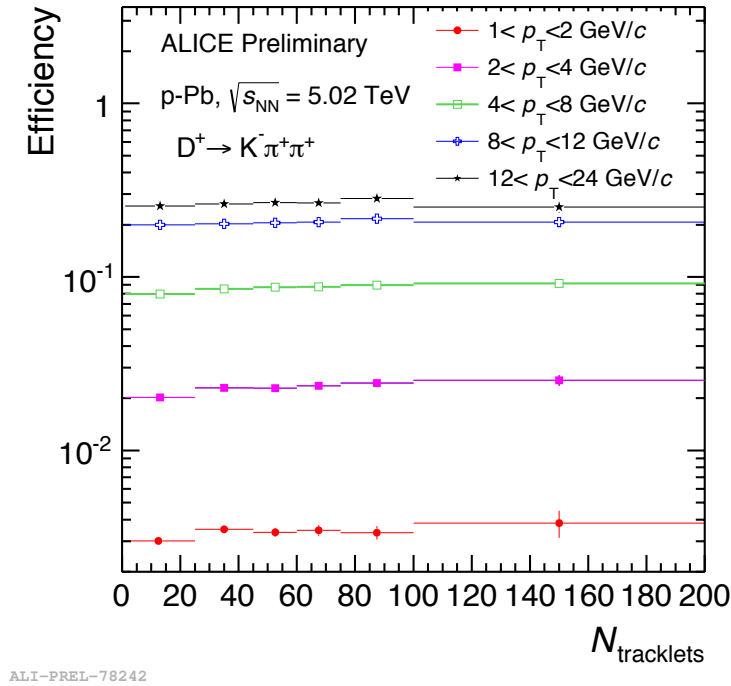


FIGURE 7.23: D^+ mesons selection efficiencies as a function of N_{trk} in five p_T intervals ranging from 1 to 24 GeV/c.

in Section 5.3. At low p_T the selection efficiency increases with increasing N_{trk} . This is due to the fact that, as shown in Figure 3.11, the resolution on the position of the primary vertex increases with multiplicity.

The acceptance correction ($kStepAcceptance$ over $kStepGeneratedLimAcc$) does not depend on multiplicity¹ and simplifies in the ratio of Equation 7.3.

For the computation of the central values of D^+ -meson self-normalized yield, the assumption that f_{prompt} does not depend on multiplicity is used, so that f_{prompt} cancels out in the numerator and denominator of Equation 7.3. However, the production of B hadrons and of prompt D^+ mesons can have a different trend with charged particles multiplicity. A systematic uncertainty due to this possible effect has been estimated and assigned, as discussed in next section.

7.2.4 Systematic Uncertainties

7.2.4.1 Systematic uncertainty on the yield extraction

The yield extraction systematic uncertainties were evaluated in the various multiplicity and p_T intervals with the same strategy described in Section 5.6.1 with two differences:

¹This is strictly true only if the p_T distribution of D^+ -meson does not depend on multiplicity. The $Q_{\text{pPb}}^{\text{mult}}$ values shown previously indicate that the p_T shape of D^+ -meson does not depend on multiplicity, within the uncertainty of the measurement.

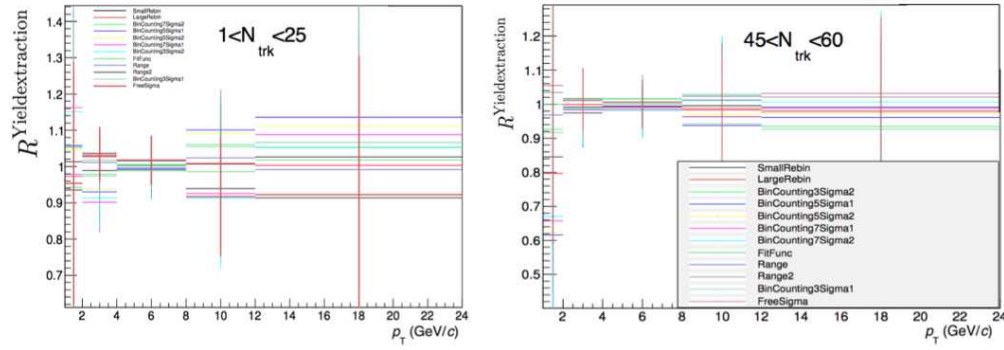


FIGURE 7.24: $R^{\text{Yield extraction}}$ as a function of p_T in the multiplicity intervals $1 < N_{\text{trk}} < 25$ and $45 < N_{\text{trk}} < 60$.

- since here the raw yields in the multiplicity intervals are evaluated fixing the sigma of the invariant mass peak to the value obtained in the multiplicity integrated case, the systematic uncertainty is evaluated letting the sigma free to vary in the fit
- the effect of the variation of the fit configuration was studied on the quantity

$$R^{\text{Yield extraction}} = \frac{Y_{\text{var}}^{\text{mult bin}} / Y_{\text{var}}^{\text{mult int}}}{Y_{\text{central}}^{\text{mult bin}} / Y_{\text{central}}^{\text{mult int}}} \quad (7.4)$$

where $Y_{\text{var}}^{\text{mult bin}}$ is the raw yield in a given multiplicity interval evaluated with the different fit strategies described in Section 5.6.1, $Y_{\text{var}}^{\text{mult int}}$ is the D^+ raw yield in the multiplicity integrated sample measured with the same variation of the fit configuration and $Y_{\text{central}}^{\text{mult bin (int)}}$ are the central values in the multiplicity intervals (multiplicity integrated)

Figure 7.24 shows the relative variations of $R^{\text{Yield extraction}}$ as a function of p_T in the multiplicity intervals $1 < N_{\text{trk}} < 25$ (left) and $45 < N_{\text{trk}} < 60$ (right). The systematic uncertainties assigned to each multiplicity and p_T interval are reported in Table 7.13.

7.2.4.2 Systematic uncertainty on the topological cut efficiency

Since in this analysis the same cuts are used in each multiplicity interval and in the multiplicity integrated sample, it is expected that the cut efficiency systematic errors

p_T (GeV/c)	Multiplicity bin					
	1-24	25-44	45-60	60-75	75-99	100-200
1-2	8 %	8%	15%	-	-	-
2-4	6 %	4%	4%	6%	8%	10%
4-8	6 %	4%	4%	6%	8%	10%
8-12	8 %	6%	6%	6%	8%	10%
12-24	10 %	10%	10%	15%	15%	-

TABLE 7.13: Summary table of the yield extraction systematic.

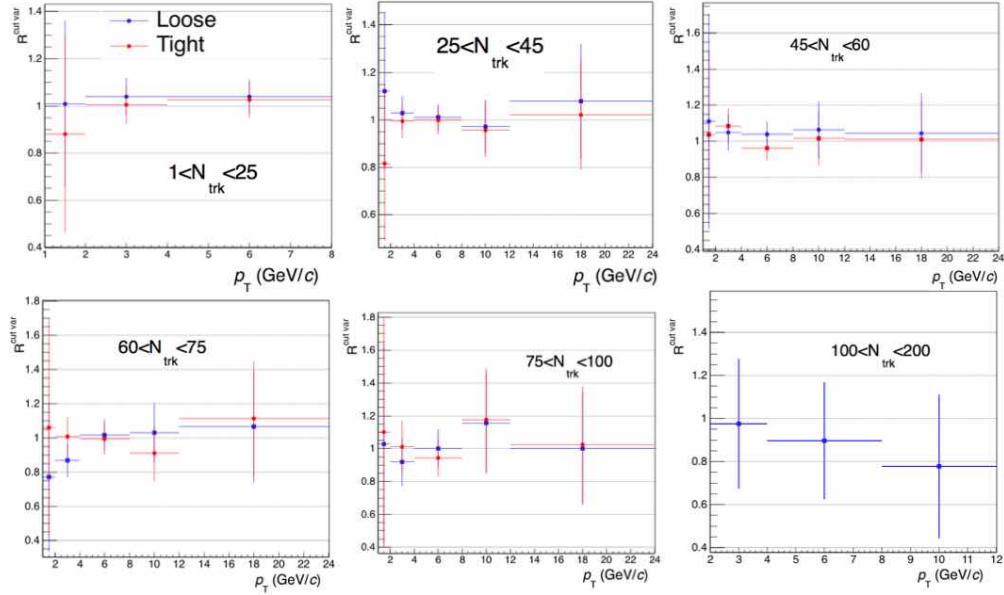


FIGURE 7.25: R^{curvar} (i.e. variation of the self normalized yields when varying the topological cuts) for the six multiplicity bins as a function of p_T .

will cancel out in the ratio of Equation 7.3 and no systematic uncertainty due to the description of the cut variables in the MC is present. As a check, the corrected yields were calculated, both in multiplicity bins and integrated over multiplicity, using different sets of cuts (tighter/looser than the central ones). To do this the raw yields and the efficiencies and the raw yields were combined according to the following formula

$$R^{\text{cutvar}} = \frac{Y_{\text{loose/tight}}^{\text{mult}} / (\epsilon_{\text{loose/tight}}^{\text{mult}}) / Y_{\text{loose/tight}}^{\text{tot}} / (\epsilon_{\text{loose/tight}}^{\text{tot}})}{Y_{\text{central}}^{\text{mult}} / (\epsilon_{\text{central}}^{\text{mult}}) / Y_{\text{central}}^{\text{tot}} / (\epsilon_{\text{central}}^{\text{tot}})} \quad (7.5)$$

The values of R^{curvar} are shown in Figure 7.25 for the six multiplicity intervals as a function of p_T . In the higher multiplicity bin the D^+ signal could not be extracted with the tight set of topological cuts. All values are compatible with unity and no systematic uncertainty is therefore assigned.

7.2.4.3 Systematic uncertainty on PID

The systematic due to PID is also expected to cancel out in the ratio of Equation 7.3. In fact, the TPC response is stable up to multiplicities of at least 400 tracks, so no variation of its response in the range considered in this analysis is expected. For what concerns the TOF information, an effect on the resolution of the start of time information t_0 (Section 3.1.3) could be expected, with better resolution at high multiplicities. However this effect has a small influence on the PID strategy discussed in Section 4.1.4. As a cross check, the same ratio of Equation 7.5 (here called R^{PID}) was evaluated using D^+ -meson the yields obtained with and without PID in all the p_T and multiplicity intervals. The result is shown in Figure 7.26. The p_T bin $1 < p_T < 2$ GeV/c is not shown since here the D^+ signal could not be extracted without PID. All ratios R^{PID} are compatible with unity (the big discrepancy in $4 < p_T < 8$ GeV/c for the interval $100 < N_{\text{trk}} < 200$ is due to the fact the fit on the invariant mass distribution obtained without PID is not stable) and no

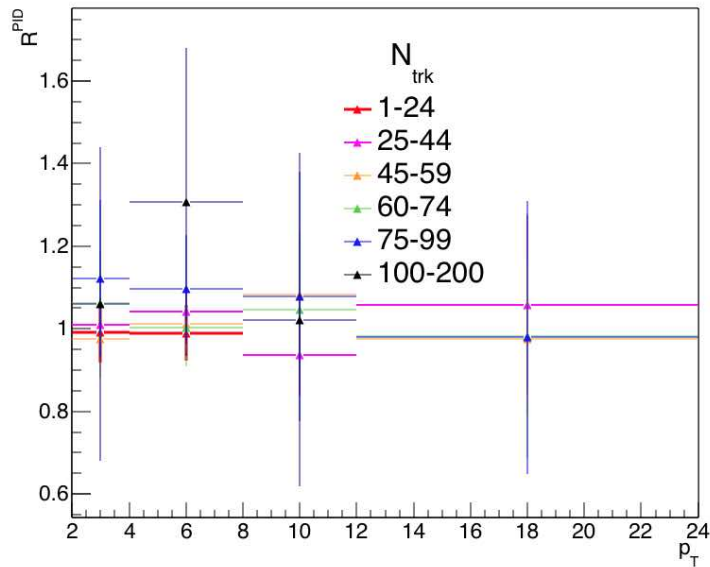


FIGURE 7.26: Relative variation of R^{PID} for the six multiplicity bins as a function of p_T .

PID uncertainty is assigned.

7.2.4.4 Systematic uncertainty on beauty feed-down subtraction

The D^+ -meson self-normalized yields are calculated assuming that the relative contribution of B decays to the D^+ -meson yields in the different multiplicity bins is constant and equal to that in the multiplicity integrated sample. However, the dependence of B hadron and prompt D^+ -meson production on the charged particles density could differ. Simulations performed with PYTHIA 6 in the extreme scenario of the hard-QCD tune [149] show that the ratio of the B to D^+ -meson relative yield evolution with multiplicity presents a linear increase with increasing multiplicity.

Therefore, to evaluate the systematic the relative fraction of D^+ from B hadrons decays was varied with charged particle multiplicity by a factor of 0.5 (at low multiplicity) to 2 (at high multiplicity) as shown in Figure 7.27 (left). The relative fraction of prompt D^+ yield, f_{prompt} , in the multiplicity integrated sample was computed with both N_b and f_c methods as described in Section 5.4. Starting from these multiplicity integrated f_{prompt} values, the f_{prompt} values in the different multiplicity intervals were obtained according to the assumptions of Figure 7.27 (left), obtaining a range of f_{prompt} values that is converted into a relative uncertainty on the D^+ -meson self-normalized yields.

The calculation was done independently for:

- the upper and lower values of the uncertainties on f_{prompt} , which originate from the variation of the pQCD parameters in the FONLL calculation discussed in Section 5.6.6
- the two methods N_b and f_c

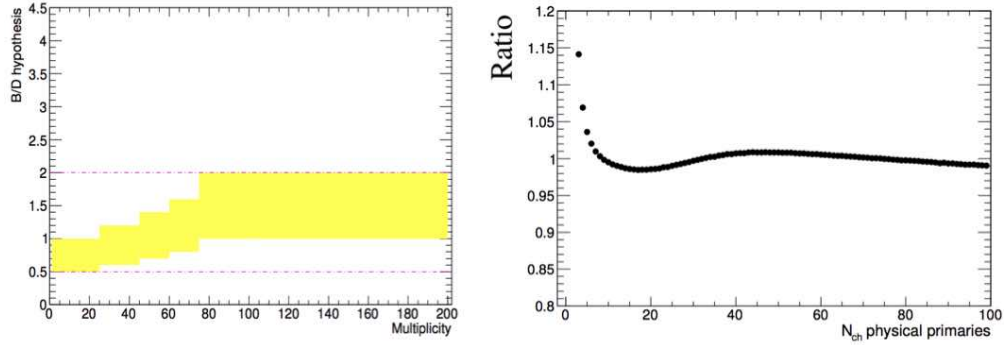


FIGURE 7.27: Left: hypothesis on the relative fraction of D^+ from B hadrons as a function of multiplicity used to evaluate the f_{prompt} systematic uncertainty. Right: deviations from the linear dependence of N_{trk} on N_{ch} .

The final relative uncertainties on the D^+ -meson self-normalized yields are assigned as the envelope of these cases.

7.2.4.5 Systematic uncertainty on the determination of N_{ch}

The systematic uncertainty on the variable used to quantify the multiplicity of the collision $dN_{\text{ch}}/d\eta/\langle dN_{\text{ch}}/d\eta \rangle_{\text{int}}^{\text{mult}}$ was assigned evaluating the deviations from the linear dependence of N_{trk} on N_{ch} shown in Figure 7.17. This was checked by dividing the actual mean of N_{trk} at each value of N_{ch} by the value of the linear fit in Figure 7.17. The resulting ratio is shown in Figure 7.27 (right). A systematic uncertainty of 3% was assigned to each multiplicity interval.

7.2.5 Results

The results of the D^+ -meson self normalized yields for the five p_{T} intervals are presented in Figure 7.28 as a function of the relative primary charged particle multiplicity $(dN_{\text{ch}}/d\eta)/\langle dN_{\text{ch}}/d\eta \rangle$. The self normalized yields are presented in the top panels with their statistical (vertical bars) and systematic (boxes) uncertainties except for the uncertainty on the feed-down fraction, which is drawn separately in the bottom panels in the form of relative uncertainties. The points are located on the x -axis at the average value of the relative charged particle multiplicity, $(dN_{\text{ch}}/d\eta)/\langle dN_{\text{ch}}/d\eta \rangle$ for every N_{trk} interval as shown in Table 7.11. The D^+ -meson self normalized yields in different p_{T} intervals are in agreement within uncertainties for all multiplicity intervals.

The self normalized yields were also computed for D^0 and D^{*+} mesons. The average D^+ , D^0 and D^{*+} mesons self normalized yields were computed for each p_{T} interval using as weights the inverse square of their relative uncertainties and is shown in Figure 7.29 (left). The average D meson self normalized yields increase with the primary charged particles multiplicity by about a factor of eight in the range $0.5 \div 4.5 \times (dN_{\text{ch}}/d\eta)/\langle dN_{\text{ch}}/d\eta \rangle$. In order to compare the trend with multiplicity in the different p_{T} intervals, the average D -meson self normalized yields in the different p_{T} intervals were divided by the one in $2 < p_{\text{T}} < 4$ GeV/c. The result is shown in Figure 7.29 (right). Within current uncertainties no p_{T} trend of the self normalized yields is visible.

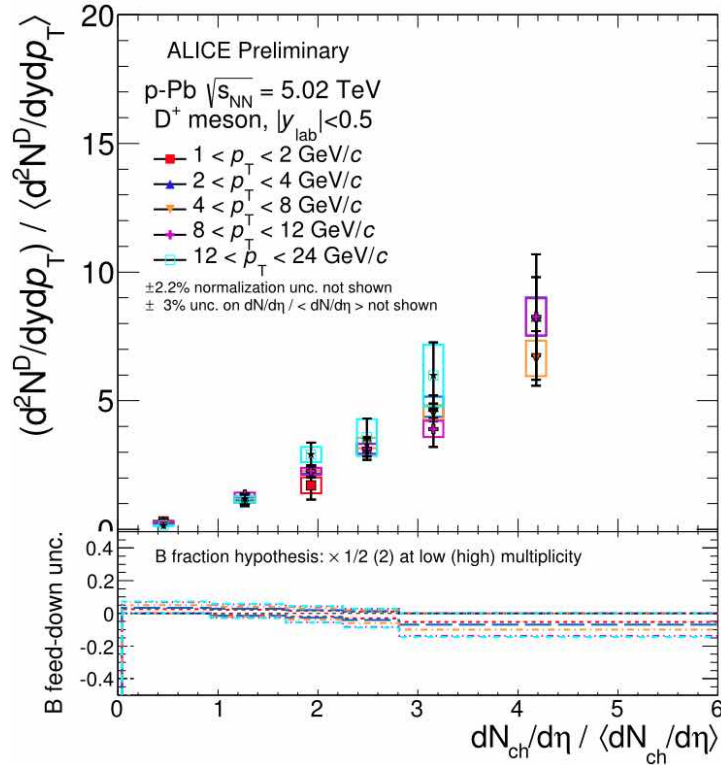


FIGURE 7.28: D^+ -meson self normalized yields in five p_T intervals as a function of the relative primary charged particle multiplicity in p-Pb collisions at $\sqrt{s_{NN}} = 5.02$ TeV. Right: average D^+ , D^0 and D^{*+} mesons self normalized yields in five p_T intervals as a function of the relative primary charged particle multiplicity in p-Pb collisions at $\sqrt{s_{NN}} = 5.02$ TeV.

It is interesting to compare the trend of the self normalized yields as a function of the relative primary charged particle multiplicity in pp and p-Pb collisions. Figure 7.30 (left) shows D^+ -meson self normalized yields as a function of multiplicity in pp collisions at $\sqrt{s} = 7$ TeV, measured in three p_T bins from 2 to 12 GeV/c. The D^+ -meson self normalized yields as a function of the relative primary charged particle multiplicity show a trend similar to the one observed in p-Pb collisions. This observation is confirmed in Figure 7.30 (right) where the D^0 self normalized yields are shown together for pp and p-Pb collisions in the p_T interval $2 < p_T < 4$ GeV/c. The increasing trend present in pp collisions is interpreted as due to MPIs and/or to a larger amount of gluon radiation in collisions where heavy quarks are produced, while in p-Pb collisions it is also due to a higher number of binary collisions.

To conclude we will compare the results relative to open charm production as a function of multiplicity to those relative to hidden charm (J/Ψ). Figure 7.31 (left) shows the average D meson and inclusive (prompt + feed-down) J/Ψ self normalized yields as a function of relative charged particle multiplicity, for D mesons in the range $2 < p_T < 4$ GeV/c and inclusive J/Ψ for $p_T > 0$ GeV/c. in two rapidity intervals, namely $2.5 < y_{lab} < 4$ and $-4 < y_{lab} < -2.5$. The inclusive J/Ψ self normalized yields also show an increase as a function of relative charged particle multiplicity, with higher values of the self normalized yields at backward rapidity, i.e. in the Pb-going direction. The different increase of inclusive J/Ψ self normalized yields at forward and backward rapidities is coherent with the $Q_{pPb}^{mult}(p_T)$ results shown in Figure 7.12 and it is due to the different cold nuclear matter effects in the two rapidity regions. The situation is different in pp collisions at \sqrt{s}

= 7 TeV: as shown in Figure 7.31 (right), a similar increase of the relative yield with the charged particle multiplicity is observed for open (D^0 -meson) and hidden (inclusive J/Ψ) charm production, the latter measured both at central ($|y_{\text{lab}}|=|y_{\text{cms}}|<0.9$) and forward ($2.5<|y_{\text{lab}}|<4$) rapidities.

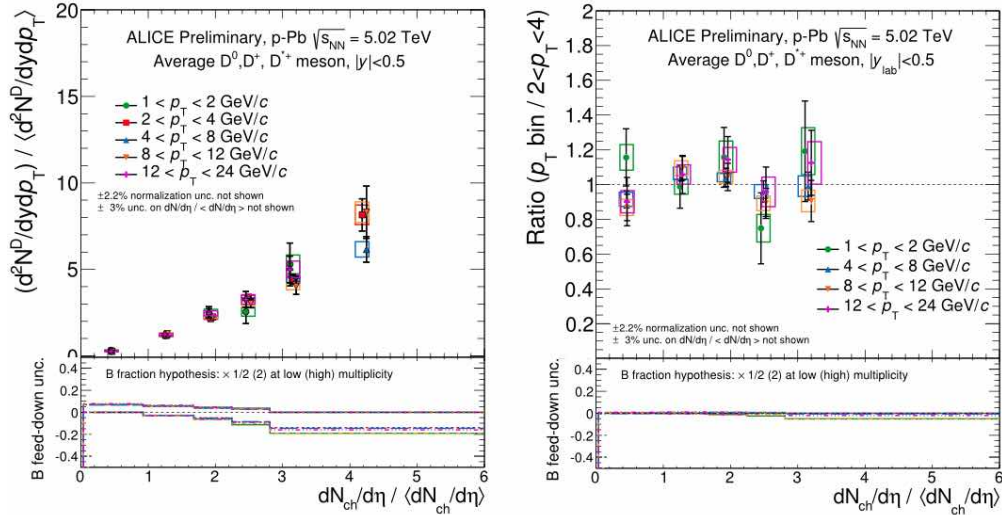


FIGURE 7.29: Left: average D^+ , D^0 and D^{*+} mesons self normalized yields in five p_T intervals as a function of the relative primary charged particle multiplicity in p-Pb collisions at $\sqrt{s_{\text{NN}}} = 5.02$ TeV. Right: average D^+ , D^0 and D^{*+} mesons self normalized yields in the different p_T intervals divided by the average self normalized yield in $2 < p_T < 4$ GeV/c in p-Pb collisions at $\sqrt{s_{\text{NN}}} = 5.02$ TeV.

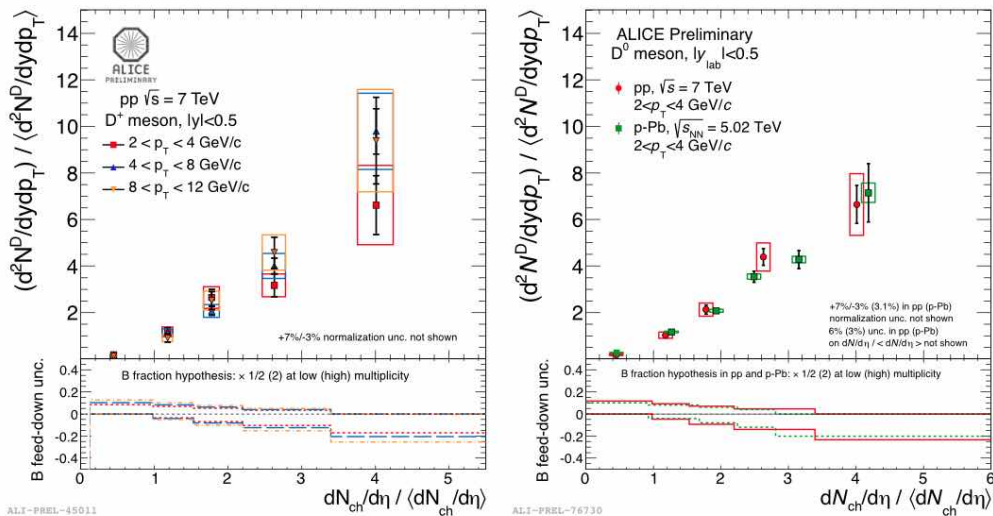


FIGURE 7.30: Left: D^+ -meson self normalized yields in three p_T intervals as a function of the relative primary charged particle multiplicity in pp collisions at $\sqrt{s_{\text{NN}}} = 7$ TeV. Right: D^0 self normalized yields in pp collisions at $\sqrt{s} = 7$ TeV and p-Pb collisions at $\sqrt{s_{\text{NN}}} = 5.02$ TeV in the p_T interval $2 < p_T < 4$ GeV/c.

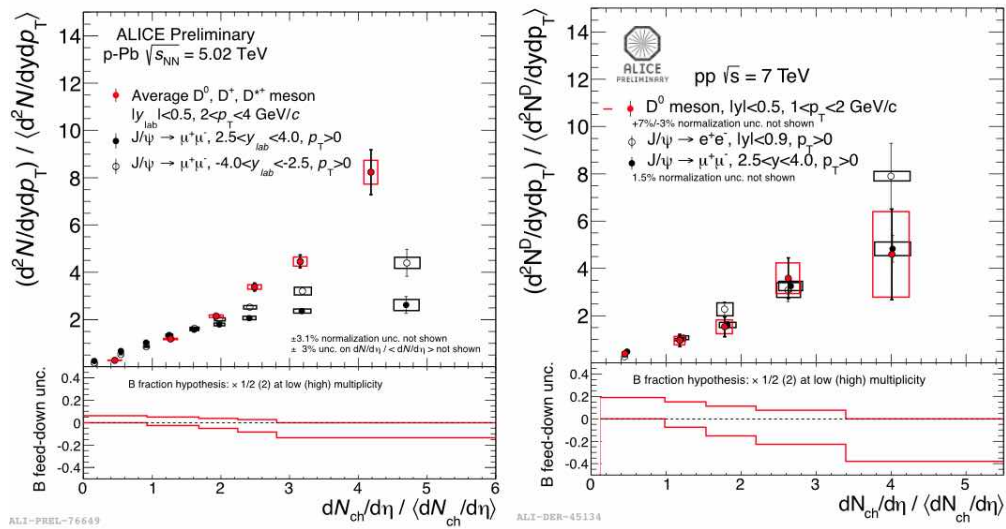


FIGURE 7.31: Left: average D meson and inclusive J/Ψ self normalized yields as a function of relative charged particle multiplicity in p-Pb collisions at $\sqrt{s_{NN}} = 5.02$ TeV. Right: D^0 meson and inclusive J/Ψ self normalized yields as a function of relative charged particle multiplicity in pp collisions at $\sqrt{s} = 7$ TeV.

Chapter 8

Conclusions

In this thesis several results were obtained by reconstructing D^+ mesons (and their antiparticles) in their $K^-\pi^+\pi^+$ hadronic decay channel at mid-rapidity in p–Pb collisions at $\sqrt{s_{\text{NN}}} = 5.02$ TeV. The vertex reconstruction and particle identification capabilities of the ALICE central barrel were exploited in order to reduce the combinatorial background, so as to be able to extract D^+ -meson signal with significance larger than three (up to 24) in different transverse momentum, rapidity and multiplicity intervals.

The D^+ -meson production cross section was measured in five rapidity intervals (measured in the centre of mass of the p–Pb system) for three wide p_{T} intervals showing no significant rapidity dependence in the range $-1.265 < y_{\text{cms}} < 0.335$.

The D^+ -meson production cross section was also measured in the rapidity range $-0.96 < y_{\text{cms}} < 0.04$ in ten transverse momentum intervals in the range $1 < p_{\text{T}} < 24$ GeV/c, and compared to the pp cross-section at $\sqrt{s_{\text{NN}}} = 5.02$ TeV/c scaled by mass number A of the Pb nucleus. The resulting nuclear modification factor of D^+ -meson is compatible with unity within uncertainties, showing that D^+ -meson production in p–Pb collisions at $\sqrt{s_{\text{NN}}} = 5.02$ TeV scales with the number of binary nucleon-nucleon collisions with respect to pp collisions at the same energy. The nuclear modification factor of D^+ -meson is described by models taking into account nuclear shadowing of PDFs and saturation models, k_{T} broadening and cold nuclear matter energy loss as well as by calculations based on gluon saturation in the initial state. This measurement allows us to conclude that the suppressions of D -meson yield at high p_{T} in central Pb–Pb collisions can not be due to initial state effects only, implying that hot nuclear matter effects must be present.

A data-driven method for subtracting the fraction of the D^+ mesons yield coming from B-hadron decays has been developed. The results are compatible with those obtained with a theory-driven method based on pQCD, although with larger uncertainties. However the uncertainty might be significantly reduced if this method is applied to a larger data sample, like the one expected from the LHC Run II.

After observing that centrality determination in p–Pb collisions is affected by several sources of bias when using centrality estimators based on multiplicity, an almost bias-free method for determining centrality has been presented, the hybrid method. The results of $Q_{\text{pPb}}^{\text{mult}}$ obtained with the hybrid method are compatible with unity within uncertainties in the four event activity classes studied, showing no evidence of strong cold nuclear matter effects in the highest event activity classes for p–Pb collisions. This result is in agreement with the $Q_{\text{pPb}}^{\text{mult}}$ measurement for charged particles.

Finally, the D^+ -meson yield has been extracted as a function of the multiplicity of charged particles produced in the collisions. The results show an increase of D^+ -meson production rate with increasing charged particle multiplicities, that might be due to the higher number of nucleon-nucleon collisions and/or to a higher number of multi-parton interactions (MPIs) for high multiplicity events. By comparing these results with those obtained in pp collisions and with model calculations, valuable information can be obtained on the role of MPIs in $c\bar{c}$ pair production and on the interplay of hard and soft processes in hadronic collisions.

Appendix A

R_{pPb} equations

I would like to demonstrate here the second equality of Equation 2.11:

$$R_{pA}(p_T) = \frac{dN^{pA}/dp_T}{\langle N_{\text{coll}} \rangle dN^{\text{pp}}/dp_T} = \frac{d\sigma^{pA}/dp_T}{A d\sigma^{\text{pp}}/dp_T} \quad (\text{A.1})$$

I recall the equations for the corrected per-event yield for prompt D^+ mesons:

$$\frac{dN^{D^+}}{dp_T} = \frac{1}{2} \frac{1}{\Delta y \Delta p_T} \frac{f_{\text{prompt}} \cdot N_{\text{raw}}^{D^{+/-}} |_{|y| < y_{fid}}}{(\text{Acc} \times \epsilon)^{\text{prompt}} \cdot BR \cdot N_{\text{ev}}} \quad (\text{A.2})$$

and for the corrected invariant cross section as:

$$\frac{d\sigma^{D^+}}{dp_T} = \frac{1}{2} \frac{1}{\Delta y \Delta p_T} \frac{f_{\text{prompt}} \cdot N_{\text{raw}}^{D^{+/-}} |_{|y| < y_{fid}}}{(\text{Acc} \times \epsilon)^{\text{prompt}} \cdot BR \cdot L_{\text{int}}} \quad (\text{A.3})$$

Then

$$\frac{\frac{d\sigma^{D^+}}{dp_T}}{\frac{dN^{D^+}}{dp_T}} = \frac{N_{\text{ev}}}{L_{\text{int}}} \quad (\text{A.4})$$

The last equation can be used to express $R_{pA}(p_T)$ in terms of $d\sigma^{pA}/dp_T$

$$R_{pA}(p_T) = \frac{dN^{pA}/dp_T}{\langle N_{\text{coll}} \rangle dN^{\text{pp}}/dp_T} = \frac{L_{\text{int}}^{pA}}{N_{\text{ev}}^{pA}} \frac{d\sigma^{pA}/dp_T}{\langle N_{\text{coll}} \rangle dN^{\text{pp}}/dp_T} = \frac{1}{\sigma_{\text{tot}}^{pA}} \frac{d\sigma^{pA}/dp_T}{\langle N_{\text{coll}} \rangle dN^{\text{pp}}/dp_T} \quad (\text{A.5})$$

Doing the same steps for dN^{pp}/dp_T in the denominator, one obtains

$$R_{pA}(p_T) = \frac{\sigma_{\text{tot}}^{\text{pp}}}{\sigma_{\text{tot}}^{pA}} \frac{d\sigma^{pA}/dp_T}{\langle N_{\text{coll}} \rangle d\sigma^{\text{pp}}/dp_T} \quad (\text{A.6})$$

Now, observing that for minimum-bias p-Pb collisions $\langle N_{\text{coll}} \rangle = A \frac{\sigma_{\text{tot}}^{\text{NN}}}{\sigma_{\text{tot}}^{pA}}$ and assuming that at this energies $\sigma_{\text{tot}}^{\text{NN}} = \sigma_{\text{tot}}^{\text{pp}}$, we finally get

$$R_{pA}(p_T) = \frac{d\sigma^{pA}/dp_T}{A d\sigma^{\text{pp}}/dp_T} \quad (\text{A.7})$$

Appendix B

ALICE Coordinate System

The ALICE coordinate system is a right-handed orthogonal Cartesian system with point of origin $x, y, z = 0$ at the beams interaction point (IP). The axes, azimuthal angle φ and polar angle θ are defined as follows:

- **x axis:** perpendicular to the mean beam direction, aligned with the local horizontal and pointing to the accelerator centre. Positive x is from the point of origin toward the accelerator centre, negative x is from the point of origin outward
- **y axis:** perpendicular to the x axis and the mean local beam direction, pointing upward. Positive y is from the point of origin upward, negative y is from the point of origin downward
- **z axis:** parallel to the mean beam direction. Negative z is from the point of origin toward the muon arm
- **azimuthal angle φ :** increases counter-clockwise from x ($\varphi=0$) to y ($\varphi=\pi/2$) with the observer standing at positive z and looking in direction of the muon arm
- **polar angle θ :** increases from z ($\theta=0$), to xy plane ($\theta=\pi/2$) to $-z$ ($\theta=\pi$)

The conversion from spherical to Cartesian coordinates is done through:

$$\begin{aligned}x &= r \sin \theta \cos \varphi \\y &= r \sin \theta \sin \varphi \\z &= r \cos \theta\end{aligned}\tag{B.1}$$

The inverse conversion from Cartesian to spherical coordinates is:

$$\begin{aligned}r &= \sqrt{x^2 + y^2 + z^2} \\ \theta &= \arccos z/r \\ \varphi &= \arctan y/x\end{aligned}\tag{B.2}$$

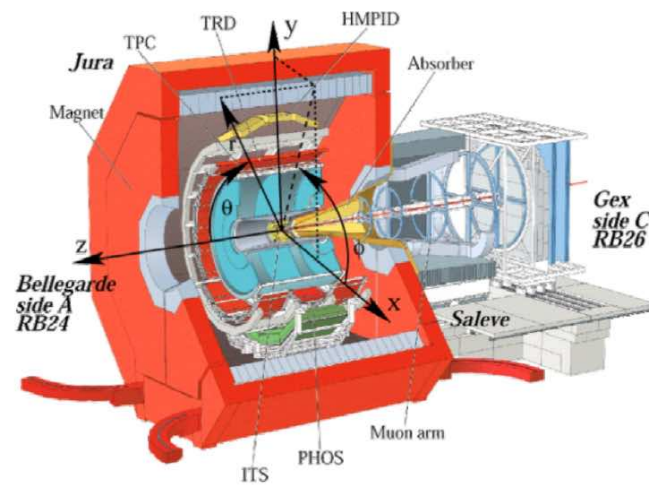


FIGURE B.1: ALICE Coordinate System (in this figure φ is tagged as ϕ).

Bibliography

- [1] ALICE Collaboration. Measurement of prompt D-meson production in p-Pb collisions at $\sqrt{s_{NN}} = 5.02$ TeV. *PRL* 113, 232301, 2014.
- [2] M.L. Mangano. Introduction to QCD in hadronic collisions. 2006.
- [3] A. Martin F. Halzen. Quarks and leptons. *John Wiley & Sons*, 1984.
- [4] E.D. Bloom et al. High energy inelastic e-p scattering at 6° and 10° . *Phys. Rev. Lett.*, 1985.
- [5] B. Muller. The physics of Quark Gluon Plasma. *Springer Verlag*, 1985.
- [6] D. Griffiths. Introduction to elementary particles. *John Wiley & Sons*, 1987.
- [7] F. Wilczek D. Gross. Asymptotically free gauge theories. *Phys. Rev. D*, 8:3633–3652, Nov 1973.
- [8] J. Bartke. Introduction to relativistic heavy ion physics. *World Scientific*, 2009.
- [9] Rolf Hagedorn. *Suppl. Nuovo Cim.* 3, 1965.
- [10] N. Cabibbo and G. Parisi. Exponential hadronic spectrum and quark liberation. *Physics Letters B*, 59(1):67 – 69, 1975.
- [11] K. Johnson A. Chodos, R. L. Jaffe and C. B. Thorn. Baryon structure in the bag theory. *Phys. Rev. D* 12 (1974) 2599, 1974.
- [12] S. Hands. The phase diagram of QCD. *Contemp.Phys.*42:209-225, 2001.
- [13] K. Yagy. Quark-Gluon Plasma. *Cambridge University Press*, 2005.
- [14] C. Wong. Introduction to high-energy heavy-ion collisions. *World Scientific*, 1995.
- [15] Mark G. Alford et al. Color superconductivity in dense quark matter. *Rev.Mod.Phys.* 80, 2008.
- [16] R. Vogt. Ultrarelativistic heavy-ion collisions. *Elsevier*, 2007.
- [17] ALICE collaboration. Physics performance report. *Journal of Physics G*, 2004.
- [18] Bikash Sinha Sourav Sarkar, Helmut Satz. The physics of the Quark-Gluon Plasma. *Springer Volume 785*, 2010.
- [19] B. Gossiaux, R. Bierkanndt, J. Aichelín. Tomography of quark gluon plasma at energies available at the BNL Relativistic Heavy Ion Collider (RHIC) and the CERN Large Hadron Collider (LHC). *PHYSICAL REVIEW C* 79, 044906 (2009), 2009.

- [20] M. Miller, K. Reygers, S. Sanders, P. Steinberg. Glauber Modeling in High Energy Nuclear Collisions. *Ann.Rev.Nucl.Part.Sci.* 57:205-243, 2007.
- [21] Nicolas Arbor for the ALICE Collaboration. Recent photon physics results from the ALICE experiment at the LHC. *EPJ Web of Conferences Volume 60*, 2013.
- [22] Benjamin Bannier (for the PHENIX collaboration). Measurements of direct photons in Au + Au collisions with PHENIX. *Nuclear Physics A 00 1-4*, 2014.
- [23] Munster University. Measurement of direct photons in pp and Pb-Pb Collisions with ALICE. *Nucl.Phys. A904-905 573c-576c*, 2013.
- [24] F. Becattini. An introduction to the statistical hadronization model. *arXiv:0901.3643*, 2009.
- [25] A. Andronic, P. Braun-Munzinger, K. Redlich, J. Stachel. The statistical model in Pb-Pb collisions at the LHC. *Nucl.Phys. A904-905*, 2013.
- [26] Michele Floris. Hadron yields and the phase diagram of strongly interacting matter. *Proceedings of the XXIV International Conference On Ultrarelativistic Nucleus-Nucleus Collisions (Quark Matter 2014)*, 2014.
- [27] ALICE Collaboration. Pion, Kaon and Proton Production in Central Pb-Pb Collisions at $\sqrt{s_{NN}} = 2.76$ TeV. *PRL 109, 252301*, 2012.
- [28] Ekkard Schnedermann, Josef Sollfrank, and Ulrich Heinz. Thermal phenomenology of hadrons from 200A GeV S+S collisions. *Phys. Rev. C 48, 2462*, 1993.
- [29] R. J. Fries, B. Muller, and C. Nonaka. Hadron production in heavy ion collisions: Fragmentation and recombination from a dense parton phase. *Phys.Rev.C68*, 2003.
- [30] PHENIX Collaboration. Spectra and ratios of identified particles in Au+Au and d+Au collisions at $\sqrt{s_{NN}} = 200$ GeV. *Phys. Rev. C 88, 024906 (2013)*, 2013.
- [31] ALICE Collaboration. Production of charged pions, kaons and protons at large transverse momenta in pp and Pb-Pb collisions at $\sqrt{s_{NN}} = 2.76$ TeV. *Physics Letters B 736 196-207*, 2014.
- [32] V. Greco, C.M. Ko, P. Levai. Parton Coalescence at RHIC. *Phys.Rev. C68 (2003) 034904*, 2003.
- [33] Piotr Bozek, Iwona Wykiel-Piekarska. Particle spectra in Pb-Pb collisions at 2.76 TeV. *Phys.Rev.C85:064915*, 2012.
- [34] ALICE Collaboration. Elliptic flow of charged particles in Pb-Pb collisions at 2.76 TeV. *Phys.Rev.Lett.105*, 2010.
- [35] Raimond Snellings. Anisotropic Flow from RHIC to the LHC. *Eur.Phys.J.C49:87-90*, 2007.
- [36] ALICE Collaboration. Anisotropic flow of charged hadrons, pions and (anti-)protons measured at high transverse momentum in Pb-Pb collisions at $\sqrt{s_{NN}}=2.76$ TeV. *Phys.Lett. B719 (2013) 18-28*, 2013.
- [37] D. Molnar, S.A. Voloshin. Elliptic Flow at Large Transverse Momenta from Quark Coalescence. *Phys. Rev. Lett. 91*, 2003.
- [38] K. Kovtun, D.T. Son, and A.O. Starinets. Viscosity in Strongly Interacting Quantum Field Theories from Black Hole Physics. *Phys. Rev. Lett. 94, 111601*, 2005.
- [39] Matthew Luzum and Paul Romatschke. Viscous Hydrodynamic Predictions for Nuclear Collisions at the LHC. *Phys. Rev. Lett. 103, 262302*, 2009.

- [40] C. Shen, U. Heinz, P. Huovinen, H. Song. Radial and elliptic flow in Pb+Pb collisions at the Large Hadron Collider from viscous hydrodynamics. *Phys.Rev. C84, 044903*, 2005.
- [41] Burak Han Alver, Clément Gombeaud, Matthew Luzum, and Jean-Yves Ollitrault. Triangular flow in hydrodynamics and transport theory. *Phys. Rev. C 82, 034913*, 2010.
- [42] ALICE Collaboration. Higher harmonic anisotropic flow measurements of charged particles in Pb-Pb collisions at $\sqrt{s_{NN}}=2.76$ TeV. *Phys.Rev.Lett. 107:032301*, 2011.
- [43] Bjoern Schenke, Sangyong Jeon, Charles Gale. Anisotropic flow in $\sqrt{s_{NN}}=2.76$ TeV Pb+Pb collisions at the LHC. *Phys.Lett. B702 59-63*, 2011.
- [44] Jan Rafelski. Strangeness and quark-gluon plasma. *Acta Physica Polonica B vol. 43*, 2012.
- [45] ALICE Collaboration. Multi-strange baryon production at mid-rapidity in Pb-Pb collisions at $\sqrt{s_{NN}} = 2.76$ TeV. *Phys. Lett. B 728 216-227*, (2014).
- [46] NA60 Collaboration. First Measurement of the ρ Spectral Function in High-Energy Nuclear Collisions. *Phys. Rev. Lett. 96, 162302*, 1996.
- [47] Ralf Rapp. Update on chiral symmetry restoration in the context of dilepton data. *J.Phys.Conf.Ser. 420 (2013) 012017*, 2013.
- [48] PHENIX Collaboration. J/Ψ Production vs Centrality, Transverse Momentum, and Rapidity in Au+Au Collisions at $\sqrt{s_{NN}} = 200$ GeV. *Phys.Rev.Lett.98:232301*, 2007.
- [49] CMS Collaboration. Observation of sequential Υ suppression in Pb-Pb collisions. *Phys. Rev. Lett. 109 (2012)*, 2012.
- [50] ALICE Collaboration. Centrality, rapidity and transverse momentum dependence of J/Ψ suppression in Pb-Pb collisions at $\sqrt{s_{NN}}=2.76$ TeV. *Phys. Lett. B 734 (2014) 314-327*, 2014.
- [51] Tiberiu Gabriel Grigorescu. Measurement of Charm Production in Deep Inelastic Scattering at HERA II. *Ph.D. Thesis, Universiteit van Amsterdam*, 2008.
- [52] M.L. Mangano. Two lectures on heavy quark production in hadronic collisions. *hep-ph/9711337*, 1997.
- [53] J. Pumplin, D.R. Stump, J. Huston, H.L. Lai, P. Nadolsky, W.K. Tung. New Generation of Parton Distributions with Uncertainties from Global QCD Analysis. *JHEP 0207:012*, 2002.
- [54] Matteo Cacciari, Paolo Nason, and Ramona Vogt. QCD Predictions for Charm and Bottom Quark Production at RHIC. *Phys. Rev. Lett. 95, 122001*, 2005.
- [55] B. A. Kniehl, G. Kramer, I. Schienbein, and H. Spiesberger. Reconciling Open-Charm Production at the Fermilab Tevatron with QCD. *Phys. Rev. Lett. 96, 012001*, 2006.
- [56] R. Vogt. Open and Hidden Heavy Flavor Production in pp, pA and AA Collisions. *Journal of Physics: Conference Series 509 (2014) 012007*, 2014.
- [57] Belle Collaboration. Charm Hadrons from charm fragmentation and beauty decays in e^+e^- annihilation at $\sqrt{s}=10.6$ GeV. *Phys.Rev.D73:032002*, 2006.
- [58] T. Kneesch, B.A. Kniehl, G. Kramer, I. Schienbein. Charmed-Meson Fragmentation Functions with Finite-Mass Corrections. *Nucl.Phys.B799:34-59*, 2008.

- [59] ALEPH Collaboration. Study of charm production in Z decays. *Eur.Phys.J.C16:597-611*, 2000.
- [60] M.Cacciari, P. Nason. Charm Cross Sections for the Tevatron Run II. *JHEP 0309 (2003) 006*, 2003.
- [61] E. Braaten, K. Cheung, S. Fleming, T.C. Yuan. Perturbative QCD Fragmentation Functions as a Model for Heavy-Quark Fragmentation. *Phys.Rev.D51:4819-4829*, 1995.
- [62] T. Kneesch, B.A. Kniehl, G. Kramer, I. Schienbein. Charmed-Meson Fragmentation Functions with Finite-Mass Corrections. *Nucl.Phys.B799:34-59*, 2008.
- [63] Opal Collaboration. Inclusive Analysis of the b Quark Fragmentation Function in Z Decays at LEP. *Eur.Phys.J.C29:463-478*, 2003.
- [64] M. Soleymaninia, A. N. Khorramian, S. M. Moosavi Nejad, F. Arbabifar. Determination of pion and kaon fragmentation functions including spin asymmetries data in a global analysis. *Phys.Rev. D88 5*, 2013.
- [65] M.G. Bowler. $e^+ e^-$ Production of Heavy Quarks in the String Model. *Z. Phys. C11 169.*, 1981.
- [66] CDF Collaboration. Measurement of Prompt Charm Meson Production Cross Sections in pp Collisions at $\sqrt{s}=1.96$ TeV. *Phys. Rev. Lett. 91, 241804*, 2003.
- [67] STAR Collaboration. Measurement of open heavy flavour production in the STAR experiment at RHIC. *Pos (DIS 2010)182*, 2010.
- [68] ALICE Collaboration. Measurement of Charm Production at central rapidity in proton-proton collisions at $\sqrt{s} = 7$ TeV. *JHEP01 128*, 2012.
- [69] Antoni Szczurek Rafal Maciula. Open charm production at the LHC - k_T -factorization approach. *Phys.Rev. D87 9*, 2013.
- [70] LHCb Collaboration. Prompt charm production in pp collisions at $\sqrt{s}=7$ TeV. *Nuclear Physics, Section B 871*, 2013.
- [71] Péter Lévai and Ramona Vogt. Thermal charm production by massive gluons and quarks. *Phys. Rev. C 56, 2707*, 1997.
- [72] Ben-Wei Zhang, Che Ming Ko, and Wei Liu. Thermal charm production in a quark-gluon plasma in Pb-Pb collisions at $\sqrt{s_{NN}}=5.5$ TeV. *Phys. Rev. C 77, 024901*, 2008.
- [73] Alberto Accardi et. al. . Impact of nuclear dependence of $R=\sigma_L/\sigma_T$ on anti-shadowing in nuclear structure functions. *Phys.Rev. C86 (2012) 045201*, 2012.
- [74] Klaus Rith. Present Status of the EMC effect. *arXiv:1402.5000*, 2014.
- [75] F. Gelis. Color Glass Condensate and Glasma. *arXiv:1211.3327*, 2012.
- [76] C. A. Salgado K. J. Eskola, H. Paukkunen. EPS09 - a New Generation of NLO and LO Nuclear Parton Distribution Functions. *HEP 0904:065*, 2009.
- [77] M. Hirai, S. Kumano, T.-H. Nagai. Determination of nuclear parton distribution functions and their uncertainties at next-to-leading order. *Phys.Rev.C76:065207*, 2007.
- [78] A. Dainese. Charm production and in-medium QCD energy loss in nucleus-nucleus collisions with ALICE. A performance study. *arXiv:nucl-ex/0311004*, 2003.
- [79] A. Dainese. Charm and beauty of the Large Hadron Collider. *J.Phys. G31*, 2005.
- [80] J. W. Cronin et al. Production of hadrons at large transverse momentum at 200, 300, and 400 Gev. *Phys. Rev. D 11*, 1975.

- [81] M. Lev and B. Petersson. Nuclear Effects at Large Transverse Momentum in a QCD Parton Model. *Z. Phys. C Particles and Fields* 21, 155-161, 1983.
- [82] R. Baier, Yu. L. Dokshitzer, A.H. Mueller, S. Peign, D. Schiff. Radiative energy loss and p_T -broadening of high energy partons in nuclei. *Nucl.Phys.B*484:265-282, 1997.
- [83] J. D. Bjorken. Energy Loss of Energetic Partons in Quark-Gluon Plasma: Possible Extinction of High p_T Jets in Hadron-Hadron Collisions. *FERMILAB-Pub-82/59-THY*, 1982.
- [84] Stephane Peigne, Andre Peshier. Collisional energy loss of a fast heavy quark in a quark-gluon plasma. *Phys.Rev.D*77:114017, 2008.
- [85] Y.L. Dokshitzer, D.E. Kharzeev. Heavy quark colorimetry of QCD matter. *Phys.Lett.B*519, 2001.
- [86] R.Baier, Yu.L.Dokshitzer, A.H.Mueller, S.Peigné, D.Schiff. Radiative energy loss of high energy quarks and gluons in a finite volume quark-gluon plasma. *Nucl.Phys. B*483 291-320, 1997.
- [87] Néstor Armesto, Andrea Dainese, Carlos A. Salgado, Urs Achim Wiedemann. Testing the Color Charge and Mass Dependence of Parton Energy Loss with Heavy-to-light Ratios at RHIC and LHC. *Phys.Rev.D*71:054027, 2005.
- [88] Xiang Wen-Changet al. Radiative Energy Loss of Heavy Quark and Dead Cone Effect in Ultra-relativistic Heavy Ion Collisions. *Chin. Phys. Lett, Vol 22, N.1 (2005) 72*, 2005.
- [89] Cao, Qin, Bass. Heavy-quark dynamics and hadronization in ultrarelativistic heavy-ion collisions: Collisional versus radiative energy loss. *Phys.Rev. C*88 (2013) 044907, 2013.
- [90] Cao, Bass. Thermalization of charm quarks in infinite and finite QGP matter. *Phys. Rev. C* 84, 064902, 2011.
- [91] Greco, Ko, Rapp. Quark coalescence for charmed mesons in ultrarelativistic heavy-ion collisions. *Phys. Lett. B* 595 202-208, 2004.
- [92] PHENIX Collaboration. Absence of Suppression in Particle Production at Large Transverse Momentum in $\sqrt{s_{NN}} = 200$ GeV d+Au Collisions. *Phys.Rev.Lett.*91, 2003.
- [93] ALICE Collaboration. Transverse Momentum Distribution and Nuclear Modification Factor of Charged Particles in p-Pb Collisions at $\sqrt{s_{NN}}= 5.02$ TeV. *Phys.Rev.Lett.* 110 (2013) 082302, 2013.
- [94] PHENIX Collaboration. Cold-nuclear-matter effects on heavy-quark production in d+Au collisions at $\sqrt{s_{NN}} = 200$ GeV. *Phys.Rev.Lett.* 109 (2012) 24, 2012.
- [95] ALICE Collaboration. J/Ψ production and nuclear effects in p-Pb collisions at $\sqrt{s_{NN}}=5.02$ TeV. *JHEP* 02 (2014) 073, 2014.
- [96] ALICE Collaboration. Suppression of charged particle production at large transverse momentum in central Pb-Pb collisions at $\sqrt{s_{NN}}=2.76$ TeV. *Physics Letters B* 696 30-39, 2011.
- [97] STAR Collaboration. Transverse momentum and collision energy dependence of high p_T hadron suppression in Au+Au collisions at ultrarelativistic energies. *Phys.Rev.Lett.*91:172302, 2003.
- [98] CMS Collaboration. Study of high- p_T charged particle suppression in Pb-Pb compared to pp collisions at $\sqrt{s_{NN}}=2.76$ TeV. *Eur. Phys. J. C* 72:1945, 2012.

- [99] PHENIX Collaboration. Energy Loss and Flow of Heavy Quarks in Au+Au Collisions at $\sqrt{s_{NN}} = 200$ GeV. *Phys. Rev. Lett.* *98*, 172301, 2007.
- [100] STAR Collaboration. Observation of D^0 meson nuclear modifications in Au+Au collisions at $\sqrt{s_{NN}} = 200$ GeV. *Phys.Rev.Lett.* *113* (2014) 142301, 2014.
- [101] Min He, Rainer J. Fries, Ralf Rapp. Heavy Flavor at the Large Hadron Collider in a Strong Coupling Approach. *arXiv:1401.3817*, 2012.
- [102] Min He, Rainer J. Fries, Ralf Rapp. Heavy-Quark Diffusion and Hadronization in Quark-Gluon Plasma. *Phys.Rev.* *C86* 014903, 2012.
- [103] M. Djordjevic, M. Djordjevic. LHC jet suppression of light and heavy flavor observables. *Physics Letters B* *734* (2014) 286–289, 2014.
- [104] Horowitz, W.A. and Gyulassy, Miklos. The Surprising Transparency of the sQGP at LHC. *Nucl.Phys.* *A872* (2011) 265-285, 2011.
- [105] Simon Wicks, William Horowitz, Magdalena Djordjevic, Miklos Gyulassy. Elastic, Inelastic, and Path Length Fluctuations in Jet Tomography. *Nucl.Phys.A* *784*:426-442, 2007.
- [106] Marlene Nahrgang, Joerg Aichelin, Pol Bernard Gossiaux, Klaus Werner. Influence of hadronic bound states above T_c on heavy-quark observables in Pb–Pb collisions at the CERN Large Hadron Collider. *Phys. Rev. C* *89*, 014905, 2014.
- [107] K. Werner, Iu. Karpenko, T. Pierog, M. Bleicher, and K. Mikhailov. Event-by-event simulation of the three-dimensional hydrodynamic evolution from flux tube initial conditions in ultrarelativistic heavy ion collisions. *PHYSICAL REVIEW C* *82* , 044904, 2010.
- [108] I. Vitev. Testing the theory of QGP-induced energy loss at RHIC and the LHC. *Phys.Lett.B* *639*:38-45, 2006.
- [109] W.M. Alberico et al. Heavy-flavor dynamics in nucleus-nucleus collisions: from RHIC to LHC. *J.Phys.* *G38* (2011) 124144, 2011.
- [110] Stefano Frixione, Paolo Nason, Giovanni Ridolfi. A positive-weight next-to-leading-order Monte Carlo for heavy flavour hadroproduction. *JHEP* *0709*:126, 2007.
- [111] Jan Uphoff, Oliver Fochler, Zhe Xu, Carsten Greiner. Open heavy flavor in Pb–Pb collisions at $\sqrt{s_{NN}}=2.76$ TeV within a transport model. *Physics Letters B* *717*, 2012.
- [112] CMS Collaboration. Suppression of non-prompt J/Ψ , prompt J/Ψ , and $\Upsilon(1S)$ in Pb–Pb collisions at $\sqrt{s_{NN}} = 2.76$ TeV. *JHEP* *05* (2012) 063, 2012.
- [113] ALICE Collaboration. Azimuthal anisotropy of D meson production in Pb–Pb collisions at $\sqrt{s_{NN}}=2.76$ TeV. *Phys. Rev. C* *90* 034904, 2014.
- [114] ALICE Collaboration. Charged Particle Multiplicity Density at Midrapidity in Central Pb–Pb Collisions at $\sqrt{s_{NN}}=2.76$ TeV. *Phys. Rev. Lett.* *105*, 2010.
- [115] ALICE Collaboration. Performance of the ALICE Experiment at the CERN LHC. *Int. J. Mod. Phys. A* *29*, 2014.
- [116] ALICE Collaboration. The ALICE experiment at the CERN LHC. *JINST* *3* S08002, 2008.
- [117] A. Akhondinov et al. Performance of the ALICE Time-Of-Flight detector at the LHC. *Eur. Phys. J. Plus* *128*: 44, 2013.
- [118] R. Fruhwirth. Application of Kalman filtering to track and vertex fitting. *Nucl. Instr. and Meth. A* *262*, 444, 1987.

- [119] ALICE Collaboration. Centrality determination of Pb–Pb collisions at $\sqrt{s_{\text{NN}}}=2.76$ TeV with ALICE. *Phys. Rev. C* 88, 2013.
- [120] M. Alvioli, M. Strikman. Color fluctuation effects in proton-nucleus collisions. *Phys. Lett. B* 722, 2013.
- [121] Ferenc Sikler. Centrality control of hadron-nucleus interactions by detection of slow nucleons. *arXiv:hep-ph/0304065*, 2003.
- [122] ALICE Collaboration. Centrality dependence of particle production in p–Pb collisions at $\sqrt{s_{\text{NN}}}=5.02$ TeV. *arXiv:1412.6828v1*, 2014.
- [123] Particle Data Group. Review of Particle Physics. *Chinese Physics C, Volume 38, Number 9*, 2014.
- [124] E.Bruna, A.Dainese, M.Masera, F.Prino. Vertex reconstruction for proton-proton collisions in ALICE. *ALICE-INT-2009-018*, 2009.
- [125] Xin-Nian Wang and Miklos Gyulassy. HIJING: A Monte Carlo model for multiple jet production in p p, p A and A A collisions. *Phys.Rev.D* 44, 3501, 1991.
- [126] ALICE Collaboration. Suppression of $\Psi(2S)$ production in p-Pb collisions at $\sqrt{s_{\text{NN}}}=5.02$ TeV. *JHEP* 1412 073, 2014.
- [127] PHENIX Collaboration. Nuclear Modification of Ψ' , χ_c , and J/Ψ Production in d+Au Collisions at $\sqrt{s_{\text{NN}}}=200$ GeV. *PRL* 111, 202301, 2013.
- [128] CMS Collaboration. Observation of long-range, near-side angular correlations in p–Pb collisions at the LHC. *Volume 718, Issue 3, 8 January 2013, Pages 795–814*, 2013.
- [129] A.M. Sickles. Possible evidence of radial flow of heavy mesons in d+Au collisions. *Phys. Lett. B* 731 51-56, 2014.
- [130] CMS Collaboration. Observation of long-range, near-side angular correlations in proton-proton collisions at the LHC. *JHEP* 1009 (2010) 091, 2010.
- [131] CMS Collaboration. Centrality dependence of dihadron correlations and azimuthal anisotropy harmonics in PbPb collisions at $\sqrt{s_{\text{NN}}}=2.76$ TeV. *Eur. Phys. J. C (2012) 72:2012*, 2012.
- [132] ALICE Collaboration. Long-range angular correlations on the near and away side in p–pb collisions at view the mathml source. *Physics Letters B* 719 (2013) 29–41, 2013.
- [133] ATLAS Collaboration. Observation of Associated Near-Side and Away-Side Long-Range Correlations in $\sqrt{s_{\text{NN}}}=5.02$ TeV Proton-Lead Collisions with the ATLAS Detector. *Phys. Rev. Lett.* 110, 182302, 2013.
- [134] S. Voloshin, Y. Zhang. Flow study in relativistic nuclear collisions by Fourier expansion of azimuthal particle distributions. *Zeitschrift für Physik C Particles and Fields December 1996, Volume 70, Issue 4, pp 665-671*, 1996.
- [135] D.J. Lange. The EvtGen particle decay simulation package. *Nucl. Instrum. Methods A* 462 152, 2011.
- [136] R. Averbeck et al. Reference heavy flavour cross sections in pp collisions at $\sqrt{s}=2.76$ TeV, using a pQCD-driven \sqrt{s} -scaling of ALICE measurements at $\sqrt{s}=7$ TeV. *arXiv:1107.3243*, 2011.
- [137] ALICE Collaboration. Measurement of visible cross sections in proton-lead collisions at $\sqrt{s_{\text{NN}}}=5.02$ TeV in van der Meer scans with the ALICE detector. *JINST* 9 (2014) 11, P11003, 2014.

- [138] ALICE Collaboration. D_s^+ meson production at central rapidity in proton–proton collisions at $\sqrt{s} = 7$ TeV. *Physics Letters B*, 718(2):279 – 294, 2012.
- [139] H. Fujii, K Watanabe. Heavy quark pair production in high energy pA collisions: Open heavy flavors. *Nuclear Physics A* 920, 78-93, 2013.
- [140] R. Sharma, I. Vitev, B. Zhang. Light-cone wave function approach to open heavy flavor dynamics in QCD matter. *PHYSICAL REVIEW C* 80 , 054902, 2009.
- [141] Gian Michele Innocenti for the CMS Collaboration. B-meson reconstruction performance and spectra in pp and pPb collisions in CMS. *Nuclear Physics A Volume 931, November 2014, Pages 1184–1188*, 2014.
- [142] ALICE Collaboration. Suppression of high transverse momentum D mesons in central Pb–Pb collisions at $\sqrt{s_{NN}}=2.76$ TeV. *JHEP* 09 (2012) 112, 2012.
- [143] L. Frankfurt, M. Strikman, and C. Weiss. Transverse nucleon structure and diagnostics of hard parton–parton processes at LHC. *Phys.Rev. D*83 054012, 2011.
- [144] NA27 Collaboration. Comparative properties of 400 GeV/c proton-proton interactions with and without charm production. *Z. Phys. C Particles and Fields* 41,191-196, 1988.
- [145] ALICE Collaboration. J/Ψ production as a function of charged particle multiplicity in pp collisions at $\sqrt{s}=7$ TeV. *Physics Letters B Volume 712, Issue 3, 6 June 2012, Pages 165–175*, 2012.
- [146] LHCb Collaboration. Observation of double charm production involving open charm in pp collisions at $\sqrt{s} = 7$ TeV. *JHEP* 1206 (2012) 141, 2012.
- [147] CMS Collaboration. Jet and underlying event properties as a function of charged-particle multiplicity in proton–proton collisions at $\sqrt{s}= 7$ TeV. *Eur.Phys.J. C*73 2674, 2013.
- [148] ALICE Collaboration. Pseudorapidity density of charged particles in p–Pb collisions at $\sqrt{s_{NN}} = 5.02$ TeV. *Phys.Rev.Lett.* 110 (2013) 3, 032301, 2013.
- [149] T. Sjostrand, S. Mrenna, P. Skands. PYTHIA 6.4 physics and manual . *JHEP* 05 026, 2006.